UNIVERSITY OF CALIFORNIA,
IRVINE

Computational study of gene expression control through chromatin regulation

DISSERTATION

submitted in partial satisfaction of the requirements
for the degree of

DOCTOR OF PHILOSOPHY

in Mathematical, Computational, and Systems Biology

by

Alvaro Manuel Fletcher

Dissertation Committee:
Professor German Enciso, Chair
Assistant Professor Zeba Wunderlich
Assistant Professor Christopher Miles

2022

DEDICATION

To Qiwen.

TABLE OF CONTENTS

LIST OF FIGURES

Page

LIST OF TABLES

ACKNOWLEDGMENTS

I would like to thank my advisor German Enciso and Zeba Wunderlich for all their guidance and support during my time at UCI. I would like to thank Christopher Miles for being part of my committee. I would also like to thank my collaborators Rachel Waymack and Ruonan Zhao for many productive discussions. Lastly, I would like to thank my friends Tessa Morris and Qingda Hu for their help throughout our graduate studies.

The text of Chapter 2 is a reprint of the material as it appears in eLife [1]. The co-authors listed in this publication are Waymack R., Fletcher A., Enciso G., and Wunderlich Z.

Figure 4.5C is a reprint of the material as it appears in BioMed Central [2]. The co-authors listed in this publication are Wang, Y., Zhang, X., Song, Q. et al.

The text of Chapter 4 is a reprint of the material as it appears in the Journal of Theoretical Biology [3]. The co-authors listed in this publication are Fletcher A., Zhao R., and Enciso G.

This work was supported by NSF-Simons Center grant DMS1763272, NIH grant T32-EB009418, Simons Foundation grant 594598 to Qing Nie, NSF grant DMS1616233 to German Enciso, NSF grant 1440386, and the UC President's Dissertation Year Fellowship. The work in Chapter 2 was also supported by NIH grants R00-HD073191, R01HD095246, and Hellman Foundation Fellowship to Zeba Wunderlich and the ARCS Foundation Fellowship to Rachel Waymack.

VITA

Alvaro Manuel Fletcher

EDUCATION

Ph.D., Mathematical, Computational, and Systems Biology **2022**
University of California, Irvine *Irvine, California*

Bachelor of Science in Mathematics **2016**
University of Maryland, Baltimore County *Baltimore, Maryland*

RESEARCH EXPERIENCE

Graduate Student Researcher **2016–2022**
University of California, Irvine *Irvine, California*

REFEREED JOURNAL PUBLICATIONS

Fletcher A, Zhao R, Enciso G. **Non-cooperative mechanism for bounded and ultrasensitive chromatin remodeling** **2022**
Journal of Theoretical Biology; 534; 110946.

Waymack R**, Fletcher A,** Enciso G, Wunderlich Z. **Shadow enhancers can suppress input transcription factor noise through distinct regulatory logic** **2020**
eLife; 9; e59351

ARTICLES IN PREPARATION

Fletcher A, Enciso G, Wunderlich Z. **Shadow enhancers mediate trade-offs between transcriptional noise and fidelity**

Fletcher A, Enciso G. **Function saturation as a mechanism for ultrasensitivity**.

ABSTRACT OF THE DISSERTATION

Computational study of gene expression control through chromatin regulation

By

Alvaro Manuel Fletcher

Doctor of Philosophy in Mathematical, Computational, and Systems Biology

University of California, Irvine, 2022

Professor German Enciso, Chair

Gene regulation is required for proper organismic development, functioning, and reproduction. Many gene regulatory systems focus on modulating distinct features such as transcriptional noise, fidelity to transcription factors (TFs), or ultrasensitivity in gene expression. These processes generally take place before the initiation of transcription and include the remodeling of chromatin topologies. Chromatin regulation partly involves unpacking the tightly bound heterochromatin as a prerequisite for transcriptional enzymes to access genetic regions. Levels of chromatin density respond ultrasensitively to TFs which results in sharp boundaries between heterochromatin and euchromatin. Viable mechanisms for this ultrasensitivity have been proposed but typically rely on cooperative assumptions which can lead to unbounded chromatin expansion. Downstream from this event, the chromatin needs to be properly structured for enhancers to be in close contact with their respective promoters. These groups of enhancers, commonly denoted as shadow enhancers, have been shown to buffer against environmental stress but the mechanisms underlying this function remain unclear. Here, we present a series of stochastic and deterministic chemical reaction network models that provide sufficient conditions for shadow enhancers and chromatin remodeling to achieve their regulatory targets. We developed a model of the *Kruppel* shadow enhancers to show that separation of TFs between enhancers is sufficient for achieving lower expression noise. Additional models were generated to determine how shadow enhancer numbers po-

tentially modulate transcriptional noise and fidelity. Separately, a model of the chromatin that does not rely on cooperative interactions between nucleosomes is shown to achieve ultrasensitive gene expression. By limiting complexity, we show that our chemical reaction network models convey clear mechanisms by which TFs, shadow enhancers, and nucleosome interactions can be used to optimize these transcriptional properties.

Chapter 1

Introduction

Quantitative models of biological systems are becoming ever more relevant in order to translate experimental data into clear mechanisms underlying observed phenomena. Several aspects of gene regulation have been modeled in this fashion in order to understand how complex networks of interacting proteins can give rise to specific phenotypes. A commonly used type of model is that of chemical reaction networks (CRNs) which aim to capture the dynamics of each chemical species within a system. While originally conceived for the study of chemical engineering, CRNs have found their way into biochemistry with a high degree of versatility [4, 5]. This is in part due to the ubiquitous prevalence of molecular biology as a way to explain cellular phenomena in a mechanistic rather than descriptive way. CRNs have amassed a large suite of analytical and computational methods for calculating or approximating the behavior of their target systems [4, 6]. This places CRNs in an ideal spot to model the biochemical mechanisms that optimize for distinct metrics of RNA transcription. Ultimately, a mechanistic understanding of gene regulation can lead to the development of pharmaceutical approaches for correcting deviations in control that can result in disease or death [7].

In this dissertation, we focus on two gene regulatory systems that are driven by or made possible by chromatin regulation. One such mechanism is the regulation of chromatin density as a way to determine whether or not a gene is expressed. Another is the regulation via shadow enhancers, which are regions of DNA located in separate parts of the genome, but which come together via a special chromatin structure in order to regulate a gene. Each of these two mechanisms is devoted independent chapters of this dissertation, in which their specific properties are studied.

We postulate that the above systems aim to optimize certain measurable properties of the transcription of the genes they regulate. For instance, for shadow enhancers in developmental systems we optimize for minimizing noise and maximizing fidelity of signal transduction [8, 9, 10]. In the case of gene regulation through chromatin remodeling, we assume that ultrasensitivity of the dose response should be maximized [11]. These are likely a subset of the many performance criteria in the system, but they illustrate the issues involved. We try to minimize the complexity of each system in order to highlight the proposed biochemical mechanisms in each case.

While CRNs are most commonly modeled deterministically, experimental data from single cells is intrinsically noisy. We incorporate this noise by using stochastic models where low numbers of molecules interact with each other discretely, using the stochastic master equation. This allows to incorporate important elements of the dynamics, as well as taking into account useful additional experimental data, and even optimizing for network topologies that minimize noise in certain circumstances.

1.1 Shadow enhancers

Enhancers are regions of the DNA that are bound by proteins known as transcription factors (TFs) and loop with the promoter in order to regulate transcription. The regulation of development by enhancers is critical for the health of many organisms, including humans [12, 13, 14, 15, 16, 17]. Furthermore, the majority of developmental genes have been found to be regulated by multiple enhancers [18, 10, 19, 20]. While much remains unknown about the link between enhancers and disease, a recent survey found that a large swath of human genes associated with disease may be regulated by shadow enhancers [20].

The set of enhancers that regulate a specific gene at a partially or fully overlapping location and time have been denoted as *shadow enhancers* [21]. This name was originally meant to indicate enhancers which are located farther away from the promoter than a so-called primary enhancer [22]. For some time, these shadow enhancers were thought to be redundant due to their overlapping activity with the primary enhancer [22]. However, later evidence suggested that shadow enhancers can increase robustness of gene expression under stressful environmental conditions [9, 8, 10]. Thus the name "shadow enhancers" was revised to incorporate all enhancers regulating a given gene as described above [21].

1.1.1 Regulation of transcriptional noise by shadow enhancers

While shadow enhancers emerged as regulatory elements that can buffer against environmental stress, it still remained unclear which mechanisms underlying shadow enhancers were responsible for this effect. In work by Waymack et al. [1], a mechanism to explain this increase in gene expression robustness was proposed. The authors hypothesized that shadow enhancers were more effective at buffering noise associated with their TFs than single or duplicated enhancers. This followed, it was argued, from having distinct kinds of TFs bind-

ing to each of the enhancers. Hence, perturbations in a TF would be limited in their effect to the subset of enhancers with binding sites for that TF. In order words, by sparing some enhancers from perturbations in their TF inputs, the resulting downstream effect would be reductions in the expression noise of an mRNA output.

In Chapter 2, we provided evidence for this idea. First, experimental data was collected from the transcriptional dynamics of the *Kruppel* gene which is active during *Drosophila* development. *Kruppel* is an ideal case study for shadow enhancers as it is regulated by only two shadow enhancers as opposed to other genes that are regulated by over 20 distinct enhancers [14]. Then, flies with duplicated shadow enhancers were engineered and their transcriptional data was collected as well. By comparing the expression noise of the wildtype and duplicated systems, the latter enhancers being bound by the same TFs, it appeared that having distinct TFs bind to the shadow enhancers may buffer stress during the development of an organism.

However, due to the complex biochemistry involved in enhancer regulation, it remained difficult to conclusively show that transcriptional noise can be buffered in this way. Thus, to complement the experimental evidence for this hypothesis, we developed stochastic CRN models corresponding to wildtype and duplicated constructs of the *Kruppel* shadow enhancers. These models had TFs as the sole prerequisites for transcription which allowed for direct measurements of the effect that fluctuations in TFs have on mRNA transcription. Through parameter fitting, the models were able to qualitatively replicate the experimental data. Specifically, our models recapitulated the experimentally observed noise resulting from transcription of *Kruppel* wild type and duplicated enhancer systems. Ultimately, these models also led to the same conclusion as the experimental approach: regulation of shadow enhancers by distinct TFs is sufficient for lowering expression noise when compared to duplicate and single enhancer systems.

The observation that shadow enhancers lower expression noise in this manner evoked a

new question: is it possible to recapitulate the functions of shadow enhancers with a single enhancer having equivalent kinds of TF binding sites? After all, a single enhancer that is bound by the same TFs as a group of shadow enhancers should, in theory, also yield lower noise than the corresponding duplicated enhancers. Nevertheless, the vast majority of developmental genes are regulated by multiple enhancers [21]. This could initially suggest that shadow enhancers are strongly favored by natural selection or that they arise from genetic drift as the result of expected probabilistic outcomes as opposed to evolutionary pressures. In the former case, the prevalence of shadow enhancers across diverse phyla would suggest that these enhancers grant a considerable fitness advantage and mutations in their sequences could result in a wide range of diseases or death. Therefore, determining whether shadow enhancers confer these advantages would lead to a more comprehensive understanding of the pathogenicity associated with certain genetic mutations that occur in many organisms including humans.

1.1.2 Trade-offs between transcriptional properties given by shadow enhancers

To analyze whether there are properties specific to shadow enhancers and not single enhancers, we considered comparing mRNA transcriptional noise and fidelity to TF inputs between systems varying in enhancer numbers with all else being constant (e.g. binding site numbers). While the scale of this analysis would be too large to be achieved experimentally in reasonable time, our previously developed model of *Kruppel* enhancers could provide an initial step for a modeling approach. This model can be simulated in a fully stochastic fashion and thus is able to capture the nuances in the relationship between TFs and mRNA expression. Moreover, the validation of this model with live-imaging data of *Kruppel* transcription supports the idea of model parameters being within a biologically acceptable range [1]. Because of these reasons, we expect that similar stochastic models that operate

in the vicinity of this parameter space could be useful for mapping the potential advantages of shadow enhancers.

Following this line of thought, the work in Chapter 3 describes the extension of the *Kruppel* model in Chapter 2 to incorporate multiple numbers of enhancers and TF binding sites. Then, by comparing the transcriptional properties of these models, we sought to determine which features are unique to shadow enhancers and how these properties change as enhancer numbers vary. An additional consideration is that shadow enhancers interact with their TFs, their promoters, and between themselves in a variety of ways. For example, some enhancers behave subadditively, that is, their combined contributions to mRNA expression are less than the sum of their individual contributions [23]. The mechanisms at play for this behavior remain unclear but enhancer competition for promoter access has been suggested [24]. Fortunately, theoretical models allow for total control, not only of model parameters, but also of model assumptions. Hence, by this approach, we were able to study the advantages of shadow enhancers for a wide range of parameters and assumptions while retaining a clear understanding of the relationship between each variable in the model.

One downside to this approach is that the number of models to be simulated can become intractable even for small numbers of enhancers and TFs. Moreover, some models can have several reactions which result in high computational time lengths when simulating these models stochastically. To counter this, we first developed a computational script for efficiently generating enhancer systems from a number of assumptions given as inputs. Each set of input assumptions generates the corresponding CRN which can then be used as an input to the third party software CERENA (ChEmical REaction Network Analyzer) [6]. The CERENA toolbox is particularly fitting for this work as it provides a suite of approximation methods for stochastic dynamics such as the moment closure method. Moment closure requires only the numerical solution of a closed system of ODEs describing the statistical moments for each species in the model [25]. This comes at a fraction of the computational

cost but at the expense of longer compilation times and potential approximation errors. In addition, moment closure does not involve doing a large number of simulations unlike other stochastic approaches where each simulation is different from each other and many samples are needed for a proper estimation of the moments.

This combination of automated model generation and approximation methods resulted in an efficient way to explore the space of parameters and model topologies. Under this approach, we generated most possible models with up to 4 enhancers and 4 binding sites that can be bound by the TFs we used in our previous *Kruppel* model. We looked at two metrics that are of interest during the development of organisms: transcriptional noise and fidelity. Typically, expression noise should be maintained below a threshold to convey a coherent downstream output from the upstream signals of TFs. On the other hand, fidelity needs to be above a certain threshold to convey an output from a given input. The resulting simulations showed that different additivity levels of shadow enhancers led to distinct outcomes in these metrics of noise and fidelity. Moreover, they also revealed that additive shadow enhancers might be the result of genetic drift as opposed to any particular evolutionary pressure. Overall, this work suggested that shadow enhancers may be the result of spontaneous genome reorganization events which do not face adverse selection pressures and, in certain cases, may provide avenues for transcriptional modulation that are not available to single enhancers.

1.2 Chromatin remodeling and ultrasensitive gene expression

Another important mechanism for regulating the expression of genes within a certain region is chromatin remodeling. This process works by expanding or compacting the DNA to allow or prevent the access of transcriptional enzymes to genetic regions. Chromatin remodeling

involves transitions between high and low density chromatin states which occur in response to the recruitment of histone acetyltransferases (HATs) by TFs. In previous studies, the boundaries between these regions have been observed to be sharp, and their disruption has been associated with disease including several growth defects [26, 27]. Nevertheless, the specific mechanisms by which chromatin remodeling achieves this so-called ultrasensitive transitions in response to increasing TF concentrations are not yet understood. In other words, how is it that the chromatin, in response to TF concentrations, can be fully accessible to transcriptional enzymes within a well-defined region but remain fully closed within the neighboring regions?

Aiming to yield sharp boundaries between chromatin density states, previous modeling work assumed that neighboring modification sites affect one another [11, 28]. In contrast, Chapter 4 presents an alternative approach with independent modification sites that produce sharp spatial bounds between chromatin density regions. This model relied on the activity range of HATs and other emergent properties of chromatin architecture to achieve ultrasensitive chromatin remodeling. The boundaries between density regions remained sharp even without the involvement of barrier proteins, and no uncontrolled expansion is possible beyond the regulated regions. Moreover, a single HAT protein bound at a DNA site was sufficient to make accessible hundreds of DNA base pairs, a longer range of interaction than previous models. Two mechanisms allowed for this in our model, namely percolation effects and multisite histone tail modifications.

Both percolation and multisite histone tail modifications can be inherently ultrasensitive and contribute to the sharpness between distinct density boundaries caused by chromatin remodeling [29, 30]. However, to translate the ultrasensitivity from these properties into chromatin remodeling, it was necessary to stochastically simulate the individual interactions between nucleosomes in the chromatin. That is, we needed to calculate whether an interaction will take place based on a certain probability. Thus, to stochastically simulate

chromatin remodeling, we modeled the chromatin as a graph composed of nodes and edges where nodes corresponded to nucleosomes and edges to nucleosome interactions. The edges to the graph were assigned with certain probabilities based on acetylation levels and the graph diameter was used as a proxy for chromatin accessibility. Then, a deterministic CRN was used to describe the TF recruitment of HATs and the acetylation of individual histone sites within the nucleosomes. The resulting dose-response of acetylated histones served as an input to the model and showed that chromatin accessibility can respond ultrasensitively to TF concentrations under the conditions given.

The ability to model chromatin as a graph allowed for the additional benefit of being able to map any two or three dimensional structure as a potential chromatin architecture and determine the corresponding effect of this topology in the process of remodeling. In our work, we translated a popular model of chromatin architecture, namely the solenoid architecture, into our own graph-based model [31]. While studying this architecture, we used a deterministic CRN to calculate the effect of TFs on histone acetylation and noticed that certain outputs generated from this network were abnormally sensitive to increasing amounts of input stimuli. Further investigation suggested that a mechanism akin to sudden saturation of the dose-responses was causing increases in ultrasensitivity in manners that have not previously been observed. This observation then inspired the work of Chapter 5.

1.3 Modulation of ultrasensitivity through biochemically induced saturation

Ultrasensitivity is useful for proper gene regulation when we consider that genes are respondents to upstream chemical signals and amplification of noise and ambiguity from such signals can be detrimental to the organism [32]. Furthermore, ultrasensitive responses have

been noted to be crucial for the proper functioning of biochemical switches present in the cell cycle, cell signaling, and cell fate decisions [33].

Several mechanisms that generate ultrasensitivity have been proposed such as zero-order ultrasensitivity, multisite phosphorylation, and allostery among others [34]. The ability of function saturation as a mechanism for increasing ultrasensitivity as described in the end of Chapter 4 does not appear to have been studied previously. The work in Chapter 5 presents a potential mechanism by which function saturation can be modulated and cause direct increases in the ultrasensitivity of dose-responses. In particular, we found that a certain topological property of CRNs known as absolute concentration robustness can give rise to dose-responses that saturate sharply. We show that a subset of the parameters in the network can be increased or decreased to directly affect the ultrasensitive behavior of the response.

We proceeded to extend this saturation framework to functions that are not typically considered in the context of ultrasensitive behavior. One type of these functions are those without a well-defined upper bound or saturation point. As such, these functions cannot be assigned a proper value of the available metrics that are used to quantify ultrasensitivity since a prerequisite for these measurements is saturation. This, in turn, could lead to an initial dismissal of these functions as ultrasensitive and therefore of biochemical processes that give rise to these functions. However, processes such as polymerization are described by non-saturating functions and have been found to have roles in gene regulation [35, 36]. These polymers are typically important components of biochemical cascades which are used to convey signals from the extracellular environment into the cell nucleus. In response to these signals, TFs are understood to be activated which leads to upregulation or downregulation of genome activity [37]. Hence, it is clear that, when forming part of a biochemical signaling cascade, this kind of non-saturating functions could increase precision and lower gene expression noise if they were to increase ultrasensitivity in the composite dose-response of the cascade. As a

result, by integrating our absolutely robust saturation mechanism with polymerization, we can give rise to saturated processes which will further increase the ultrasensitivity present in the composition of all functions forming a biochemical cascade.

In studying non-saturating functions within biochemical cascades, we also wished to determine the extent to which any given cascade can be optimized for ultrasensitivity. For example, consider the Hill function defined by $ax^n/(x^n + k)$ where n, a, and k are positive constants. This function, while originally used by A.V. Hill for modeling oxygen transport through hemoglobin, has become a standard model for a wide-range of ultrasensitive phenomena [38, 39]. Ferrell claimed in one of his works that the Hill coefficient –a well known measure for ultrasensitivity which equals to n for a Hill function– of the composition of two Hill functions is bounded above by the product of the Hill coefficients of the functions making up the composition [40]. However, this result was only suggested by example. In this chapter we show a formal proof for this result that works for any two arbitrary Hill functions. Moreover, we also prove that the claim by Ferrell does not extend to general sigmoidal functions. Lastly, we present some formal results concerning the Hill coefficients and sensitivity for any two general functions. We also provide some general examples of saturated functions and the Hill coefficients arising from their compositions. Overall, this chapter provides a partial mathematical foundation for the study of ultrasensitivity in biochemical cascades and how they might be optimized for precise activation of downstream genes.

1.4 Absolute concentration robustness as an ideal regulator of biochemical systems

In chapter 5, we relied on absolute robustness as a key property in achieving ultrasensitive function saturation. This is the ability of a chemical species to converge to the same steady

state regardless of the initial conditions given to the system. Such a behavior is not only relevant to our mechanism, but has been used for explaining several biochemical phenomena that rely upon strong robustness in one of their properties [41]. For example, the ideal housekeeping gene has been described as that which maintains a constant amount of a given transcript [42]. Nevertheless, absolute robustness can be difficult to detect in large networks that rely upon hundreds or thousands of species for signal transduction such as those involved in gene regulation. Work by Shinar and Feinberg showed sufficient conditions for proving that a species within a network is absolutely robust [41]. The power of this approach relied on the nature of such conditions being solely dependent on network topology rather than on rate parameters. Hence, we could search for submodules within a large biochemical network that satisfy the topological conditions derived by Shinar and Feinberg. However, it is still not clear whether the absolute robustness found in these submodules extends to the parent network of which they are a part of. In the first section of Chapter 6, we present a subset of conditions under which the steady state of a species within a submodule is equivalent to its steady state within the parent network. These results allow for a more formal foundation to the extension of absolute concentration robustness from a submodule to a larger network which, in conjunction with the result by Shinar and Feinberg, leads to a more efficient way of inferring sources of robustness in any gene regulatory network.

As we previously noted, certain properties of dose-responses are highly desirable in biochemical processes. For example, high ultrasensitivity is crucial for maintaining the switch-like behavior of genes and preventing noise in upstream signals from significantly perturbing gene expression [43]. The second section of Chapter 6 describes a convenient approach to extend the dose-response properties of one species in the network to another. In particular, we focus on enabling the ultrasensitivity of one species to be replicated in another one. As a result, this new species behaves at the same level of ultrasensitivity as the original species. To achieve this, we relied once again on absolute robustness as a medium for extending the time-dependent behavior of one chemical species to another. In essence, by introducing a

new reaction into a network that contains absolutely robust species in the network, we can tune the dose-response of such a species to be a scaled version of the ultrasensitive dose-response of another species in the network. We present a basic gene regulatory network and show that the response of the translated protein can be made as ultrasensitive as a neighboring trimerization process. While not formally generalized, we expect this approach to lead to a more comprehensive approach that eventually could include the inheritance of dose-response properties from a parent network to a submodule in a similar fashion as was done in the previous section. In addition, procedures of this nature may be well-suited for building synthetic biological systems that wish to extend a desired biochemical property from an introduced circuit to the rest of the biological system.

While absolute robustness can be shown to be the case for a given species within a network, sometimes it is not clear whether the control output associated with such a species is also absolutely robust. One notable example is that of the EnvZ-OmpR osmoregulatory system which contains an absolutely robust component [41]. In particular, this component is the phosphorylated version of OmpR that is in charge of regulating the porin proteins OmpF and OmpC [44]. These proteins are themselves involved in regulating cell osmolarity by limiting the amount of solute that enters or leaves the cell. However, while the absolute robustness of phosphorylated OmpF has been linked to the maintenance of an isotonic cell under repeated osmotic perturbations, current models do not address the osmoregulation done by this protein. The last section of Chapter 6 expands a previously developed network of the EnvZ-OmpR system to include osmoregulation and suggest a potential implementation of an absolutely robust phosphorylated OmpR leading to absolutely robust isotonicity within the cell. We expect that an example of such a system will guide future modeling of absolutely robust controllers to establish concrete links between the absolutely robust species and their intended biochemical output within the biological system.

1.5 Mathematical background

1.5.1 Chemical Reaction Networks

Chemical reaction networks are described by a set of reactants, a set of products, and a set of reactions. As is standard, through this work we assume mass action kinetics which states that reaction rates are proportional to the product of the concentrations of the reactants. Consider the following reaction network consisting of reactants A and B alongside their reaction into the product C at a rate k.

$$A + B \xrightarrow{k} C$$

Whenever A or B are found in large enough numbers, mass action kinetics dictates that the concentrations over time for each species in the network can be described by the following ODEs

$$\begin{aligned}
\frac{d[A]}{dt} &= -k[A][B] \\
\frac{d[B]}{dt} &= -k[A][B] \\
\frac{d[C]}{dt} &= k[A][B].
\end{aligned}$$

In this system, the square brackets denote the concentration of the species inside of them. Approximating concentrations in this manner is considered to be a deterministic approach to modeling chemical networks since the behavior over time does not involve randomness whether the system is solved analytically or using numerical approximations.

If the species counts are low, it is more accurate to opt for describing the network by its master equation rather than a system of ODEs. In particular, the master equation gives the rate of change of the probability that the system will be at a given state. For the network

described above, we can construct the master equation by specifying the transitions in state from all possible reactions as follows

$$\frac{dx_{a,b,c}}{dt} = k(a+1)(b+1)x_{a+1,b+1,c-1} - kabx_{a,b,c}, \tag{1.1}$$

where a, b and c correspond to the counts of A, B, and C respectively and x is the state vector of the network. Equation 1.1 can then be solved analytically to obtain the corresponding distributions for each species. Alternatively, the Gillespie algorithm can be used to obtain sample trajectories of species in the network.

1.5.2 Gillespie simulations

The Gillespie algorithm is a well-studied Monte Carlo procedure that yields statistically correct sample trajectories of chemical species over time [45, 46]. This algorithm specifies the probability of the system remaining in its current state – in this case, the counts for each chemical species in the network – depends on an exponential distribution with a rate equal to the sum of the rate constants of the outgoing reactions times the number of all possible reactions.

Nevertheless, while the Gillespie algorithm can be rigorously shown to accurately reproduce instances of the network trajectories over time, it can become computationally expensive when performed several times. On the other hand, in order to obtain the moments of every species in the network, moment closure requires only a numerical solution to a system of ODEs which is considerably cheaper in computational terms than Gillespie simulations. Naturally, this comes at the expense of having approximation errors in the results. One additional advantage of moment closure methods is their ability to calculate moments in a deterministic manner such that multiple simulations are not necessary. To achieve the same feat using the Gillespie algorithm, a large enough but unclear number of simulations would

be required.

Chapter 2

Shadow enhancers can suppress input transcription factor noise through distinct regulatory logic

Material in this chapter is adapted from a manuscript by Rachel Waymack, Alvaro Fletcher, German Enciso, and Zeba Wunderlich [1].

2.1 Introduction

Shadow enhancers are groups of two or more enhancers that control the same target gene and drive overlapping spatiotemporal expression patterns [22, 47]. Shadow enhancers are found in a wide range of organisms, from insects to plants to mammals, particularly in association with developmental genes [18, 10, 48, 49]. While seemingly redundant, the individual enhancers of a shadow enhancer group have been shown to be critical for proper gene expression in the face of both environmental and genetic perturbations [8, 10, 9]. Such

perturbations may exacerbate fluctuations in upstream regulators [50, 51]. Although shadow enhancers are shown to be pervasive in developmental systems and necessary for robust gene expression, their precise mechanism of action is still unknown. One proposed mechanism is that having multiple enhancers controlling the same promoter reduces the effective 'failure rate' of the promoter and ensures a critical threshold of gene expression is reached [52, 53]. An alternative, but not mutually exclusive, possibility is that shadow enhancers ensure robust expression by buffering noise in upstream regulators. Several studies suggest that individual enhancers of a shadow enhancer group tend to be controlled by different sets of TFs, which we call a 'separation of inputs' [54, 18, 55]. We hypothesize that this separation of inputs allows shadow enhancers to buffer against fluctuations in upstream TF levels to drive more consistent expression levels.

The first evidence that transcription occurred in bursts, as opposed to as a smooth, continuous process, was observed in *Drosophila* embryos. Electron micrographs showed that even highly transcribed genes had regions of chromatin lacking associated transcripts in between regions densely associated with nascent transcripts [56]. As visualization techniques have improved, it is increasingly clear that transcriptional bursting is the predominant mode of expression across organisms from bacteria to mammals [57, 58, 59, 60, 61]. These bursts of transcriptional activity, separated by periods of relative silence, have important implications for cellular function, as mRNA numbers and fluctuations largely dictate these quantities at the protein level [62, 63]. Such fluctuations in regulatory proteins, like TFs and signaling molecules, can propagate down a gene regulatory network, significantly altering the expression levels or noise of downstream target genes [64]. Many mechanisms that buffer against expression noise, either inherent or stemming from genetic or environmental variation, have been observed [65, 66, 67]. For example, organisms use temporal and spatial averaging mechanisms and redundancy in genetic circuits to achieve the precision required for proper development [66, 67, 68, 65]. Here, we focus on how shadow enhancers may also establish and maintain the precise levels of gene expression seen during development, where expression

patterns can be reproducible down to half-nuclear distances in *Drosophila* embryos [69, 70, 47].

The *Drosophila* gap gene *Kruppel* (*Kr*) provides a useful system in which to probe the mechanisms of action of shadow enhancers. During early embryogenesis, *Kr* expression is critical for thorax formation, and like the other gap genes in the *Drosophila* embryo, has quite low noise [71, 69]. During this time, *Kr* is controlled by the activity of two enhancers, proximal and distal [53], that drive overlapping expression in the center of the embryo (Figure 2.11). We call the two individual enhancers together the shadow enhancer pair. Previous experiments have shown that each enhancer is activated by different TFs (Figure 2.1A; [54]). Here, we focus on differences in activation, as the key repressors of *Kr*, *Knirps* and *Giant*, are likely to regulate both enhancers. By measuring live mRNA dynamics, we can use the *Kr* system in *Drosophila* embryos to assess whether and how shadow enhancers act to buffer noise and to identify the sources of noise in the developing embryo.

To test our hypothesis, we measured live mRNA dynamics driven by either single *Kr* enhancer, duplicated enhancers, or the shadow enhancer pair and compared the dynamics and noise associated with each. We showed that the individual *Kr* enhancers can act largely independently in the same nucleus, while identical enhancers display correlated activity. We constructed a simple mathematical model to describe this system and found that TF fluctuations are necessary to reproduce the correlated activity of identical enhancers in the same nucleus. The shadow enhancer pair drives lower noise than either duplicated enhancer, and using the model, we found that this is a natural consequence of the separation of TF inputs. Additional experiments, including simultaneous measurements of TF levels and expression and a decomposition of noise sources, further demonstrate that the shadow enhancer pair is less sensitive to fluctuations in TF levels than is a single enhancer. Additionally, the shadow enhancer pair is uniquely able to maintain low levels of expression noise across a wide range

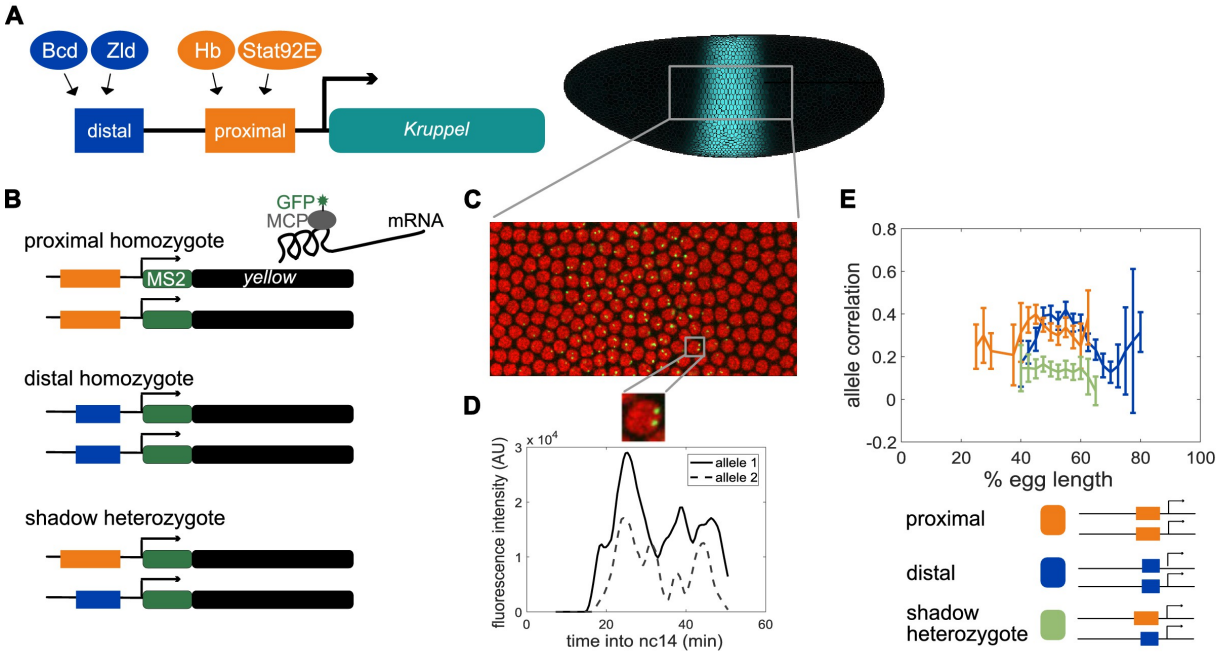

Figure 2.1: Dual allele imaging shows the individual *Kruppel* enhancers drive largely independent transcriptional dynamics. (A) Schematic of the endogenous Kruppel locus with distal (blue) and proximal (orange) shadow enhancers driving *Kr* (teal) expression in the central region of the embryo. Known transcriptional activators of the two enhancers are shown. (B) Schematics of single enhancer reporter constructs driving expression of MS2 sequence and a yellow reporter. When transcribed, the MS2 sequence forms stem loops that are bound by GFP-tagged MCP expressed in the embryos. Proximal embryos have expression on each allele controlled by the 1.5 kb proximal enhancer at its endogenous spacing from the *Kr* promoter, while distal embryos have expression on each allele controlled by the 1.1 kb distal enhancer at the same spacing from the *Kr* promoter. Shadow heterozygote embryos have expression on one allele controlled by the proximal enhancer and expression on the other allele controlled by the distal enhancer. (C). Still frame from live imaging experiment where nuclei are red circles and active sites of transcription are green spots. MCP-GFP is visible as spots above background at sites of nascent transcription [72]. (D) The fluorescence of each allele in individual nuclei can be tracked across time as a measure of transcriptional activity. The graph shows a representative trace of transcriptional activity of the two alleles in a single nucleus across the time of nc14. These traces are used to calculate the Pearson correlation coefficient between the transcriptional activity of the two alleles in a nucleus across the time of nc14. Correlation values are grouped by position of the nucleus in the embryo and averaged across all imaged nuclei in all embryos of each construct. (E) Graph of average correlation between the two alleles in each nucleus as a function of egg length. 0% egg length corresponds to the anterior end. Error bars indicate 95% confidence intervals. The shadow heterozygotes have much lower allele correlation than either homozygote, demonstrating that the individual shadow enhancers drive nearly independent transcriptional activity and that upstream fluctuations in regulators are a significant driver of transcriptional bursts. The total number of nuclei used in calculations for each construct by anterior-posterior (AP) bin are given in Supplementary file 1.

of temperatures. We suggest that this noise suppression ability is one of the key features that explains the prevalence of shadow enhancers in developmental systems.

2.2 Individual enhancers in the shadow enhancer pair act nearly independently within a nucleus

To test our hypothesis that the separation of inputs between *Kruppel*'s (*Kr*) shadow enhancers provides them with noise-buffering capabilities, we needed to first test the ability of each enhancer to act independently. In previous work, we found that the individual enhancers in the shadow enhancer pair are controlled by different activating TFs [54]. These experiments established that the enhancers responded differently to perturbations in key TFs, indicating that each enhancer uses a distinct regulatory logic. The proximal enhancer is activated by Hunchback (Hb) and Stat92E, and the distal enhancer is activated by Bicoid (Bcd) and Zelda (Zld) (Figure 2.1A). Given this separation of inputs, the shadow enhancer pair could provide a form of noise buffering if variability in gene expression is driven primarily by fluctuations in upstream factors. Conversely, variability in upstream regulators may be low enough in the developing embryo that these fluctuations are not the primary driver of downstream expression noise. If this were the case, the separation of inputs is unlikely to be a key requirement of shadow enhancer function.

To investigate these possibilities, we measured and compared the correlation of allele activity in homozygous or heterozygous embryos that carry two reporter genes. Proximal homozygotes contained the proximal enhancer driving a reporter, inserted in the same location on both homologous chromosomes, and distal homozygotes similarly had the distal enhancer driving reporter expression on both homologous chromosomes (Figure 2.1B). We also made heterozygous embryos, called shadow heterozygotes, which had one proximal and one distal

reporter, again in the same location on both homologous chromosomes. To measure live mRNA dynamics and correlations in allele activity, we used the MS2-MCP reporter system (Figure 2.1C,D). This system allows the visualization of mRNAs that contain the MS2 RNA sequence, which is bound by an MCP-GFP fusion protein [73]. In the developing embryo, only the site of nascent transcription is visible, as single transcripts are too dim, allowing us to measure the rate of transcription [72, 74]. In blastoderm-stage embryos with two MS2 reporter genes, we can observe two distinct foci of fluorescence corresponding to the two alleles (Figure 2.1D; Videos 1, 2, 3, 4, 5, 6), in line with previous results that suggest there are low levels of transvection [75, 76]. To confirm our ability to distinguish the two alleles, we imaged transcription in embryos hemizygous for our reporter constructs, which only show one spot of fluorescence per nucleus. Our counts of active transcription sites in homozygous embryos correspond well to the expected value calculated from hemizygous embryos (Figure 2.11). Therefore, we are able to measure the correlation of allele activity, although we cannot identify which spot corresponds to which reporter.

We predicted that if variability in gene expression is driven by fluctuations in input TFs, we would observe lower correlations of allele activity in shadow heterozygotes than in either the proximal or distal homozygotes. However, if global factors affecting both enhancers dominate, there would be no difference in allele activity correlations. During the 1 hr of nuclear cycle 14 (nc14) we found that allele activity is more than twice as correlated in both proximal and distal homozygotes than in shadow heterozygote embryos at 47–57% egg length, which encompasses the central region of *Kr* expression during this time period (Figure 1). The difference in our ability to measure allele correlation in the more anterior and posterior regions of the embryo stems from the slightly different expression patterns driven by the proximal and distal enhancers (Figures 2.11 and 2.12). The lower allele correlation in shadow heterozygote embryos indicates not only that the individual member enhancers of the shadow enhancer pair can act largely independently in the same nucleus, but that differential TF inputs are likely the primary determinants of transcriptional bursts in this

system. Notably, heterozygotes still show marginal allele correlation, indicating that some correlation is induced by either shared input TFs or factors that affect transcription globally. The independence of individual *Kr* enhancers allows for the possibility that shadow enhancers can act to buffer noise by providing distinct inputs to the same gene expression output.

2.2.1 Conversion of integrated fluorescence to mRNA molecules

To put our results in physiologically relevant units, we calibrated our fluorescence measurements in terms of mRNA molecules. As in Lammers et al., 2018 [77], for our microscope, we determined a calibration factor, α, between our MS2 signal integrated over nc13, FMS2, and the number of mRNAs generated by a single allele from the same reporter construct in the same time interval, NFISH, using the hunchback P2 enhancer reporter construct [72]. Using this conversion factor, we can calculate the integrated fluorescence of a single mRNA (F1) as well as the instantaneous fluorescence of an mRNA molecule (FRNAP). With our microscope, FRNAP is 379 AU/RNAP and F1 is 1338 AU/RNAP•min. With these values, we are able to convert both integrated and instantaneous fluorescence into total mRNAs produced and number of nascent mRNAs present at a single time point, by dividing by F1 and FRNAP, respectively.

Table 2.1: Summary of relevant parameters.

N_{FISH}	220 mRNA
F_{MS2}	294511 AU
L_1	1.275 kb
L_2	4.021 kb
v_{elong}	1.5 kb/min

The conversion factor α is defined as the ratio of N_{FISH} molecules of mRNA to their respective integrated fluorescence F_{MS2} from traversing a genetic construct. Then, the integrated

fluorescence of a single mRNA molecule is given by

$$\begin{aligned} F_1 &= \frac{1}{\alpha}, \\ &= \frac{F_{MS2}}{N_{FISH}}, \\ &= 1338\,\mathrm{AU}\cdot\mathrm{min}\cdot\mathrm{mRNA}^{-1}. \end{aligned}$$

The instantaneous fluorescence of an mRNA molecule can now be calculated as

$$F_{RNAP} = \frac{F_1}{t_{elong}}, \tag{2.1}$$

where t_{elong} is the time it takes for one RNAp molecule to traverse the genetic construct. Our particular construct is composed of the MS2 loops and the gene encoding for Hb with lengths L_1 and L_2 respectively. Then, letting v_{elong} be the speed of an RNA polymerase , we have that

$$\begin{aligned} t_{elong} &= \frac{L_1 + L_2}{v_{elong}}, \\ &= 3.5306\,\mathrm{min}. \end{aligned}$$

Substituting this value into equation 2.1 we get that

$$F_{RNAP} = \frac{1338}{3.5306} = 379\,\mathrm{AU}\cdot\mathrm{mRNA}^{-1}.$$

2.3 Transcription factor fluctuations are required for the observed differences in the correlations of enhancer activity

To explore the conditions needed for the two *Kr* enhancers to act nearly independently within the same nucleus, we generated a simple model of enhancer-driven dynamics. We considered an enhancer E_i that interacts with a transcription factor T_i, which together bind to the promoter to form the active promoter-enhancer complex C_i (Figure 2.2A). When the promoter is bound by the enhancer, it drives the production of mRNA. Since the MS2 system only allows us to observe mRNA at the site of transcription, we modeled the diffusion of mRNA away from the transcription site as decay. The transcription factor T_i is produced in bursts of n_i molecules at a time, and it degrades linearly. For simplicity, the transcription factor T_i is an abstraction of the multiple activating TFs that interact with the enhancer, and T_i corresponds to a different set of TFs for the proximal and distal enhancer. This nonlinear model generalizes the linear model by Bothma et al., 2015 [24] by explicitly taking into account the presence of TFs.

We estimated some model parameters directly from experimental data and others by fitting using simulated annealing. The mRNA degradation parameter α and production parameter r were measured directly from fluorescence data without any input from the model (see Materials and methods for details). The remaining parameters were first estimated using mathematical analysis, then fine-tuned using simulated annealing. We found separate parameter sets for the proximal and distal enhancers that, when used to simulate transcription, fit the experimentally measured characteristics of the transcriptional traces, including transcription burst size, frequency, and duration, as well as the total mRNA produced (Figure 2.3).

We hypothesized that a model that lacks fluctuations in the input TFs could not recapitulate

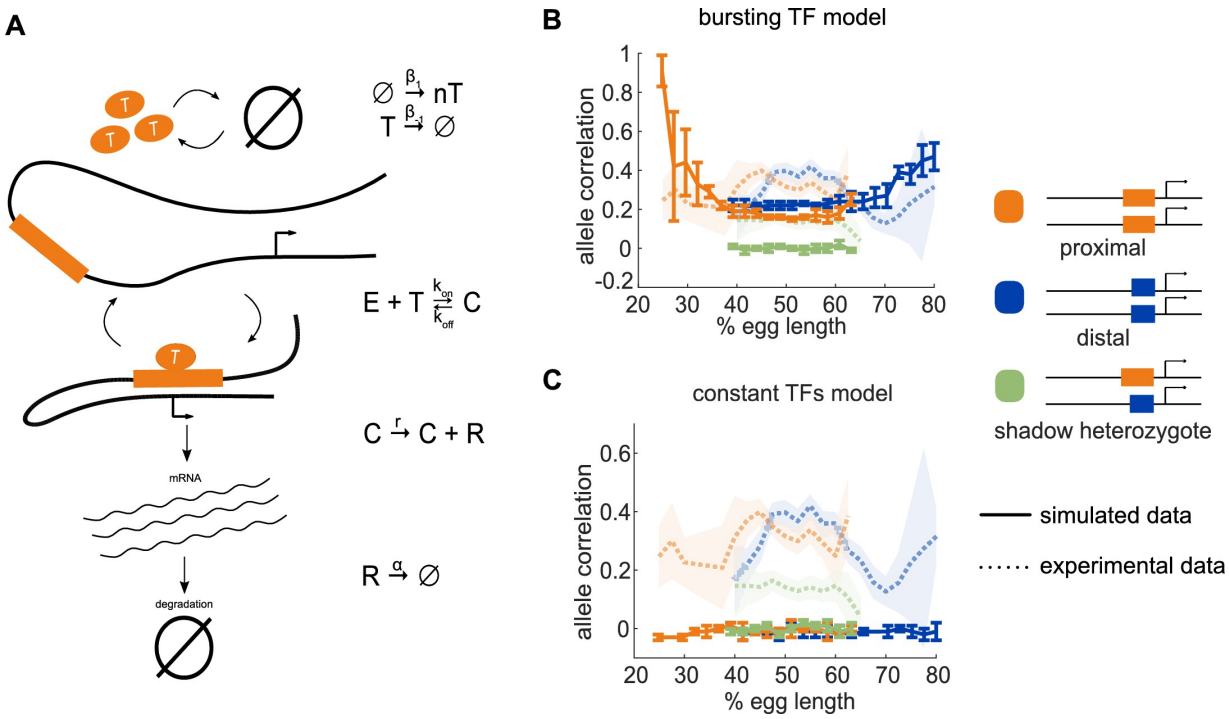

Figure 2.2: Model of enhancer-driven dynamics demonstrates TF fluctuations are required for correlated reporter activity. To investigate the factors required for the observed correlated behavior of identical enhancers and largely independent behavior of the individual enhancers, we developed a simple stochastic model of enhancer-driven transcription. (A) Schematic of model of transcription driven by a single enhancer (the bursting TFs model). For each enhancer, we assume there is a single activating TF, T_i, that appears in bursts of size n_i molecules at a rate β_1, which varies by the position in the embryo. TFs degrade linearly at rate β-1. When present, T_i can bind the enhancer, E_i, to form a transcriptionally active complex, C_i, at a rate k_{on} and dissociates at rate k_{off}. This complex then produces mRNA at an experimentally determined rate r that degrades at an experimentally determined rate, α. (B) The bursting TFs model is able to recapitulate the experimentally observed pattern of allele correlation. We plot the correlation between the two alleles in a nucleus as a function of egg length. Simulated data is created using the lowest energy parameter set for each enhancer. The data shown is the average of five simulated embryos that have 80 transcriptional spots per AP bin. In B and C, simulated data are shown by solid lines, experimental data are shown by dotted lines. (C) The constant TFs model fails to recapitulate the experimentally observed pattern of allele correlation. Without TF fluctuations, both heterozygous and homozygous embryos display independent allele activity. Error bars and shaded regions in B and C represent 95% confidence intervals.

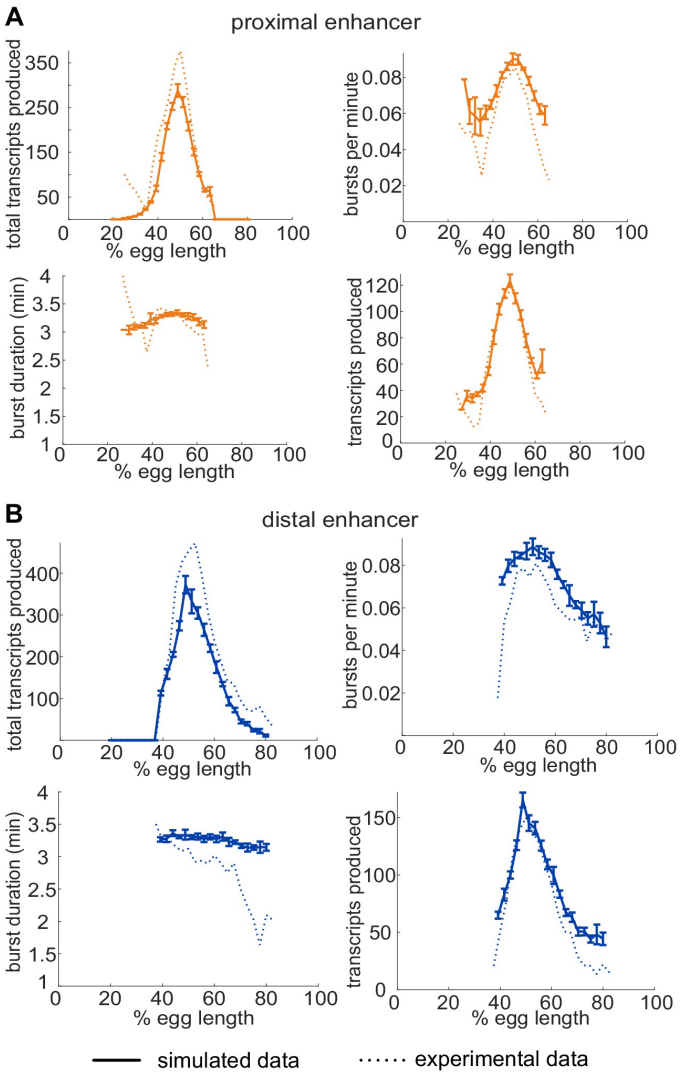

C

	median	CV
β_{-1}	2.7	2.4
k_{off}	1.8	0.40
k_{on}	0.36	0.90
n	4	2.0
c	6.8	0.75
σ	8.1	0.08

D

	median	CV
β_{-1}	3.9	1.2
k_{off}	1.5	0.13
k_{on}	0.19	1.3
n	12.5	1.3
c	9.2	0.34
σ	12.5	0.13

Figure 2.3: Single enhancer models recreate observed transcriptional bursting properties. To investigate whether our model is accurately simulating our experimental system, we compared the transcriptional burst properties produced by model simulations of transcription to those observed experimentally (see Figure 2—figure supplement 3 for description of burst properties). (A) Graphs of average values of transcriptional burst properties, total mRNA produced during nc14, burst frequency, burst duration, and burst size associated with the proximal enhancer as a function of egg length. In A and B, simulated data are represented with solid lines and experimental data are shown with dotted lines. (B) Graphs of average values of transcriptional burst properties as in A, associated with the distal enhancer. For both the proximal and distal enhancers, our model is largely able to recapitulate the experimentally observed transcriptional burst properties associated with each enhancer. (C) The median and CV values of the model parameters for the proximal enhancer in the top 10 performing parameter sets. (D) The median and CV values of the model parameters for the distal enhancer in the top 10 performing parameter sets. Explanations of model parameters are given in the Materials and methods. Error bars represent 95% confidence intervals.

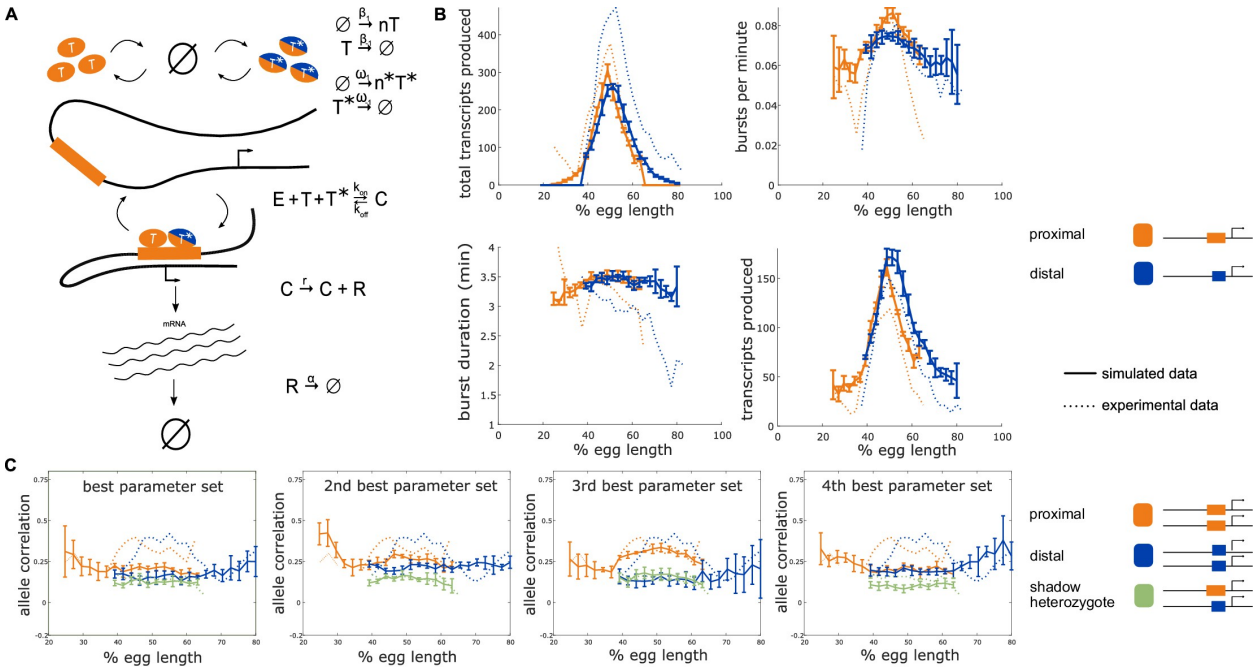

Figure 2.4: Incorporating a common TF into the model yields nonzero heterozygote allele correlations. To determine whether the observed nonzero heterozygote correlation can be explained by common TF activity, we incorporated into our model a TF that can bind to both the proximal and distal enhancers. (A) Schematic of a model that includes an additional TF denoted T^* which can bind to both the proximal and distal enhancers. The production of T^* occurs at a rate ω_1 which varies across the embryo in a similar manner to β_1. T^* degrades linearly at a rate ω_{-1} and appears in bursts of size $n*$. The presence of both the enhancer-specific TF T_i and the common TF T^* are necessary to initiate transcription. (B) The addition of a common TF does not hinder the model from recapitulating the experimentally observed burst properties of single enhancer constructs. Simulated data is created using the second-best parameter set for each enhancer. The data shown is the average of five simulated embryos that have 80 transcriptional spots per AP bin. In B, C, and D simulated data are shown by solid lines, experimental data are shown by dotted lines. (C) The addition of the common TF T^* consistently produces nonzero heterozygote allele correlations. However, some of the best parameter sets do not conserve the experimental relationship between homozygote and heterozygote correlations. Other parameter sets do not match the experimental data well, suggesting that the model accepts a narrower range of parameter combinations than the bursting TF model. Error bars in B and C represent 95% confidence intervals.

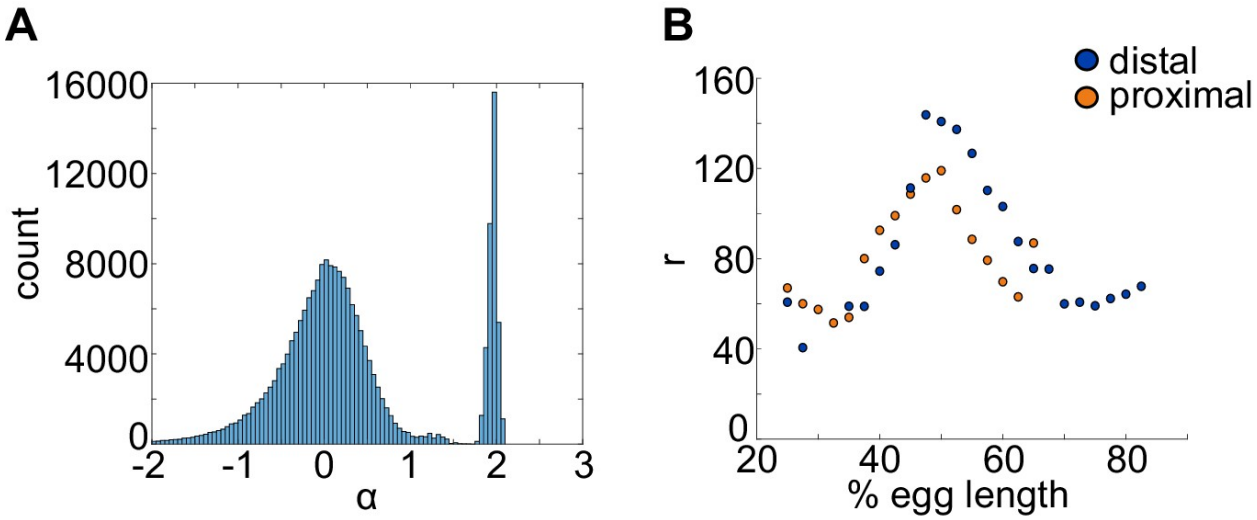

Figure 2.5: mRNA production and decay rates can be directly estimated from experimental data. The mRNA degradation parameter α and production parameter r were measured directly from fluorescence data without any input from the model. (A) To estimate α, we used adjacent measurements of fluorescence intensity to approximate the slope at each point in the fluorescence traces. These values are compared with an exponential rate of mRNA decay (see Materials and methods) and the resulting predicted values are shown in the histogram. Periods of mRNA production have negative α values and periods of decay have positive values. The histogram shows a distinct peak for $\alpha > 0$, which provided us with an estimate of $\alpha \approx 1.95$. (B) A similar computational approach was used to calculate values of r from fluorescence data (see Materials and methods). We calculated different values of r for each bin to account for differences in transcriptional efficiency across the length of the embryo due to factors that are not explicitly included in the model. For example, different combinations of TF bound to the enhancer may give rise to different mRNA production rates. Different values of r were found for the proximal and distal enhancers. Notice that distal r values shown correspond to the distal enhancer at the proximal location.

the high correlation of transcriptional activity in homozygotes versus the low correlation in heterozygotes. To test this hypothesis, we generated another model of TF production. We call our original model described above bursting TFs. The other model is one in which TF numbers are constant over time, which we call constant TFs and is equivalent to the model in Bothma et al., 2015 [24]. If the difference in transcription correlation between homozygotes and heterozygotes is due to fluctuating numbers of TFs, we expected that the bursting TFs model will recapitulate this behavior, while the constant TFs model will not. However, if the constant TFs model is also able to recapitulate the observed difference in correlations, then the correlations are likely a consequence of the identical enhancers simply being regulated by the same set of TFs.

For each model, we used the 10 best parameter sets to simulate transcriptional activity in homozygote and heterozygote embryos and analyzed the resulting allele correlations. We found that the bursting TFs model always produced results in which both homozygote allele correlations are significantly higher than the heterozygote, which qualitatively mirrors the experimental observations (Figure 2.2B). None of the best fitting parameter sets for the constant TF model were able to produce the experimentally-observed behavior and always resulted in near zero correlations for both the homozygote and heterozygote embryos (Figure 2.2C). Notably, using the bursting TFs model, all the simulated allele correlations were lower than the experimentally observed values, for example the simulated heterozygote allele correlation was near zero, while the experimental value was 0.14 at the embryo's midpoint. We hypothesized that this discrepancy was because the model assumes complete independence of the proximal and distal enhancer input TFs, while in reality, there may be some degree of shared inputs, either of known TFs or a general component of the transcriptional machinery. To test this hypothesis, we generated a model that added a common TF to the bursting TFs model and attempted to fit the model parameters. Some of the best parameter sets recapitulated the nonzero correlation of the heterozygote embryos, indicating that a shared factor may play a role in this system; however, this behavior was inconsistent from

one parameter set to the next (Figure 2.4). Therefore, we concluded that the simpler bursting TFs model, which consistently recapitulated the key features of the allele correlation data, was more suitable for subsequent analysis.

In conclusion, in our minimalist model of enhancer-driven transcription, the presence of TF fluctuations is required for the observed differences in allele correlation. These results also demonstrate the advantage of using a single generic TF for each enhancer. By abstracting away TF interactions, we reduced the complexity and number of parameters in the model, which allowed us to explore the relationship between TF production and allele correlation.

2.3.1 Description of the single enhancer model and associated parameters

We constructed a model of enhancer-driven transcription based on the following chemical reaction network,

$$T + E \underset{k_{\text{off}}}{\overset{k_{\text{on}}}{\rightleftharpoons}} C \xrightarrow{r} C + R$$

$$\emptyset \xrightarrow{\beta_1} nT$$

$$T \xrightarrow{\beta_{-1}} \emptyset$$

$$R \xrightarrow{\alpha} \emptyset$$

where E is an enhancer that interacts with a transcription factor T, which together bind to the promoter at a rate k_{on} to form the active promoter-enhancer complex C. When the promoter is in this active form, it leads to the production of mRNA denoted by R, which degrades by diffusion from the gene locus at a rate α. Transcription is interrupted whenever

the complex C disassociates spontaneously at a rate k_{off}. In the bursting TFs model, the transcription factor T appears at a rate β_1 and degrades at a rate β_{-1} To recapitulate *Kruppel* expression patterns, the value of β_1 was assumed to be given by

$$f(x) = c\frac{1}{\sqrt{2\pi\sigma^2}}e^{-\frac{(x-\mu)^2}{2\sigma^2}}, \tag{2.2}$$

where x is the percentage along the length of the egg and and c is a scaling constant. Since *Kruppel* activity peaks near the center of the egg, we chose $\mu = 50$, while c and σ were fitted along with the other parameters. Lastly, n was assumed to be fixed across the length of the egg.

We also generated a constant TF model, which is an adaptation of the model in (Bothma et al., 2015) [24]. This model implicitly assumes that TF numbers are constant and, therefore, are incorporated into the value of k_{on} as described by the reactions

$$E \underset{k_{\text{off}}}{\overset{Tk_{\text{on}}}{\rightleftharpoons}} C \xrightarrow{r} C + R$$

$$R \xrightarrow{\alpha} \emptyset$$

In this case, the value for T was fitted for each bin in a similar way to how β_1 was fitted; i.e. the constant number of TFs was assumed to be described by equation (2.2) (values were rounded to the nearest integer).

To simulate the transcriptional traces, we implemented a stochastic approach. Individual chemical events such as enhancer-promoter looping take place at random times and are influenced by transcription factor numbers. Individual trajectories of chemical species over time were calculated using the Gillespie algorithm (Gillespie, 1976), and these trajectories are comparable to the experimentally measured transcriptional traces. Since the enhancer

is either bound or not bound to the promoter, we imposed the constraint that $C + E = 1$ when simulating model dynamics.

2.3.2 Estimation of model parameters from experimental data

To yield a starting estimate for the k_{on} and k_{off} parameters, we defined the start and end of a burst as the time when the reactions E $\xrightarrow{\text{k}_{\text{on}}}$ C and C $\xrightarrow{\text{k}_{\text{off}}}$ E occur, respectively. The length of the i^{th} burst was defined as the range of $[b_i, p_i]$ where b_i corresponds to the time of the i^{th} instance of the reaction E $\xrightarrow{\text{k}_{\text{on}}}$ C and p_i to the time of the i^{th} instance of the reaction C $\xrightarrow{\text{k}_{\text{off}}}$ E. The time between the i^{th} burst and the $i + 1^{\text{th}}$ burst is $[p_i, b_{i+1}]$. The Gillespie algorithm dictates that the time spent in any given state is determined by an exponentially distributed random variable with a rate parameter equal to the product of two parts: the sum of rate constants of the outgoing reactions, and the number of possible reactions. If the enhancer is either bound or unbound, we have that $C = 1$ or $E = 1$, respectively. Therefore, by letting t_b be the average time between bursts and t_d be the average duration of a burst, we can write

$$t_b = \lim_{M\to\infty} \frac{1}{M} \sum_{j=1}^{M} \left(\frac{1}{N-1} \sum_{i=1}^{N-1} (b_{i+1_j} - p_{i_j}) \right) = \frac{1}{k_{\text{on}} ET} \approx \frac{1}{k_{\text{on}}},$$

and

$$t_d = \lim_{M\to\infty} \frac{1}{M} \sum_{j=1}^{M} \left(\frac{1}{N} \sum_{i=1}^{N} (p_{i_j} - b_{i_j}) \right) = \frac{1}{k_{\text{off}} C} = \frac{1}{k_{\text{off}}},$$

where N is the number of bursts for spot j, b_{i_j} and p_{i_j} denote the beginning and end of burst i in spot j respectively, and M denotes the total number of spots in the egg. The right-hand sides are given by the expected value of the exponential distribution and the

assumption that, on average, T is close to 1. While this may not be the case for T, the assumption provides a convenient upper bound for the average time between bursts which is likely not to have a much smaller value for a lower bound (a low enough value of t_b would imply nearly constant fluorescence intensity instead of bursts). Finally, the average duration of a burst t_d can be calculated directly from the data and used to obtain k_{off} by calculating $1/t_d$. Similarly, the average time between bursts t_b is readily available from the data giving us $k_{\text{on}} \approx 1/t_b$.

We were able to directly estimate mRNA production and degradation rates from the experimental data. To estimate α, we focused on periods of mRNA decay; i.e. periods where no active transcription is taking place and are thus described by

$$R' = -\alpha R,$$

which in turn can be solved to be

$$R = ce^{-t\alpha}, \tag{2.3}$$

where c is a constant of integration. Taking the derivative of equation 2.3 yields

$$R'(t) = -\alpha c e^{-t\alpha}, \tag{2.4}$$

which corresponds the slope of the decaying burst. We define the interval of decay of the i^{th} burst as $[p_i, b_{i+1}]$. For some point $t_0 \in (p_i, b_{i+1})$, let $R_0 = R(t_0) = ce^{-t_0\alpha}$. Solving this expression for c gives that $c = R_0 e^{t_0\alpha}$. Substituting for c in equation 2.4 evaluated at t_0 results in $R'(t_0) = -\alpha R_0 e^{t_0\alpha} e^{-t_0\alpha} = -\alpha R_0$. Then, it follows that

$$\alpha = -\frac{R'(t_0)}{R_0}. \tag{2.5}$$

In other words, the rate of decay of mRNA fluorescence can be calculated from any trace by taking the ratio of the slope during burst decay and its intensity at a given time $t_0 \in (p_i, b_{i+1})$.

Adjacent measurements of fluorescence intensity from the single enhancer systems were used to approximate the slope at each point in the traces. Then, equation 2.5 was applied to each point. A histogram of all calculated values was generated (Figure 2 - figure supplement 3). In this figure, there was a clear peak, which provided us with an estimate of $\alpha \approx 1.95$.

The estimation of r was done for periods of active transcription which are also accompanied by simultaneous mRNA decay. By noting that $C = 1$ during mRNA transcription, we can approximate these periods as the zeroth order process

$$\emptyset \quad \underset{\alpha}{\overset{r}{\rightleftharpoons}} \quad R$$

The differential equation associated with this system is given by

$$R' = r - \alpha R, \tag{2.6}$$

and has steady state $R^* = r/\alpha$. Equation 2.6 can be solved explicitly for R by choosing

$$R(t) = \frac{r}{\alpha} + ce^{-t\alpha},$$

where c is a constant of integration. For two adjacent measurements at times t_1 and t_2 we can write their respective measured amounts of mRNA as

$$R_1 = \frac{r}{\alpha} + c_1 e^{-t_1\alpha}, \tag{2.7}$$

and

$$R_2 = \frac{r}{\alpha} + c_2 e^{-t_2\alpha}. \tag{2.8}$$

Solving for c_1 and c_2 gives

$$c_1 = (R_1 - \frac{r}{\alpha})e^{t_1\alpha},$$

and

$$c_2 = (R_2 - \frac{r}{\alpha})e^{t_2\alpha}.$$

The short term fluctuations of mRNA from R_1 to R_2 between two adjacent discrete time points in the stochastic system can be approximated by equations 2.7 and 2.8. This implies that

$$(R_1 - \frac{r}{\alpha})e^{t_1\alpha} = (R_2 - \frac{r}{\alpha})e^{t_2\alpha},$$

which in turn gives

$$r = \alpha\frac{R_1 - R_2e^{\alpha\Delta t}}{1 - e^{\alpha\Delta t}}.$$

Therefore, the estimation of r can be computed given two adjacent measurements of fluorescence and the time between them. Finally, a similar approach as done with α was used to calculate values of r from fluorescence data. However, unlike α, r was calculated for each bin to account for differences in transcriptional efficiency across the length of the embryo.

2.3.3 Parameter fitting with simulated annealing

Simulations and parameter fitting were done with MATLAB®. Optimization in fitting was done by minimizing the sum of squared errors (SSE) between the normalized vectors of burst properties and allele correlations of the experimental and simulated data. In particular, a

vector y of experimental data was created by concatenating the following vectors: burst size, integrated fluorescence, frequency, duration, and allele correlation across the length of the embryo. The vector y was subsequently normalized by dividing each burst property by the largest element in their respective vectors (except correlation which by definition is unitless between -1 and 1). A vector x was created in an analogous fashion to y but using simulated instead of experimental data. However, x was normalized using the same elements that were used to normalize y. Then, the discrepancy between the experimental and simulated data was measured by

$$SSE = \sum_{i=1}^{n} (y_i - x_i)^2.$$

We used a high-performance computing cluster to compute 200 independent runs of parameter fitting with simulated annealing for each model variant. The algorithm requires an initial guess of the parameter set P_0, an initial temperature Γ_0, a final temperature Γ', the number of iterations per temperature N, and a cooling factor μ. Then, each iteration is as follows:

1. If the current iteration i is such that $i > N$, then update the current temperature $\Gamma_k = \mu^k \Gamma_0$ to $\mu^{k+1}\Gamma_0$ and set $i = 0$. Otherwise, set i to $i + 1$.

2. Check if $\Gamma_k < \Gamma'$. If so, return the current parameter set P_j and terminate.

3. Choose a parameter randomly from P_j and multiply it by a value sampled from a normal distribution with a mean equal to 1. The standard deviation of such distribution should be continuously updated to be Γ_k. The result of this step is the newly generated parameter set P_{j+1}.

4. Calculate ΔE as the difference in SSE between the data generated by P_j and that generated by P_{j+1}. Update P_j to P_{j+1} if $\Delta E < 0$ or with probability $p < e^{\Delta E/\Gamma_k}$ where p is a uniformly distributed random number.

5. Repeat all steps until termination.

To generate our results, we chose $\Gamma_0 = 1$, $\Gamma' = \Gamma_0/10$, $N = 30$, and $\mu = 0.8$. We observed an improvement in the quality of the fittings by using analysis-derived parameter values as initial guesses instead of values given through random sampling. The sampled space ranged from 10^{-3} to 10^3 for all parameters except n which was sampled from 10^0 to 10^2 and σ which was randomly chosen to be an integer between 1 and 20. Equal numbers of parameter values were sampled at each order of magnitude. The analysis in the section above was used to estimate the parameters in P_0. Parameters that were not estimated in the previous section were given the following initial guesses: $n = 10$, $\beta_{-1} = 1$, $\sigma = 6$, and $c = 40$. Initial guesses for c and σ were based on the experimental observation that there is little transcription outside of 20-80% egg length. Based on this observation, simulations were limited to this egg length range, as well. For the constant TFs model, both analysis-derived and random initial parameter values were used to maximize the likelihood of finding any parameter set capable of recapitulating the observed allele correlation.

2.3.4 Generation of simulated experimental data

Parameter sets resulting from fitting were sorted in ascending order based on their sum of squared errors, and the 10 lowest error parameter sets are what we called the 10 best parameter sets. For all figures, we simulated 80 spots per bin and simulated each bin 5 times to generate error bars. Data for the distal enhancer at the proximal location was used to reproduce simulated allele correlations in all cases.

Gillespie simulations update the counts of each chemical species at random time intervals. However, for ease of parameter fitting and to better recapitulate the experiments, we generated data in two distinct timescales: one consisting of 30 second intervals after which mRNA counts were recorded, and another consisting of random time intervals generated by

the algorithm after which chemical counts were updated. The former one was used for all parameter fitting rounds and generation of figures.

2.4 The shadow pair's activity is less sensitive to fluctuations in Bicoid levels than is the activity of a single enhancer

Both the experimental measurements of allele correlation and the computational model suggest that input TF fluctuations are an appreciable source of noise for enhancer activity. Further, previous experimental work [54] and the low correlation of transcriptional activity in heterozygotes (Figure 2.1E) indicates that each individual *Kr* enhancer receives different TF input signals. This suggests that the shadow enhancer pair will be less sensitive to an input TF fluctuation than a single enhancer, because the shadow enhancer pair's activity is dependent on a broader range of TF inputs. To directly observe the relationship between input TF levels and enhancer output, we simultaneously tracked Bcd levels and enhancer activity in individual nuclei (Figure 2.6; Supp. Videos 7–8). We measured this relationship for both the distal enhancer, which is activated by Bcd, and the shadow enhancer pair, and predicted that the distal enhancer's transcription dynamics are more strongly influenced by fluctuations in Bcd levels.

To allow for tracking of both Bcd levels and enhancer activity, we crossed female flies that express eGFP-tagged Bcd in the place of endogenous Bcd (called Bcd-GFP from here on [70]) and MCP-mCherry with male flies homozygous for either the shadow pair or distal enhancer reporter. As the Bcd-GFP transgene was inserted in a Bcd null background, the resulting embryos should receive roughly WT levels of Bcd. The females flies were heterozygous for the maternally deposited Bcd-GFP, and therefore, we estimate that roughly half of the Bcd

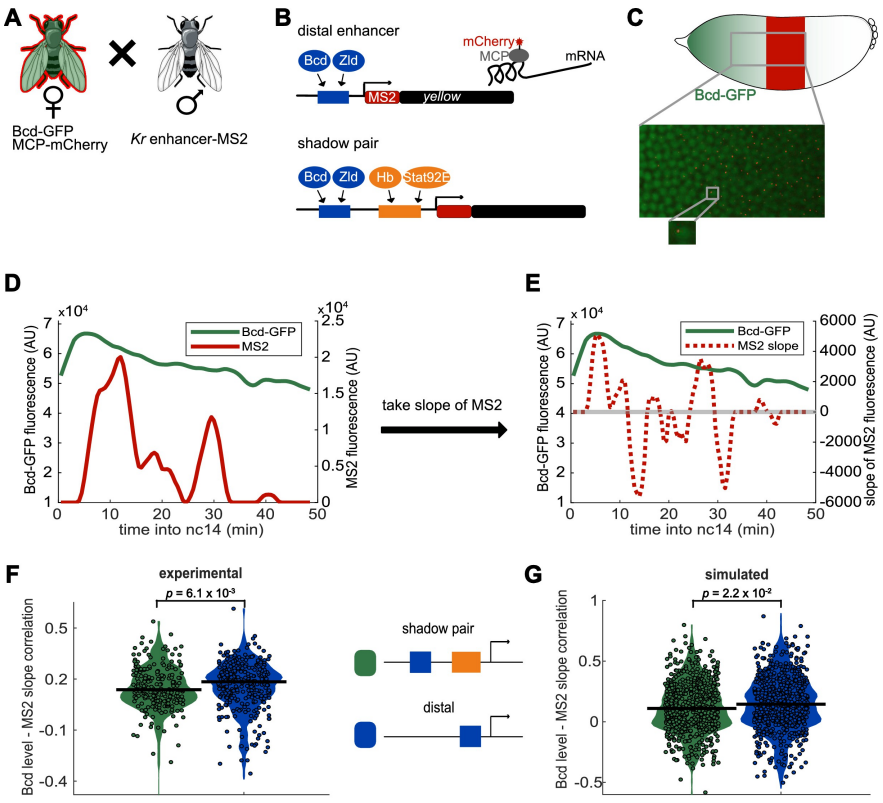

Figure 2.6: Activity of *Kr* shadow pair is less correlated with Bcd levels than is activity of single distal enhancer. To assess whether fluctuations in enhancer activity across time are associated with fluctuations in TF levels, we simultaneously measured Bcd levels and enhancer-driven transcription in individual nuclei. (A) To track Bcd levels and enhancer activity in the same nuclei, we crossed flies expressing a *Kr* enhancer-MS2 transgene to flies expressing Bcd-GFP and MCP-mCherry. In the resulting embryos, Bcd levels can be measured by GFP fluorescence and enhancer reporter activity can be measured by mCherry fluorescence. (B) Schematic of the enhancer reporters used for simultaneous tracking of TF levels and enhancer activity. As in Figure 1, the transcribed MS2 sequence forms stem loops that are bound by MCP, which is here tagged with mCherry. (C) Bcd-GFP expression forms a gradient from the anterior to posterior of the embryo, whereas the *Kr* enhancer reporters drive expression in the center region of the embryo. The magnified section of the embryo shows a still frame from live imaging indicating nuclei (green) and active transcription spots (red). (D) Bcd levels and enhancer activity can be simultaneously tracked in individual nuclei. Graph shows a representative trace of Bcd-GFP levels (in green) and distal enhancer transcriptional activity (in red) in a nucleus across the time of nc14. (E) Activator TF levels regulate enhancer activity, so to assess the sensitivity of our enhancer constructs to input TF fluctuations, we compare the levels of nuclear Bcd-GFP to the slope of MS2 fluorescence across the time of nc14. Positive slope values indicate an increase in enhancer activity, while negative values indicate a decrease in enhancer activity. The graph shows nuclear Bcd-GFP levels (as in D), in solid green line, and MS2 slope values (of the MS2 trace shown in D), in dashed red line, across the time of nc14. Horizontal grey line indicates a slope value of 0. (F) Changes in the shadow pair's activity are significantly less correlated with Bcd-GFP levels than are changes in the distal enhancer's activity. Shown are violin plots of the distribution of correlation values between Bcd-GFP levels and MS2 slopes in individual nuclei for either the shadow pair or distal enhancer. Circles correspond to the correlation values of individual nuclei and the horizontal lines indicate the median. This correlation is significantly higher for the distal enhancer than it is for the shadow pair (median r values are 0.18 and 0.14, respectively. p-Value=6.1×10^{-3} from Kruskal-Wallis pairwise comparison.) The total number of nuclei used in calculations for each construct by AP bin are given in Supplementary file 2.

proteins were labeled. Given the previous work demonstrating the normal function and expression levels of tagged Bcd, we expect the Bcd-GFP levels to be a representative sample of total Bcd [70].

Higher activator TF levels increase enhancer activity. We therefore measured the correlation of nuclear Bcd-GFP levels to the slope of MS2 signal. When the enhancer is active, MS2 signal has a positive slope, when the enhancer is inactive, slope is negative. If the shadow enhancer pair is less sensitive than the distal enhancer to fluctuations in Bcd levels, we would predict higher correlation between Bcd-GFP levels and the activity of the distal enhancer than that of the shadow enhancer pair. We find that the transcription dynamics driven by the distal enhancer are indeed significantly more correlated to nuclear Bcd-GFP levels (median $r = 0.18$) than the dynamics driven by the shadow pair (median $r = 0.14$; Figure 2.6F; p-Value=6.1×10^{-3}), although both correlations are modest (see Discussion). The lower correlation indicates that transcription driven by the shadow pair is less sensitive to Bcd level fluctuations than is the distal enhancer. Our modeling recapitulates this finding, showing that the separated TF inputs of the shadow pair are sufficient to explain the observed decreased sensitivity to TF fluctuations (median $r = 0.14$ for the distal enhancer; 0.11 for the shadow pair; p-Value=2.2×10^{-2}; Figure 2.6G: Our enhancer model recapitulates the lower correlation between Bcd-GFP levels and enhancer activity seen with the shadow pair than with the distal enhancer. Graph is as in F, but showing the distribution of correlation values in simulated nuclei, using 100 nuclei per AP bin. Median r values for simulation are 0.14 for the distal enhancer and 0.11 for the shadow pair. p-Value=2.2×10^{-2} from Kruskal-Wallis pairwise comparison of correlations.). These findings indicate that the shadow enhancer pair is better able to buffer fluctuations in a single activating TF than a single enhancer, likely due to the shadow enhancer pair's separation of TF inputs.

2.5 The shadow enhancer pair drives less noisy expression than enhancer duplications

We wanted to further test whether the shadow enhancer pair drives less noisy gene expression output than a simple enhancer duplication. We compared the noise in expression driven by the shadow enhancer pair to that driven by two copies of either the distal or proximal enhancer (Figure 2.7). If the shadow enhancer pair drives lower noise, this suggests that having two independently acting enhancers is a critical feature of shadow enhancers' ability to reduce variability and mediate robustness. Alternatively, if duplicated enhancers drive similar levels of expression noise, this suggests that enhancer independence is not critical for shadow enhancer function and that shadow enhancers mediate robustness through a different mechanism, such as ensuring a critical threshold of expression is met [52, 53].

We tracked transcriptional activity in embryos expressing MS2 under the control of the shadow enhancer pair, a duplicated proximal enhancer, or a duplicated distal enhancer (Figure 2.7). To measure noise associated with each enhancer, we used these traces to calculate the coefficient of variation (CV) of transcriptional activity across nc14. CV is the standard deviation divided by the mean and provides a unitless measure of noise to allow comparisons among our enhancer constructs. We then grouped these CV values by the embryo position of the transcriptional spots and found the average CV at each position for each enhancer construct. All the enhancer constructs display the lowest expression noise at the embryo position of their peak expression (Figure 2.7A), in agreement with previous findings of an inverse relationship between mean expression and noise levels [78] (Figure 2.15). The shadow enhancer pair's expression noise is ˜30% or 15% lower, respectively, than that of the duplicated proximal or distal enhancers in their positions of maximum expression (Figure 2.7C).

If the primary function of shadow enhancers is only to ensure a critical threshold of expression is reached, we would not expect to also see the lower expression noise associated

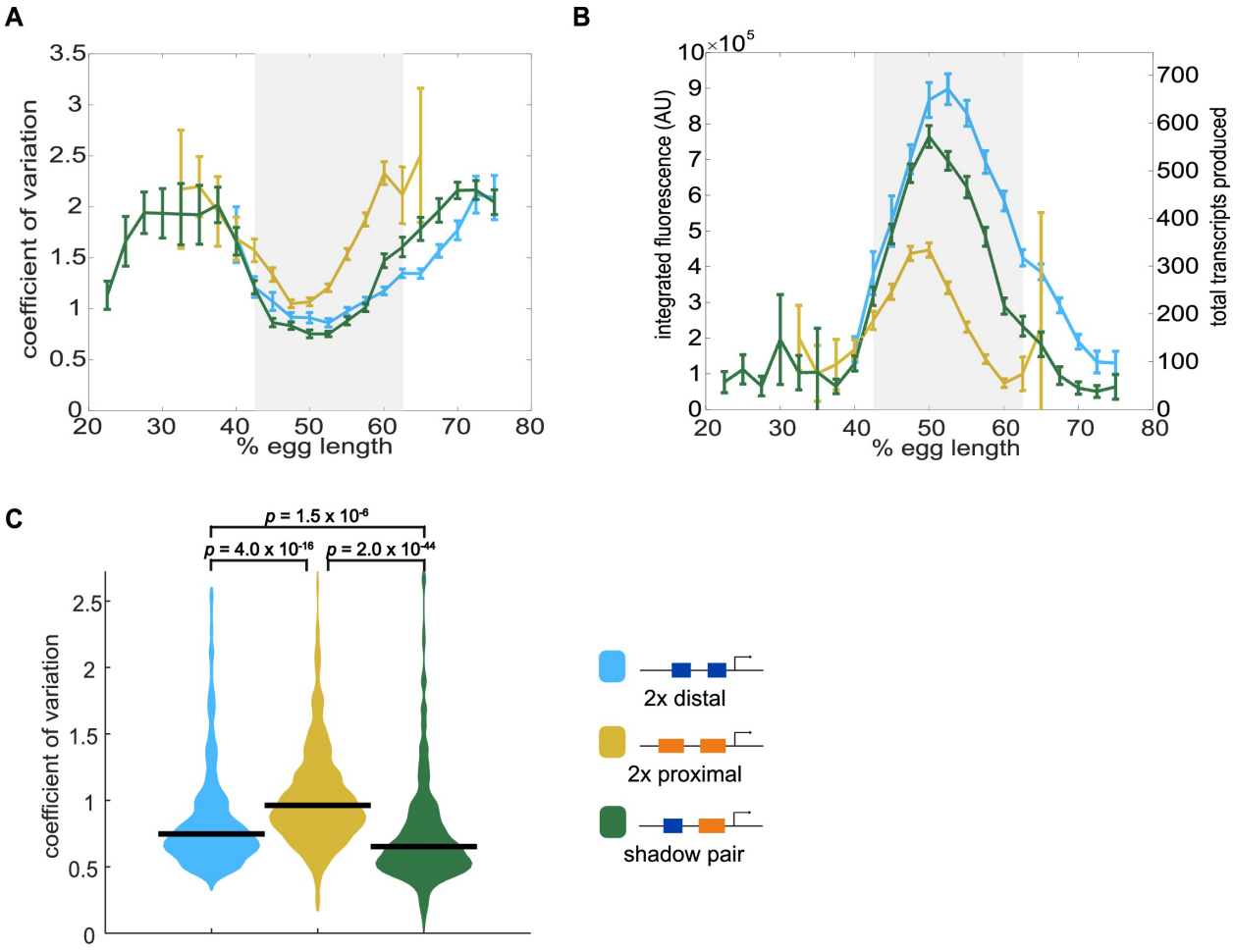

Figure 2.7: Shadow enhancer pair produces lower expression noise than duplicated enhancers. To investigate whether the shadow enhancer pair drives less noisy expression, we calculate the coefficient of variation (CV) associated with the shadow enhancer pair or either duplicated enhancer across time of nc14. (A) The shadow enhancer pair displays lower temporal expression noise than either duplicated enhancer. Graph is mean coefficient of variation of fluorescence traces across time as a function of embryo position. The grey rectangle in A and B highlights the region of endogenous *Kr* expression (boundaries where 33% maximal expression occurs). (B) The shadow enhancer pair shows the lowest expression noise, but not the highest expression levels, indicating that the lower noise is not simply a function of higher expression. Graph is average total expression during nc14 as a function of embryo position. Error bars in A and B represent 95% confidence intervals. Total number of transcriptional spots used for graphs are given in Supplementary file 3 by construct and AP bin. (C) Violin plot of distribution of CV values at AP bin of peak expression for each enhancer construct (corresponding to 50% egg length for shadow pair and duplicated proximal, 52.5% egg length for duplicated distal), horizontal bar indicates median. Y-axis limited to 99th percentile of the construct with highest expression noise (duplicated proximal). The shadow pair drives significantly lower expression noise than either duplicated enhancer (p-Value=1.5×10^{-6} for duplicated distal and shadow pair. p-Value=2.0×10^{-44} for duplicated proximal and shadow pair). p-Values were calculated using Kruskal Wallis pairwise comparison with Bonferroni multiple comparison correction.

with the shadow enhancer pair compared to either duplicated enhancer. Furthermore, this decreased expression noise is not simply a consequence of higher expression levels, as the shadow enhancer pair produces less mRNA than the duplicated distal enhancer during nc14 (Figure 2.7C). The lower expression noise associated with the shadow enhancer pair suggests that it is less susceptible to fluctuations in upstream TFs than multiple identical enhancers.

To explore which factors drive the difference in CVs between the duplicated and shadow enhancer constructs, we extended our model to have a single promoter controlled by two enhancers (Figure 2.8A). To do so, we assumed that either or both enhancers can be looped to the promoter and drive mRNA production. The rate of mRNA production when both enhancers are looped is the sum of the rates driven by the individual enhancers. We assumed that some parameters, for example the TF production rates and mRNA decay rate, are the same as the single enhancer case. We allowed the parameters describing the promoter-enhancer looping dynamics (the k_{on} and k_{off} values) to differ, depending on the enhancer's position in the construct relative to the promoter and whether another enhancer is present. To fit the k_{on} and k_{off} values, we used the medians of the 10 best single enhancer parameter sets as a starting point and performed simulated annealing to refine them.

This approach allowed us to examine how the model parameters that describe promoter-enhancer looping dynamics change when two enhancers are controlling the same promoter. We compared the k_{off} and k_{on} values for each enhancer in the two enhancer constructs to their values from the single enhancer model. We generally found that k_{off} values increased and k_{on} values decreased (Figure 2.8B). The effect is most pronounced in the duplicated distal enhancer, with large changes to the k_{off} and k_{on} values for the enhancer in the position far from the promoter (position 2). Given that our model assumes that enhancers act additively and only allows for changes in the k_{off} and k_{on} values, these observed effects may indicate that either the presence of a second enhancer interferes with promoter-enhancer looping or that the promoter can be saturated. Our model cannot distinguish between these two possibilities,

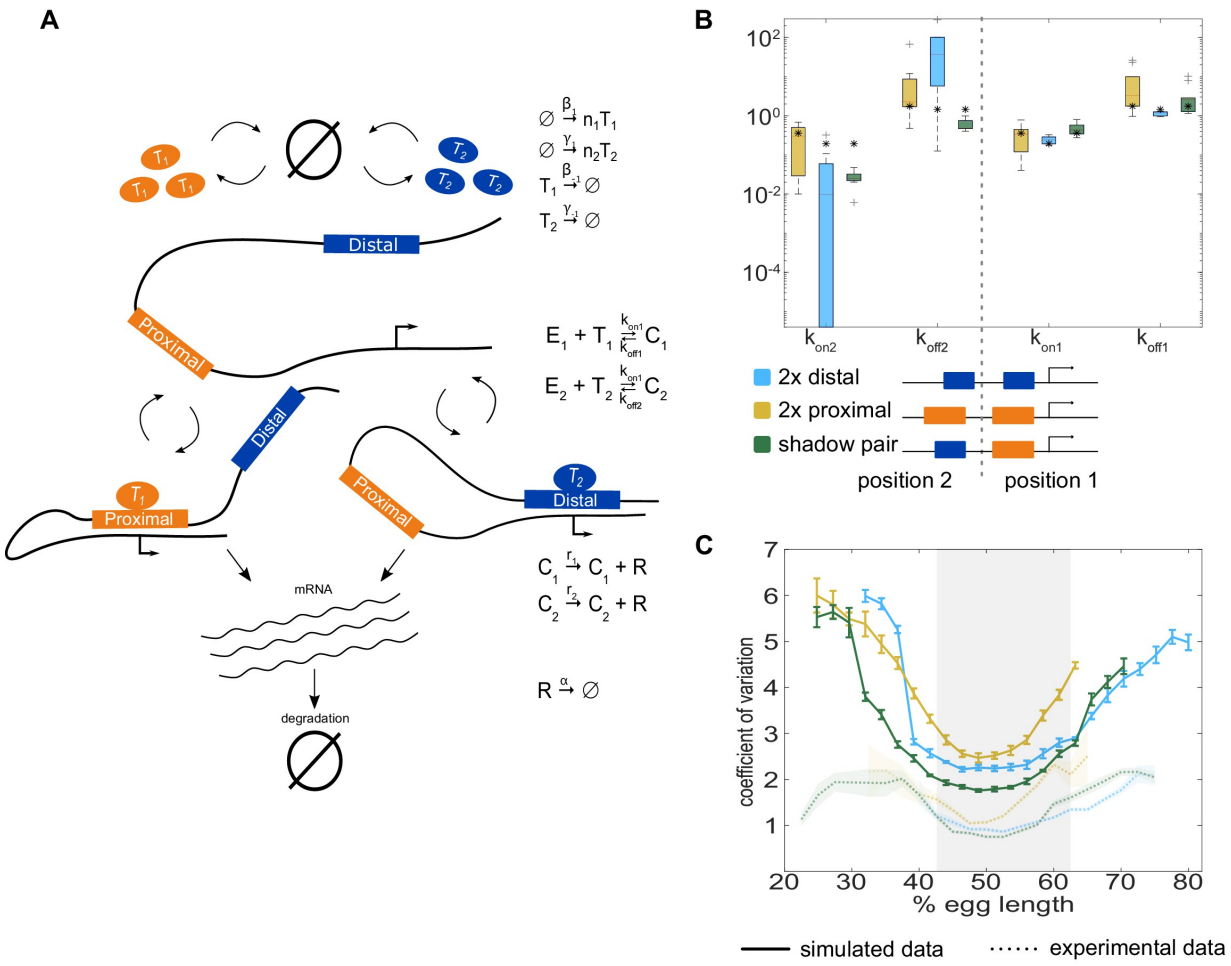

Figure 2.8: The two enhancer model recapitulates low expression noise associated with the shadow enhancer pair. To assess whether the separation of input TFs mediates the lower expression noise driven by the shadow enhancer pair, we expanded our model to incorporate two enhancers driving transcription. (A) Schematic of the two enhancer model. We assume that when two enhancers control a single promoter, either or both can loop to the promoter and drive transcription. We defined model parameters as in Figure 2, and only allowed the k_{on} and k_{off} values to vary from the single enhancer model. (B) To understand the effect of adding a second enhancer, we examined how the k_{on} and k_{off} values vary from those in the single enhancer model. We plotted the distribution of the values for k_{on} and k_{off} for each enhancer in the three different constructs measured. The distribution shows the values derived from the 10 best-fitting parameter sets, and the black star in each column indicates the k_{on} or k_{off} value from the corresponding single enhancer model. In general, the k_{off} values increased relative to the single enhancer model, and the k_{on} values decreased, indicating that the presence of a second enhancer inhibits the activity of the first. (C) Graph of average coefficient of variation of simulated (solid lines) or experimental (dotted lines) transcriptional traces as a function of egg length. The model is able to recapitulate the lower expression noise seen with the shadow enhancer pair with no additional fitting, indicating that the separation of TF inputs to the two enhancers is sufficient to explain this observation. Error bars of simulated data and shaded region of experimental data indicate 95% confidence intervals.

but these observations are consistent with our (Figure 2.16) and previous results indicating that the *Kr* enhancers can act sub-additively [23]. Additionally, the dramatic changes in k_{off} and k_{on} values in the duplicated distal enhancer are consistent with a previous assertion that enhancer sub-additivity is most pronounced in cases of strong enhancers [24].

We used these models to simulate transcription and predict the resulting CVs from the duplicated enhancer and shadow pair constructs. In line with experimental data, we found the model predicts that the shadow pair construct drives lower noise than the duplicated distal or duplicated proximal enhancer constructs in the middle of the embryo (Figure 2.8C). This is particularly notable, as we did not explicitly fit our model to reproduce the experimentally observed CVs. There is only one fundamental difference between the shadow pair and duplicated enhancer models, namely the use of separate TF inputs for the shadow pair. Therefore, in our simplified model, we can conclude that the separation of input TFs is sufficient to explain the lower noise driven by the shadow enhancer pair construct.

2.5.1 Description of two enhancer model, parameter estimation, and fitting

To explore two enhancer systems, we expanded our previous model to include an additional enhancer. First, we considered duplicated enhancer systems, which consist of either two proximal or two distal enhancers. Enhancers were denoted by E_1 and E_2, which correspond to two identical enhancers that exist in different locations relative to the promoter. They are activated by the same transcription factors as described by the reactions

$$T + E_1 \underset{k_{\text{off}_1}}{\overset{k_{\text{on}_1}}{\rightleftharpoons}} C_1 \xrightarrow{r_1} C_1 + R$$

$$T + E_2 \underset{k_{\text{off}_2}}{\overset{k_{\text{on}_2}}{\rightleftharpoons}} C_2 \xrightarrow{r_2} C_2 + R$$

$$\emptyset \xrightarrow{\beta_1} nT$$

$$T \xrightarrow{\beta_{-1}} \emptyset$$

$$R \xrightarrow{\alpha} \emptyset$$

Without loss of generality, we used E_1 to denote the enhancer at the proximal location and E_2 to denote the enhancer at the distal location. This model describes independent enhancer dynamics; i.e. the behavior of one enhancer does not affect the behavior of the other, and, as such, both enhancers can be simultaneously looped to the promoter. Consequently, to account for potential enhancer interference or competition for the promoter, we assumed distinct k_{on} and k_{off} values for each enhancer in the duplicated enhancer constructs. We also used distinct values of r for each distal enhancer in the duplicated distal construct since fluorescence data was available for this enhancer at the proximal and endogenous location. For proximal enhancers, we assume $r_1 = r_2$.

To describe the dynamics of the shadow enhancer pair, we denoted the activators for E_1 (the proximal enhancer) and E_2 (the distal enhancer) by T_1 and T_2 respectively as shown in the network

$$T_1 + E_1 \underset{k_{\text{off}_1}}{\overset{k_{\text{on}_1}}{\rightleftharpoons}} C_1 \xrightarrow{r_1} C_1 + R$$

$$T_2 + E_2 \underset{k_{\text{off}_2}}{\overset{k_{\text{on}_2}}{\rightleftharpoons}} C_2 \xrightarrow{r_2} C_2 + R$$

$$\emptyset \xrightarrow{\beta_1} n_1 T_1$$

$$\emptyset \xrightarrow{\gamma_1} n_2 T_2$$

$$T_1 \xrightarrow{\beta_{-1}} \emptyset$$

$$T_2 \xrightarrow{\gamma_{-1}} \emptyset$$

$$R \xrightarrow{\alpha} \emptyset$$

The production rate of T_2, γ_1, was calculated in the same way as production rate of T_1, β_1, but differed in the values of c and σ. The two enhancer models were also used to calculate allele correlation between homozygotes and heterozygotes because a distinction between the mRNA produced by C_1 and C_2 was made. This approach works because, e.g., when considering the homozygote embryos, each single enhancer resides in the same nucleus and is therefore affected by the same fluctuating TF numbers. In the duplicated enhancer model, each enhancer E_1 or E_2 is affected by the same fluctuations in the number of transcription factor T. An analogous logic applies to the heterozygotes.

To fit the two enhancer models to experimental data, we retained several parameters from the single enhancer models. Parameters r and α were directly calculated from the data, and, as such, did not vary across models. We assume that parameters concerning transcription factors (β_1, β_{-1} γ_1, γ_{-1}, n_1, and n_2) are not affected by the presence of an additional enhancer. Therefore, in our model, only k_{on} and k_{off} are free to change. To fit the values of k_{on1}, k_{on2}, k_{off1}, and k_{off2}, we set the other model parameters to the median values of the 10 best parameter sets in the respective single enhancer model. We then used a similar simulating annealing approach to fit the k_{on} and k_{off} values. We used the resulting values to simulate transcriptional traces and to calculate the predicted CV values shown in Figure 2.8.

2.6 The shadow enhancer pair buffers against intrinsic and extrinsic sources of noise

To further understand the sources of noise the shadow enhancer pair is able to buffer, we compared the extrinsic and intrinsic noise associated with the shadow enhancer pair to that associated with either single or duplicated enhancers. To do so, we measured the transcriptional dynamics of embryos with two identical reporters in each nucleus and calculated noise sources using the approach of Elowitz et al., 2002. [79] Intrinsic noise corresponds to sources of noise, such as TF binding and unbinding, that affect each allele separately. It is quantified by the degree to which the activities of the two reporters in a single nucleus differ. Extrinsic noise corresponds to global sources of noise, such as TF levels, that affect both alleles simultaneously. It is measured by the degree to which the activities of the two reporters change together. Intrinsic and extrinsic noise are defined such that, when squared, their sum is equal to total $noise^2$, which corresponds to the CV^2 of the two identical alleles in each nucleus in our system (see Materials and methods). Because our data do not meet one key assumption needed to measure extrinsic and intrinsic noise with the two-reporter approach (see Discussion;Figure 2.17), we use the terms inter-allele noise and covariance in place of intrinsic and extrinsic noise.

Based on our separation of inputs hypothesis and CV data, we expected the total noise associated with the shadow enhancer pair to be lower than that associated with the duplicated enhancers. We predicted that the shadow enhancer pair will mediate lower total expression noise through lower covariance, as the two member enhancers are regulated by different TFs. Given the complexity of predicting inter-allele noise from first principles (Materials and methods; Figure 2.18), we predicted that constructs with two enhancers will have lower inter-allele noise than single enhancer constructs but did not have a strong prediction regarding the relative inter-allele noise among the different two-enhancer constructs.

Comparisons of noise between the single and duplicated enhancer constructs would further allow us to discern whether reductions in noise are generally associated with two-enhancer constructs or whether this is a particular feature of the shadow enhancer pair.

Neither the duplicated proximal nor distal enhancers drive significantly lower total noise than the corresponding single enhancers, indicating that the addition of an identical enhancer is not sufficient to reduce expression noise in this system (Figure 2.9A). The shadow enhancer pair drives lower total expression noise than either single or duplicated enhancer, consistent with the temporal CV data in Figure 2.7. The median total expression noise associated with the duplicated distal and duplicated proximal enhancers is 1.4 or 2.4 times higher, respectively, than that associated with the shadow enhancer pair (Figure 2.9A). Note that for measurements of noise, our distal construct places the enhancer at the endogenous spacing from the promoter, as we wanted to control for positional effects on expression and noise [23] (Figure 2.19).

In line with our expectations, the shadow enhancer pair has significantly lower covariance levels than either single or duplicated enhancer (Figure 2.9B). The shadow enhancer pair also has lower inter-allele noise than all of the other constructs, though these differences are only marginally significant ($p = 0.13$) when compared to the duplicated distal enhancer. Covariance makes a larger contribution to the total noise for the duplicated distal enhancer and the shadow enhancer pair, while inter-allele noise is the larger source of noise for the single distal enhancer and the single or duplicated proximal enhancers (Figure 2.9B).

The lower total noise and covariance of the shadow enhancer pair support our hypothesis that, by separating regulation of the member enhancers, the shadow enhancer pair can buffer against upstream fluctuations. The lower inter-allele noise associated with the shadow enhancer pair warrants further investigation. A simple theoretical approach predicts that two enhancer constructs will have lower inter-allele noise (Figure 2.18). Given that this is not universally observed in our data, this suggests that there is still much to discover about

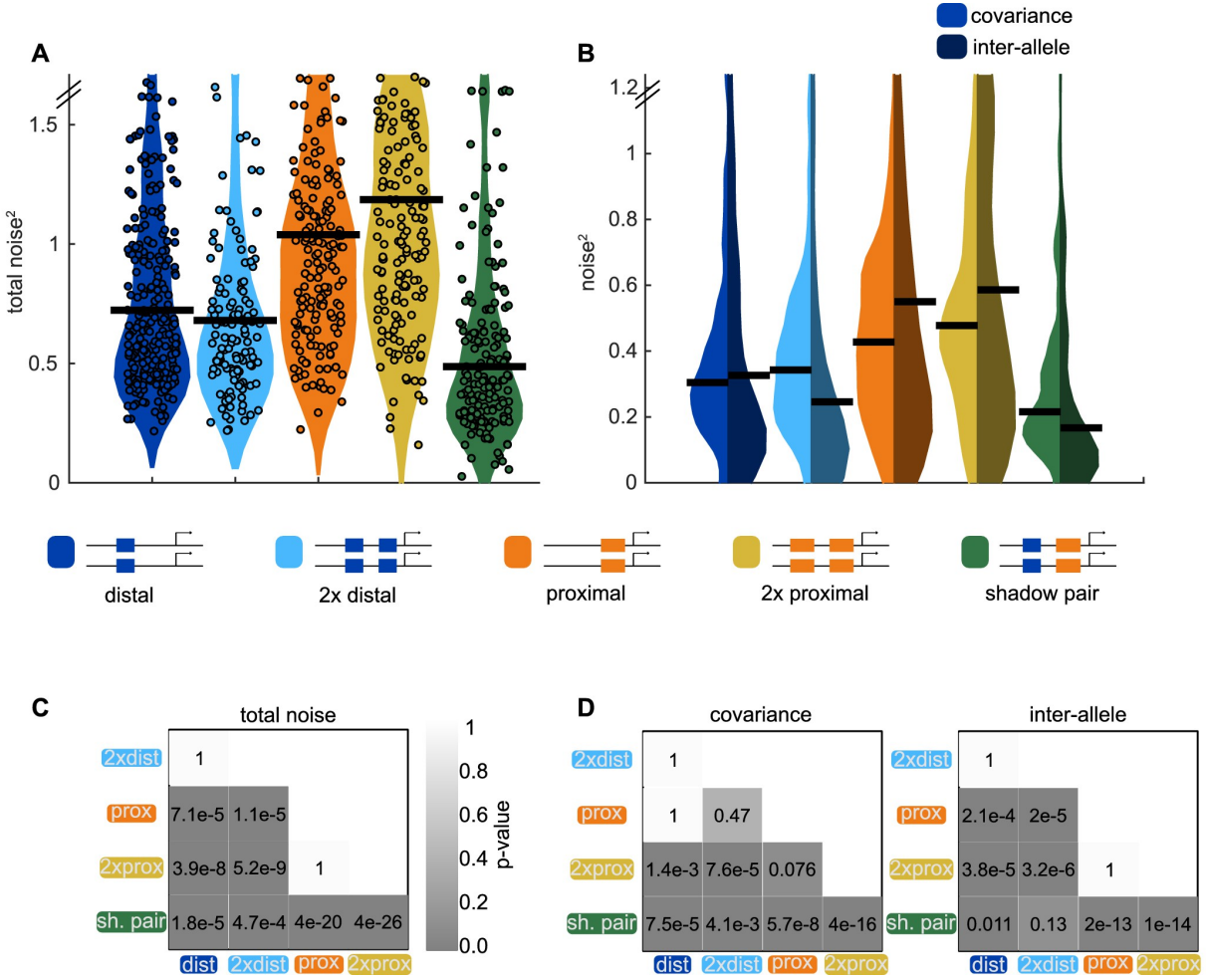

Figure 2.9: Shadow enhancer pair achieves lower total noise by buffering global and allele-specific sources of noise. To determine how the shadow enhancer pair produces lower expression noise, we calculated the total noise associated with each enhancer construct and decomposed this into the contributions of covariance and inter-allele noise. Covariance is a measure of how the activities of the two alleles in a nucleus change together and is indicative of global sources of noise. Inter-allele noise is a measure of how the activities of the two alleles differ and is indicative of allele-specific sources of noise. (A) The shadow enhancer pair has lower total noise than single or duplicated enhancers. Circles are total noise values for individual nuclei in AP bin of peak expression for the given enhancer construct. Horizontal line represents the median. The y-axis is limited to 75th percentile of the proximal enhancer, which has the largest noise values. The shadow enhancer pair has significantly lower total noise than all other constructs. (B) The shadow enhancer pair displays significantly lower covariance than either single or duplicated enhancer and significantly lower inter-allele noise than both single enhancers and the duplicated proximal enhancer. The left half of each violin plot shows the distribution of covariance values of nuclei in the AP bin of peak expression, while the right half shows the distribution of inter-allele noise values. Horizontal lines represent median. The y-axis is again limited to the 75th percentile of enhancer with the largest noise values, which is duplicated proximal. The lower covariance and inter-allele noise associated with the shadow enhancer pair indicates it is better able to buffer both global and allele-specific sources of noise. (C) p-Value table of Kruskal-Wallis pairwise comparison of the total noise values of each enhancer construct. p-Value gradient legend applies to C and D. (D) p-Value table of Kruskal-Wallis pairwise comparison of covariance (on left) and inter-allele noise (on right) values for each enhancer construct. Bonferroni multiple comparison corrections were used for p-Values in C and D. Total number of nuclei used in noise calculations are given in Supplementary file 1.

how inter-allele noise changes as additional enhancers control a gene's transcription.

We showed the *Kr* shadow enhancer pair drives expression with lower total noise than either single or duplicated enhancer, yet previous studies have generally found individual member enhancers of a shadow enhancer set are dispensable under ideal conditions [8, 53, 10]. However, in the face of environmental or genetic stress, the full shadow enhancer group is necessary for proper development [8, 10, 53]. We therefore decided to investigate whether temperature stress causes significant increases in expression noise and whether the shadow enhancer pair or duplicated enhancers can buffer these potential increases in noise.

Similar to our findings at ambient temperature (26.5°C), the shadow enhancer pair drives lower total noise than all other tested enhancer constructs at 32°C (Figure 7B). At 32°C, the duplicated distal and duplicated proximal enhancers display 35% or 52%, respectively, higher total noise than the shadow enhancer pair. At 17°C, the shadow enhancer pair has approximately 46% lower total noise than either the single or duplicated proximal enhancer, 21% lower total noise than the single distal enhancer, and is not significantly different than the duplicated distal enhancer (Figure 2.10A). As seen by the variety of shapes in the temperature response curves (Figure 2.10C), temperature perturbations have enhancer-specific effects, suggesting input TFs may differ in their response to temperature change. The low noise driven by the shadow enhancer pair across conditions is consistent with previous studies showing shadow enhancers are required for robust gene expression at elevated and lowered temperatures [8, 9].

To calculate the temporal CV each transcriptional spot i, we used the formula:

$$CV(i) = \frac{standard\ deviation(m_i(t))}{mean(m_i(t))}$$

where $m_i(t)$ is the fluorescence of spot i at time t.

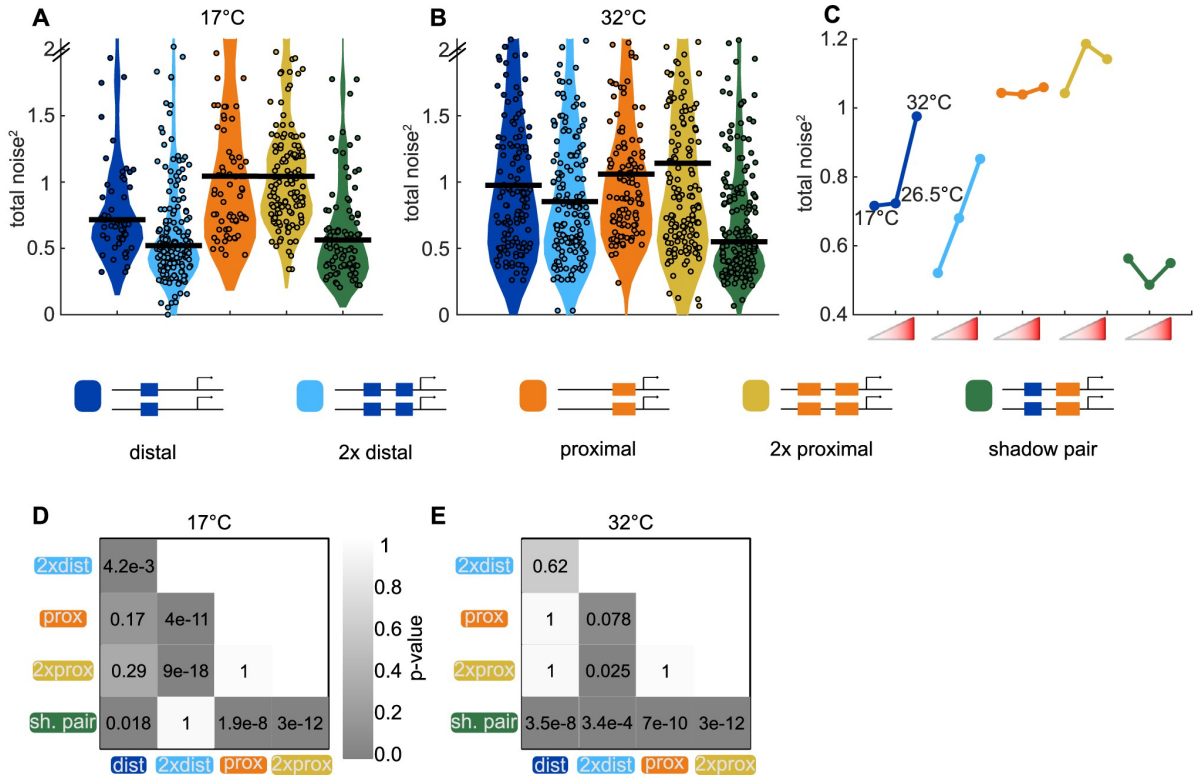

Figure 2.10: Shadow enhancer pair maintains lower total noise across temperature perturbations. To test the ability of each enhancer construct to buffer temperature perturbations, we measured the total expression noise associated with each for embryos imaged at 17°C or 32°C. (A) The shadow enhancer pair displays significantly lower total noise than the single or duplicated proximal enhancer and the single distal enhancer at 17°C. Circles are total noise values for individual nuclei in AP bin of peak expression for the given enhancer construct and horizontal bars represent medians. The y-axis is limited to 75th percentile of construct with highest total noise at 17°C (single proximal). (B) The shadow enhancer pair has significantly lower total noise than all other constructs at 32°C. The y-axis is limited to 75th percentile of the enhancer construct with highest total noise at 32°C (duplicated proximal). (C) Temperature changes have different effects on the total noise associated with the different enhancers. The median total noise value at the AP bin of peak expression at the three measured temperatures is shown for each enhancer construct. Within each enhancer, the median total noise values are shown left to right for 17°C, 26.5°C, and 32°C. (D) p-Value table of Kruskal-Wallis pairwise comparison of the total noise values of each enhancer construct at 17°C. p-value gradient legend applies to D and E. (E) p-Value table of Kruskal-Wallis pairwise comparison of the total noise values of each enhancer construct at 32°C. Bonferroni multiple comparison corrections were used for p-Values in D and E.

We also decomposed the total noise experienced in each nucleus to inter-allele noise and co-variance, analogous to the approach of Elowitz et al., 2002 [79].

Inter-allele noise is calculated one nucleus at a time. It is the mean square difference between the fluorescence of the two alleles in a single nucleus:

$$\eta^2_{IA} = \frac{\langle (m_1(t) - m_2(t))^2 \rangle}{2\langle m_1(t) \rangle \langle m_2(t) \rangle}$$

where $m_1(t)$ is the fluorescence of one allele in the nucleus at time t, and $m_2(t)$ is the fluorescence of the other allele in the same nucleus and the angled brackets indicate the mean across the time of nc14.

Covariance is the covariance of the activity of the two alleles in the same nucleus across the time of nc14:

$$\eta^2_{CV} = \frac{\langle (m_1(t) m_2(t)) \rangle - \langle m_1(t) \rangle \langle m_2(t) \rangle}{\langle m_1(t) \rangle \langle m_2(t) \rangle}$$

The inter-allele and covariance values are defined such that they sum to give the total transcriptional noise displayed by the two alleles in a single nucleus.

$$\eta^2_{tot} = \frac{\langle (m_1(t)^2 + m_2(t)^2) \rangle - 2\langle m_1(t) \rangle \langle m_2(t) \rangle}{2\langle m_1(t) \rangle \langle m_2(t) \rangle}$$

This total noise value is equal to the coefficient of variation of the expression of the two alleles in a single nucleus across the time of nc14.

To determine any significant differences in total noise, covariance, or inter-allele noise values between the different enhancer constructs, we performed Kruskal-Wallis tests with the

Bonferroni multiple comparison correction.

2.7 Discussion

Fluctuations in the levels of transcripts and proteins are an unavoidable challenge to precise developmental patterning [80, 81, 63]. Given that shadow enhancers are common and necessary for robust gene expression [10, 8, 9], we proposed that shadow enhancers may function to buffer the effects of fluctuations in the levels of key developmental TFs. To address this, we have, for the first time, extensively characterized the noise associated with shadow enhancers critical for patterning the early *Drosophila* embryo. By either tracking biallelic transcription or simultaneously measuring input TF levels and transcription, we tested the hypothesis that shadow enhancers buffer noise through a separation of TF inputs to the individual member enhancers. Our results show that TF fluctuations play a significant role in transcriptional noise and that a shadow enhancer pair is better able to buffer both extrinsic and intrinsic sources of noise than duplicated enhancers. Using a simple mathematical model, we found that fluctuations in TF levels are required to reproduce the observed correlations between reporter activity and that the low noise driven by the shadow enhancer pair may be a natural consequence of the separation of TF inputs to the member enhancers. Lastly, we showed that a shadow enhancer pair is uniquely able to buffer expression noise across a wide range of temperatures. Together, these results support the hypothesis that shadow enhancers buffer input TF noise to drive robust gene expression patterns during development.

2.7.1 Temporal fluctuations in transcription factor levels drive expression noise in the embryo

When measured in fixed embryos, the TFs used in *Drosophila* embryonic development show remarkably precise expression patterns, displaying errors smaller than the width of a single nucleus [69, 70, 82, 83]. It therefore was unclear whether fluctuations in these regulators play a significant role in transcriptional noise in the developing embryo. By measuring the temporal dynamics of the individual *Kr* enhancers, each of which is controlled by different transcriptional activators, we show that TF fluctuations do significantly contribute to the noise in transcriptional output of a single enhancer. Within a nucleus, expression controlled by the two different *Kr* enhancers is far less correlated than expression driven by two copies of the same enhancer, indicating that TF inputs, as opposed to more global factors, are the primary regulators of transcriptional bursting in this system. Our current findings leave open the possibility that additional mechanisms, such as differences in 3D nuclear organization between different reporters, may also contribute to the differences in noise that we see.

We also showed that activity driven by the *Kr* shadow enhancer pair is less sensitive to levels of a single TF than is activity driven by an individual *Kr* enhancer. While prior work has shown that changes in TF levels precede changes in target transcription [84], the sensitivity of individual enhancers to changes in TF levels had not been previously quantified. The correlation between Bcd levels and activity of the distal enhancer is modest, and we expect that this reflects both the influence of additional TF inputs and nuclear heterogeneity that causes the local Bcd levels available to the enhancer to differ from total nuclear levels [85]. We suspect that the correlation between the activity of the distal enhancer and Bcd levels in the microenvironment surrounding the enhancer is higher than what we were able to measure here. New and emerging technologies will likely allow for live measurements of multiple TF inputs at higher spatial resolution, enabling further insights into the dynamics of expression regulation.

The finding that the *Kr* shadow enhancer pair is less sensitive to TF levels helps reconcile our finding that the individual *Kr* enhancers are influenced by fluctuations in input TFs with previous studies showing that endogenous *Kr* expression patterns are rather reproducible [82]. Previous work has cited the role of spatial and temporal averaging, which buffers noisy nascent transcriptional dynamics to generate more precise expression levels. Shadow enhancers operate upstream of this averaging, driving less noisy nascent transcription than either single enhancers or enhancer duplications.

2.7.2 A stochastic model underscores importance of transcription factor fluctuations

We developed a stochastic mathematical model of *Kr* enhancer dynamics and mRNA production that recapitulates our main experimental results. This model is based on that by Bothma et al., 2015 [24], but it is expanded to include the dynamics of a TF that regulates each enhancer. We placed a strong emphasis on the simplicity of this model, for example by using a single abstract TF for each enhancer. This choice both avoids a combinatorial explosion of parameters and makes the model results and parameters easier to interpret. One of the most notable features of the model is that it recreates the differences in noise between shadow and duplicated enhancer constructs without any additional fitting, indicating that these differences in the model system are a direct result of the separation of input TFs to the proximal and distal enhancers.

Future versions of this model can include refinements. For example, in the current model, we do not include the influence of repressive TFs or consider the multiple modes of action used by activating TFs. Future experiments and models can also be designed to identify the mechanism of enhancer non-additivity: changes in promoter-enhancer looping, saturation of the promoter, or other mechanisms.

2.7.3 Noise source decomposition suggests competition between reporters

In our investigation of sources of noise, we decomposed total noise into extrinsic and intrinsic components as in Elowitz et al., 2002 [79]. In that study, the authors showed that the activity of one reporter did not inhibit expression of the other reporter, and therefore their calculations assumed no negative covariance between the reporters' expression output. In our system, we found a small amount of negative covariance between the activity of two alleles in the same nucleus (Figure 2.17). For this reason, we called our measurements covariance and inter-allele noise. The negative covariance we observed indicates that activity at one allele can sometimes interfere with activity at the other allele, suggesting competition for limited amounts of a factor necessary for reporter visualization. The two possible limiting factors are MCP-GFP or an endogenous factor required for transcription. If MCP-GFP were limiting, we would expect to see the highest levels of negative covariance at the center of the embryo, where the highest number of transcripts are produced and bound by MCP-GFP. Since the fraction of nuclei with negative covariance is highest at the edges of the expression domain (Figure 2.17), the limiting resource is likely not MCP-GFP, but instead a spatially-patterned endogenous factor, like a TF.

Currently, the field largely assumes that adding reporters does not appreciably affect expression of other genes. However, sequestering TFs within repetitive regions of DNA can impact gene expression [86, 87], and a few case studies show that reporters can affect endogenous gene expression [88, 89]. If TF competition is responsible for the observed negative covariance between reporters, a closer examination of the effects of transgenic reporters on the endogenous system is warranted. In addition, TF competition may be a feature, not a bug, of developmental gene expression control, as modeling has indicated that molecular competition can decrease expression noise and correlate expression of multiple targets [90].

2.7.4 Additional functions of shadow enhancers and outlook

There are likely several features of shadow enhancers selected by evolution outside of their noise-suppression capabilities. Preger-Ben Noon, et al. showed that all shadow enhancers of shavenbaby, a developmental TF gene in *Drosophila*, drive expression patterns in tissues and times outside of their previously characterized domains in the larval cuticle [91]. This suggests that shadow enhancers, while seemingly redundant at one developmental stage, may play separate, non-redundant roles in other stages or tissues. Additionally, a recent study investigating shadow enhancer pairs associated with genes involved in *Drosophila* embryonic development found that CRISPR deletions of the individual enhancers result in different phenotypes, suggesting each plays a slightly different role in regulating gene expression [92]. In several other cases, both members of a shadow enhancer pair are required for the precise expression pattern generated by the endogenous locus [93, 94, 95, 53, 96]. These sharpened expression patterns achieved by a shadow enhancer pair may reflect enhancer dominance or other forms of enhancer-enhancer interaction and are likely another important function of shadow enhancers [93].

In the case of *Kr*, the endogenous expression pattern is best recapitulated by the shadow enhancer pair, with the individual enhancers driving slightly more anterior or posterior patterns of expression [93] (Figure 2.11). Additionally, the early embryonic *Kr* enhancers drive observable levels of expression in additional tissues and time points, but these expression patterns overlap those driven by additional, generally stronger, enhancers, suggesting that the primary role of the proximal and distal enhancers is in early embryonic patterning [97]. Therefore, while we cannot rule out the possibility that the proximal and distal enhancers perform separate functions at later stages, it seems that their primary function, and evolutionary substrate, is controlling *Kr* expression pattern and noise levels during early embryonic development.

Here, we have investigated the details of shadow enhancer function for a particular system, and we expect that some key observations may generalize to many sets of shadow enhancers. Shadow enhancers seem to be a general feature of developmental systems [18, 10], but the diversity among them has yet to be specifically addressed. While we worked with a pair of shadow enhancers with clearly separated TF activators, shadow enhancers can come in much larger groups and with varying degrees of TF input separation between the individual enhancers [18, 10]. To discern how expression dynamics and noise driven by shadow enhancers depend on their degree of TF input separation, we are investigating these characteristics in additional sets of shadow enhancers with varying degrees of differential TF regulation. Our current results combined with data gathered from additional shadow enhancers will inform fuller models of how developmental systems ensure precision and robustness.

All data generated or analysed during this study are included in the manuscript and supporting files. Code for analyzing the transcriptional traces and for creating the computational models is available on GitHub:
https://github.com/WunderlichLab/KrShadowEnhancerCode
(copy archived at https://github.com/elifesciences-publications/KrShadowEnhancerCode).

Appendix

The work in this appendix was done by Rachel Waymack and Zeba Wunderlich as published in Waymack et al. [1].

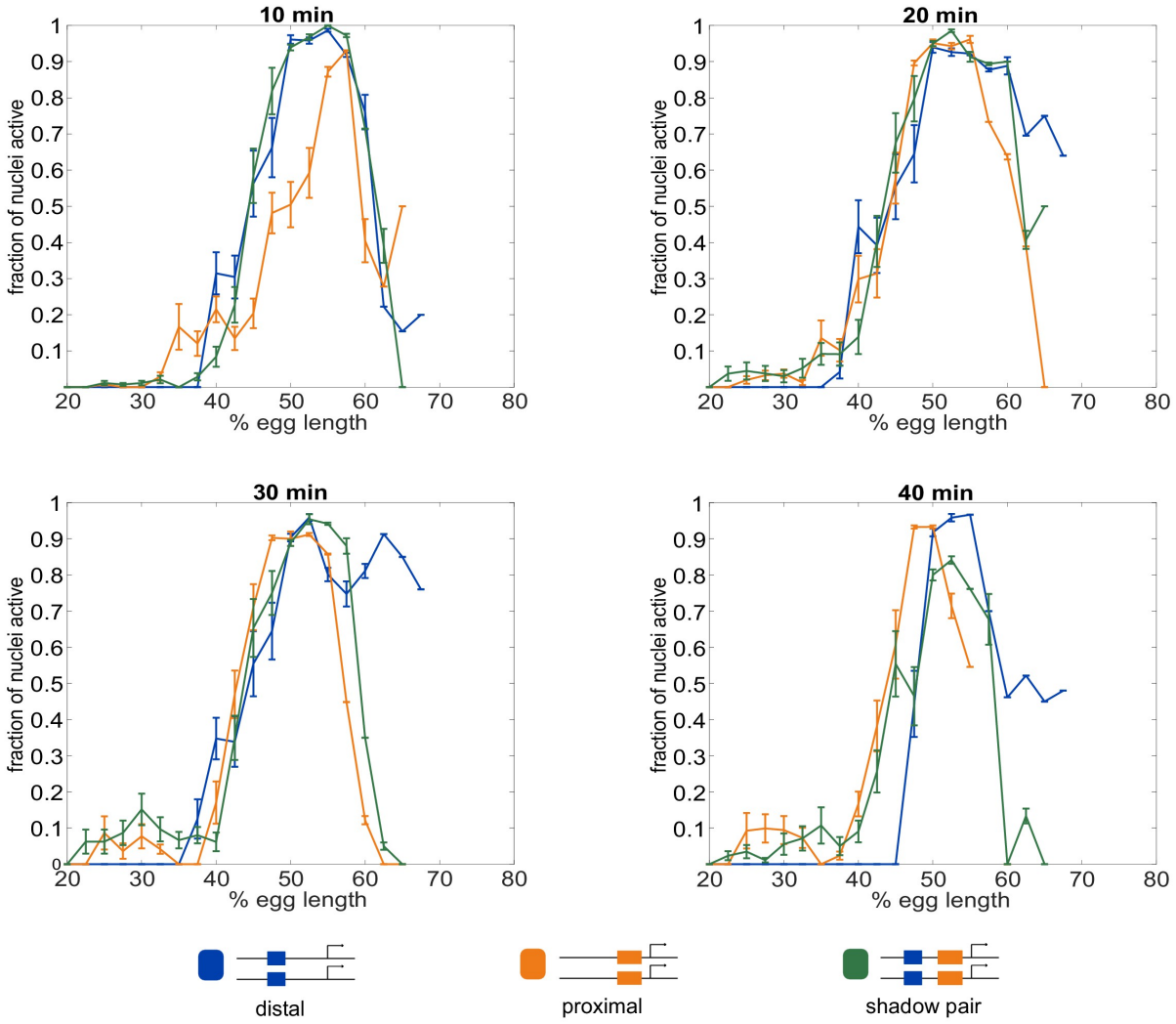

Figure 2.11: **Fraction of nuclei transcribing as a function of embryo position.** The different enhancer constructs display different spatial and temporal patterns of activity. Shown in all graphs are the fraction of nuclei actively transcribing as a function of embryo position at each indicated time point into nc14. (A) 10 min into nc14. (B) 20 min into nc14. (C) 30 min into nc14. (D) 40 min into nc14. Error bars are 95% confidence intervals. We note that differences in the individual *Kr* enhancers become more pronounced throughout progression of nc14. The more anterior pattern driven by the proximal enhancer in the second half of nc14 mimics the anterior shift previously observed for the *Kr* expression domain [98, 93]

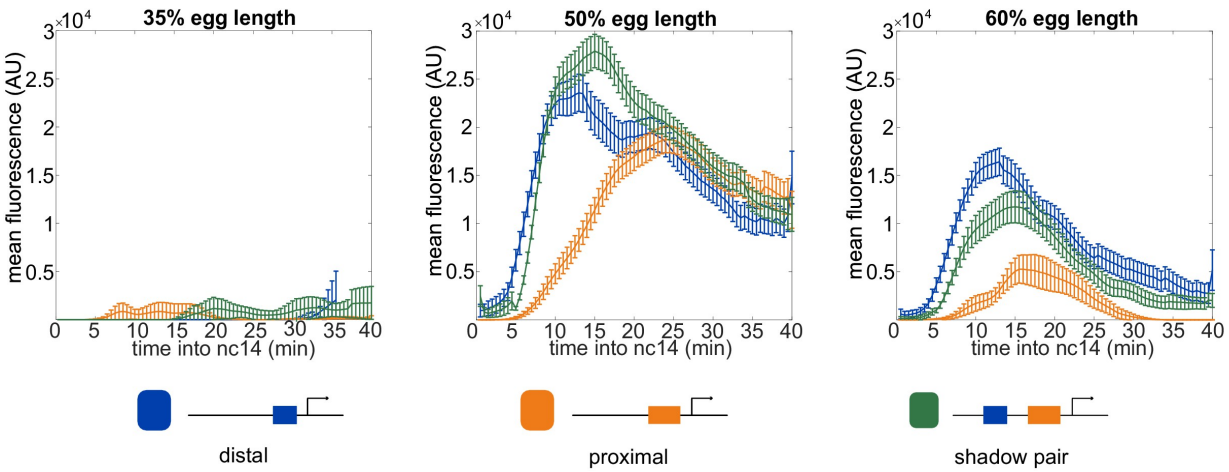

Figure 2.12: **Expression across time at different embryo positions.** The activity levels of the different enhancer constructs vary both across time and space. Shown in each graph is the mean fluorescence of all transcriptional traces of the indicated enhancer construct as a function of time into nc14 at the indicated position in the embryo. The earlier activation of the shadow pair and distal enhancer compared to the proximal enhancer at 50% and 60% egg length may stem from the input of the pioneer TF Zelda (Zld) to the distal and shadow pair. Error bars are 95% confidence intervals.

2.7.5 Generation of transgenic reporter fly lines

The single, duplicated, or shadow enhancers were each cloned into the pBphi vector, upstream of the *Kruppel* promoter, 24 MS2 repeats, and a yellow reporter gene as in Fukaya et al., 2016 [101]. We defined the proximal enhancer as chromosome 2R:25224832–25226417, the distal enhancer as chromosome 2R:25222618–25223777, and the promoter as chromosome 2R:25226611–25226951, using the *Drosophila* melanogaster dm6 release coordinates. The precise sequences for each reporter construct are given in Supplementary file 4. For the allele correlation experiments, each enhancer was cloned 192 bp upstream of the *Kr* promoter, separated by the endogenous sequence found between the proximal enhancer and the promoter. For transcriptional noise experiments, the distal enhancer was placed at its endogenous spacing, 2835 bp upstream of the promoter, and the proximal enhancer se-

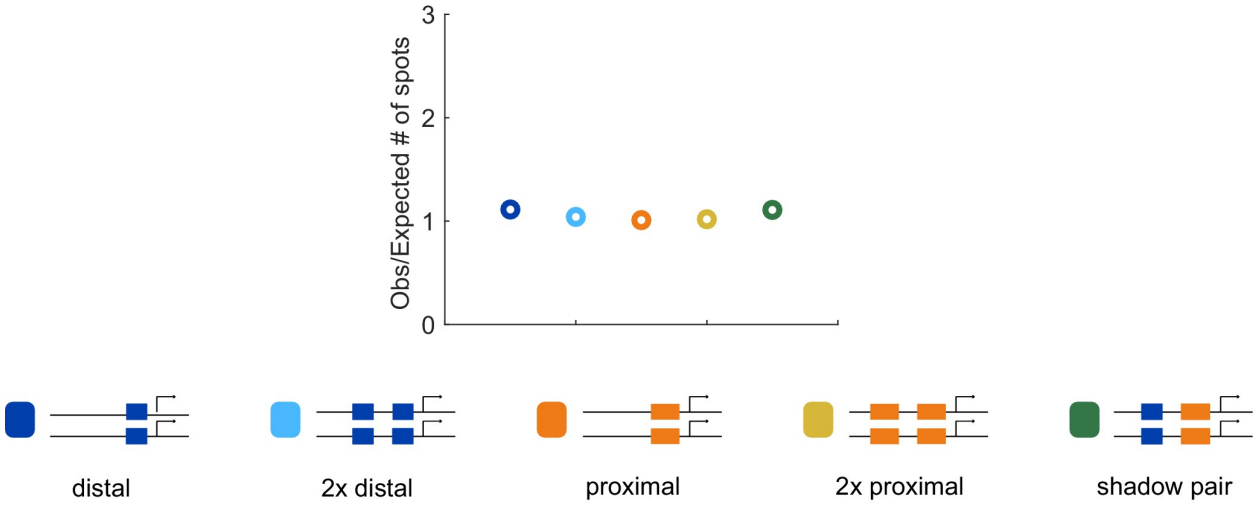

Figure 2.13: **Correspondence of observed and expected number of spots.** To ensure that we can accurately measure two spots of expression in the embryo, we compared the number of transcriptional spots seen in embryos hemizygous or homozygous for each construct. Our rationale was that in the absence of transvection, the number of transcriptional spots in homozygous embryos should be twice the number in embryos expressing the reporter on only one allele. The number of transcriptional spots tracked during nc14 in the AP bin of maximum expression was counted for all embryos imaged for each homozygous and hemizygous construct. The graph shows the average of this value for homozygous embryos, divided by double the value observed in the corresponding hemizygous construct. Assuming no transvection occurs, this value should be close to 1. The ratio of observed to expected number of spots is close to one for all our enhancer constructs, indicating we are reliably able to track the two individual spots of transcription in single nuclei.

Reagent type (species) or resource	Designation	Source or reference	Identifiers	Additional information
Genetic reagent (*Drosophila* melanogaster)	ChrII attP site; PBac{y[+]-attP-3B}VK00002	Bloomington *Drosophila* Stock Center	BDSC:9723 FLYB: FBti0076425	Fly line injected for transgenic reporters
Genetic reagent (D. melanogaster)	*Kr* proximal enhancer	This paper		Fly line with MS2 expression driven by *Kr* proximal enhancer inserted on chromosome II
Genetic reagent (D. melanogaster)	*Kr* distal enhancer	This paper		Fly line with MS2 expression driven by *Kr* distal enhancer inserted on chromosome II
Genetic reagent (D. melanogaster)	shadow enhancer pair	This paper		Fly line with MS2 expression driven by *Kr* shadow enhancer pair inserted on chromosome II
Genetic reagent (D. melanogaster)	duplicated distal enhancer	This paper		Fly line with MS2 expression driven by two copies of *Kr* distal enhancer inserted on chromosome II
Genetic reagent (D. melanogaster)	duplicated proximal enhancer	This paper		Fly line with MS2 expression driven by two copies of *Kr* proximal enhancer inserted on chromosome II
Genetic reagent (D. melanogaster)	endogenous distal enhancer	This paper		Fly line with MS2 expression driven by *Kr* distal enhancer at endogenous spacing from promoter, inserted on chromosome II
Genetic reagent (D. melanogaster)	Bcd-GFP; Bcd-eGFP	Gregor et al., 2007 [70], Cell		Fly line with mutated endogenous Bcd (bcdE1) rescued with GFP-tagged Bcd transgene on X chromosome
Genetic reagent (D. melanogaster)	MCP-GFP	Garcia et al., 2013 [72], Current Biology		Fly line expressing MCP-GFP on chromosome III and His-RFP on chromosome II
Genetic reagent (D. melanogaster)	MCP-mCherry	Hernan Garcia Lab		Fly line expressing MCP-mCherry as transgene on Chromosome II
Genetic reagent (D. melanogaster)	hunchback P2 enhancer	Garcia et al., 2013 [72], Current Biology		Fly line with MS2 expression driven by hb P2 enhancer on chromosome II
Software, algorithm	mRNADynamics	Garcia et al., 2013 [72], Current Biology		MATLAB pipeline for tracking and analysing MS2 transcriptional spots

Table 2.2: Key resources table

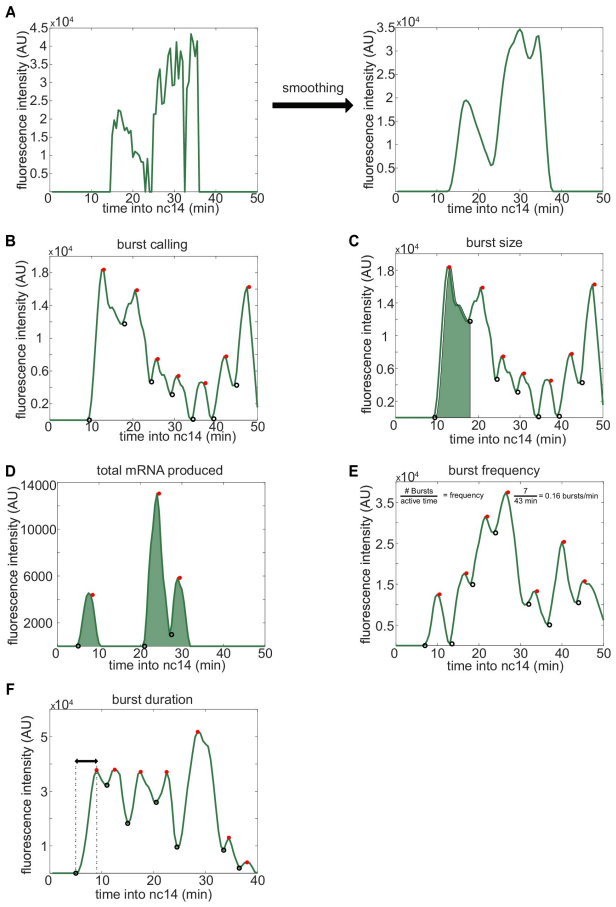

Figure 2.14: **Visual inspection of burst calling algorithm.** To extract the bursting parameters examined (burst size, frequency, and duration), individual fluorescence traces were first smoothed using the LOWESS method with a span of 0.1. Our burst calling algorithm then determined the periods of promoter activity or inactivity based on the slope of the fluorescence trace. (A) Representative example of smoothing of transcriptional traces. (B) Representative fluorescence trace of a single spot across the time of nc14. Black open circles indicate time points where the promoter is switched to being called 'on', red filled circles indicate time points where the promoter is switched to being called 'off'. (C) A representative transcriptional trace with shading representing the area under the curve used to calculate the size of the first burst. This area is calculated using the trapz function in MATLAB and is done for each burst, from the time point the promoter is called 'on' until the next time it is called 'on'. (D-F) show additional representative fluorescence traces of single transcriptional spots across the time of nc14. (D) A trace with shading representing the area under the entire curve during nc14 used to calculate the total amount of mRNA produced. This area is calculated using the trapz function in MATLAB and is done from the time the promoter is first called active until 50 min into nc14 or the movie ends, whichever comes first. (E) Burst frequency is calculated by dividing the number of bursts that occur from the time the promoter is first called active until 50 min into nc14 or the movie ends, whichever comes first. (F) Burst duration is defined as the amount of time between when the promoter is called active and it is next called inactive.

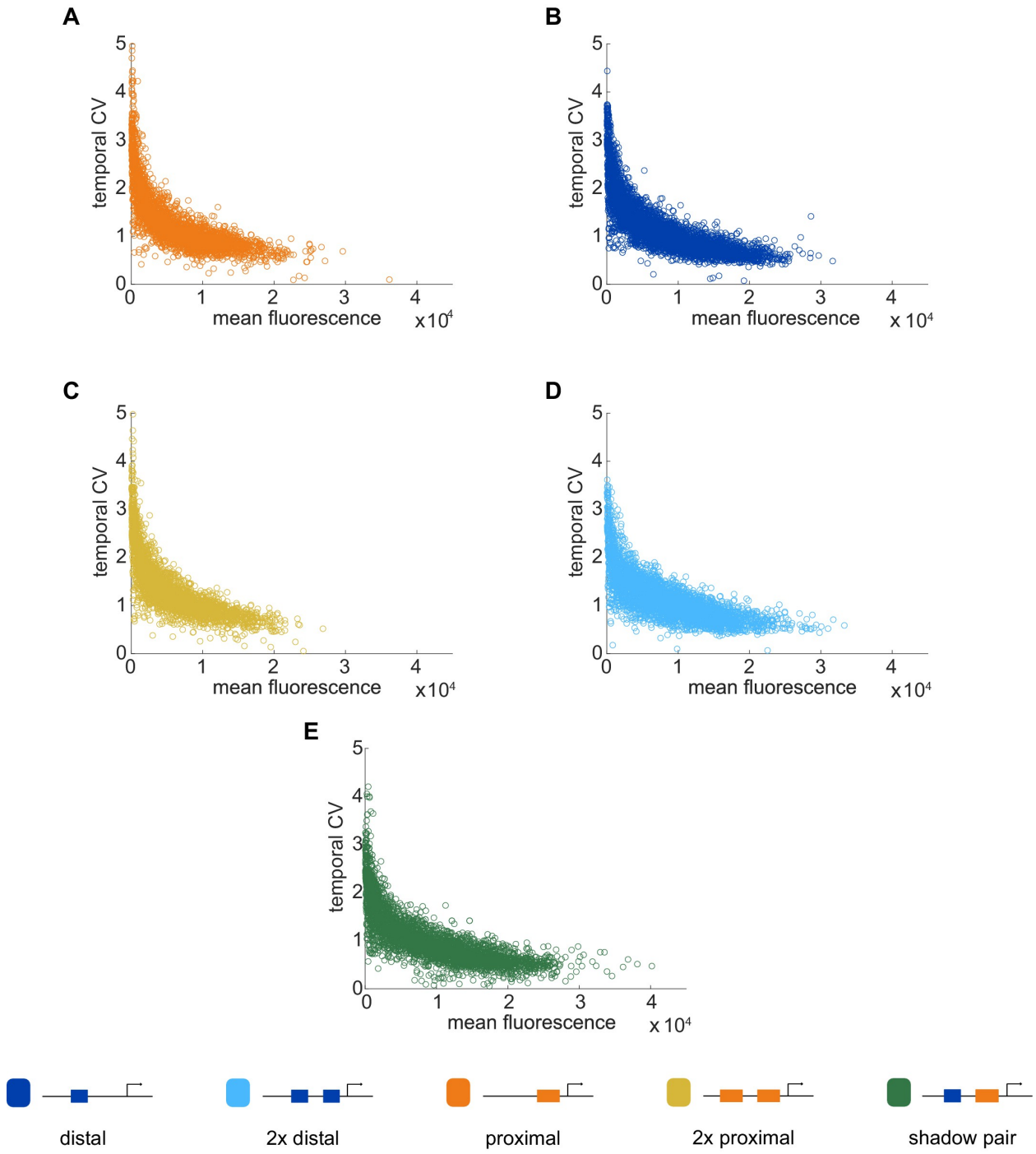

Figure 2.15: **Temporal CV as a function of mean fluorescence.**To investigate the relationship between our noise measurement of temporal CV and the mean activity of each construct, we plotted the temporal CV of each transcription spot as a function of its mean fluorescence. (A) Distal; (B) Proximal; (C) 2x Proximal; (D) 2x Distal; (E) Shadow pair. With all constructs, we find the general trend that CV decreases with increasing average expression, flattening out at a baseline noise level specific to each enhancer construct.

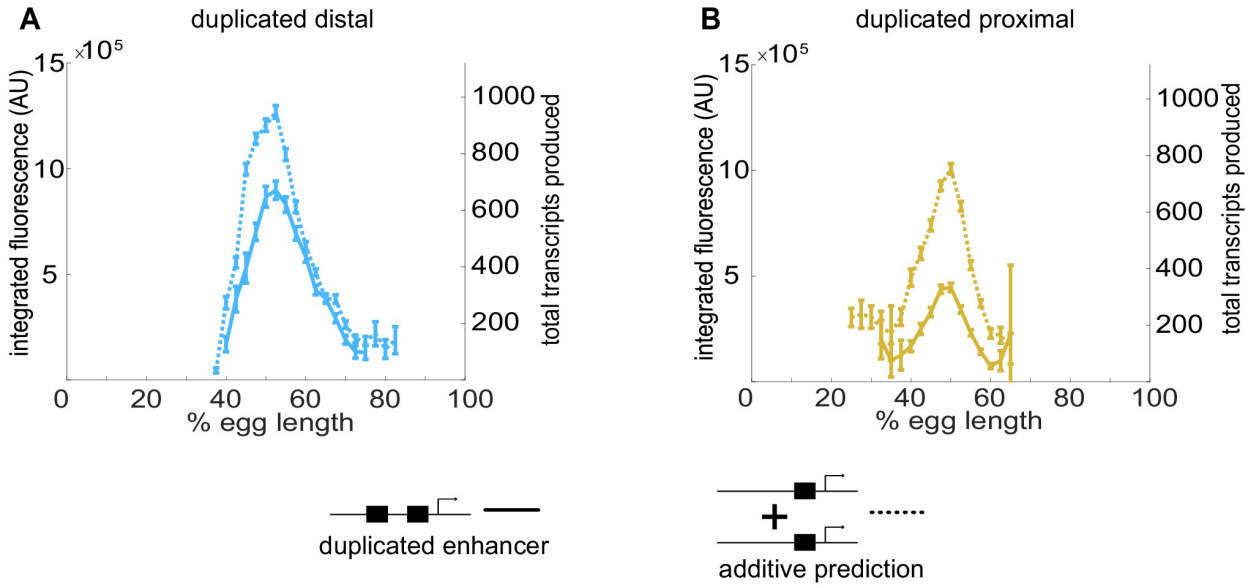

Figure 2.16: **Individual *Kr* enhancers display sub-additive behavior.**To assess the way input from two enhancers is integrated at the *Kr* promoter, we compared the experimentally observed mRNA production of duplicated enhancers to that predicted from additive behavior of the single enhancers. (A) The duplicated distal enhancer displays sub-additive behavior. The solid line is the experimentally observed total mRNA produced by the duplicated distal enhancer during nc14 as a function of egg length and the dotted line is that expected by doubling the total mRNA produced by the single distal enhancer. (B) The duplicated proximal enhancer also acts sub-additively. The solid line is the experimentally observed total mRNA produced by the proximal enhancer during nc14 as a function of egg length and the dotted line is that expected by doubling the total mRNA produced by the single proximal enhancer. These results, along with the observation that k_{off} values increased and k_{on} values decreased in our model with the addition of a second enhancer, suggests that the *Kr* enhancers compete with each other for interactions with the promoter. Error bars represent 95% confidence intervals.

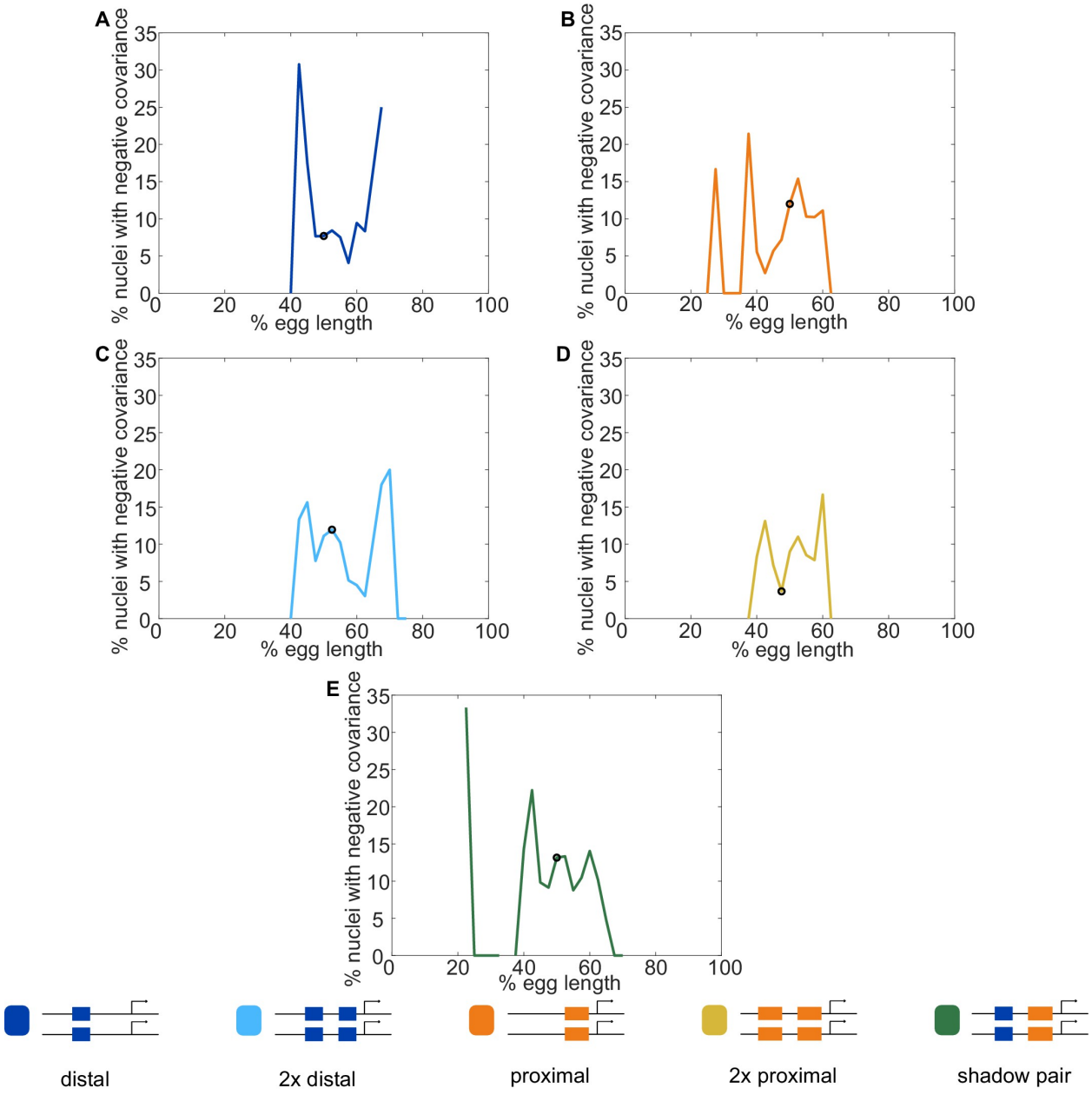

Figure 2.17: **Fraction of nuclei with negative covariance of allele activity.** To identify the likely cause of the observed negative covariance between allele activity in some nuclei, we calculated the fraction of nuclei displaying negative covariance out of all nuclei that had active reporter transcription. Graphs show the fraction of transcribing nuclei with negative covariance as a function of egg length for each reporter construct, with a black circle indicating the position along the embryo of maximal expression for that construct. (A) Distal; (B) Proximal; (C) 2x Proximal; (D) 2x Distal; (E) Shadow pair. Note that for all constructs, the highest rates of negative covariance are outside of the region of maximal reporter expression. MCP-GFP is expressed uniformly along the length of the embryo and we would therefore expect if MCP-GFP were the limiting factor, we would see the highest rates of negative covariance in the center of the expression pattern, where the highest number of transcripts are produced. Instead, the highest rates of negative covariance are seen at the edges of the *Kr* expression pattern, suggesting a spatially patterned factor, such as a TF, may be what is limiting.

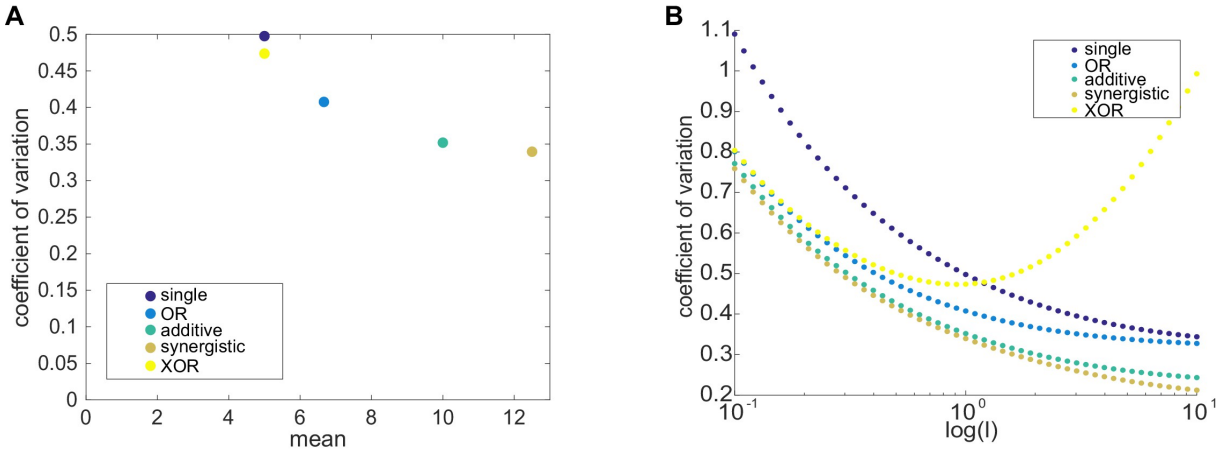

Figure 2.18: **In most cases, two enhancer models drive lower noise than the single enhancer model.** To theoretically explore the behavior of instrinsic noise in one- and two-enhancer models, we used the formalism of Sanchez et al., 2011; Sánchez and Kondev, 2008 [99, 100]. As described in Materials and methods, the predicted CVs from these models are estimates for intrinsic noise. (A) We plot the mean expression level versus CV for the five different enhancer models and one set of parameters, k = l = 1, p=1, $\gamma = 0.1$. The single enhancer model (dark purple) drives the highest CV, indicating that, under the assumptions of our models, adding an additional enhancer generally lowers intrinsic noise. Except for XOR model (yellow), all other models produce more mRNA than the single enhancer model. The other colors are: blue, OR model; green, additive model; brown, synergistic model. (B) Here, we plot the CV as a function of l, the rate of promoter-enhancer dissociation, for the five models above and vary l from 0.1 to 10 on a logarithmic scale with k = 1, p=1, $\gamma = 0.1$. With the exception of the XOR model with high l, the single enhancer model drives a higher CV than the models with two enhancers for the same value of l. These results show that, under the simplifying assumptions made in these models, the addition of a second enhancer generally lowers the predicted intrinsic noise. In our experimental data (Figure 6), we only observe a significant decrease in interallele noise for the shadow enhancer pair compared to the single distal or single proximal enhancer. Duplications of either the proximal or distal enhancer do not have significantly lower noise than their respective single enhancer constructs. Therefore, we expect that the simple addition of an identical enhancer likely does not fulfill the simplifying parameter assumptions used here and suggests that further investigation is needed to understand the complexity of the relationship between interallele noise and the numbers of enhancers controlling a promoter.

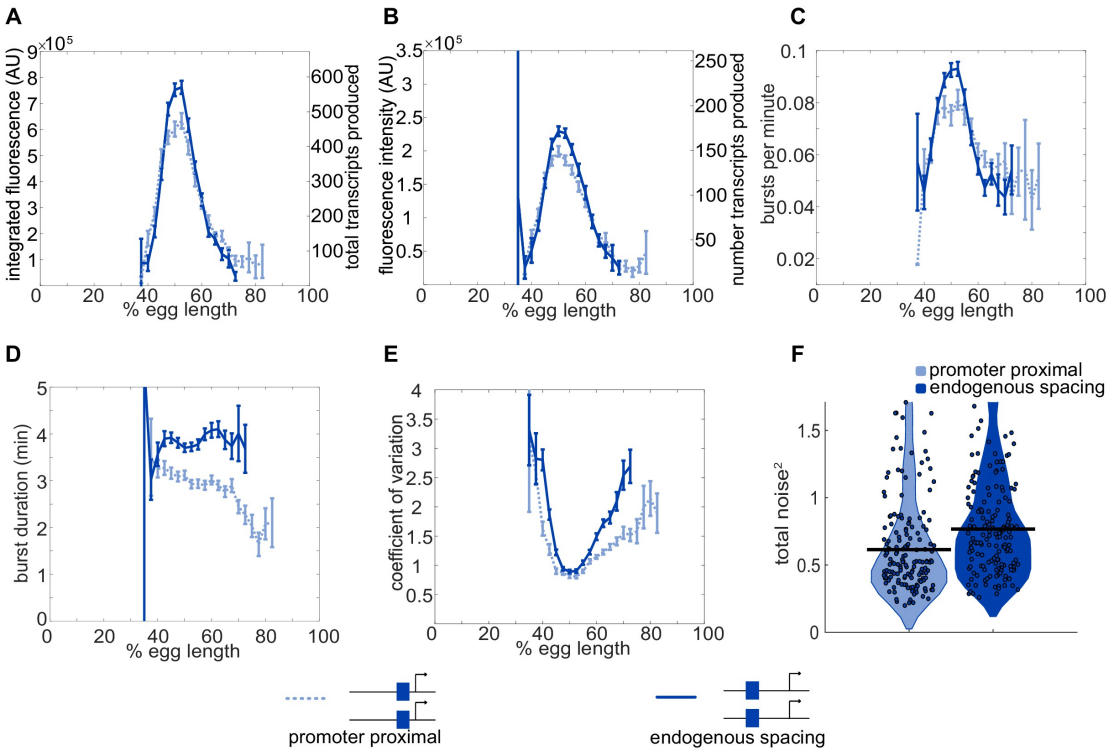

Figure 2.19: **Position-dependent effects on distal enhancer.** To best mimic the endogenous system, we looked at expression driven by the distal enhancer at its endogenous spacing from the promoter for our noise calculations. In this construct, we replaced the sequence of the proximal enhancer with sequence of the same length from the lambda phage genome predicted to have low number of Drosophila TF binding sites. This increased distance from the promoter had observable effects on the transcriptional dynamics and noise associated with the distal enhancer. (A) Comparison of total transcriptional expression mediated by the distal enhancer at its endogenous spacing or proximal to the promoter. The distal enhancer at its endogenous spacing, shown as the solid line, produces significantly more total mRNA in the center region of expression than the distal enhancer proximal to the promoter, shown as the dotted line. (B) Comparison of the average number of transcripts produced per transcriptional burst by each distal enhancer configuration as a function of egg length. (C) Average burst frequency associated with either distal enhancer configuration as a function of egg length. (D) Average burst duration associated with either distal enhancer configuration as a function of egg length. (E) Coefficient of variation of transcriptional activity across nc14 for each distal enhancer configuration as a function of egg length. (F) Total expression noise associated with either distal enhancer configuration at the AP bin of that construct's peak expression. The total noise distribution for the distal enhancer proximal to the promoter is on the left and that for the distal enhancer at its endogenous spacing from the promoter is on the right. The distal enhancer at its endogenous spacing displays significantly higher total noise ($p = 0.018$) than the distal enhancer proximal to the promoter. Each circle represents the total noise of an individual nucleus and the horizontal bar marks the median total noise value. Y-axis limited to the 75th percentile of the construct with the highest total noise values (distal promoter at endogenous spacing). Error bars in A-E represent 95% confidence intervals.

quence was replaced by a region of the lambda genome that is predicted to have few relevant TF-binding sites. In the shadow enhancer pair or duplicated enhancer constructs, the two enhancers were separated by the sequence separating the proximal and distal enhancers in the endogenous locus.

Using phiC31-mediated integration, each reporter construct was integrated into the same site on the second chromosomes by injection into yw; PBac{y[+]-attP-3B}VK00002 (BDRC stock #9723) embryos by BestGene Inc (Chino Hills, CA). To produce embryos with biallelic expression of the MS2 reporter, female flies expressing RFP-tagged histones and GFP-tagged MCP (yw; His-RFP/Cyo; MCP-GFP/TM3.Sb) were crossed with males containing one of the enhancer-MS2 reporter constructs. Virgin female F1 offspring were then mated with males of the same parental genotype, except in the case of shadow heterozygous flies, which were mated with males containing the other single enhancer-MS2 reporter.

2.7.6 Sample preparation and image acquisition

Live embryos were collected prior to nc14, dechorionated, mounted on a permeable membrane, immersed in Halocarbon 27 oil, and put under a glass coverslip as in Garcia et al., 2013 [72]. Individual embryos were then imaged on a Nikon A1R point scanning confocal microscope using a 60X/1.4 N.A. oil immersion objective and laser settings of 40uW for 488 nm and 35uW for 561 nm. To track transcription, 21 slice Z-stacks, at 0.5 um steps, were taken throughout the length of nc14 at roughly 30 s intervals. To identify the Z-stack's position in the embryo, the whole embryo was imaged after the end of nc14 at 20x using the same laser power settings. Later in the analysis, each transcriptional spot's location is described as falling into one of 42 anterior-posterior (AP) bins, with the first bin at the anterior of the embryo. Unless otherwise indicated, embryos were imaged at ambient temperature, which was on average 26.5°C. To image at other temperatures, embryos were either heated or

cooled using the Bioscience Tools (Highland, CA) heating-cooling stage and accompanying water-cooling unit.

2.7.7 Burst calling and calculation of transcription parameters

Tracking of nuclei and transcriptional spots was done using the image analysis Matlab pipeline described in Garcia et al., 2013. [72] For every spot of transcription imaged, background fluorescence at each time point is estimated as the offset of fitting the 2D maximum projection of the Z-stack image centered around the transcriptional spot to a gaussian curve, using Matlab lsqnonlin. This background estimate is subtracted from the raw spot fluorescence intensity. The resulting fluorescence traces across the time of nc14 are then subject to smoothing by the LOWESS method with a span of 10%. The smoothed traces were used to measure transcriptional parameters and noise. Traces consisting of fewer than three time frames were removed from calculations. To calculate transcription parameters, we used the smoothed traces to determine if the promoter was active or inactive at each time point. A promoter was called active if the slope of its trace (change in fluorescence) between one point and the next was greater than or equal to the instantaneous fluorescence value calculated for one mRNA molecule (FRNAP, described below). Once called active, the promoter is considered active until the slope of the fluorescence trace becomes less than or equal to the negative instantaneous fluorescence value of one mRNA molecule, at which point it is called inactive until another active point is reached. The instantaneous fluorescence of a single mRNA was chosen as the threshold because we reasoned that an increase in fluorescence greater than or equal to that of a single transcript is indicative of an actively producing promoter, while a decrease in fluorescence greater than that associated with a single transcript indicates transcripts are primarily dissociating from, not being produced from, this locus. Visual inspection of fluorescence traces agreed well with the burst calling produced by this method (Figure 2.14).

Using these traces and promoter states, we measured burst size, frequency and duration. Burst size is defined as the integrated area under the curve of each transcriptional burst, from one 'ON' frame to the next 'ON' frame, with the value of 0 set to the floor of the background-subtracted florescence trace (Figure 2 2.14 panel C). Duration is defined as the amount of time occurring between the frame a promoter is determined active and the frame it is next determined inactive (Figure 2.14 panel F). Frequency is defined as the number of bursts occurring in the period of time from the first time the promoter is called active until 50 min into nc14 or the movie ends, whichever is first (Figure 2.14 panel E). The time of first activity was used for frequency calculations because the different enhancer constructs showed different characteristic times to first transcriptional burst during nc14. For these, and all other measurements, we control for the embryo position of the transcription trace by first individually analyzing the trace and then using all the traces in each AP bin (anterior-posterior; the embryo is divided into 41 bins each containing 2.5% of the embryo's length) to calculate summary statistics of the transcriptional dynamics and noise values at that AP position.

All Matlab codes used for burst calling, noise measurements, and other image processing are available at the Wunderlich Lab GitHub (Waymack, 2020; copy archived at https://github.com/elifesciences publications/KrShadowEnhancerCode).

2.7.8 Simultaneous tracking of Bcd-GFP and enhancer activity

To compare the sensitivity of the activity of the shadow pair and distal enhancer to Bcd levels, we tracked the fluorescence of Bcd-GFP and MCP-mCherry in individual nuclei across the time of nc14. To obtain embryos for simultaneous tracking, we crossed female flies heterozygous for Bcd-GFP and MCP-mcherry with male flies homozygous for either the shadow pair or distal enhancer reporter. Bcd-GFP and MCP-mCherry are maternally deposited and

thereby allow us to measure levels of Bcd and enhancer activity in individual nuclei of the resulting embryos. Embryo collection and preparation was performed as described above. The same microscope, objective, and Z-step profile were used as described above, but laser settings were switched to 40uW for 561 nm and 35uW for 488 nm. Analysis of transcriptional activity was performed as described above. Time traces of Bcd-GFP levels in individual nuclei were subjected to background correction by subtracting the average fluorescence of the regions of the image not containing a nucleus at each time point from the raw Bcd-GFP fluorescence. The resulting Bcd-GFP time traces were then subjected to smoothing by the MATLAB smooth function, using the LOWESS method with a span of 10%. To measure the sensitivity of enhancer activity to Bcd levels, we correlated the slope of MS2 traces to the corresponding Bcd-GFP levels in the same nucleus. Slope was calculated between the MS2 values at consecutive time points and compared to the Bcd-GFP value at the earlier of the two time points. This process was done for all time points through 50 min into nc14.

Chapter 3

Shadow enhancers mediate trade-offs between transcriptional noise and fidelity

Material in this chapter is adapted from a manuscript by Alvaro Fletcher, Zeba Wunderlich, and German Enciso [102].

3.1 Introduction

Enhancers are non-coding regions of the DNA that are bound by transcription factors (TFs) and interact with the promoter to regulate transcription. Developmental genes are frequently expressed in multiple tissues or time points and are regulated by multiple enhancers. Until recently, these enhancers were perceived as modular, with each driving a distinct portion of a gene's spatiotemporal expression pattern, and together generating the entirety of a gene's expression pattern. However, work in *Drosophila* revealed the presence of "shadow

enhancers" – sets of two or more enhancers that control the same gene and drive identical or overlapping expression patterns [22]. Similar enhancer groups have been identified in *C. elegans*, mice, zebrafish, and humans [12, 13, 14, 15, 16, 17]. Here, we aim to use theory and computational models to shed light on the regulatory advantages of shadow enhancers, as well as under what conditions a single enhancer and a set of shadow enhancers are interchangeable.

On the surface, shadow enhancers appear redundant – they drive overlapping expression patterns and can often be knocked out without meaningfully affecting phenotype. However, in multiple loci in both flies and mice, shadow enhancers are essential for driving normal development under conditions of stress [103, 8, 104, 10]. For instance, under high temperatures but not ideal temperatures, deletion of a shadow enhancer for the *Drosophila* gene *snail* leads to abnormal development of the *Drosophila* embryo. The earliest work describing "shadow enhancers" designated the enhancer farther away from the promoter as the shadow enhancer and the promoter-proximal enhancer as the "primary enhancer." For the purposes of this work, we use the more recently formulated definition of shadow enhancers, which refers to the entire group of enhancers regulating the same target gene over space and time [21].

Progress in methods for identifying enhancers genome-wide has revealed the pervasiveness of shadow enhancers in developmental gene loci. A study revealed that a majority of genes involved in *Drosophila* muscle development are controlled by sets of three or more shadow enhancers, and large-scale data analysis on mouse tissue samples from genomic databases showed widespread shadow enhancer activity [18, 10, 19]. Meanwhile, in humans, assays involving enhancer-derived RNAs suggested that approximately 80% of examined genes are under the regulation of two or more shadow enhancers [20]. Overall, these results and others suggest that most developmental genes in multi-cellular organisms are regulated by sets of shadow enhancers.

In addition to ensuring proper development in stressful conditions, shadow enhancers interact

in multiple ways to fine-tune gene expression. For example, shadow enhancers might be assumed to behave additively – the sum of their individual mRNA outputs equals that of their combined output. However some shadow enhancers display subadditive or superadditive interactions, in which the combined activity of both enhancers is either less or more than the sum of their individual contributions, e.g. [24, 23]. Shadow enhancers can also repress one another, creating a composite gene expression pattern that is weaker or more restricted that either enhancer produces alone [93, 92]. Lastly, by binding distinct sets of input TFs, shadow enhancers can collectively buffer temporal noise in TF levels, yielding more consistent gene expression as a function of time [1].

Many of the mechanisms, e.g. synergy and repression, that are observed in shadow enhancers may also be achieved in single enhancers. This observation leads to the core question of this chapter: which properties are specific to shadow enhancers and not possible in single enhancer regulation? To do so, we focus on two important functions of enhancers. The first is their ability to faithfully translate an upstream signal, like a difference in TF concentration, into downstream expression output. This feature is needed to allow output expression patterns to determine developmental cell fate in response to upstream signals. The second is their ability to buffer stochastic noise either from random fluctuations in the upstream signals or from internal enhancer dynamics. This feature is needed to buffer the noise that inevitably arises from molecular interactions to drive consistent expression patterns. For this purpose, we construct theoretical models of enhancer systems with different properties and analyze the resulting dynamics. In addition to exploring a larger number of configurations and parameter sets than is experimentally practical, we expect this approach to elucidate the selection pressures that can shape the creation of shadow enhancers and opportunities for transcriptional modulation that appear in the presence of shadow enhancers.

Previous work on theoretical models of shadow enhancers has proven to be fruitful in predicting and understanding the behavior of these systems. For example, a simple model

of *hunchback* and *knirps* enhancers by Bothma et al. [24] was used to show that frequent interactions among enhancers may lead to competition for promoter access and thus give rise to subadditive behavior. Likewise, a model of *hunchback* regulation of the even-skipped enhancers by Staller et al. [105] suggested that two different enhancers can recreate the same expression patterns with distinct regulatory logic. Grah et al. [106] studied a model related to the Monod-Wyman-Changeux hemoglobin system [107] in the context of enhancer regulation and considered several performance metrics. The work by Nousiainen et al. presented a computational framework for identifying model families that can predict enhancer activation dynamics in a mechanistic fashion [108]. In this work, we focused our approach on a set of minimalist reaction network models in which each of the reactions is stochastic, and the parameters were derived from previous transcriptional data of *Kruppel* enhancers [1]. Hence, we expect that this fully stochastic approach may capture nuances in the relationship between TF fluctuations and transcription.

In section 3.2.1, we describe a reaction network model of the *Kruppel* gene enhancer system. This is a minimal model that was developed and validated in Waymack et al. [1] that recapitulates the dynamics of enhancer-mediated transcription. We then describe how to use this model to approximate mean transcriptional output and derive the corresponding noise and fidelity. Section 3.2.2 describes our approach to generate similar models that differ in their numbers of enhancers and TF binding sites. By simulating these models, we can compare the effects of distinct shadow enhancer systems on transcriptional noise and fidelity. Since shadow enhancers can behave sub- or superadditively, we incorporate this behavior into our models in Section 3.2.3 and once again perform simulations to determine how the noise and fidelity are affected. Lastly, in Section 3.2.4, we use our modeling framework to compare the changes in noise and fidelity resulting from an enhancer duplication and an enhancer splitting. We consider these events to be potential mechanisms for the origin of shadow enhancers and study them in this context.

3.2 Results

3.2.1 The *Kruppel* enhancer model

As a case study for our work, we use *Kruppel*, a gene required for early embryonic patterning in *Drosophila*. Around two hours post-fertilization, *Kruppel* is expressed in a stripe around the middle of the embryo, and this expression pattern is generated by a pair of shadow enhancers (Figure 3.1A). A minimal version of the *Kruppel* enhancer system was described in Waymack et al. [1] using the model in Figure 3.1B. Here, A corresponds to the proximal enhancer closest to the promoter, while B corresponds to the other, distal enhancer. The subscripts for A and B alternate between 0 and 1 to denote whether there is a TF bound to them at a given time. In this model, it is assumed that each enhancer interacts with the promoter immediately after a TF binds to it. Waymack, et al. measured the dynamic expression output of *Kruppel's* shadow enhancers individually and together. Using these data, we estimated the model parameters either directly or by using simulated annealing, which systematically simulates the model over several parameter sets until the difference between the model output and experimental data falls within an acceptable tolerance (Table 3.1.) To recapitulate our previously-published experimental data, we stochastically simulated our model to yield the number of mRNA transcripts over time. Using the parameters in Table 3.1, simulated mRNA bursts resemble those observed during live transcription in *Drosophila* embryos (Figure 3.1C) and properties such as the size and duration of bursts were consistent with those from *Kruppel* experimental data [1]. Based on this work, the model shown in Figure 3.1B is used as a description of shadow enhancer dynamics.

One disadvantage of using stochastic simulations to estimate mean mRNA transcription is the significant computational cost. To do this more efficiently, we use moment closure methods that create ordinary differential equations (ODEs) describing the first and second moments of the chemical species [25, 6]. The solution to the ODE for the first moment

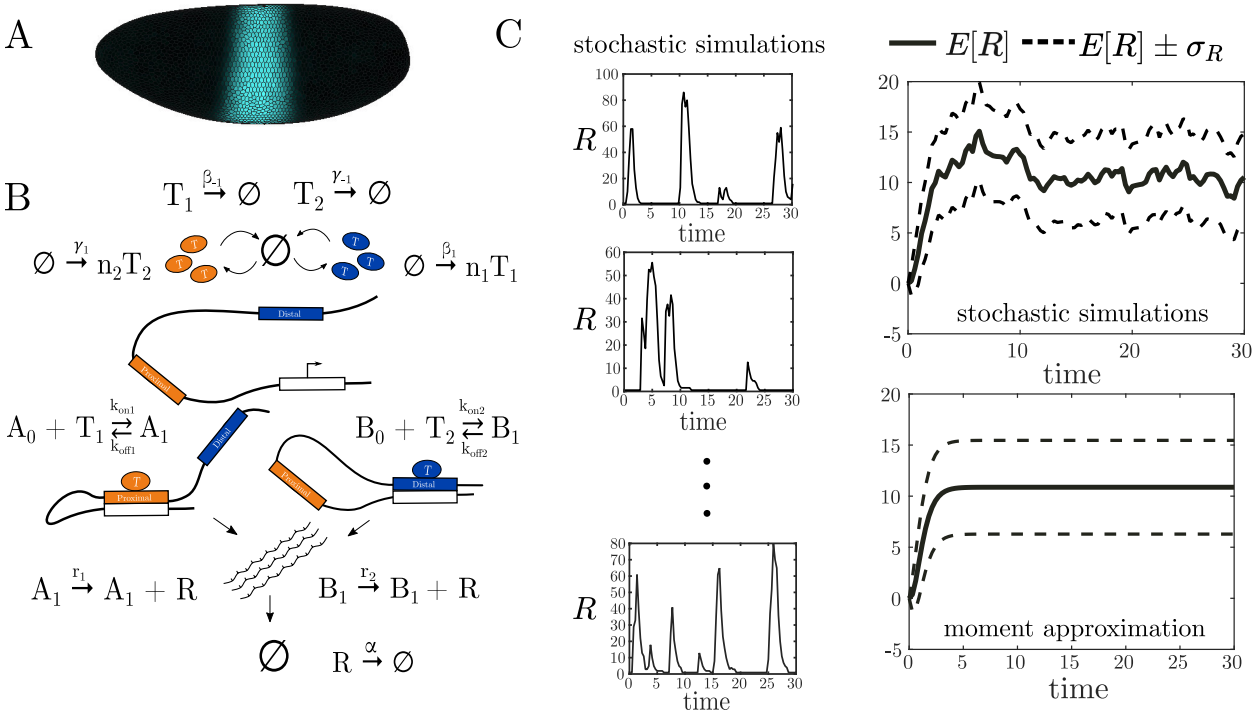

Figure 3.1: Simulation of enhancer models and calculation of transcriptional noise and fidelity. (A) *Drosophila* embryo where the region of *Kruppel* expression has been highlighted [1]. (B) Cartoon depicting a reaction network model of *Kruppel* shadow enhancers [1]. (C) Sample stochastic traces of mRNA from simulations of the model in (B) and their average over time $E[R]$ which estimates the mean mRNA concentration. The values of $E[R]$ and the standard deviation σ_R can also be approximated by moment closure techniques and be used to estimate the transcriptional noise and fidelity of the modeled enhancer system.

Table 3.1: Parameter values that were fitted to *Kruppel* expression data.

Parameter Values	
β_1	0.33
β_{-1}	2.7
γ_1	0.29
γ_{-1}	3.9
k_{off_1}	1.8
k_{on_1}	0.36
k_{off_2}	1.5
k_{on_2}	0.19
α	1.96
r_1	120
r_2	140
n_1	4
n_2	12

approximates the limit to infinity of the mean mRNA denoted by $E[R]$. For example, the top right of Figure 3.1C shows $E[R]$ and the standard deviation σ_R derived from a finite number of stochastic traces while the plot below shows the moment closure approximation of $E[R]$ and σ_R.

Using the approximations from the moment closure technique, we can now efficiently estimate the transcriptional fidelity and noise of our modeled enhancer system. To capture the transcriptional fidelity, we used the mutual information between mean TF values and the corresponding levels of gene expression. The mutual information $I(R, T_1)$ quantifies the dependence of mRNA transcription on T_1 concentrations, regardless of whether this dependence is linear or not [109]. To study the transcriptional noise, we used the coefficient of variation (CV) by normalizing the standard deviation of mRNA expression by its mean. The CV can be obtained as functions of the moments while the transcriptional fidelity is derived from the probability distributions of a TF and the mRNA. In particular, we have that

$$CV = \frac{\sigma_R}{E[R]},$$

while

$$I(R, T_1) = \sum_R \sum_{T_1} P(R, T_1) \log \frac{P(R, T_1)}{P(R)P(T_1)}.$$

When calculating the CV, R is taken to be the mean mRNA produced under a fixed rate of TF production β_1 or γ_1. Meanwhile, R in $I(R, T_1)$ corresponds to the mean mRNA produced at different levels of TF production β_1.

3.2.2 Models with varying number of enhancers and total binding sites

Using the *Kruppel* model as a starting point, we first wanted to explore if transcriptional fidelity and noise are dependent on TF binding sites being arranged into two distinct enhancers. Our previous experimental and computational work found that having two enhancers with distinct TF binding sites – T_1 in the proximal enhancer and T_2 in the distal enhancer – drove lower expression noise than two enhancers with identical TF binding sites. From this work, however, it was not clear whether the TF binding sites had to be split among two enhancers, or whether a single enhancer with sites for both T_1 and T_2 could achieve the same noise reduction. It also was not clear if there might be a trade-off between noise and fidelity.

To explore these questions, we constructed 48 models with up to four enhancers and four total binding sites, as shown in Figure 3.3A. Each enhancer has a given number of binding sites for T_1 and T_2 and every diagram in this figure corresponds to a set of chemical reactions. For an example of the specific networks associated with two of these diagrams, see Figure 3.2. We then input each network into the CERENA software (ChEmical REaction Network Analyzer) [6], which allows us to calculate the ODE equations for the mean and other

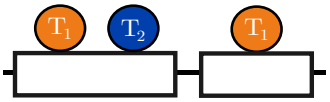

$$A_{00} + T_1 \underset{k_{off1}}{\overset{k_{on1}}{\rightleftarrows}} A_{10} \xrightarrow{r_1} A_{10} + R \qquad B_0 + T_1 \underset{k_{off1}}{\overset{k_{on1}}{\rightleftarrows}} B_1 \xrightarrow{r_1} B_1 + R$$

$$A_{10} + T_2 \underset{k_{off2}}{\overset{k_{on2}}{\rightleftarrows}} A_{11} \xrightarrow{r_1+r_2} A_{11} + R \qquad T_1 \xrightarrow{\beta_{-1}} \emptyset \qquad T_2 \xrightarrow{\gamma_{-1}} \emptyset$$

$$A_{00} + T_2 \underset{k_{off2}}{\overset{k_{on2}}{\rightleftarrows}} A_{01} \xrightarrow{r_2} A_{01} + R \qquad \emptyset \xrightarrow{\beta_1} n_1 T_1 \qquad \emptyset \xrightarrow{\gamma_1} n_2 T_2$$

$$A_{01} + T_1 \underset{k_{off1}}{\overset{k_{on1}}{\rightleftarrows}} A_{11} \xrightarrow{r_1+r_2} A_{11} + R \qquad R \xrightarrow{\alpha} \emptyset$$

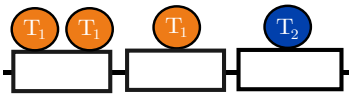

$$A_{00} + T_1 \underset{k_{off1}}{\overset{k_{on1}}{\rightleftarrows}} A_{10} \xrightarrow{r_1} A_{10} + R \qquad B_0 + T_1 \underset{k_{off1}}{\overset{k_{on1}}{\rightleftarrows}} B_1 \xrightarrow{r_1} B_1 + R$$

$$A_{10} + T_1 \underset{k_{off1}}{\overset{k_{on1}}{\rightleftarrows}} A_{11} \xrightarrow{2r_1} A_{11} + R \qquad C_0 + T_2 \underset{k_{off2}}{\overset{k_{on2}}{\rightleftarrows}} C_1 \xrightarrow{r_2} C_1 + R$$

$$A_{00} + T_1 \underset{k_{off1}}{\overset{k_{on1}}{\rightleftarrows}} A_{01} \xrightarrow{r_1} A_{01} + R \qquad T_1 \xrightarrow{\beta_{-1}} \emptyset \qquad T_2 \xrightarrow{\gamma_{-1}} \emptyset$$

$$A_{01} + T_1 \underset{k_{off1}}{\overset{k_{on1}}{\rightleftarrows}} A_{11} \xrightarrow{2r_1} A_{11} + R \qquad \emptyset \xrightarrow{\beta_1} n_1 T_1 \qquad \emptyset \xrightarrow{\gamma_1} n_2 T_2$$

$$R \xrightarrow{\alpha} \emptyset$$

Figure 3.2: Two different models and their corresponding reaction networks.

moments of all chemical species in the network. CERENA uses an array of approximation methods that allow for a more streamlined implementation of these ODE equations, in particular several methods of moment closure. The use of this software is significantly faster as compared with many repeated runs of the Gillespie algorithm [46]. We calculated ODEs up to the second moments in order to calculate the variance, and we used the method of zero cumulants for moment closure [110]. The results were found to be generally consistent with simulations of individual models carried out with the more standard Gillespie algorithm (Figure 3.1C, right).

To create the reaction equations for all our configurations of interest, we needed to decide how to assign the model parameters in a way that made the comparisons meaningful. Most of the parameters, including the k_{on} and k_{off} rates, were assigned the same values that were found to be consistent with experimental data in Waymack et al. [1] and used in Figure 3.1C. The rates of transcription for each enhancer state are initially defined using the following additive scheme. Any enhancer with n bound T_1 and m bound T_2 will produce mRNA at a rate $nr_1 + mr_2$ where r_1 and r_2 are the rates of transcription of the *Kruppel* model in

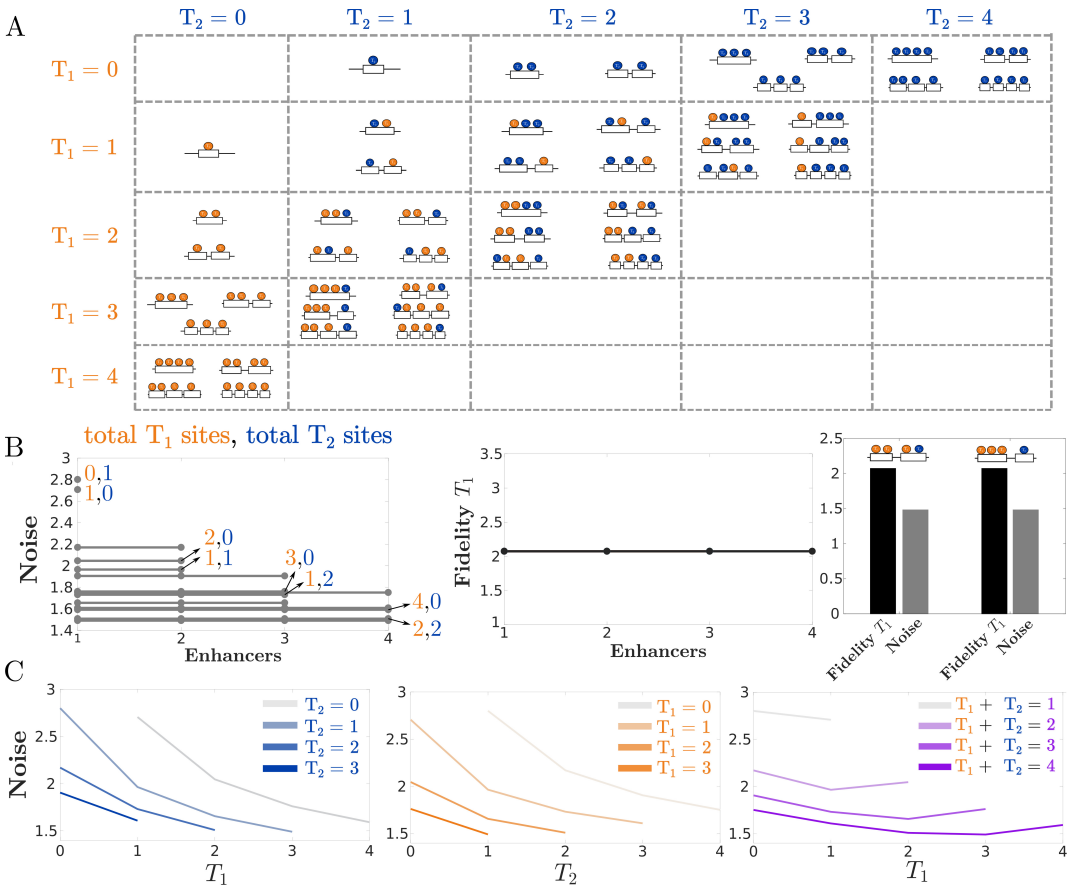

Figure 3.3: Under additive assumptions, transcriptional fidelity is independent of binding site and enhancer numbers, while noise is only dependent on binding site numbers. (A) Different enhancer models used in the simulations. Each model has different total binding sites for T_1, total binding sites for T_2, distribution of binding sites, and number of enhancers. (B) Simulations for the models in (A) show that fidelity and noise are independent of the number of enhancers and the distribution of binding sites. Fidelity is also independent of total binding site numbers, while the noise remains dependent on the total binding sites for each TF. The bar graph on the right shows the fidelity and noise values for two different configurations of TF binding sites among two enhancers. (C) Noise calculated as functions of the total binding sites for T_1 or T_2. As the total number of binding sites increases, the noise generally decreases.

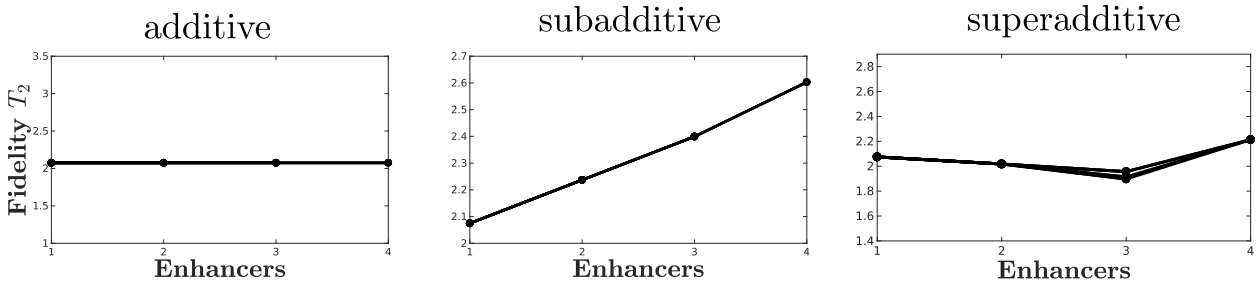

Figure 3.4: Transcriptional fidelities with respect to T_2 for enhancers that behave additively, subadditively, and superadditively. The fidelity trends with respect to T_2 for all models in Figure 3.3A do not differ significantly from those corresponding to the fidelities with respect to T_1.

Figure 3.1B. Similarly, if two or more shadow enhancers are bound to the promoter, the overall mRNA transcription rate is the sum of the transcription rates for each enhancer. This way, we have an additive scenario where a single enhancer system with four fully bound sites of T_1 will produce mRNA at the same rate as four independent enhancers that are each bound by a single T_1.

We calculated the transcriptional noise and fidelity for all the models in Figure 3.3A to discern the effect of different configurations of binding sites and enhancers. The results are shown in Figure 3.3B, left (Figure 3.4 shows the results for fidelity with respect to T_2). The noise does not appear to change when altering the number of enhancers, as long as the number of binding sites for T_1 and T_2 remain constant. Moreover, even after fixing the number of enhancers, the actual distribution of TF binding sites among the enhancers appears to have no effect on transcriptional noise (Figure 3.3B, right). The fidelity, on the other hand, remains constant for all models regardless of enhancers and TF binding site numbers or distributions. One can conclude that, in this additive regime, there may be negligible selection pressures on the number of enhancers regulating a gene and the distribution of TF binding sites among these enhancers.

Though noise does not depend on enhancer number, it does vary with binding site number. The plots in Figure 3.3C show that enhancers with more binding sites generally lead to lower

transcriptional noise. This may be because as the number of binding sites increases, there are more inputs in the system, which can serve to average each other out. Each binding site can be thought of as akin to a coin toss. When n independent coin tosses are made, the expected number of heads grows linearly but its standard deviation grows sublinearly, leading to an overall decrease in the noise.

Not only does transcriptional noise depend on binding site number, but it is also dependent on binding site identity. Shifting the total number of binding sites $T_1 + T_2$ shows non-monotonic changes in noise (rightmost plot in Figure 3.3C). The leftmost data points at $T_1 = 0$ correspond to enhancers that are bound exclusively by T_2 while the rightmost points at $T_1 = 4$ correspond to enhancers that are bound exclusively by T_1. As T_1 sites increase, the ratio between T_1 and T_2 binding sites becomes more even and the noise decreases. However, once enhancers adopt too many T_1 sites at the expense of T_2 sites, noise begins to increase. This agrees with previous observations that having a single kind of TF binding site leads to higher noise in transcription than systems bound by multiple kinds of TF binding sites [1]. In summary, these models demonstrate that when enhancer output combines in an additive fashion, the fidelity does not depend on the number of enhancers. Noise is sensitive to the number and identity of binding sites, but not to their arrangement among one or more enhancers. Thus, the prevalence of shadow enhancers under additive assumptions might be the result of genome dynamics and genetic drift, as opposed to selection.

3.2.2.1 Proof of equivalence between multiple additive enhancers and a single enhancer

Here, we present a formal proof showing that two kinds of enhancers with an arbitrary number of copies yield the same transcriptional output as a single enhancer with an equivalent number of binding sites. In particular, these enhancers are set to behave additively and operate under stochastic dynamics. Unlike the systems simulated in Figure 3.3, the systems

shown here do not take into account transcription factor fluctuations but we expect this proof to be an initial step for reaching similar conclusions of the systems in Figure 3.3.

Consider a system with n copies of E and m copies of W each having reactions of the form

$$E_0^{(i)} \underset{1}{\overset{1}{\rightleftharpoons}} E_1^{(i)} \xrightarrow{1} R + E_1^{(i)}$$

$$W_0^{(j)} \underset{1}{\overset{1}{\rightleftharpoons}} W_1^{(j)} \xrightarrow{1} R + W_1^{(j)}$$

$$R \xrightarrow{1} \emptyset$$

for $i = 0, 1, \ldots, n$ and $j = 0, 1, \ldots, m$. We wish to show that the above system is equivalent to

$$Z_0 \underset{1}{\overset{1}{\rightleftharpoons}} Z_1 \xrightarrow{1} R + Z_1$$

$$R \xrightarrow{1} \emptyset$$

such that $Z_0 = \sum_{i=1}^{n} E_0^{(i)} + \sum_{j=1}^{m} W_0^{(j)}$ and $Z_1 = \sum_{i=1}^{n} E_1^{(i)} + \sum_{j=1}^{m} W_1^{(j)}$. Then,

$$\begin{aligned}
Z_0' &= \sum_{i=1}^{n} \left(-E_0^{(i)} + E_1^{(i)} \right) + \sum_{j=1}^{m} \left(-W_0^{(j)} + W_1^{(j)} \right) = Z_1 - Z_0, \\
Z_1' &= \sum_{i=1}^{n} \left(E_0^{(i)} - E_1^{(i)} \right) + \sum_{j=1}^{m} \left(W_0^{(j)} - W_1^{(j)} \right) = Z_0 - Z_1, \\
R' &= -R + \sum_{i=1}^{n} E_1^{(i)} + \sum_{j=1}^{m} W_1^{(j)} = -R + Z_1.
\end{aligned}$$

Hence, the two systems are deterministically equivalent. Now we show that they are stochastically equivalent as well. The master equation for the system with n copies of E and m

copies of W is

$$\begin{aligned}
x'_{i,n-i,j,m-j,k} &= (i+1)x_{i+1,n-(i+1),j,m-j,k} + (n-(i-1))x_{i-1,n-(i-1),j,m-j,k} \\
&\quad + (j+1)x_{i,n-i,j+1,m-(j+1),k} + (m-(j-1))x_{i,n-i,j-1,m-(j-1),k} \\
&\quad + (n-i+m-j)x_{i,n-i,j,m-j,k-1} + (k+1)x_{i,n-i,j,m-j,k+1} - ix_{i,n-i,j,m-j,k} \\
&\quad - (n-i)x_{i,n-i,j,m-j,k} - jx_{i,n-i,j,m-j,k} - (m-j)x_{i,n-i,j,m-j,k} \\
&\quad - (n-i+m-j)x_{i,n-i,j,m-j,k} - kx_{i,n-i,j,m-j,k},
\end{aligned}$$

while the master equation for the system with a η copies of Z for $\eta = n+m$ sites is

$$\begin{aligned}
z'_{l,\eta-l,k} &= (l+1)z_{l+1,\eta-(l+1),k} + (\eta-(l-1))z_{l-1,\eta-(l-1),k} \\
&\quad + (\eta-l)z_{l,\eta-l,k-1} + (k+1)z_{l,\eta-l,k+1} - 2(\eta-l)z_{l,\eta-l,k} \\
&\quad - lz_{l,\eta-l,k} - kz_{l,\eta-l,k}.
\end{aligned}$$

Define

$$\begin{aligned}
y_{l,\eta-l,k} &= P(Z_0 = l, Z_1 = \eta - l, R = k), \\
&= \sum_{\substack{i,j\geq 0 \\ i+j=l}} P(Z_0 = l, Z_1 = \eta - l, R = k) \\
&= \sum_{\substack{i,j\geq 0 \\ i+j=l}} x_{i,n-i,j,m-j,k}.
\end{aligned}$$

Then, the chemical master equation of this system is

$$y'_{l,\eta-l,k} = \sum_{\substack{i,j\geq 0 \\ i+j=l}} x'_{i,n-i,j,m-j,k}.$$

Now, to show stochastic equivalence, it suffices to show that $y'_{l,\eta-l,k} = z'_{l,\eta-l,k}$. For a particular

l, we can write

$$
\begin{aligned}
y'_{l,\eta-l,k} &= \sum_{\phi=0}^{l} x'_{\phi,n-\phi,l-\phi,m-(l-\phi),k} \\
&= \sum_{\phi=0}^{l} x'_{\phi,n-\phi,l-\phi,m-l+\phi,k} \\
&= \sum_{\phi=0}^{l} ((\phi+1)x_{\phi+1,n-(\phi+1),l-\phi,m-l+\phi,k} + (n-(\phi-1))x_{\phi-1,n-(\phi-1),l-\phi,m-l+\phi,k} \\
&\quad + (l-\phi+1)x_{\phi,n-\phi,l-\phi+1,m-(l-\phi+1),k} + (m-(l-\phi-1))x_{\phi,n-\phi,l-\phi-1,m-(l-\phi-1),k} \\
&\quad + (n-\phi+m-l+\phi)x_{\phi,n-\phi,l-\phi,m-l+\phi,k-1} + (k+1)x_{\phi,n-\phi,l-\phi,m-l+\phi,k+1} \\
&\quad - \phi x_{\phi,n-\phi,l-\phi,m-l+\phi,k} - (n-\phi)x_{\phi,n-\phi,l-\phi,m-l+\phi,k} - (l-\phi)x_{\phi,n-\phi,l-\phi,m-l+\phi,k} \\
&\quad - (m-l+\phi)x_{\phi,n-\phi,l-\phi,m-l+\phi,k} - (n-\phi+m-l+\phi)x_{\phi,n-\phi,l-\phi,m-l+\phi,k} \\
&\quad - kx_{\phi,n-\phi,l-\phi,m-l+\phi,k}), \\
&= \sum_{\phi=0}^{l} ((\phi+1)x_{\phi+1,n-\phi-1,l-\phi,m-l+\phi,k} + (n-\phi+1)x_{\phi-1,n-\phi+1,l-\phi,m-l+\phi,k} \\
&\quad + (l-\phi+1)x_{\phi,n-\phi,l-\phi+1,m-l+\phi-1,k} + (m-l+\phi+1)x_{\phi,n-\phi,l-\phi-1,m-l+\phi+1,k} \\
&\quad + (n+m-l)x_{\phi,n-\phi,l-\phi,m-l+\phi,k-1} + (k+1)x_{\phi,n-\phi,l-\phi,m-l+\phi,k+1} \\
&\quad - \phi x_{\phi,n-\phi,l-\phi,m-l+\phi,k} - (n-\phi)x_{\phi,n-\phi,l-\phi,m-l+\phi,k} - (l-\phi)x_{\phi,n-\phi,l-\phi,m-l+\phi,k} \\
&\quad - (m-l+\phi)x_{\phi,n-\phi,l-\phi,m-l+\phi,k} - (n+m-l)x_{\phi,n-\phi,l-\phi,m-l+\phi,k} \\
&\quad - kx_{\phi,n-\phi,l-\phi,m-l+\phi,k}).
\end{aligned}
$$

Before we proceed, we denote three groups of terms that correspond to different processes. In particular, we pick the terms ${z'_{l,\eta-l,k}}^{(i)}$ for $i = 1, 2, 3$ to correspond to TF binding, TF

unbinding, and mRNA production or degradation respectively. These groups are given by

$$
\begin{aligned}
{z'_{l,\eta-l,k}}^{(1)} &= (l+1)z_{l+1,\eta-(l+1),k} - lz_{l,\eta-l,k} \\
{z'_{l,\eta-l,k}}^{(2)} &= (\eta-(l-1))z_{l-1,\eta-(l-1),k} - (\eta-l)z_{l,\eta-l,k} \\
{z'_{l,\eta-l,k}}^{(3)} &= (\eta-l)z_{l,\eta-l,k-1} + (k+1)z_{l,\eta-l,k+1} - (\eta-l)z_{l,\eta-l,k} - kz_{l,\eta-l,k}.
\end{aligned}
$$

Similarly, we can define

$$
\begin{aligned}
{x'_{\phi,n-\phi,l-\phi,m-l+\phi,k}}^{(1)} &= (\phi+1)x_{\phi+1,n-\phi-1,l-\phi,m-l+\phi,k} + (l-\phi+1)x_{\phi,n-\phi,l-\phi+1,m-l+\phi-1,k} \\
&\quad - \phi x_{\phi,n-\phi,l-\phi,m-l+\phi,k} - (l-\phi)x_{\phi,n-\phi,l-\phi,m-l+\phi,k} \\
{x'_{\phi,n-\phi,l-\phi,m-l+\phi,k}}^{(2)} &= (n-\phi+1)x_{\phi-1,n-\phi+1,l-\phi,m-l+\phi,k} + (m-l+\phi+1)x_{\phi,n-\phi,l-\phi-1,m-l+\phi+1,k} \\
&\quad - (n-\phi)x_{\phi,n-\phi,l-\phi,m-l+\phi,k} - (m-l+\phi)x_{\phi,n-\phi,l-\phi,m-l+\phi,k} \\
{x'_{\phi,n-\phi,l-\phi,m-l+\phi,k}}^{(3)} &= (n+m-l)x_{\phi,n-\phi,l-\phi,m-l+\phi,k-1} + (k+1)x_{\phi,n-\phi,l-\phi,m-l+\phi,k+1} \\
&\quad - (n+m-l)x_{\phi,n-\phi,l-\phi,m-l+\phi,k} - kx_{\phi,n-\phi,l-\phi,m-l+\phi,k},
\end{aligned}
$$

and

$$
\begin{aligned}
{y'_{l,\eta-l,k}}^{(1)} &= \sum_{\phi=0}^{l} {x'_{\phi,n-\phi,l-\phi,m-l+\phi,k}}^{(1)} \\
{y'_{l,\eta-l,k}}^{(2)} &= \sum_{\phi=0}^{l} {x'_{\phi,n-\phi,l-\phi,m-l+\phi,k}}^{(2)} \\
{y'_{l,\eta-l,k}}^{(3)} &= \sum_{\phi=0}^{l} {x'_{\phi,n-\phi,l-\phi,m-l+\phi,k}}^{(3)}.
\end{aligned}
$$

To show stochastic equivalence, it suffices to show that ${y'_{l,\eta-l,k}}^{(i)}$ is an equivalent description to ${z'_{l,\eta-l,k}}^{(i)}$ for $i = 1, 2, 3$ since $\sum_{i=1}^{3} {y'_{l,\eta-l,k}}^{(i)} = y'_{l,\eta-l,k}$ and $\sum_{i=1}^{3} {z'_{l,\eta-l,k}}^{(i)} = z'_{l,\eta-l,k}$. First,

we show for the TF binding terms that

$$
\begin{aligned}
{y'_{l,\eta-l,k}}^{(1)} &= \sum_{\phi=0}^{l}(\phi+1)x_{\phi+1,n-\phi-1,l-\phi,m-l+\phi,k} + \sum_{\phi=0}^{l}(l-\phi+1)x_{\phi,n-\phi,l-\phi+1,m-l+\phi-1,k} \\
&\quad - \sum_{\phi=0}^{l}\phi x_{\phi,n-\phi,l-\phi,m-l+\phi,k} - \sum_{\phi=0}^{l}(l-\phi)x_{\phi,n-\phi,l-\phi,m-l+\phi,k}, \\
&= \sum_{\phi=0}^{l+1}\phi x_{\phi,n-\phi,l-\phi+1,m-l+\phi-1,k} + \sum_{\phi=0}^{l}(l-\phi+1)x_{\phi,n-\phi,l-\phi+1,m-l+\phi-1,k} \\
&\quad - \sum_{\phi=0}^{l} l x_{\phi,n-\phi,l-\phi,m-l+\phi,k}, \\
&= x_{l+1,n-(l+1),l-(l+1)+1,m-l+(l+1)-1,k} + \sum_{\phi=0}^{l}(l+1)x_{\phi,n-\phi,l-\phi+1,m-l+\phi-1,k} \\
&\quad - \sum_{\phi=0}^{l} l x_{\phi,n-\phi,l-\phi,m-l+\phi,k}, \\
&= \sum_{\phi=0}^{l+1}(l+1)x_{\phi,n-\phi,l-\phi+1,m-l+\phi-1,k} - l\sum_{\phi=0}^{l} x_{\phi,n-\phi,l-\phi,m-(l-\phi),k}, \\
&= (l+1)\sum_{\phi=0}^{l+1} x_{\phi,n-\phi,l+1-\phi,m-(l+1-\phi),k} - l\sum_{\phi=0}^{l} x_{\phi,n-\phi,l-\phi,m-(l-\phi),k} \\
&= (l+1)y_{l+1,\eta-(l+1),k} - l y_{l,\eta-l,k}.
\end{aligned}
$$

Now for the TF unbinding terms we have that

$$
\begin{aligned}
{y'_{l,\eta-l,k}}^{(2)} &= \sum_{\phi=0}^{l}((n-\phi+1)x_{\phi-1,n-\phi+1,l-\phi,m-l+\phi,k} + (m-l+\phi+1)x_{\phi,n-\phi,l-\phi-1,m-l+\phi+1,k} \\
&\quad - (n-\phi)x_{\phi,n-\phi,l-\phi,m-l+\phi,k} - (m-l+\phi)x_{\phi,n-\phi,l-\phi,m-l+\phi,k}), \\
&= \sum_{\phi=0}^{l}(n-\phi+1)x_{\phi-1,n-\phi+1,l-\phi,m-l+\phi,k} + \sum_{\phi=0}^{l}(m-l+\phi+1)x_{\phi,n-\phi,l-\phi-1,m-l+\phi+1,k} \\
&\quad - (n+m-l)\sum_{\phi=0}^{l}x_{\phi,n-\phi,l-\phi,m-(l-\phi),k}, \\
&= \sum_{\phi=0}^{l-1}(n-\phi)x_{\phi,n-\phi,l-\phi-1,m-l+\phi+1,k} + \sum_{\phi=0}^{l}(m-l+\phi+1)x_{\phi,n-\phi,l-\phi-1,m-l+\phi+1,k} \\
&\quad - (n+m-l)\sum_{\phi=0}^{l}x_{\phi,n-\phi,l-\phi,m-(l-\phi),k}, \\
&= \sum_{\phi=0}^{l-1}(n-\phi)x_{\phi,n-\phi,l-\phi-1,m-l+\phi+1,k} + \sum_{\phi=0}^{l-1}(m-l+\phi+1)x_{\phi,n-\phi,l-\phi-1,m-l+\phi+1,k} \\
&\quad - (n+m-l)\sum_{\phi=0}^{l}x_{\phi,n-\phi,l-\phi,m-(l-\phi),k}, \\
&= (n+m-(l-1))\sum_{\phi=0}^{l-1}x_{\phi,n-\phi,(l-1)-\phi,m-(l-1-\phi),k} - (n+m-l)\sum_{\phi=0}^{l}x_{\phi,n-\phi,l-\phi,m-(l-\phi),k}, \\
&= (\eta-(l-1))y_{l-1,\eta-(l-1),k} - (\eta-l)y_{l,\eta-l,k}.
\end{aligned}
$$

Lastly, we show that

$$
\begin{aligned}
{y'_{l,\eta-l,k}}^{(3)} &= \sum_{\phi=0}^{l}((n+m-l)x_{\phi,n-\phi,l-\phi,m-l+\phi,k-1} + (k+1)x_{\phi,n-\phi,l-\phi,m-l+\phi,k+1} \\
&\quad - (n+m-l)x_{\phi,n-\phi,l-\phi,m-l+\phi,k} - kx_{\phi,n-\phi,l-\phi,m-l+\phi,k}), \\
&= (n+m-l)\sum_{\phi=0}^{l} x_{\phi,n-\phi,l-\phi,m-l+\phi,k-1} + (k+1)\sum_{\phi=0}^{l} x_{\phi,n-\phi,l-\phi,m-l+\phi,k+1} \\
&\quad - (n+m-l)\sum_{\phi=0}^{l} x_{\phi,n-\phi,l-\phi,m-l+\phi,k} - k\sum_{\phi=0}^{l} x_{\phi,n-\phi,l-\phi,m-l+\phi,k}, \\
&= (\eta-l)y_{l,\eta-l,k-1} + (k+1)y_{l,\eta-l,k+1} - (\eta-l)y_{l,\eta-l,k} - ky_{l,\eta-l,k}.
\end{aligned}
$$

Hence the two systems are stochastically equivalent.

3.2.3 Subadditivity and Superadditivity

The results in the previous section showed that the number of additive enhancers does not affect transcriptional noise and fidelity. In turn, the number of additive enhancers may be under minimal selection pressure and instead originate through stochastic processes such as genetic drift. However, shadow enhancers have been observed to behave subadditively and superadditively – their combined activity either results in a lesser or greater amount of gene expression than the sum of their independent contributions. To investigate whether different levels of additivity could result in different fidelity and noise properties, we modified our models in the previous section to recapitulate this effect.

To capture varying enhancer additivity in our models, we increased or decreased the binding rates k_{on} and k_{off} to approximate the biochemical mechanisms underlying varying levels of additivity. We chose this approach to implementing sub- or superadditivity because it was consistent with previous experimental data [1]. Using this approach, any enhancer model

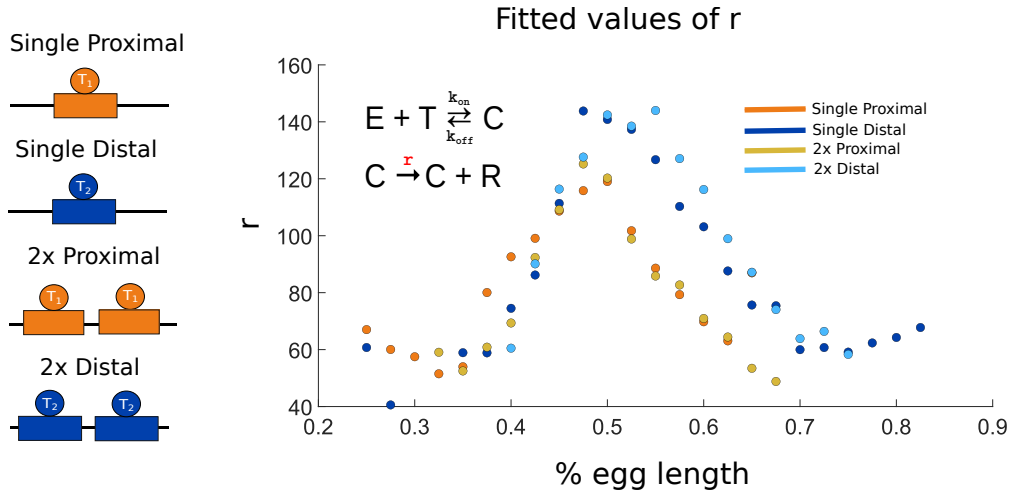

Figure 3.5: Fitted rates of mRNA transcription for single and duplicated models suggest that a single enhancer is sufficient to saturate polymerase loading rates. The polymerase loading rates r_1 and r_2 were fitted for the 4 models shown above according to the same methodology described in Waymack et al. [1]. Parameter fittings were done directly on the raw mRNA transcriptional data of *Kruppel* and show minimal differences between the single enhancer models and their duplicated counterparts.

can be made subadditive by decreasing k_{on} and increasing k_{off}. Similarly, enhancer models can be made superadditive by increasing the values of k_{on} and decreasing the values of k_{off}. In addition, we briefly considered the cases where the polymerase loading rates are saturated by a single enhancer or remain null until all enhancers bound to the promoter (Figures 3.5 and 3.6).

For simplicity, we limited our approach to linearly updating the binding rates with the number of enhancers such that n enhancers would decrease k_{on} by $d_1 n$ and increase k_{off} by $d_2 n$ for constants d_1 and d_2 (Figures 3.7A and 3.9A). We selected values of d_1 and d_2 to broadly explore the effect of subadditivity while still allowing the moment closure method to accurately estimate noise and fidelity.

Unlike the additive case, when enhancers interact subadditively, their numbers affect noise and fidelity (Figure 3.7B, Figure 3.4). Systems with more enhancers achieve larger transcriptional fidelities at the expense of larger transcriptional noise, suggesting that an evolutionary trade-off between these two properties might be in place. Subadditive enhancers will also

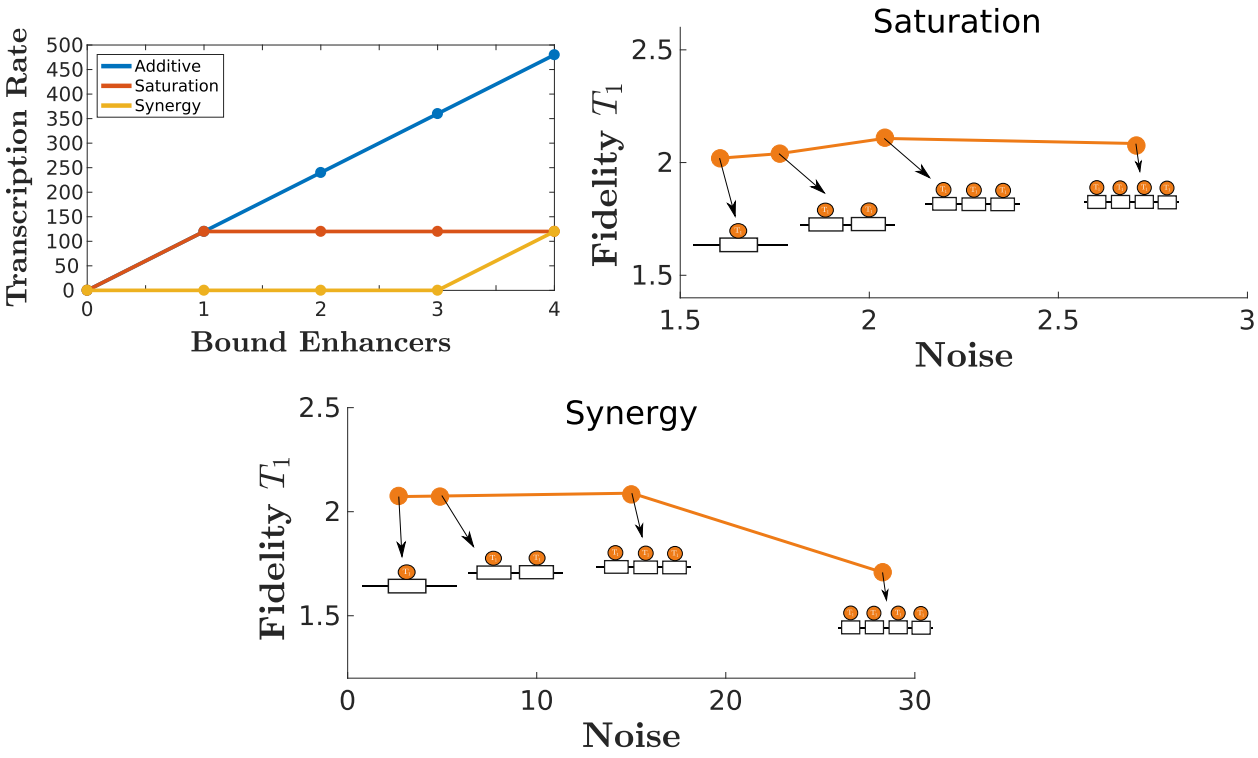

Figure 3.6: Varying additivity through modulation of polymerase loading rates does not produce significant changes to the fidelity but can increase or decrease transcriptional noise. A saturated system yields mRNA at the same rate for any positive number of enhancers bound. On the other hand, a synergistic system becomes active only when all enhancers are bound to the promoter. The resulting plots of fidelity and noise corresponding to these systems show no significant changes to the fidelity with respect to enhancer numbers. Meanwhile, noise becomes significantly larger for synergistic models and smaller for saturated models as enhancer numbers increase.

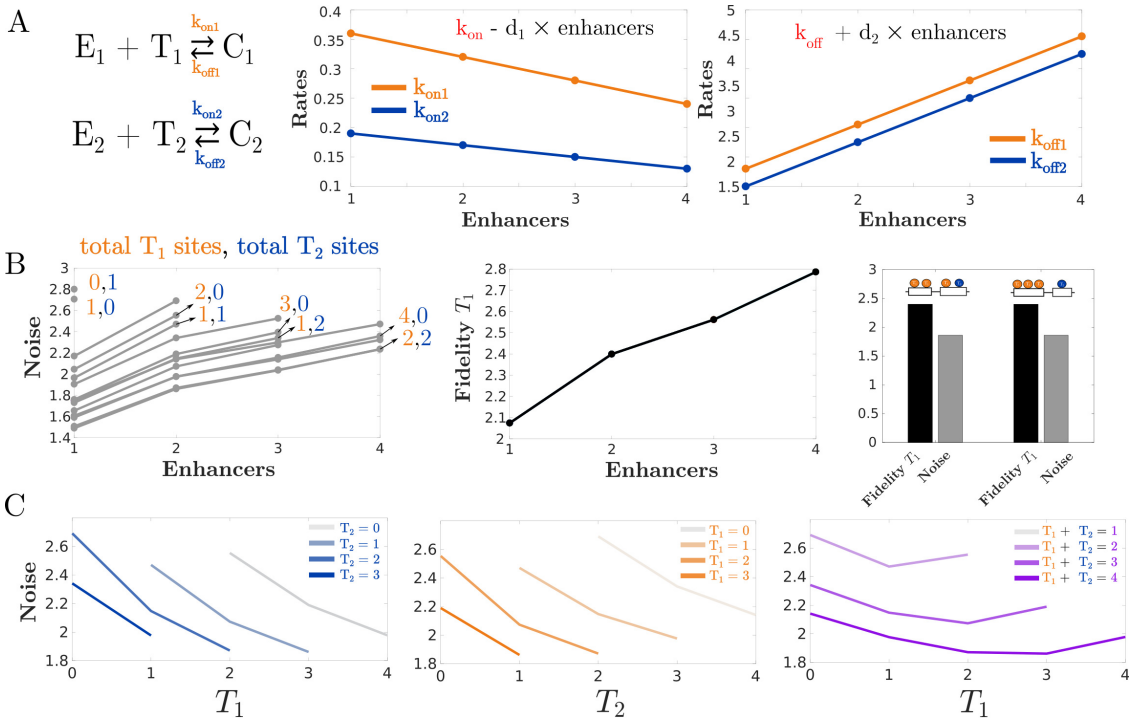

Figure 3.7: Subadditive enhancers achieve higher transcriptional fidelity at the expense of higher noise. (A) Subadditivity is implemented in our model by linearly decreasing k_{on} rates and linearly increasing k_{off} rates. In this case d_1, the rate of decrease for k_{on}, was chosen to be 0.04 for T_1 and 0.02 for T_2. Meanwhile d_2, the rate of increase for k_{off}, was chosen to be 0.75 for both T_1 and T_2. (B) Systems with more subadditive enhancers achieve higher transcriptional fidelity while exhibiting higher noise. The distribution and number of binding sites do not affect the fidelity. Noise is also independent of binding site distribution but varies with respect to the number of binding sites. (C) Plots showing the relationship between binding site numbers and transcriptional noise for two subadditive enhancers. Increasing binding site numbers leads to less noise in gene expression.

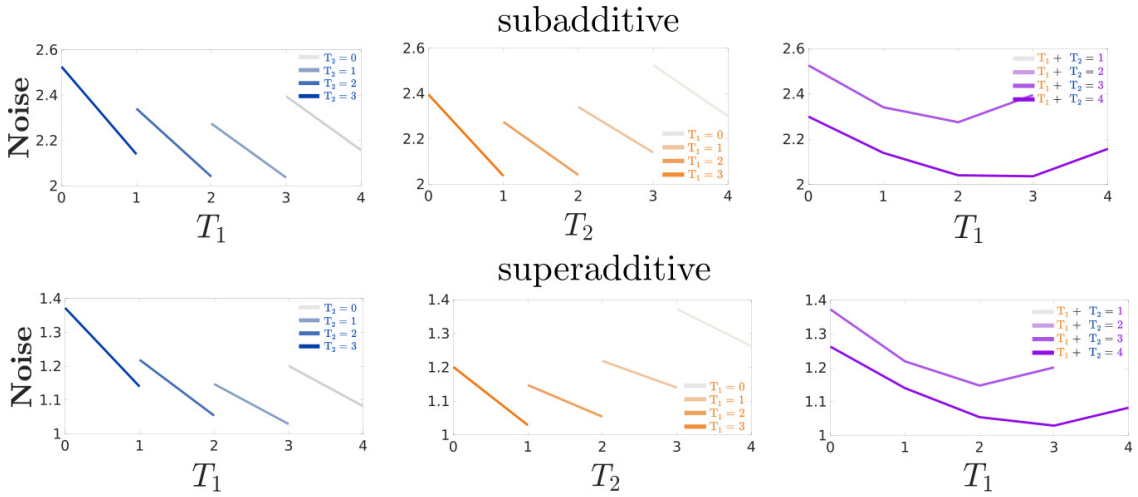

Figure 3.8: Increasing the binding site numbers in systems with three enhancers leads to decreases in noise. Noise trends with respect to binding site numbers for systems with three enhancers that operate subadditively and superadditively. Higher binding site numbers lead to lower transcriptional noise.

produce less mRNA transcripts than their additive counterparts, which could present an additional trade-off if gene expression output levels need to be above a certain threshold to achieve a biological function.

Similar to the additive case, binding site numbers in subadditive enhancers do not affect the fidelity, but they do affect the transcriptional noise. Generally, two-enhancer systems with more binding sites achieve lower noise (subadditive systems with three enhancers display the same trends as shown in Figure 3.8). Moreover, systems with binding sites for both T_1 and T_2 are less noisy than systems with a single kind of binding site (Figure 3.7C). The distribution of binding sites among enhancers has no effect on the fidelity or the noise. In sum, the subadditive models are distinct from the additive models in that they show that increasing enhancers numbers increases transcriptional fidelity at the expense of noise. However, the relationship between the numbers and types of binding sites and transcriptional noise are similar between the additive and subadditive cases.

Systems with superadditive enhancers also show decreasing transcriptional noise with increasing numbers of enhancers. However, unlike subadditive enhancers, superadditive sys-

tems do not show the same trade off between noise and fidelity – increasing enhancer numbers cause negligible differences in fidelity (Figure 3.9B, Figure 3.4). We note, however, that superadditivity could lead to the production of excessive amounts of transcript, which incurs a metabolic cost.

Once again, binding site numbers and distributions in superadditive enhancers do not affect the fidelity. The small deviation in the middle plot of Figure 3.9B could be due to an approximation error resulting from moment closure to determine expected values of mRNA transcription. Moreover, superadditive enhancers with more binding sites display lower transcriptional noise as we noted for additive and subadditive enhancers (Figure 3.9C, Figure 3.8).

Overall, these results show that subadditive enhancers face a trade-off between increasing transcriptional fidelity at the cost of increasing transcriptional noise. Meanwhile, superadditive enhancers do not face such a trade-off as they do not alter the fidelity while decreasing expression noise. It is plausible, however, that excessive amounts of transcript produced by superadditive enhancer present trade-offs elsewhere. In conclusion, varying levels of enhancer additivity might allow for modulation of transcriptional properties in ways that are not available to a single enhancer with the same number of binding sites.

3.2.4 Shadow Enhancer Duplication

While not explicitly stated, the models in Figure 3.3A correspond to a collection of single enhancers that split into multiple enhancers. Analyzing our results through this lens would suggest that the splitting of an enhancer into subadditive or superadditive enhancers could occur based on a need to modulate noise, fidelity, or absolute levels of gene expression. For additive enhancers, such a split would not face any adverse selection pressures based on the absence of changes to the mRNA output. However, the mechanisms by which shadow enhancers come to being remain unclear and the splitting of an enhancer might not be

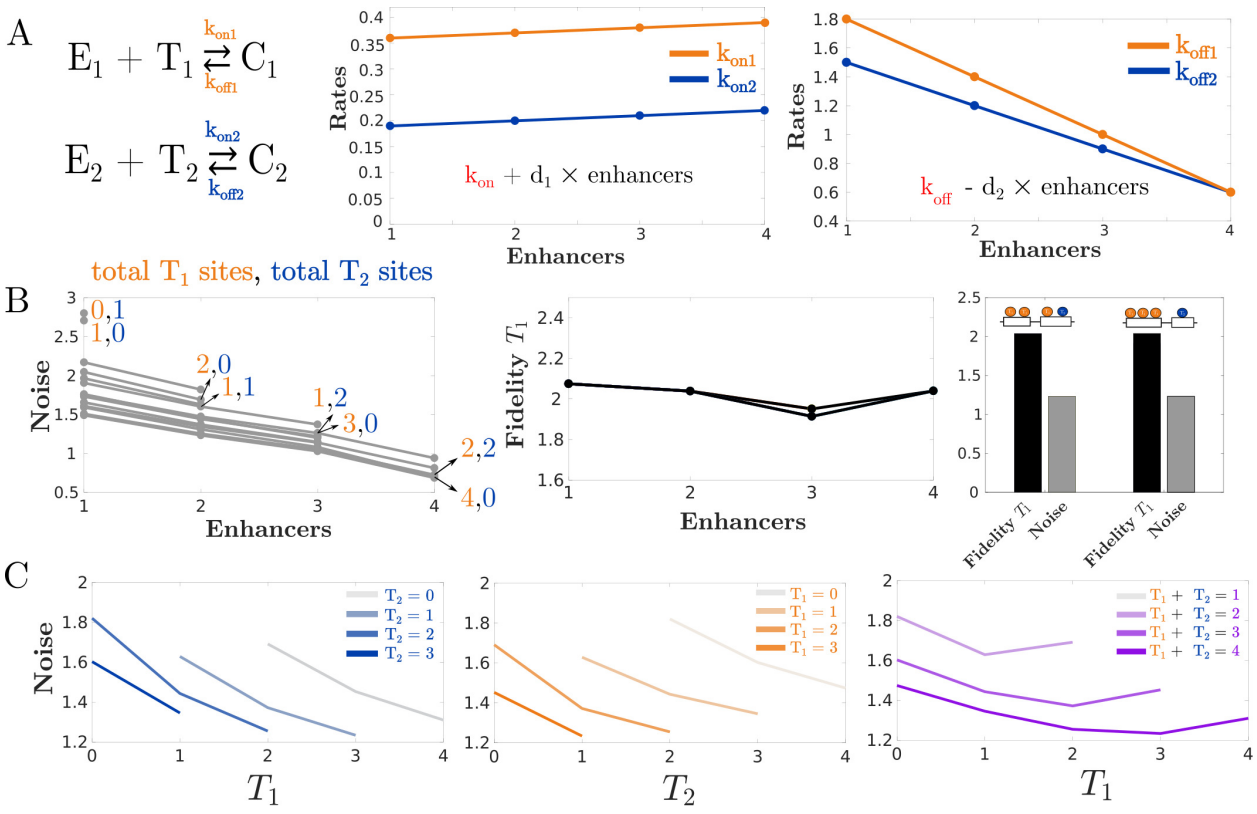

Figure 3.9: Superadditive enhancers maintain nearly constant transcriptional fidelity while achieving lower transcriptional noise. (A) Superadditivity is implemented in our model by linearly increasing k_{on} rates and linearly decreasing k_{off} rates. In this case d_2, the rate of decrease for k_{off}, was chosen to be 0.4 for T_1 and 0.3 for T_2. Meanwhile d_1, the rate of increase for k_{on}, was chosen to be 0.01 for both T_1 and T_2 (B) Unlike in the subadditive case, enhancer numbers do not appear to have a significant effect on transcriptional fidelity. Meanwhile, systems with more superadditive enhancers exhibit lower noise. The number of binding sites has a negligible effect on the fidelity but a more noticeable effect on the noise. The distribution of binding sites does not affect either the noise or the fidelity all else being constant. (C) Plots showing the relationship between binding site numbers and transcriptional noise for two superadditive enhancers. Increasing binding site numbers leads to less noise in gene expression.

the only viable route to create shadow enhancers [21]. Hence, to contrast our results with a different mechanism, we apply our analysis to shadow enhancer systems that arise by enhancer duplication.

First, we generated models that are repeated duplications of single enhancer models. Cartoons depicting these models are shown in Figure 3.10A. In some cases, where each enhancer had multiple binding sites, we had to limit the number of enhancers simulated due to their large number of reactions and the associated computational costs. Given the experimental observations of subadditivity with enhancer duplication, we focused our analysis on the duplication of subadditive enhancers and compared it with the alternative of splitting subadditive enhancers [1, 23].

Unlike splitting, enhancer duplication not only increases the number of enhancers but also the number of binding sites (Figure 3.10B). For this reason, the number of binding sites for each model in the plots of Figure 3.10C is shown as a product of the binding sites per enhancer times the number of enhancers. These plots show that the duplication of subadditive enhancers does not significantly affect transcriptional noise while it does increase transcriptional fidelity. The effect of duplication on transcriptional noise is consistent with the experimental measurements of the *Kruppel* enhancers [1]. These results are in contrast to those observed in Figure 3.7B where splitting subadditive enhancers displayed an increase in fidelity at the expense of increasing transcriptional noise.

Ultimately, enhancer duplication shows the potential for increasing transcriptional fidelity while simultaneously reducing expression noise, albeit with the additional metabolic cost of increasing RNA output. The duplication of subadditive enhancers presents distinct trade-offs from those observed in the splitting scenario and expands the possibilities of transcriptional modulation from those available for single enhancer systems.

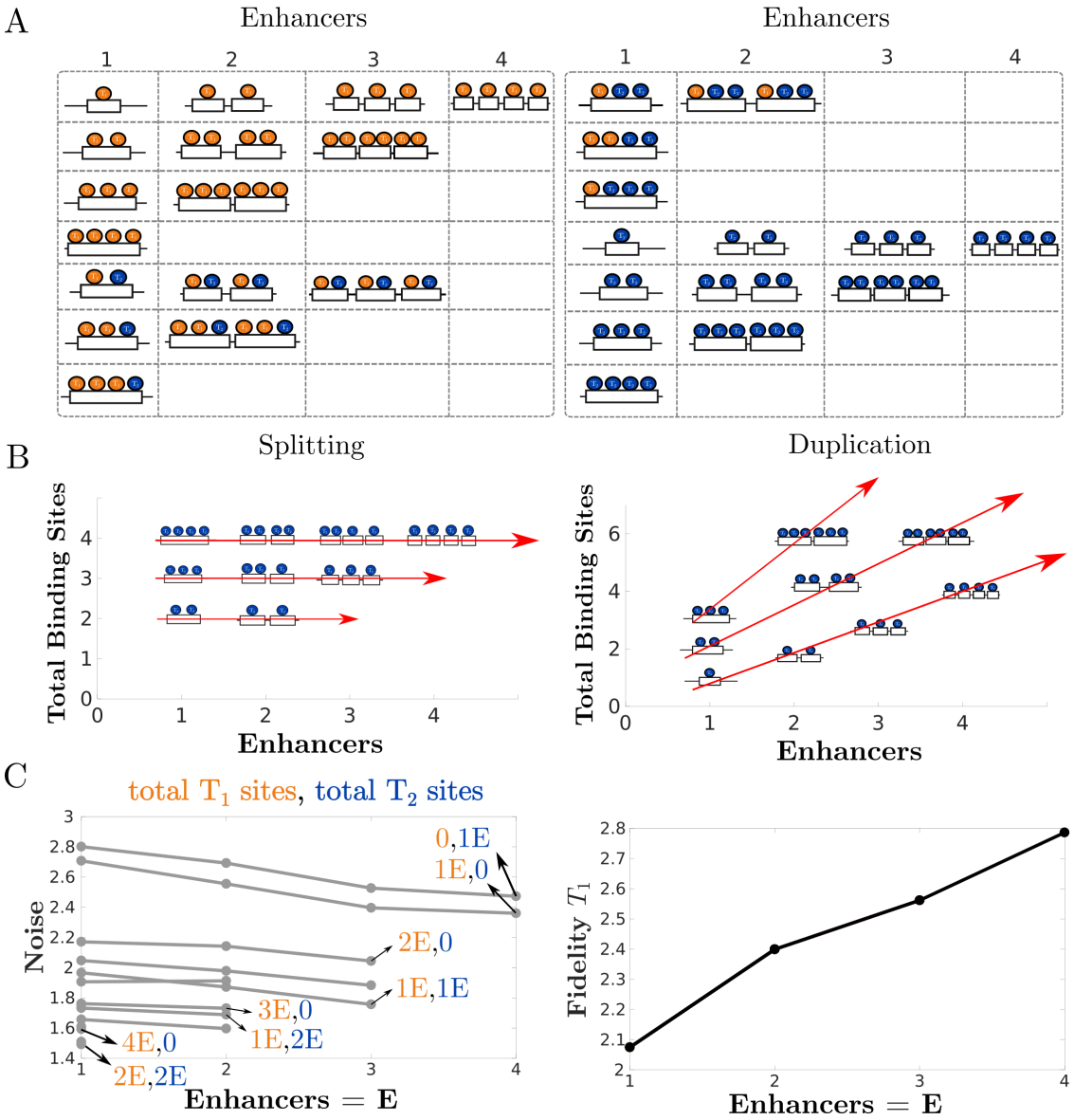

Figure 3.10: Duplication of subadditive enhancers can increase transcriptional fidelity without causing significant changes to the noise. (A) Single enhancer models and those that result from repeated enhancer duplications. (B) Plots showing the relationship between total binding sites and enhancers for the case of enhancer splitting and enhancer duplication. Splitting does not affect total binding site numbers while it increases enhancer numbers. On the other hand, duplication increases both enhancer numbers and total binding sites at different rates. (C) Plots depicting transcriptional fidelity and noise for subadditive versions of the models in (A). Enhancer duplications increase transcriptional fidelity while the noise decreases only slightly.

3.3 Discussion

In this work, we sought to determine the effect of varying the number of shadow enhancers as well as the nature of their interactions, and to understand whether a single enhancer can recapitulate their dynamical behavior. To do so, we simulated models with differing numbers of enhancers and TF binding sites and calculated the transcriptional noise and fidelity for each model. Sufficiently high fidelity is required for a gene's expression to meaningfully reflect changes in upstream signals intended to shape a cell's fate. On the other hand, sufficiently low noise is needed for transcription to convey consistent signals of expression in the face of unavoidable molecular fluctuations. Consequently, a balance is needed between these properties in order to properly pattern a developing organism.

We began by considering additive enhancers – enhancers which have a combined transcriptional rate equal to the sum of their individual contributions. Our models revealed that the number of additive enhancers has no effect on transcriptional noise and fidelity. Therefore, in the case of additive shadow enhancers, there would seem to be no particular pressure to have multiple shadow enhancers, as opposed to one large enhancer. How might we explain the preponderance of shadow enhancers in this case? Here, the dynamics of genome evolution may be at play. If we imagine that a genome contains a single, large enhancer, there are processes, like transposable element insertions [111, 112] or DNA polymerase slippage [113, 114] that may split this enhancer into shadow enhancers. If these shadow enhancers can control gene expression similarly to the ancestral single enhancer, as our model suggests, there would be no particular pressure to remove the intervening sequence. In fact, it may be entropically more favorable to split an enhancer into shadow enhancers that to merge shadow enhancers into a single enhancer, given that many more splitting events could lead to two functional enhancers, while deletion or excision events would have to be a great deal more specific to avoid removing functional enhancer sequence.

Many experimental studies have shown that shadow enhancers can interact in a wide range of manners – sub- and superadditively, as well as repressively [24, 52, 23, 93, 95, 92, 96]. We therefore modified our models to recapitulate this behavior. The resulting simulations revealed that increasing numbers of subadditive enhancers corresponded to higher levels of transcriptional fidelity at the expense of higher transcriptional noise. On the other hand, increasing numbers of superadditive enhancers led to insignificant changes in fidelity while significantly decreasing expression noise, albeit at the expense of producing increasing amounts of RNA, which incurs a metabolic cost [115]. This implies that when shadow enhancers interact in more intricate ways, there is a complex landscape of transcriptional noise, fidelity, and output that selection may act upon to determine the number of enhancers controlling a gene.

Though there are many hypotheses about the mechanisms that drive enhancers to act sub or superadditively, like enhancer competition for the promoter or synergy between recruited TFs and co-factors, we are not yet able to predict how two or more enhancers will interact [24, 116]. Superadditivity and subadditivity may be structural properties that may not be tunable, but instead are the result of existing constraints for each individual system. Thus there are likely many mechanisms by which enhancers become non-additive and other evolutionary trade-offs beyond transcriptional noise and fidelity that elude our simplified models.

We also wished to examine the impacts on noise and fidelity of different mechanisms that could result in the creation of shadow enhancers [21, 117]. In particular, we wanted to contrast the case of an enhancer that splits into multiple enhancers and an enhancer that duplicates itself. To study enhancer duplication, we adapted our models to this scenario and noted that repeated duplications of subadditive enhancers induced lower transcriptional noise alongside minimal changes in transcriptional fidelity. This result was in contrast to repeated splittings of an enhancer which led to increases in fidelity at the expense of increases

in noise. It remains unclear whether splitting or duplication of genomic regions are common mechanisms for the origin of shadow enhancers and whether they presents additional trade-offs with respect to genome size. Our analysis was also limited in that it assumes exact duplications of each enhancer, which is inconsistent with the stochasticity typically involved in genome duplication [118].

Naturally, our approach was also limited by the constraints we imposed on our models. Throughout this work, we used parameters that were fitted to experimental data derived from studying the *Kruppel* enhancer system. This parameter space, however, may not be in accordance with the dynamics of other enhancer systems found in *Drosophila* and other organisms. We also note that our implementation of subadditivity and superadditivity assumed that binding rates scale linearly with enhancer numbers, which might not be true in all cases. For instance, enhancers could behave synergistically such that transcription can only begin when all enhancers are bound to the promoter (Figure 3.6).

Our modeling suggests experiments that could prove useful in further exploring the mechanisms of shadow enhancer function. For instance, one could imagine constructing a synthetic system within an embryo to directly test the impact of varying enhancer numbers and TF binding site distribution on the associated noise and fidelity of the transcriptional output [119, 120]. In addition, a bioinformatic analysis comparing enhancer DNA sequences in different organisms could be used to determine the relative prevalence of enhancer splitting, duplication, and other ways of generating new shadow enhancers.

Overall, this work shows that different strategies for shadow enhancer interaction present a variety of trade-offs. In the additive scenario, increasing the number of enhancers appears to face no transcriptional trade-offs or advantages. In the subadditive scenario, additional enhancers could be favored if the benefits of increasing in transcriptional fidelity outweigh those of increasing noise. On the other hand, superadditive enhancers could supersede a single enhancer if an excess of mRNA transcript can be tolerated in exchange for decreased

noise. We also showed that repeated enhancer splittings lead to distinct outcomes in noise and fidelity than repeated duplications. Ultimately, the preponderance of shadow enhancers may be due to a combination of genetic drift and to the variety of transcriptional modulation strategies possible with multiple, but not single enhancers.

3.4 Methods

3.4.1 Description of enhancer models and parameters

The model of *Kruppel* gene enhancers in Figure 3.1B is described by the following chemical reaction network.

$$T_1 + A_0 \underset{k_{\text{off}_1}}{\overset{k_{\text{on}_1}}{\rightleftharpoons}} A_1 \xrightarrow{r_1} A_1 + R$$

$$T_2 + B_0 \underset{k_{\text{off}_2}}{\overset{k_{\text{on}_2}}{\rightleftharpoons}} B_1 \xrightarrow{r_2} B_1 + R$$

$$\emptyset \xrightarrow{\beta_1} n_1 T_1$$

$$\emptyset \xrightarrow{\gamma_1} n_2 T_2$$

$$T_1 \xrightarrow{\beta_{-1}} \emptyset$$

$$T_2 \xrightarrow{\gamma_{-1}} \emptyset$$

$$R \xrightarrow{\alpha} \emptyset.$$

Here, two enhancers denoted as A and B have a single binding site for their respective TFs T_1 and T_2. The subscripts for each enhancer reflect how many TFs are bound to them. For

example, A_0 denotes the enhancer A with no TFs bound while A_1 denotes the same enhancer with a single TF bound. Our modeling framework assumes that a single TF bound to the enhancer is sufficient for an enhancer-promoter interaction. Once an enhancer is bound to the promoter, the rates of transcription correspond to a linear combination of the TFs bound to that enhancer. In this case, since A and B possess only one binding site, the transcriptional rates are only the single terms r_1 and r_2. The TFs T_1 and T_2 appear in clusters of sizes n_1 and n_2 and dissipate or degrade linearly at rates β_{-1} and γ_{-1}. These particular properties of TFs were previously noted to be necessary for recapitulating *Kruppel* transcriptional data. Lastly, mRNA denoted by R degrades at a constant rate α. Details about fitting the reaction rates to experimental data and further justification for the topology of this model can be found in Waymack et al. [1].

We expanded the reasoning above to construct models for any number of enhancers each with an arbitrary number of binding sites. In particular, take a set of n enhancers given by $A^{(1)}, A^{(2)}, \ldots, A^{(n)}$. We denote an enhancer $A_I^{(i)}$ where I is a vector composed of 0s or 1s with the k^{th} entry being a 1 if there is a TF bound to the k^{th} binding site of $A^{(i)}$ and 0 otherwise. Denote e_j as the vector with 0s at all entries except for a 1 at the j^{th} entry and having the same number of entries as I. Any binding of a TF T_m to the (empty) j^{th} binding site of $A_I^{(i)}$ is described by a reaction of the form

$$A_I^{(i)} + T_m \xrightarrow{k_{\text{on}_m}} A_{I+e_j}^{(i)}$$

Similarly, an unbinding of T_m from $A_I^{(i)}$ is described by the reaction

$$A_I^{(i)} \xrightarrow{k_{\text{off}_m}} A_{I-e_j}^{(i)} + T_m$$

Suppose the enhancer $A_I^{(i)}$ is bound by TFs $T_{l_1}, T_{l_2}, \ldots, T_{l_p}$ where the binding sites for an arbitrary TF T_{l_c} are located between the entries $f_1^{(c)}$ and $f_2^{(c)}$ of I. Then any enhancer with

subscript I will initiate transcription at a rate equal to $\sum_{c=1}^{p} \sum_{d=f_1^{(c)}}^{f_2^{(c)}} I_d r_{l_c}$ where I_d is the d^{th} entry of I. Lastly, any TF T_m appears in clusters of size n_m as described by the reaction

$$\emptyset \quad \longrightarrow \quad n_m T_m$$

and degrades at a linear rate. Two concrete examples of this procedure are shown in Figure 3.2 for enhancer systems that were included in Figure 3.3A.

3.4.2 Estimation of noise and fidelity

The expression noise of any given model was measured by the coefficient of variation (CV) which itself is calculated as

$$CV = \frac{\sigma_R}{E[R]},$$

where $E[R]$ is the first moment of mRNA and σ_R is the standard deviation of mRNA. Here, the first moment is equivalent to $E[R]$ while the standard deviation σ_R corresponds to the second moment centered around the mean, that is, $\sigma_R = (E[(R-E[R])^2])^{1/2}$. This expression for σ_R can also be manipulated to be a function of the first moment and the second moment centered around zero to yield $\sigma_R = \sqrt{E[R^2] - (E[R])^2}$.

It can be shown that the derivatives for the mean and variance of any chemical species can be derived from the master equation. For example, in the system described by equation 1.1, we can calculate the derivative of the first moment of A by multiplying the left hand side of

the equation by a and summing over all species,

$$\sum_{a,b,c} a\frac{dx_{a,b,c}}{dt} = \frac{d}{dt}\sum_{a,b,c} ax_{a,b,c}$$
$$= \frac{dE[A]}{dt}$$

and thus

$$\frac{dE[A]}{dt} = \sum_{a,b,c} a(k(a+1)(b+1)x_{a+1,b+1,c-1} - kabx_{a,b,c}) \tag{3.1}$$
$$= k\sum_{a,b,c} ax_{a,b,c} + k\sum_{a,b,c} a^2x_{a,b,c} + k\sum_{a,b,c} abx_{a,b,c} \tag{3.2}$$
$$= kE[A] + kE[A^2] + E[AB]. \tag{3.3}$$

At this point, we can see that derivative of the first moment depends on the second moment of A, namely $E[A^2] = \sum_{a,b,c} a^2x_{a,b,c}$. In fact, the derivative of the n^{th} moment of A will in general depend on the $n^{\text{th}} + 1$ moments. Hence, it is not possible to construct a closed system of ODEs that would allow us to solve this system and obtain concrete values for the mean and the variance of A.

One alternative approach, however, is to use moment closure methods that are designed for estimation of the moments. These methods focus on closing the ODE systems that include equations such as 3.1. This, in turn, allows such systems to be solved numerically or analytically. A particular type of moment closure method is known as zero cumulants closure which, as the name suggests, involves setting equal to 0 all the cumulants with an order greater than a specified truncation value. The application of zero cumulants closure can be justified when distributions have low variability and are fairly symmetric [25]. Also, the first, second, and third cumulants are equivalent to the first, second, and third moments centered around the mean. For example, an application of zero cumulants closure with truncation order 1 to the reaction network described by equation 1.1 would amount to setting $E[A^2] = 0$

in equation 3.1 and setting equal to zero all the second moments present in the derivatives of $E[B]$ and $E[AB]$. Ultimately, this approach yields a closed system of ODEs that can be solved analytically or with numerical algorithms.

To estimate the noise in mRNA expression for all the models in Figure 3.3A, we approximated the moments for R using zero cumulants closure with a second order truncation. In other words, we assumed that all cumulants of the specified output with order larger than 2 were negligible when calculating the moments. However, unlike the simple example shown above, our models may have several dozen reactions which can make the process of calculating the moments extremely laborious. Fortunately, the CERENA toolbox provides a suite of moment closure methods, including zero cumulants closure, that are conveniently arranged to take reaction networks as inputs [6]. We generated these input files for the 48 models in Figure 3.3A using a Python script that takes as inputs a number of enhancers and TF binding sites and generates the corresponding model file for CERENA. Then, using the moments that were calculated with CERENA, we derived the CV for each of the models. These measurements of noise as the CV were plotted in Figures 3.3, 3.7, 3.9, and 3.10.

The transcriptional fidelity between T_1 and mRNA was estimated using the mutual information given by

$$I(R, T_1) = \sum_{R} \sum_{T_1} P(R, T_1) \log \frac{P(R, T_1)}{P(R)P(T_1)}.$$

Unlike the expression for the CV, R here denotes a vector composed of the mean mRNA $E[R]$ produced at different levels of T_1 production β_1. Similarly, T_1 is a vector denoting the mean levels of TF $E[T_1]$ for a range of β_1 values. The values of β_1 used ranged from 0.01 to 1 in increments of 0.05 resulting in 20 distinct values. Thus, R and T_1 had 20 entries each and were obtained from calculations using CERENA in the same fashion as was done for the noise but under different values of β_1. To calculate the distributions $P(R)$, and $P(T_1)$

we used histograms with one bin per three samples. The number of samples in this case being the number of entries in R and T_1. From these individual histograms, we derived the joint histogram to approximate $P(R, T_1)$. All of these values were then plugged into the equation above to give the mutual information between R and T_1 which we defined as the transcriptional fidelity with respect to T_1 (Figures 3.3, 3.7, 3.9, and 3.10). The same process was done for calculating the transcriptional fidelity with respect to T_2 given by $I(R, T_2)$ (Figure 3.4).

3.4.3 Implementation of sub and superadditivity

The implementation of varying additivity levels was done by modulation of the binding rates k_{on} and k_{off} as shown in Figures 3.7A and 3.9A. For example, to make the *Kruppel* model in Figure 3.3A subadditive, we would proceed as follows. Let $k^{(1)}_{\text{on}_1}$ and $k^{(1)}_{\text{off}_1}$ be the rates of binding and unbinding for T_1 to and from a single enhancer. Since the model in Figure 3.3A has two enhancers, we would set k_{on_1} in this model equal to $k^{(1)}_{\text{on}_1} - 2d_1$ and k_{off_1} to $k^{(1)}_{\text{off}_1} + 2d_2$ where d_1 and d_2 are positive constants. Then, repeat the same procedure for the binding and unbinding rates T_2 for another set of d_1 and d_2 values. This way, the TFs will bind to the enhancers less often leading to an overall decrease in mRNA production. This approach was found to be sufficient for consistently recapitulating the subadditivity of *Kruppel* enhancers observed in the work by Waymack et al [1]. Superadditivity, on the other hand, can be implemented for the model in Figure 3.3A in a similar way by having k_{on_1} equal to $k^{(1)}_{\text{on}_1} + 2d_1$ and k_{off_1} to $k^{(1)}_{\text{off}_1} - 2d_2$. The same procedure can also be applied to the binding rates of T_2.

In general, any model can be made subadditive according to the following scheme. Take once again the system with n enhancers given by $A^{(1)}, A^{(2)}, \ldots, A^{(n)}$ as described above. Denote $k^{(1)}_{\text{on}_m}$ and $k^{(1)}_{\text{off}_m}$ be the rates of binding and unbinding for some TF T_m to and from a single enhancer. Then, set k_{on_m} in the reactions of the form

$$A_I^{(i)} + T_m \xrightarrow{k_{\text{on}_m}} A_{I+e_j}^{(i)}$$

and k_{off_m} in the reactions of the form

$$A_I^{(i)} \xrightarrow{k_{\text{off}_m}} A_{I-e_j}^{(i)} + T_m$$

equal to $k_{\text{on}_1}^{(1)} - nd_1^{(m)}$ and $k_{\text{off}_1}^{(1)} + nd_2^{(m)}$ respectively for some positive constants $d_1^{(m)}$ and $d_2^{(m)}$. Lastly, repeat these steps for all values of m. The same reasoning can be applied when designing superadditive systems but the signs in the equations of binding rate modulation need to be flipped, that is, use instead $k_{\text{on}_1}^{(1)} + nd_1^{(m)}$ and $k_{\text{off}_1}^{(1)} - nd_2^{(m)}$ for modifying the corresponding binding rates. These procedures were implemented for all the models in Figure 3.3A and the resulting transcriptional noise and fidelity for these modified models was plotted in Figures 3.7 and 3.9. All calculations and simulations were done using MATLAB 2016b under GCC C/C++ 4.9 in conjunction with the CERENA toolbox [6]. The code is available at `https://github.com/WunderlichLab/TheoreticalEnhancerModels.git`.

Chapter 4

Non-cooperative mechanism for bounded and ultrasensitive chromatin remodeling

Material in this chapter is adapted from a manuscript by Alvaro Fletcher, Ruonan Zhao, and German Enciso [3].

4.1 Introduction

Chromatin remodeling is used by many organisms as an important form of gene regulation, expanding or compacting DNA to allow or prevent access to genetic regions. Chromatin changes between high and low density states respectively known as heterochromatin and euchromatin, with high density heterochromatin typically silencing gene expression. The boundaries between these regions have been observed to be sharp, and their disruption has been associated with conditions such as growth defects [26, 27].

Much experimental progress has been made in understanding the regulation of sharp boundaries between euchromatin and heterochromatin [121, 122, 123, 124]. On the modeling side, previous work on transitions between chromatin states has mostly relied on cooperative assumptions to obtain ultrasensitive transitions [125, 28, 126, 11].

Erdel et al. [127] showed that a non-cooperative looping model was able to create an extended domain of modified nucleosomes. This model makes use of the contact probabilities between two chromatin segments to determine the rates of histone modification. However among models of ultrasensitive behavior, cooperativity or allostery is usually assumed. For instance, work by Sneppen et al. [11] modeled cooperative histone modifications, and it is ultrasensitive but potentially subject to uncontrolled chromatin expansion beyond the intended boundaries of gene expression. In order to correct for this, more recent work [128] accounts for spatially bounded chromatin remodeling through the introduction of silencer elements and barriers. Modeling work by Mirny [28] includes allosteric binding of transcription factors which sterically hinders DNA interactions. Additional work includes models of bounded chromatin modification, such as [127, 129, 130] in which nearest neighbor interactions are used in a cooperative manner, and the work by Jost and Valliant [131] in which long range interactions are considered for chromatin expansion. For instance, Hodges et al. [129] focus on the bounded nature of modifications with nucleation, nearest neighbor cooperativity, and first-order turnover.

In this work, we present an alternative non-cooperative model that produces sharp spatial bounds and ultrasensitive transitions in response to transcription factors. This approach has the added advantage of not requiring silencer elements or barriers to prevent uncontrolled chromatin expansion. We will operate under the hypothesis that histone modifications are independent from one another. In other words, our model assumes that the modification of any one histone does not influence the rate of modification for any other histone. Our model has the potential to complement cooperative models, and it can be particularly helpful in

circumstances where experimental data indicate a lack of cooperativity.

Unlike Erdel et al. [127], our non-cooperative approach relies on the acetylation range of HAT proteins [132] and emergent properties of the chromatin architecture. The chromatin boundaries remain sharp even without the involvement of barrier proteins, and no uncontrolled expansion is possible beyond the regulated regions. Moreover, a single HAT protein bound at a DNA site can make accessible hundreds of DNA base pairs, a longer range of interaction than steric transcription factor binding. Two mechanisms allow for this in our model, namely percolation effects and multisite histone tail modifications.

To develop an intuition for the concept of percolation, consider a body of water being pushed under pressure through porous soil. The water will flow from the top to the bottom of the soil only if there are sufficiently many connected pores to form a path. As the prevalence of pores inside the soil increases, it is well known that the probability for a path increases in an ultrasensitive manner [29]. That is, a small increase in the pore prevalence can lead to a large increase in the probability of water flow.

The chromatin, despite having a high number of close range interactions, has yet to be studied in the context of percolation to the best of our knowledge. Unlike the soil, the presence of linker DNA between the nucleosomes implies that there is always a path between the two ends of the DNA. To address this issue, we turn to measuring the length of the shortest such path under different levels of acetylation. We show that the ultrasensitivity derived from the percolation analysis is conserved by using this measurement. Hence, in a similar way to the percolation in the soil, the first few nucleosome acetylation events in a high density region of chromatin will have a limited effect. But once the acetylation events reach a critical number, they can suddenly lead to a large expansion of the chromatin.

Levels of ultrasensitivity were further increased by multisite effects at the level of histone tail modification. Each nucleosome has eight different histones and at least eight histone

tails, some of which in turn may have multiple acetylation sites. While each acetylation may increase the tendency for nucleosomes to detach from the chromatin, we assume that a sufficient number of acetylation events must take place between two nucleosomes before their interaction is affected. This mechanism is based on work of Wang et al. [30] in the context of multisite protein phosphorylation but applies equally well in this different system. Ultrasensitivity is increased once again without the need to assume cooperative interactions between the histone tails, although such interactions could further increase ultrasensitive responses.

We also include a comparison with an experimental system involving histone acetylation inhibitor drug mitoxantrone. By including additional reactions in our mathematical model to account for the presence of this inhibitor, we were able to closely reproduce the experimental dose response relation. A high Hill coefficient of 3.8 indicates that this system is ultrasensitive, and we postulate that this behavior may be due to the effects described above.

We begin with Section 4.2 by providing background on chromatin architectures and the role of histone acetylation in chromatin remodeling. In Section 4.3.1, we describe in more detail on how we represented chromatin as a graph. In particular, we define the shortest path from one end of DNA to the other as a proxy to measure chromatin density. Section 4.3.2 introduces the idea of percolation and its relationship to the model. In Section 4.3.3 we outline the multisite assumptions for nucleosome interactions and demonstrate the ultrasensitive relation between the probability of acetylation and DNA accessibility. In Section 4.4 we display the activity domain of a HAT protein [132] and the results of incorporating such data into the model. Section 4.5 constructs a reaction network in order to derive the probability of histone acetylation from a transcription factor input. Section 4.6 calculates an ultrasensitive response in chromatin accessibility as a function of transcription factor concentration. In Section 4.7 we examine the ultrasensitivity of the transcription factor dose response for different model parameters. Lastly, in Section 4.5 we reproduce data measured experimentally for a similar

system involving inhibitor drug mitoxantrone.

4.2 Biological Background

The eukaryotic nucleus accommodates large amounts of DNA by packaging it into a form known as chromatin, which can have different levels of density. DNA is usually wrapped around histone octamers forming structures known as nucleosomes. When DNA is tightly packed around the nucleosomes it forms a dense version of the chromatin known as heterochromatin or 30 nm chromatin fiber, named after its diameter when observed under an electron microscope [133]. For a region of DNA to be actively expressed, the corresponding chromatin region usually needs to be loosened into a lower density state known as euchromatin or 10 nm chromatin fiber. While the shape of the 10 nm fiber is well-characterized to the point that it has been described as "beads-on-a-string" [134], it still remains unclear what shape the chromatin takes as a 30 nm fiber when it is compact and the corresponding DNA regions are silenced [135].

The existence of the 30 nm chromatin structure has been disputed ([136, 137, 138, 139, 140, 141]), and it has been theorized that 30 nm fibers could consist of an irregular pattern of interdigitated 10 nm fibers [142]. Recent research studying gene regulation has uncovered an important role for so-called *enhancers*, which are segments of DNA that regulate genes located outside of the promoter DNA region. In many cases these enhancer regions regulate their targets by being physically located near the promoter in their 3D structure. This indicates that the 3D chromatin structure might be highly regulated and conserved. The presented work can easily be extended to such a situation, by defining a 3D chromatin structure interaction graph. Several other models for the shape of the 30 nm fiber have been proposed, among them the solenoid model and the zig-zag model which themselves can be modified to form different kinds of models [31, 143].

It has been hypothesized that heterochromatin is able to remain compact due to interactions between neighboring nucleosomes [144]. In particular, it is thought that the histone tails, which extend from the nucleosome center, are able to interact with other histone tails, enabling communication between nucleosomes that are far apart relative to their position in the DNA [145, 146]. Therefore, nucleosomes are partially reliant on the state of their neighbors for maintaining a particular state of chromatin compaction under certain conditions.

One condition that determines the presence of nucleosome interactions is the acetylation of the histone tails. Acetylation can weaken the attraction between the positively charged histones and the negatively charged DNA, thereby breaking nucleosome bonds, loosening the chromatin, and facilitating the transition from heterochromatin to euchromatin [147, 148, 149, 150, 151]. Once euchromatin is present, the regulatory elements of transcription can more easily bind to the DNA and start the production of mRNA [152]. This way, high levels of acetylation around a gene locus are thought to facilitate transcription.

Transcription is regulated to take place at specific regions in order to prevent uncontrolled global expression of the DNA. This is possible because of transcription factors which selectively bind to chromatin regions that need to be decompressed [153, 154]. These transcription factors, once bound to the DNA, recruit histone acetyltransferases (HATs) which then proceed to acetylate histone tails [155]. This way, only regions that have a specific transcription factor binding site will be capable of being decompressed and subsequently expressed (Figure 4.1).

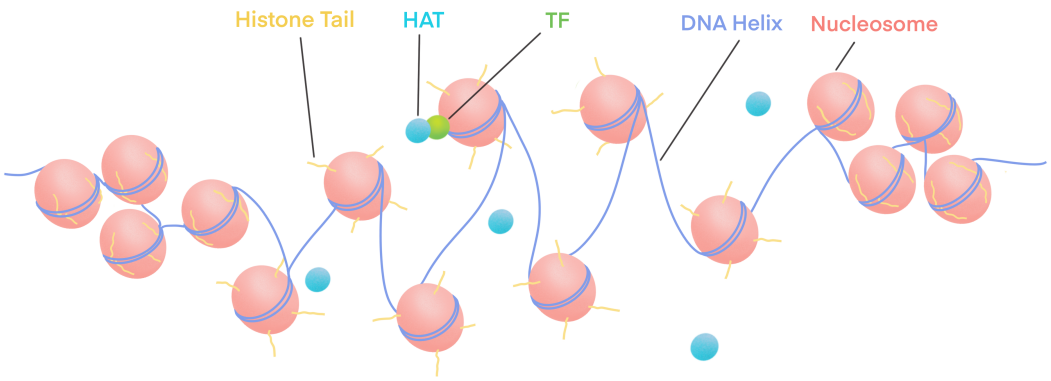

Figure 4.1: HAT proteins are recruited by site-specific transcription factors (TFs). Once bound to the chromatin, HAT proteins acetylate nearby histone tails, which can lead to chromatin decompression.

4.3 Chromatin Model

4.3.1 Chromatin as a graph

For a mathematical description of the chromatin, we create a 2D graph of nucleosomes connected by linker DNA and capable of nucleosome interactions, which aims to capture the 3D structure of different chromatin architectures. The nucleosomes are depicted as red nodes while the linker DNA and the nucleosome interactions are shown as black and green edges in Figures 2b and 2d. Importantly, acetylation events tend to *reduce* the presence of green edges.

We use two alternative chromatin structures for our analysis, the so-called *interdigitation* (Figure 4.2a) and *solenoid* (Figure 4.2c) models. We choose the solenoid model since it is perhaps the best-known chromatin model. Moreover, we also use an interdigitation model because of its simplicity and because it is not a traditional 30 nm model. The latter point is important since the existence of 30 nm fibers *in situ* has been disputed [136, 138, 137, 139, 140, 141] and the interdigitation model as an arrangement of 10

nm fibers has been proposed as one of the alternatives to the 30 nm fibers. We note, however, that our approach can be generalized to any chromatin model by simply changing the structure of our graph to describe the interactions among histones, even in a non-uniform fashion.

The nucleosomes in both models have distinct conformations, and each nucleosome has a different set of neighbors. The interdigitation model describes a chromatin where nucleosomes are arranged in a shape similar to the fingers of two hands being interlocked. In the solenoid model, nucleosomes are arranged in a 3D spiral shape. Each of these topologies determines which nucleosome interactions are possible and consequently affects the rate of transitions between chromatin density states.

Given a graph with a particular set of nucleosome interactions, an important problem is to quantitatively measure the overall chromatin density, which inversely correlates with gene activation levels. We estimate chromatin density by calculating the length of the *shortest path* from one end of the DNA sequence to the other, also known as the diameter of the graph. For example, consider an interdigitation graph with nodes arranged in n rows and m columns. If n is even, the length of the shortest path would be $n - 1$ under no acetylation (all green edges present). Meanwhile if n is odd, the length of the shortest path when all edges are present is $n - 1 + m - 1$. On the other hand, under complete acetylation (no green edges present), the shortest path is the length of the entire DNA sequence, that is $nm - 1$, regardless of the parity of n. Note that highly acetylated chromatin (euchromatin) will correspond to larger diameters since nucleosome interactions will be less abundant. On the other hand, non-acetylated chromatin (heterochromatin) will correspond to smaller diameters since nucleosome interactions will be more abundant.

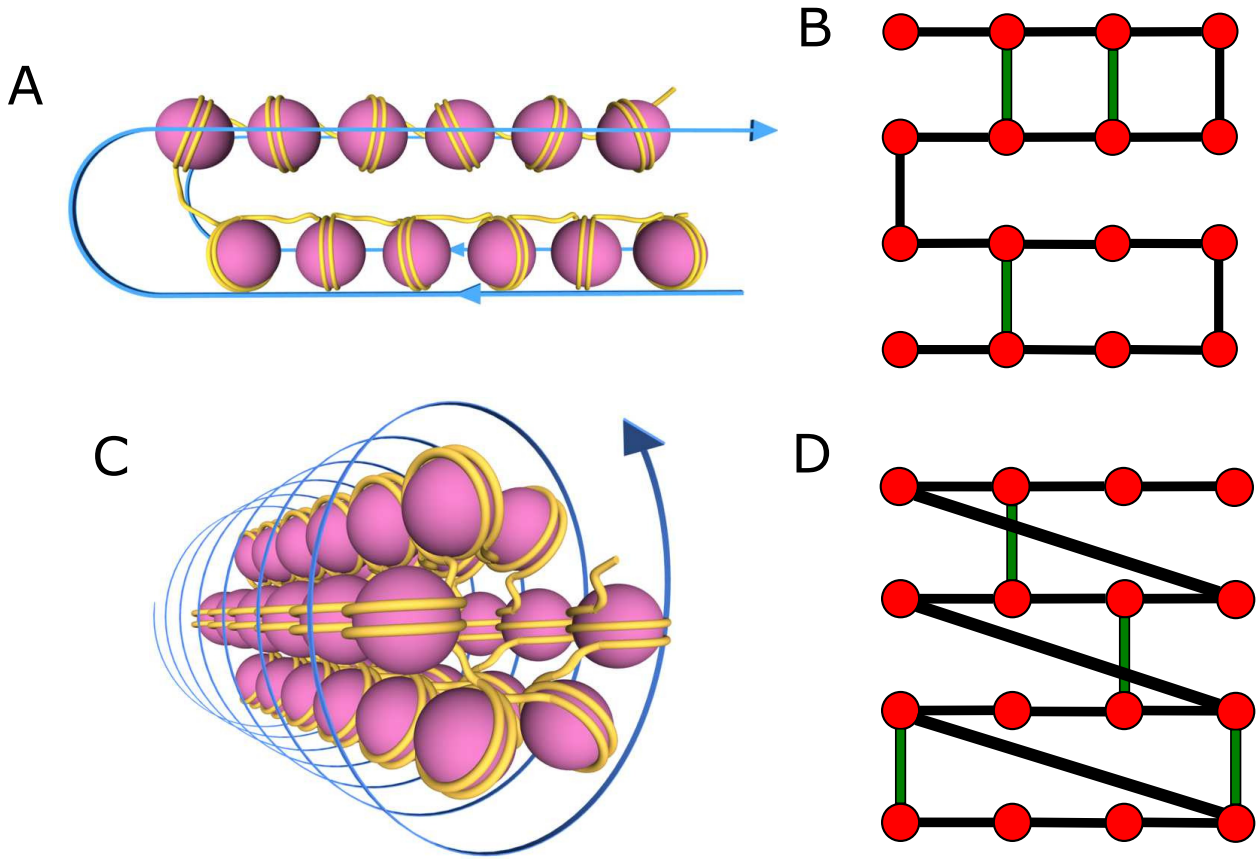

Figure 4.2: (A) The interdigitation architecture has been proposed to describe the 30 nm chromatin structure. Nucleosomes can interact with their neighbors depending on their level of acetylation. (B) Interdigitated DNA represented using an abstract graph. Red nodes correspond to nucleosomes, black edges to linker DNA, and green edges to nucleosome interactions. The shortest path between the two ends of the DNA (DNA diameter) provides a convenient way to estimate chromatin density. (C) Solenoid chromatin architecture. (D) Representation of the solenoid architecture using a similar graph and notation as in (B).

4.3.2 Percolation Theory

Consider water flowing through the soil to an unconfined aquifer (Figure 4.3a). The water flows through passages until it reaches the aquifer. To capture this behavior, we can represent the soil as a two-dimensional graph where the edges between nodes correspond to water passages between two different locations (Figure 4.3b). From such a graph, one can determine if a path exists from the top row to the bottom row and determine the shortest path between these two rows.

We generalize the graph in Figure 4.3b by considering a grid with 9 rows and 5 columns. Suppose that each edge between two neighboring nodes (vertical or horizontal) is present with a given probability, independently of each other. Probabilities with high values can be expected to lead to more edges and highly interconnected graphs while low probabilities can be expected to create few edges and poorly connected graphs. Such an experiment can be repeated for distinct probabilities and, for each unique probability, the existence of a path from the top row to the bottom row is recorded (Figure 4.3c).

In the percolation problem of the soil, a path may or may not exist, depending on the distribution of pores within the soil. However, our chromatin architecture always has a path from the top row to the bottom row, which is guaranteed by the presence of linker DNA. As a consequence, the model of the soil differs from our chromatin architecture. Thus, we want to use a new metric to describe our problem of chromatin expansion. In order to resolve this problem, we turn our attention to the diameter of the graph as defined in the previous section. We show below that if the probability of path existence is replaced with a measurement of the mean graph diameter, then the same ultrasensitive response is preserved.

For the same random graph as above, the mean shortest path length is calculated after several simulations for a fixed edge probability. We use a procedure known as *Dijkstra's algorithm* to quickly compute the shortest path [156]. If no path existed, then we record the

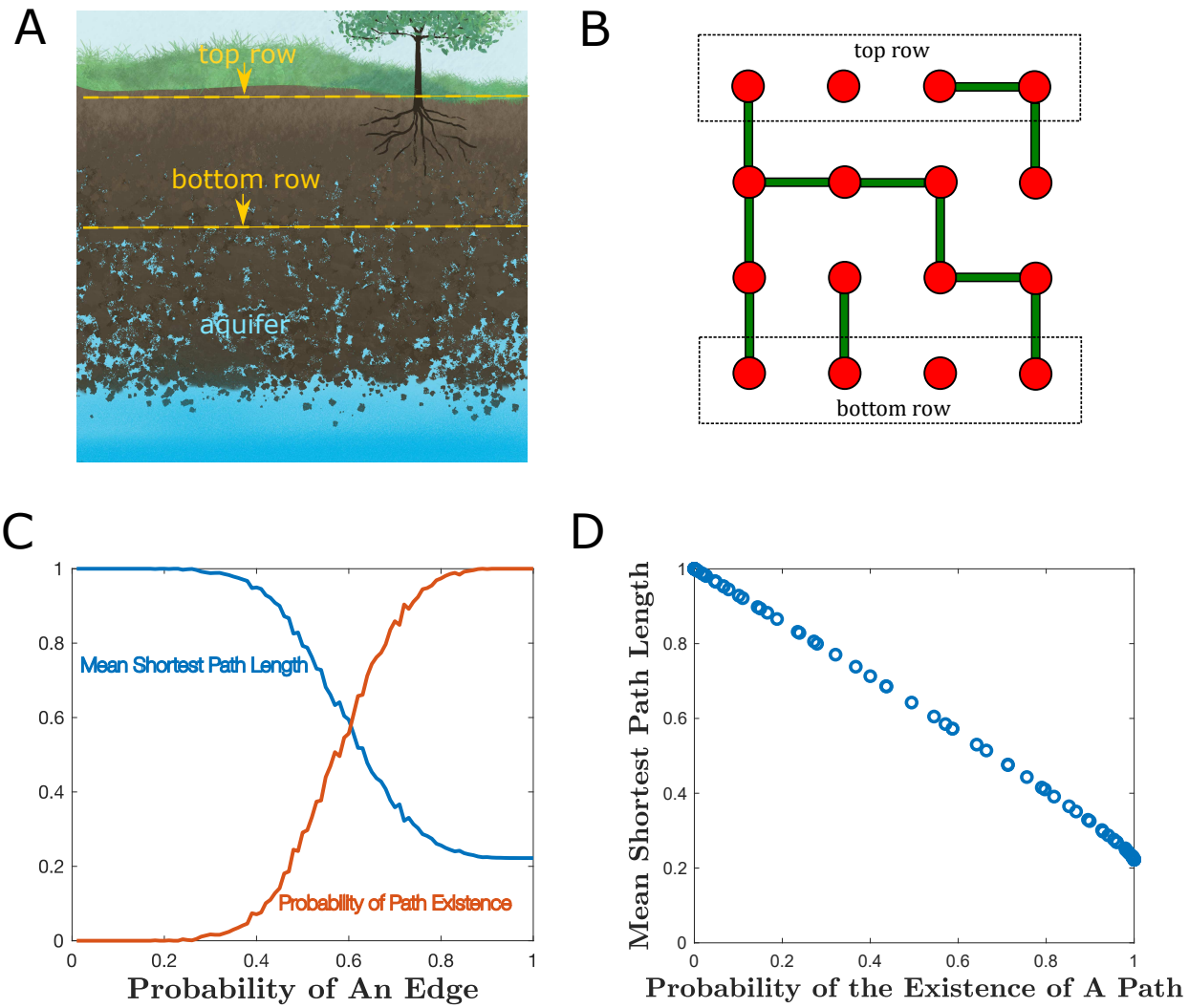

Figure 4.3: (A) Water flows from the soil surface to an aquifer through passages in the soil. (B) A graph representation of the soil where water passages are shown as edges between nodes. In this case there exist two paths from the surface (top row) to the aquifer (bottom row), and the shortest path has length 3. (C) Normalized mean shortest path lengths and probabilities of path existence for a 9×5 graph. Each data point is calculated using 1000 independent simulations for each edge probability. (D) The relationship between mean shortest path lengths and the probability of path existence.

length of the longest possible path (36 in this case).

This is akin to the chromatin graphs in Figure 4.2 where having no edges implies the longest path is the diameter of the graph. After normalizing path lengths to 1, they are plotted alongside the probability of path existence as in Figure 4.3c.

Notice that both of the graphs in Figure 4.3c observe an ultrasensitive behavior. It has been proved in the literature that as the size of a square grid grows, the probability of path existence becomes increasingly and arbitrarily ultrasensitive [29].

In Figure 4.3d we plot the mean shortest path length and the probability of path existence in the same graph. Notice that there appears to be a linear relationship between the two. Indeed, suppose M, Q are the mean shortest path length and the probability of path existence, respectively. The formula $M = 1 - aQ$ would imply that if one of these two functions is ultrasensitive as a function of edge probability, then so is the other.

4.3.3 Formation of Nucleosome Interactions

Nucleosomes can form interactions between them, shown as green edges in Figures 2b and 2d. We assume that nucleosomes placed diagonally from each other cannot interact, and nucleosomes placed horizontally from each other are already connected by linker DNA (black edges). Therefore, only vertical neighbors are allowed to form nucleosome interactions.

In the text below we define the concept of nucleosome receptiveness, which broadly speaking means that a nucleosome has a limited number of acetylated sites. Any two neighboring nucleosomes are then joined by a green edge if and only if both of the nucleosomes are receptive.

We assume that there are s acetylation sites in each nucleosome, and we define the nucleosome

to be *receptive* if at least k out of these s sites were non-acetylated. We set $s = 8$ since there are eight histones in every nucleosome, and we thought of each histone as having one acetylation site in its tail. In reality, the number of acetylation sites in a nucleosome could be higher as multiple sites have been identified in the H4, H3, H2A, and H2B histones [157, 158]. To account for this variability, the model can be given any positive number of sites s depending on the system being modeled.

Define p to be the probability of acetylation of a given histone site. Unlike in cooperative models, we assume here that histone acetylations are independent from each other. Therefore, the number W of non-acetylated histone sites in a nucleosome has a binomial distribution, and the probability of a nucleosome being receptive can be calculated as

$$\begin{aligned} P(W \geq k) &= P(W = k) + P(W = k+1) + ... + P(W = s), \\ &= \sum_{i=k}^{s} \binom{s}{i} q^i p^{s-i}, \end{aligned} \tag{4.1}$$

where $q = 1 - p$. We also set $k = 4$, which is consistent with previous work on multisite modification systems where the probability of transition to another state is given by equation (4.1) [30]. This work showed that the ultrasensitivity of the resulting dose response was maximized for $k \approx s/2$. Hence, only when sufficient histone sites are not acetylated as given by equation (4.1) does a nucleosome become receptive and is able to form green edges with its receptive neighbors. Note that the number of acetylation sites is the same for all nucleosomes, and it is therefore independent of the number of neighboring nucleosomes.

There is experimental evidence in support of this set of assumptions. Durrin et al [159, 160] considered different acetylation sites in the tail of histone H4, and when any one of these sites was shut down (by replacement of the lysine residue with arginine which mimics the nonacetylated state), no significant effect was measured in gene expression. However when

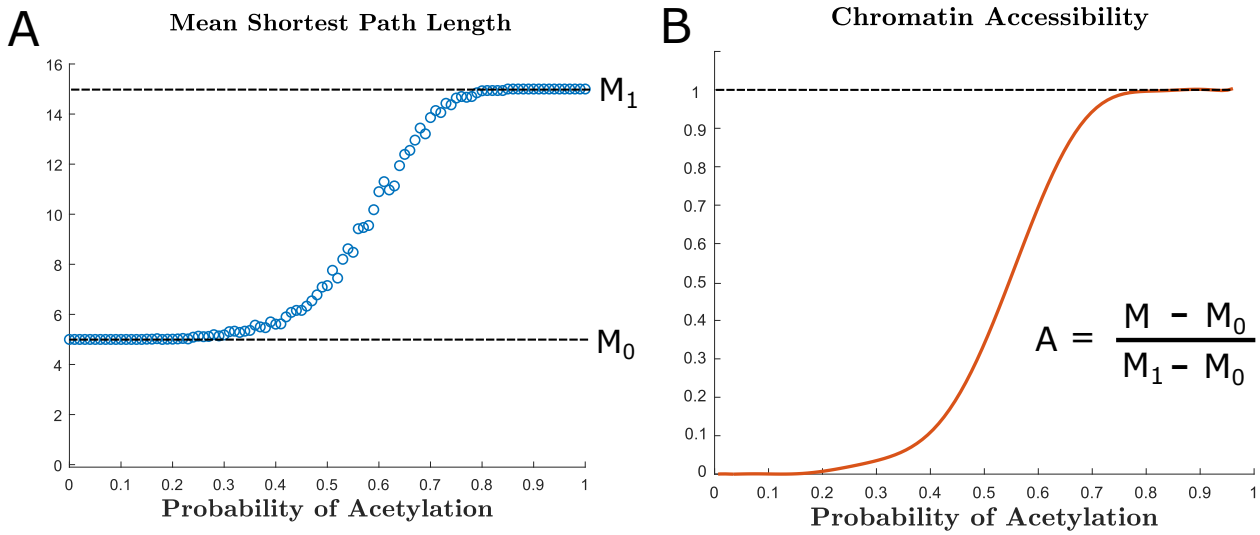

Figure 4.4: The mean shortest path length is calculated as a function of the acetylation probability p using a 4×4 solenoid DNA structure as in Figure 4.2d. Mean shortest path lengths were calculated from 100 independent simulations for each value of p, and this data was fitted with a polynomial function. Chromatin accessibility was estimated by vertical translation of this graph.

three or four sites were eliminated in this way, gene expression was significantly decreased. This experiment effectively estimated the number $k = 4$ of nonacetylated sites that are necessary and sufficient to make a histone receptive in our context. If $s = 8$ and $k = 4$, then replacing e.g. two lysine residues with arginine facilitates making a nucleosome receptive, in effect lowering the values of s and k to $s = 6$ and $k = 2$.

Under these conditions, we simulate the acetylation of a 4×4 solenoid graph as shown in Figure 4.2d. The mean shortest path length for several probabilities of acetylation p are calculated and plot in Figure 4.4a. Once p surpasses an apparent threshold, the mean shortest path length quickly shifts from its minimum value to its maximum value. Hence, we expect that the chromatin will exhibit some degree of bimodality as the conditions for p vary.

To describe the relationship between mean shortest path length and chromatin accessibility, notice that more nucleosome interactions generally lead to less chromatin accessibility. But chromatin accessibility is not merely determined by the number of interactions, since inter-

actions could be clustered around a single small region of the DNA. A better measure of how accessible the DNA is would include the number of interactions as well as their distribution, which is described by the graph diameter. Also, if the nodes of a given 2D interaction graph were allowed to expand by diffusion, the graph diameter would indicate how widely the graph can spread. This is similar to the situation in the chromatin, which is constantly subject to diffusion by Brownian motion.

Following the reasoning above, we can provide a formula to calculate the accessibility of the chromatin by transcriptional enzymes using the mean shortest path lengths. First, note that, for $p = 0$, the shortest path length is equal to 5 as shown in Figure 4.4. This corresponds to chromatin that is fully compact and has interactions between all nucleosome neighbors. This chromatin has minimal accessibility and we can assign it a value of 0 to denote this. We assume a linear mapping between mean shortest path length and chromatin accessibility, and we derive a relationship between them as follows. Let M be the mean diameter (that is the mean shortest path length), M_0 the minimum diameter, and M_1 the maximum diameter. Then the chromatin accessibility A can be described with the formula $A = (M - M_0)/(M_1 - M_0)$. This amounts to vertically translating and normalizing the mean shortest path length graph in Figure 4.4a. The resulting graph in Figure 4.4b shows chromatin that has an accessibility range from 0 (minimally accessible) to 1 (fully accessible) when $p = 0$ and $p = 1$, respectively.

4.4 Spatially-bounded Chromatin Density Regions

To understand the range of acetylation for HAT proteins, we refer to work by Vignali et al. [132] which studied the SAGA and NuA4 HATs found in *Saccharomyces cerevisiae*. They consider an *in vitro* assay with DNA bound to unacetylated histones, which they stimulate with HAT molecules. They show that HAT proteins only operate in the presence of transcrip-

tion factors such as Gal4-VP16. In order to determine the location and extent of histone acetylation along the DNA, they use a ChIP assay with antibodies specific to acetylated histones.

Importantly, they found that stimulation by transcription factor Gal4-VP16 results in characteristic distributions of acetylated histones, i.e., that SAGA and NuA4 acetylate the nucleosomes in their vicinity with differing probabilities (Figure 4.5a). In the case of SAGA, the probability of acetylation decreases as the distance from the HAT binding site increases. We can use this information together with the data in Figure 4.4b in order to calculate the chromatin accessibility as a function of base pair location (Figure 4.5b). To do this, we simply compose the probability of acetylation for SAGA in Figure 4.5a with the function in Figure 4.4b. In other words, letting chromatin accessibility in Figure 4.4b be denoted by $f(p)$ and the probability of acetylation p be given by Figure 4.5a such that $p = g(b)$ for any base pair location b. Then, Figure 4.5b would be given by $f(g(b))$.

The ultrasensitivity of the function in Figure 4.4b is conserved in this composition where it creates sharp boundaries between regions of heterochromatin and euchromatin. These results suggest how a single HAT can decompress a region of the chromatin while maintaining sharp boundaries in accessibility between chromatin regions. Such accessibility peaks have been recorded experimentally under certain conditions and the ranges of chromatin expansion are similar to that of our simulated data [2]. An example of this behavior is shown in Figure 4.5c from Wang et al. [2]. This study performed ATAC-seq on cells from APP/PS1 mice models to measure their chromatin accessibility. The resulting average peaks happen to also be approximately 2000 bp long and in some cases define clear regions of expansion with sharp boundaries.

Whenever multiple transcription factor binding sites are present, a histone site can potentially be acetylated by one of multiple SAGA proteins. In order to model the effect of multiple sites interacting with each other, we make the assumption that each bound SAGA acts upon

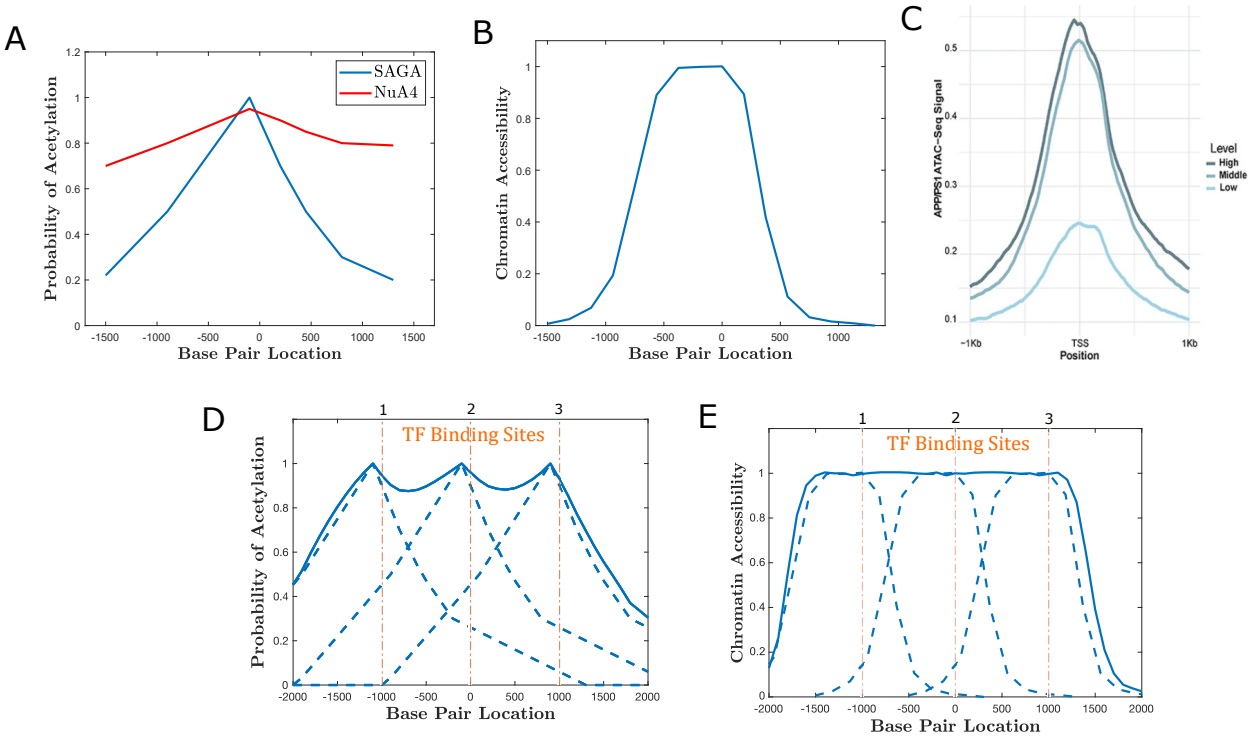

Figure 4.5: (A) Data from Vignali et al. [132] showing the percentage of acetylated histones at each base pair location relative to the binding site of the SAGA and NuA4 HAT proteins. (B) Chromatin accessibility calculated from a single bound SAGA protein as a function of base pair location, using (A) and the accessibility data from Figure 4.4b. (C) ATAC-seq data from APP/PS1 mice as part of an analysis on chromatin accessibility in Alzheimer's disease [2].(D) Probability of being acetylated by at least one of three bound SAGA proteins at a given base pair location (solid line). The probabilities of acetylation from individual SAGA proteins are marked in dashed lines. Binding sites are separated by 1000 base pairs each. (E) Levels of chromatin accessibility resulting from three bound SAGA proteins (solid line), calculated using data from (D) and Figure 4.4b. Levels of accessibility resulting from individual bound SAGA proteins are marked using dashed lines.

histones independently of other bound SAGA proteins. Given three separate binding sites, the probability of a histone site being acetylated by at least one of the three bound SAGA proteins is equal to $1-(1-p_1)(1-p_2)(1-p_3)$, where $p_i = g_i(b)$ corresponds to the probability of being acetylated by the SAGA protein at the i-th binding site (Figure 4.5D). Moreover, when multiple SAGA are bound, a larger region of the chromatin can be decompressed. Specifically, the accessibility is now given by $f(1-(1-g_1(b))(1-g_2(b))(1-g_3(b)))$. If transcription factor binding sites are not too far apart, then a large single region is created that has consistently high accessibility and a sharp boundary with the rest of the chromatin (Figure 4.5e). Each of the functions in this figure is calculated by composing the corresponding function in Figure 4.5d with the function f above.

4.5 Chemical Reaction Network

To estimate the probability p of histone acetylation as a function of transcription factor concentrations, we construct a chemical reaction network that describes a simplified version of this process. Denote T to be an abstract representation of a transcription factor. T binds to a piece of DNA denoted by D to form complex C_1. Once C_1 is present, it proceeds to recruit a HAT (denoted by H) and forms complex C_2. A non-acetylated histone site S can be acetylated into A by interacting with C_2. Acetylated sites spontaneously go back to being non-acetylated at a fixed rate, in effect by assuming a constant background amount of histone deacetylase (HDAC) that is not explicitly modeled in this system. The reaction network can be summarized as in Figure 4.6a.

This system uses kinetic rate parameters $k_1, k_2, k_{-1}, k_{-2}, \alpha, \beta$ as described in the reactions, with values shown in the Methods section. The system also has total protein concentrations which do not change over time, such as the total concentration of histone sites $S_{\text{tot}} = S + A$ and the total transcription factor $T_{\text{tot}} = T + C_1 + C_2$, as well as D_{tot} and H_{tot}.

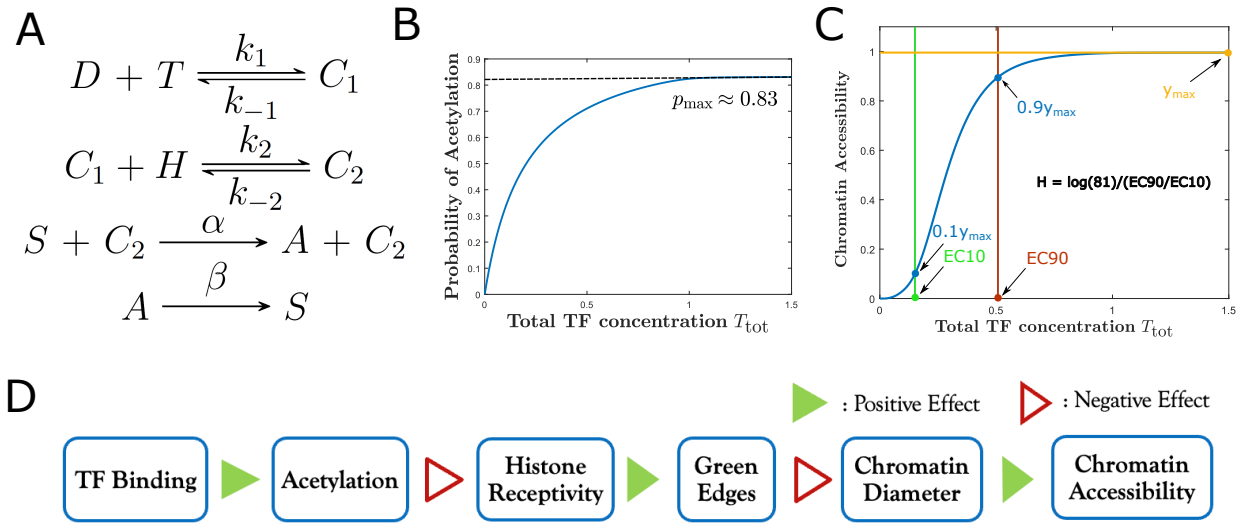

Figure 4.6: (A) Chemical reactions describing HAT forming a complex with DNA and transcription factor, and reversible histone acetylation. (B) Probability of acetylation p calculated as a function of total TF concentration T_{tot}. (C) Modeled relationship between total transcription factor and levels of chromatin expansion, using (A) and data from Figure 4.4b. Here $k_1 = 1$, $k_2 = 1$, $\alpha = 1$, $k_{-1} = 0.2$, $k_{-2} = 0.2$, $\beta = 0.2$, $D_{\text{tot}} = 1$, $H_{\text{tot}} = 16$, $D_0 = D_{\text{tot}}$, $S_0 = S_{\text{tot}}$, $H_0 = H_{\text{tot}}$, and $T_0 = T_{\text{tot}}$. (D) Summary diagram of the different variables involved in the model, from transcription factor binding input to chromatin accessibility output.

We model this system deterministically using mass action kinetics [161]. Under nonzero initial conditions, the network eventually converges to a steady state of nonzero acetylated and nonzero non-acetylated histone sites. Therefore, we can calculate the probability of acetylation for a histone site. First, we compute the steady state of acetylated sites which turns out to be

$$\begin{aligned} A &= \frac{S_{\text{tot}} k_1 k_2 \alpha DTH}{k_1 k_2 \alpha DTH + k_{-1} k_{-2} \beta}, \\ &= \frac{S_{\text{tot}} DTH}{DTH + K}, \end{aligned}$$

where $K = k_{-1}k_{-2}\beta/(k_1 k_2 \alpha)$. Then, dividing A by the total number of sites S_{tot} yields the probability of acetylation at the steady state

$$p = \frac{A}{S_{\text{tot}}}. \tag{4.2}$$

We will calculate the value of p as a function of total concentrations and rate parameters in section 4.5.1.

4.5.1 p as a function of total concentrations and rate parameters

We wish to show that p in equation (4.2) depends only on rate constants and total concentrations. First note that the chemical reaction network in section 4.5 can be written by mass-action kinetics as

$$\begin{cases} \frac{dT}{dt} & = k_{-1}C_1 - k_1 DT \\ \frac{dD}{dt} & = k_{-1}C_1 - k_1 DT \\ \frac{dC_1}{dt} & = k_1 DT - k_{-1}C_1 - k_2 C_1 H + k_{-2}C_2 \\ \frac{dC_2}{dt} & = k_2 C_1 H - k_{-2}C_2 \\ \frac{dS}{dt} & = \beta A - \alpha S C_2 \\ T_{\text{tot}} & = T + C_1 + C_2 \\ D_{\text{tot}} & = D + C_1 + C_2 \\ H_{\text{tot}} & = H + C_2 \\ S_{tot} & = S + A \end{cases} \tag{4.3}$$

At steady state,

$$\begin{cases} k_1 DT & = k_{-1}C_1 \\ k_2 C_1 H & = k_{-2}C_2 \\ \beta A & = \alpha S C_2 \end{cases} \quad \text{or} \quad \begin{cases} K_1 DT & = C_1 \\ K_2 C_1 H & = C_2 \\ K_3 S C_2 & = A \end{cases},$$

where $K_1 = k_1/k_{-1}$, $K_2 = k_2/k_{-2}$, and $K_3 = \alpha/\beta$. By mass conservation laws in (4.3),

$$\begin{aligned} D &= D_{\text{tot}} - (C_1 + C_2) \\ &= D_{\text{tot}} - (T_{\text{tot}} - T) \\ &= T - Q_1, \end{aligned} \tag{4.4}$$

where $Q_1 = T_{\text{tot}} - D_{\text{tot}}$. We can then perform the appropriate substitutions in the expression for T_{tot} to obtain

$$\begin{aligned} T_{\text{tot}} &= T + C_1 + C_2 \\ &= T + K_1 DT + K_2 K_1 DTH. \end{aligned} \tag{4.5}$$

If $C_2 \leq D_{\text{tot}}$ and D_{tot} is much less than H_{tot}, then C_2 is much less than H_{tot}, and thus

$$H = H_{\text{tot}} - C_2 \approx H_{\text{tot}}.$$

Then, by (4.5),

$$\frac{T_{\text{tot}}}{T} \approx 1 + D(K_1 + K_1 K_2 H_{\text{tot}}) = 1 + (K_1 + K_1 K_2 H_{\text{tot}})(T - Q_1). \tag{4.6}$$

Let $f_1(T) = T_{\text{tot}}/T$, and $f_2(T) = 1 + (K_1 + K_1 K_2 H_{\text{tot}})(T - Q_1)$. We show that there is a unique positive solution for T in (4.6).

First note that f_1 is a decreasing function for $T > 0$. Also, the function f_2 is a straight line with slope $K_1 + K_1 K_2 H_{\text{tot}} > 0$. Therefore, f_1 and f_2 have a single intersection which corresponds to a unique, positive solution for T. From equation (4.6), we can write

$$(K_1 + K_1 K_2 H_{\text{tot}})T^2 + (1 - K_1 - K_1 K_2 H_{\text{tot}})Q_1 T - T_{\text{tot}} = 0,$$

and solving for T yields

$$T = \frac{((K_1 + K_1K_2H_{\text{tot}}) - 1)Q_1 \pm \sqrt{(1 - (K_1 + K_1K_2H_{\text{tot}}))^2Q_1^2 + 4(K_1 + K_1K_2H_{\text{tot}})T_{\text{tot}}}}{2(K_1 + K_1K_2H_{\text{tot}})}.$$

Since T has a unique, positive solution and

$$\begin{aligned}((K_1 + K_1K_2H_{\text{tot}}) - 1)Q_1 &\leq |((K_1 + K_1K_2H_{\text{tot}}) - 1)Q_1| \\ &= \sqrt{(((K_1 + K_1K_2H_{\text{tot}}) - 1)Q_1)^2} \\ &\leq \sqrt{(1 - (K_1 + K_1K_2H_{tot}))^2Q_1^2 + 4((K_1 + K_1K_2H_{\text{tot}})T_{\text{tot}}},\end{aligned}$$

then it must be that

$$T = \frac{((K_1 + K_1K_2H_{\text{tot}}) - 1)Q_1 + \sqrt{(1 - (K_1 + K_1K_2H_{\text{tot}}))^2Q_1^2 + 4(K_1 + K_1K_2H_{tot})T_{\text{tot}}}}{2(K_1 + K_1K_2H_{\text{tot}})}.$$

Solving for A, we have that

$$A = K_3SC_2 = K_3K_2C_1HS = K_3K_2K_1DTHS,$$

which implies

$$\begin{aligned}A &= \frac{K_3K_2K_1DTH_{\text{tot}}S_{\text{tot}}}{1 + K_3K_2K_1DTH_{\text{tot}}} \\ &= \frac{\frac{\alpha}{\beta}\frac{k_2}{k_{-2}}\frac{k_1}{k_{-1}}DTHS_{\text{tot}}}{1 + \frac{\alpha}{\beta}\frac{k_2}{k_{-2}}\frac{k_1}{k_{-1}}DTH} \\ &= \frac{\alpha k_2k_1DTHS_{\text{tot}}}{\beta k_{-2}k_{-1} + \alpha k_2k_1DTH}.\end{aligned}$$

Therefore,

$$p = \frac{A^*}{S_{tot}} = \frac{\alpha k_2k_1DTH}{\beta k_{-2}k_{-1} + \alpha k_2k_1DTH}.$$

By substituting the above expressions for T, $D = T - T_{\text{tot}} + D_{\text{tot}}$ and $H \approx H_{\text{tot}}$ into the equation for p, we can obtain p as a function of parameters $k_1, k_{-1}, k_2, k_{-2}, \alpha, \beta, H_{\text{tot}}, S_{\text{tot}}, T_{\text{tot}}$.

4.6 Ultrasensitive Chromatin Remodeling

Using the chemical reaction formalism above, we can now write the probability of acetylation as a function of total transcription factor concentration. It is important to note that even when transcription factor is bound with very high frequency, the probability of acetylation depends on the balance between histone acetylation and histone deacetylation. In other words, in the limit as T_{tot} increases, the probability of acetylation does *not* converge to 1 in this system. If the value of p remains low even for very large T_{tot}, then chromatin will never decompress per Figure 4.4b.

In particular, whenever there is saturation of T and H, the values of D and C_1 become small enough so that $C_2 = D_{\text{tot}}$ and our chemical reaction network reduces to

$$S \underset{\beta}{\overset{D_{\text{tot}}\alpha}{\rightleftharpoons}} A.$$

Since there is a limited number of binding sites in a given chromatin region, we can expect that D_{tot} is small, and we set for simplicity $D_{\text{tot}} = 1$. Then, the steady of state of A at saturation of T and H can be written as

$$A_{\text{sat}} = \frac{S_{\text{tot}} D_{\text{tot}} \alpha}{D_{\text{tot}} \alpha + \beta} = \frac{S_{\text{tot}} \alpha}{\alpha + \beta}. \tag{4.7}$$

It is clear that, under these conditions, the rate of acetylation α, the rate of deacetylation β, and the total number of sites S_{tot} play the only role in determining the number of acetylated sites at steady state. Since $p_{\max} = A_{\text{sat}}/S_{\text{tot}}$, then α and β determine maximum value of

p when T and H are saturated. From this, we can choose $\alpha = 1$ and $\beta = 0.2$ to obtain $p_{\max} = 1/(1 + 0.2) \approx 0.83$. Under a fixed large value of H, p takes the shape in Figure 4.6b which in the limit of T_{tot} approximates our calculation of $p_{\max} \approx 0.83$ (see Methods for the other parameter choices). A large value of $p_{\max}$ implies that, for the function in Figure 4.4b, the chromatin will decompress for a large enough T_{tot}.

To determine ultrasensitivity of the mean shortest path length with respect to T_{tot}, we compose the functions in Figures 4b and 6b. The plot in Figure 4.6c shows an apparent ultrasensitive dose-response between total transcription factor concentration and chromatin expansion. To quantify these levels of ultrasensitivity, we use the Hill coefficient which in the case of Hill functions $x^n/(x^n + c)$ corresponds to the parameter n. The higher the value of n, the more ultrasensitive this function becomes. For general functions, such as that in Figure 4.6c, we can use the generalized definition of the Hill coefficient derived by Goldbeter and Koshland [162, 34] with the formula $\log(81)/(\log(EC90/EC10))$. Here EC10 and EC90 refer to the input concentrations that produce 10% and 90% of the maximal response, respectively. It can be shown that applying this formula to the function $x^n/(x^n+c)$, one obtains the original Hill coefficient n.

The Hill coefficient of the function in Figure 4.6c was calculated to be 3.7. Typically, Hill coefficients above 2 are characteristic of ultrasensitive responses [163]. This confirms that our modeled chromatin can give rise to ultrasensitive responses, thus preventing state transitions until a critical concentration of transcription factors is present.

To recapitulate how we arrived at this result, we summarize the entire process of acetylation leading to chromatin remodeling, which is also outlined in Figure 4.6d. First, for a given transcription factor concentration, determine the probability of acetylation using the given chemical reaction network (Figure 4.6a). This probability p is then used to calculate the probability that a nucleosome will be receptive in the chromatin graph (4.1). If two neighboring nucleosomes are receptive, then a green edge corresponding to a nucleosomal

interaction should be added between them. This yields a chromatin graph as those in Figure 4.2b from which a shortest path and associated chromatin accessibility can be derived. Repeating these steps for different amounts of T_{tot} ultimately gives a graph similar to the one in Figure 4.6c and the ultrasensitivity of the chromatin remodeling can be measured by taking the Hill coefficient of this graph.

4.6.1 Simulated HAT acetylation ranges

Recall that the rate α in our chemical reaction network describes the rate at which sites become acetylated. To replicate the experimentally measured acetylation profiles for the SAGA and NuA4 HAT proteins, we assumed that α decreases exponentially as a function of the distance from the HAT binding site. In particular we set

$$\alpha = \alpha_0 e^{-c|b|}, \tag{4.8}$$

where α_0 is the maximum value of α, c is a constant, and b is base pair location. The probability of acetylation p in equation 4.2 can then be calculated as a function of base pair location by appropriately changing the value of α. Plotting these values of p yields simulated acetylation profiles that resemble their experimental counterparts for SAGA and NuA4 (Figure 4.7).

4.7 Effects of s, k, and graph sizes on Hill Coefficients

We determine the sensitivity of the Hill coefficient to different parameter values by running multiple additional simulations. The parameters that we vary include the number of rows and columns of the DNA interaction grid, as well as the parameters s, k that determine the nucleosomal interactions.

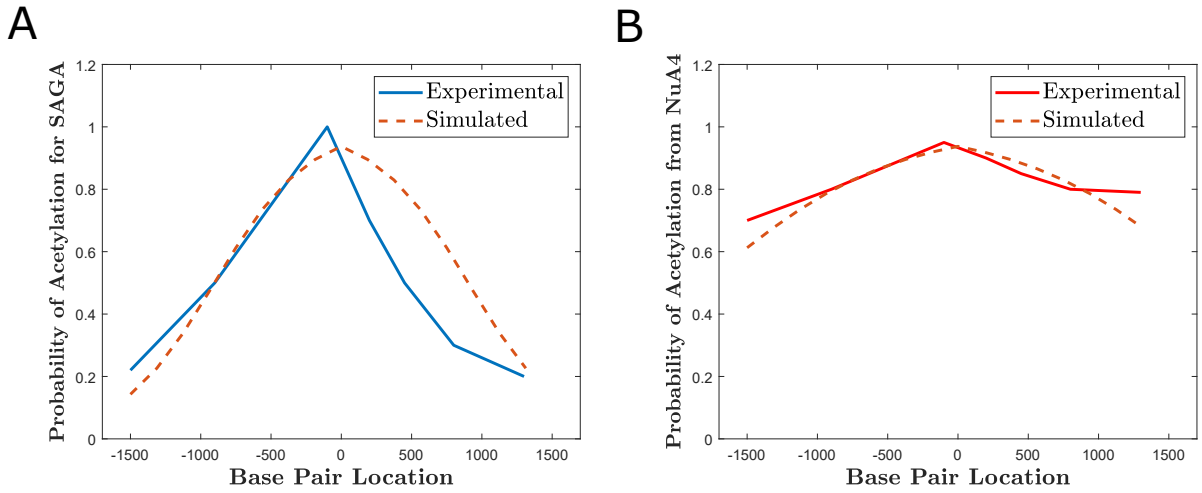

Figure 4.7: Probabilities of acetylation with respect to base pair location for rates of acetylation α that decrease exponentially from the HAT binding site. Under these conditions, simulated HAT acetylation profiles can be made to resemble their experimental counterparts. Different exponential rates were enough to account for the differences between the SAGA and NuA4 acetylation profiles. Simulations were done for 16 nucleosomes (each with 8 sites). Parameters were chosen as $D_{\text{tot}} = 1$, $T_{\text{tot}} = 1.5$, $H_{\text{tot}} = 16$, $k_1 = 5$, $k_2 = 5$, $k_{-1} = 1$, $k_{-2} = 1$, and $\beta = 1$. The values of α in equation (4.8) were given by $\alpha_0 = 25$ with values for c equal to 0.003 and 0.0015 for SAGA and NuA4 respectively. Initial conditions were set to $D = D_{\text{tot}}$, $S_0 = S_{\text{tot}}$, $H_0 = H_{\text{tot}}$, and $T_0 = T_{\text{tot}}$.

We first choose a large value of α relative to β and use equation (4.7) to obtain a $p_{\max}$ large enough that it guarantees full chromatin decompression for all values of s and k in our chosen range (Figure 4.8b). The resulting Hill coefficients for each combination of s and k are displayed as a heat map shown in Figure 4.8a. In this case, Hill coefficients are maximized whenever $k \approx s/2$, with $H > 4$ for $s = 10, k = 6$. This suggests that ultrasensitivity in chromatin remodeling can be maximized by having twice as many sites than the minimum number of non-acetylated sites required for nucleosome interactions.

For lower values of $p_{\max}$, the chromatin may not fully decompress for some combinations of s and k (Figure 4.8d). Hill coefficients appear to be maximized for large values of s and small values of k (Figure 4.8c), with $H > 4.5$ for $s = 10$, $k = 2$. In this case the maximal DNA accessibility reaches around 40% of the full expansion. This illustrates a parameter regime in which a dose response of chromatin expansion is highly ultrasensitive, even though

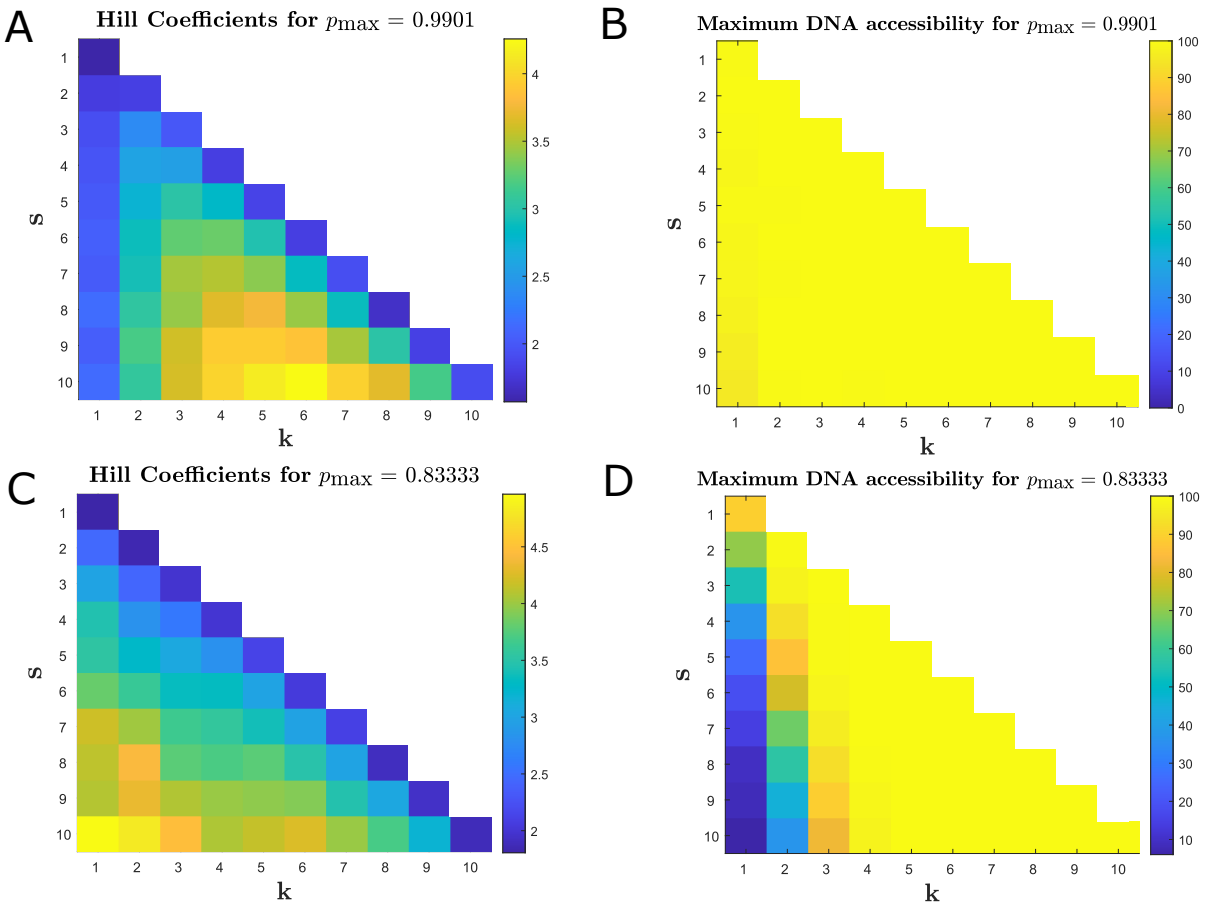

Figure 4.8: (A) In a parameter regime where the probability of acetylation p saturates as a function of T_{tot}, the Hill coefficient can be higher than 4 for certain combinations of s, k. (B) Using the same parameters as in (A), DNA accessibility saturates near 100% for most values of s, k. (C) If the probability of acetylation doesn't fully saturate, the maximum Hill coefficient of approximately 4 is found for small k and high s. (D) Using the same parameters, the values of s, k that optimize ultrasensitivity have low saturation of DNA accessibility. That is, the DNA response is ultrasensitive but it never fully opens for increasing TF concentration. For subfigures (C) and (D) we used the same parameters as in Figure 4.6. Similarly for (A) and (B) with the exception of $k_{-1} = 10^{-2}$, $k_{-2} = 10^{-2}$ and $\beta = 10^{-2}$, we use the same parameters.

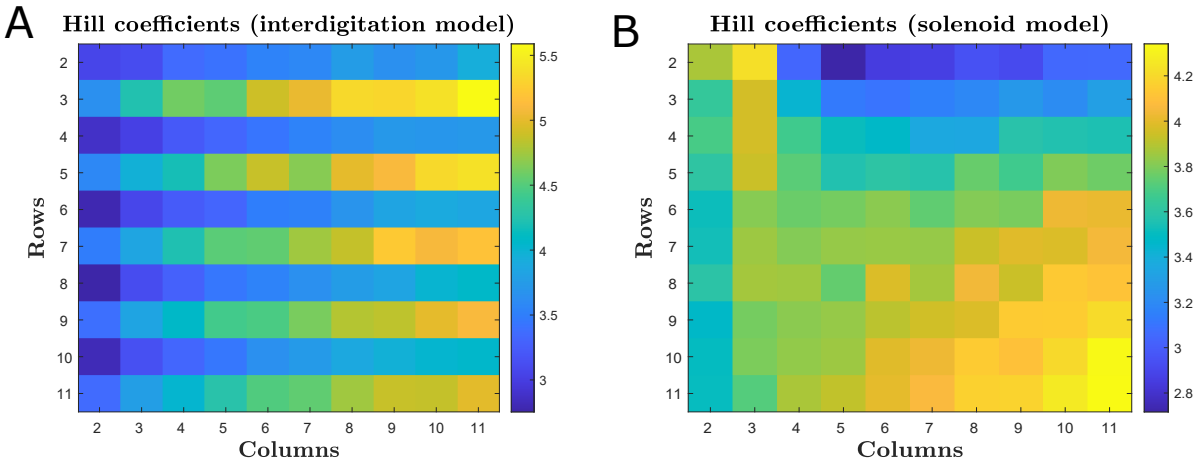

Figure 4.9: (A) Hill coefficients for different grid sizes of the solenoid model. Higher numbers of rows and columns tend to increase the ultrasensitivity of the transcription factor dose-response. (B) Hill coefficients for different grid sizes of the interdigitation model. Higher numbers of columns raise the ultrasensitivity of the transcription factor dose-response. Parameters were chosen as in Figure 4.8a.

chromatin is never fully expanded.

We note that these heat maps also separate between the effect of percolation and the nucleosomal interactions to determine the Hill coefficient. Specifically, when $s = k = 1$ in Figure 4.8c, nucleosomal interactions are simplified and $H \approx 2$ in the solenoid model.

In the same manner as with s and k, we simulate chromatin graphs with different row and column numbers. The Hill coefficients for the solenoid and interdigitation graphs of different sizes are calculated and shown as heat maps in Figures 8a and 8b respectively. For the solenoid architecture, the trend appears to be that increasing the number of rows and columns increases the ultrasensitivity of the response. Note that, in three dimensions, the number of columns could be interpreted as the magnitude of the solenoid radius. Interdigitation architectures, however, tend to become more ultrasensitive solely with increases in the number of columns. Here, more columns correspond to longer stretches of the chromatin before each fold in the architecture. Notice also that even numbers of rows tend to lead to very low Hill coefficients regardless of the number of columns. We believe this to be an artifact, since in this case the end points of the DNA are located in the same column.

4.8 Comparison with Experimental Results

Experimental work by Hajihassan and collaborators measured ultrasensitive chromatin aggregation in response to increasing concentrations of the anticancer drug mitoxantrone [164]. This drug is believed to bind to histones and DNA and to prevent the activity of HAT enzymes, leading to higher chromatin density. We postulate that the ultrasensitive behavior they found could be due to the percolation effects described in our work, and we have recapitulated their experimental data using an expanded model of histone acetylation.

Hajihassan et al. created an *in vitro* extract of rat liver cell chromatin, and they measured chromatin aggregation under different concentrations of mitoxantrone. Chromatin aggregation was measured indirectly by determining the light absorbance of the solution at 400 nm frequency, which is known to measure the turbidity of a solution. In the words of Hajihassan et al, "Addition of drug to SE-chromatin solution resulted in chromatin aggregation and precipitation which could be detected by monitoring the absorbance at 400 nm (turbidity)." The authors found a dose-response between turbidity and mitoxantrone concentration with a Hill coefficient of approximately 3.6. They conclude that the binding of the drug to DNA is likely cooperative, however we postulate here a possible alternative explanation.

The ability of mitoxantrone to inhibit HAT in a dose-dependent manner has been previously documented [165]. We incorporated mitoxantrone into our chemical reaction system by assuming that it binds to the HAT-DNA complex, forming a new complex in which HAT is inactive (Figure 4.10a). In this way, mitoxantrone reduces overall levels of histone acetylation, which decreases chromatin accessibility in an ultrasensitive manner.

In Figure 4.10b, we calculate overall levels of histone acetylation and chromatin accessibility for different drug concentrations. In order to quantitatively relate chromatin accessibility with normalized turbidity data, we assume a simple linear relationship $turbidity = 1 - accessibility$. Using this relationship we are able to recapitulate the experimental mea-

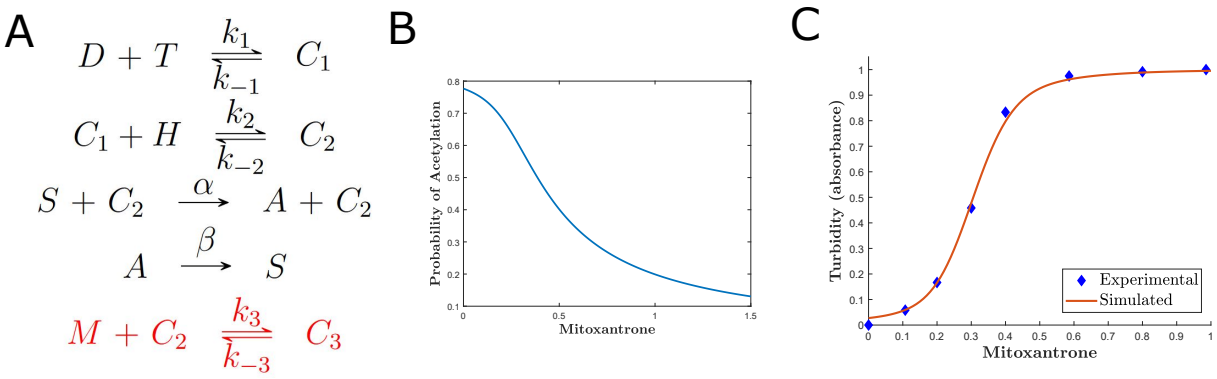

Figure 4.10: (A) Expanded chemical reaction network including reversible enzyme inactivation through mitoxantrone binding to the DNA-HAT complex, forming a new complex C_3. (B) Simulated probability of acetylation p calculated as a function of total mitoxantrone concentration. (C) Experimental data of chromatin turbidity as a function of mitoxantrone concentration along with the modeled relationship between using (A) and data from Figure 4.4b. Here $k_1 = 0.0005$, $k_2 = 0.031$, $\alpha = 1.5$, $k_{-1} = 1.5$, $k_{-2} = 0.18$, $\beta = 0.02$, $k_3 = 1.5$, $k_{-3} = 0.0001$, $D_{\text{tot}} = 1$, $H_{\text{tot}} = 16$, $T_{\text{tot}} = 50$, $D_0 = D_{\text{tot}}$, $S_0 = S_{\text{tot}}$, $H_0 = H_{\text{tot}}$, $T_0 = T_{\text{tot}}$, and $M_0 = M_{\text{tot}}$.

surement using our model, and we show that it displays a similar ultrasensitive behavior with a simulated Hill coefficient of approximately 3.8 (Figure 4.10c).

4.9 Discussion

We develop a theoretical model that uses ideas from percolation theory and nonessential modification sites in order to create ultrasensitive regulation of chromatin expansion. This regulation is naturally limited to the regions of transcription factor binding and is not based on cooperativity of histone acetylation. This results in sharp spatial boundaries between low and high density regions and ultrasensitive chromatin decompaction in response to HAT-recruiting transcription factors. Further analysis shows the effect that changing the DNA configuration has in the resulting ultrasensitive behavior. In particular, that wide and/or long DNA solenoids have greater Hill coefficients, as do interdigitation structures with long DNA stretches between folds.

Overall, our work describes a mechanism for how chromatin accessibility may be able to respond in an all-or-none manner to the acetylation of histone sites. This response could be explored experimentally with a ChIP-seq assay to measure the fraction of acetylated histone sites in a particular chromatin region. Chromatin accessibility, in turn, could be approximated using ATAC-seq, by proxy through gene expression levels, or through direct inspection using electron microscopy. These experiments are out of the scope of this paper and are left for a future publication, for instance using the ENCODE database and comparing data for single cells or tissues using different assays. We have also predicted a relation between DNA structure and Hill coefficient which could be tested experimentally.

The ultrasensitive behavior in our model is due in part to a proposed mechanism in which a critical mass of acetylations between two neighboring histones are required before the histones alter the interaction with each other and the underlying DNA. Previous modeling and experimental results show that this critical mass is ideally less than the total number of acetylation sites, leading to the concept of *nonessential* sites. Overall, our results suggest that chromatin features that appear nonessential could play a role in the context of ultrasensitive remodeling.

An expanded version of our model was able to account for experimental data using an anti-cancer drug measured by Hajihassan and collaborators [164]. While the actual mechanism for the observed ultrasensitivity is not yet determined, one possibility is that it may be due to percolation effects and nonessential interaction histone sites.

In summary, the model calculates the steady state probability p that a histone will be modified and determines the presence of green edges corresponding to nucleosomal interactions. The shortest path of the resulting chromatin graph is used to calculate the chromatin accessibility, which will have different values for different amounts of T_{tot}. This yields the dose response of chromatin accessibility as a function of local transcription factor concentration. The Hill coefficient of this graph represents the level of ultrasensitivity at which the

chromatin transitions between density states.

A future version of this model could incorporate additional factors that can be biologically relevant. Perhaps most immediately, the effects of methylation could be incorporated. Methylation is a covalent modification that prevents acetylation of a given amino acid, and it therefore blocks DNA expansion. It is often used to silence blocks of DNA in the genome. In the context of our work, one could include methylation simply by adding methylation reactions $S \Leftrightarrow M$ to the chemical reaction network, with the forward reaction mediated by an appropriate HMT enzyme.

While we include nucleosome modifications in the model, we do not include the possibility of nucleosome eviction from the DNA, which would likely alter DNA configuration. Also, additional DNA interactions resulting from higher order three-dimensional folds may result in new neighbors between nucleosomes and can be included by adding interactions to the 2D structure graph. Other factors that are known to play a role in chromatin remodeling are the topology of linker DNA, and the presence of proteins such as the H1 linker histone.

Chapter 5

Function saturation as a mechanism for ultrasensitivity

Material in this chapter is adapted from a manuscript by Alvaro Fletcher and German Enciso.

5.1 Introduction

Ultrasensitivity is colloquially used to describe a response to a stimulus that is initially small but increases rapidly after a certain input level of the stimulus is reached. Responses which behave ultrasensitively are studied in the biological sciences as they reduce ambiguity in bistable systems [166, 167]. In essence, they approximate a binary response whereby a system can be said to be either ON or OFF without an ambiguous half-ON or half-OFF state. This way, ultrasensitive responses are able to filter out environmental noise by preventing insignificant levels of stimuli to elicit a response [168, 169, 170]. These properties are typically desired in the context of gene regulation and have been found to be crucial for the proper function of biochemical switches in the cell cycle [171], cell signaling [172], and cell fate

decisions [173].

Several mechanisms that generate ultrasensitive responses have been proposed such as zero-order ultrasensitivity [174], multisite phosphorylation [175], and allostery [176] among others. In this work, we propose an additional mechanism by which ultrasensitivity can be incorporated and modulated into functions that are not typically able to be considered in the context of ultrasensitive dose-responses. We show that by having a complementary system which contains an absolutely robust controller, then the original system can be forced to sharply saturate at a predetermined point. This critical point can be modulated through the parameters within the absolutely robust subsystem and made to be more or less ultrasensitive depending on whether certain parameters are increased or decreased.

Formally, a response is said to ultrasensitive if it is more sensitive than a Michaelis-Menten response given by

$$f(x) = \frac{x}{x+k} \tag{5.1}$$

for some constant $k > 0$. In order to quantify the sensitivity of a response, it is common to resort to using the so-called Hill coefficient originally derived from the work on the oxygen transport of hemoglobin by A.V. Hill [39]. To calculate the Hill coefficient of some function h, we can simply write

$$H_h = \frac{\ln 81}{\ln(v_h/u_h)},$$

where H_h denotes the Hill coefficient of h, while u_h and v_h correspond to the inputs that generate 10% and 90% of the maximum value of the response. In particular, if we denote the maximal response to be h_∞, then $u_h = h^{-1}(0.1h_\infty)$ and $v_h = h^{-1}(0.9h_\infty)$. We can see

that the Hill coefficient of the Michaelis-Menten response in equation 5.1 is equal to 1 since

$$\frac{v_f}{u_f} = \frac{\frac{0.9}{1-0.9}}{\frac{0.1}{1-0.1}} = 81$$

and thus $H_f = \ln 81 / \ln 81 = 1$. Hence, any function h such that $H_h \geq 1$ would be considered ultrasensitive even though, in this work, it will be more useful to consider ultrasensitivity as continuous range rather than as a binary property of dose-responses. In other words, rather than assigning a response the property of being ultrasensitive, it will be more pertinent to compare its Hill coefficient relative to that of other responses.

While many biochemical processes are described by functions that reach a well-defined saturation point and thus can be assigned a proper Hill coefficient, others do not. One notable example is that of polymerization which gives rise to many kinds of polypeptides, polysaccharides, polynucleotides and proteins. These polymers play crucial roles in building a variety of biological tissues, cell scaffolding, and gene regulation [177, 178, 35, 36]. However, the dose-response of the largest polymer with respect to the individual monomers may be described as a power process of the form x^n which does not saturate. As such, one cannot quantify whether these processes contribute to the ultrasensitivy of some cascading signaling process. Given that polymerization and other biochemical processes do not appear to achieve proper saturation, it is then worth considering whether through natural or synthetic approaches these processes could be made to saturate and tentatively become ultrasensitive.

In this work, we present an example of such an approach that is capable of saturating a simple polymerization process involving n monomers. To achieve this, we resort to a well-studied property of chemical reaction networks known as absolute concentration robustness. Within a certain phase space, a species is said to be absolutely robust if its steady state depends only on rate constants. In other words, if the steady state of this species does not depend on the initial conditions of the system nor the steady state of other species. We show

that the integration of the toy model for absolute robustness with a simple polymerization process is sufficient for the saturation of the latter. Moreover, we show that the resulting saturated process is ultrasensitive. In doing so, we suggest that a more general theoretical and practical approach could be developed for saturation of other processes using absolutely robust chemical modules.

The prevalence of biochemical signaling cascades across a wide range of organisms suggests that the saturation of biochemical processes through absolute robustness could be a plausible mechanism to increase the ultrasensitivity of the composite function describing the cascade. However, this raises another question, how ultrasensitive can biochemical cascades become? If our proposed mechanism is implemented in nature, then it is possible that such a mechanism could be the consequence of selection pressures. These pressures, in turn, would be presumed to drive the adoption of our mechanism in response to an unmet upper bound in ultrasensitivity from the composite response of the cascade. For this reason, determining how ultrasensitive certain biochemical cascades can become provides an initial step for understanding whether our mechanism could be found in nature. First, we formally show the upper bound of the composition of two general Hill functions which confirms previous observations by Ferrell [166]. Then, we suggest that these same observations do not hold true for general sigmoid-like functions which initially increase and eventually reach a well-defined saturation point. We also state some results that apply for all generally increasing functions.

In section 5.1.1 we show an example of our proposed saturation mechanism for the polymerization reaction using the toy model for absolute robustness developed by Shinar and Feinberg [41]. Then, section 5.1.2 formally shows that the ultrasensitivity of the composition of two general Hill functions cannot exceed the product of the individual functions. Section 5.2 proceeds to show that this observation does not hold true for all general sigmoid-like functions while section 5.3 shows some general statements of the ultrasensitivity derived from composing any two general functions. Lastly, section 5.4 shows some examples of

composing piecewise saturated functions to show tentative limits to effects of modulated saturation on ultrasensitivity.

5.1.1 Toy model for function saturation

Consider a biochemical reaction involving n monomers A that link at a rate γ to form a polymer C. The polymer C can then decompose into n monomers of A at a rate δ. Such a process can be described by the chemical reactions

$$nA \underset{\delta}{\overset{\gamma}{\rightleftharpoons}} C$$

The concentration of C under deterministic mass-action kinetics can be written as

$$C' = \gamma A^n - \delta C \tag{5.2}$$

which at steady state yields

$$C^* = \frac{\gamma}{\delta} A^{*n}.$$

We can see that the dose response of the largest polymer C is described by a power function with respect to its monomers A. As a result, the addition of more monomers will result in larger amounts of polymer leading to a never saturating concentration of this polymer. In order to force this polymer to sharply achieve a a saturation point, consider now the toy model for absolute robustness described by the following reactions

$$A + B \xrightarrow{\alpha} 2B$$

$$B \xrightarrow{\beta} A$$

This chemical reaction network has a mass conservation law given by $\Omega = A + B$. We can write the concentration of B over time as

$$B' = \alpha AB - \beta B$$

and solving for A^* at steady state yields

$$A^* = \frac{\beta}{\alpha}$$

whenever $\Omega \geq \beta/\alpha$ and $A^* = \Omega$ otherwise. Given that A admits a steady state that is independent of initial conditions, A is said to be absolutely robust. Let A_0 and B_0 denote the initial concentrations of A and B in a given system and let $B_0 = 0$ such that $\Omega = A_0$. If we think of the dose response of A^* with respect to its initial concentration A_0, it becomes clear that A^* will increase linearly and sharply saturate when $A_0 \geq \beta/\alpha$ (Figures 5.1A and 5.1B). As such, the toy model for absolute robustness can also be thought of as a toy model for function saturation since we can set the level of this saturation by simple modulation of α or β.

Note that the steady state of A can be derived to be β/α directly from the equation for B'. It follows that $A^* = \beta/\alpha$ even for the system that combines both the polymerization process above and the toy model for absolute robustness as long as B admits a positive steady state. This new system is described by

$$nA \underset{\delta}{\overset{\gamma}{\rightleftharpoons}} C$$

$$A + B \xrightarrow{\alpha} 2B$$

$$B \xrightarrow{\beta} A$$

and one can show that B admits a positive steady state. Here, the steady state concentrations

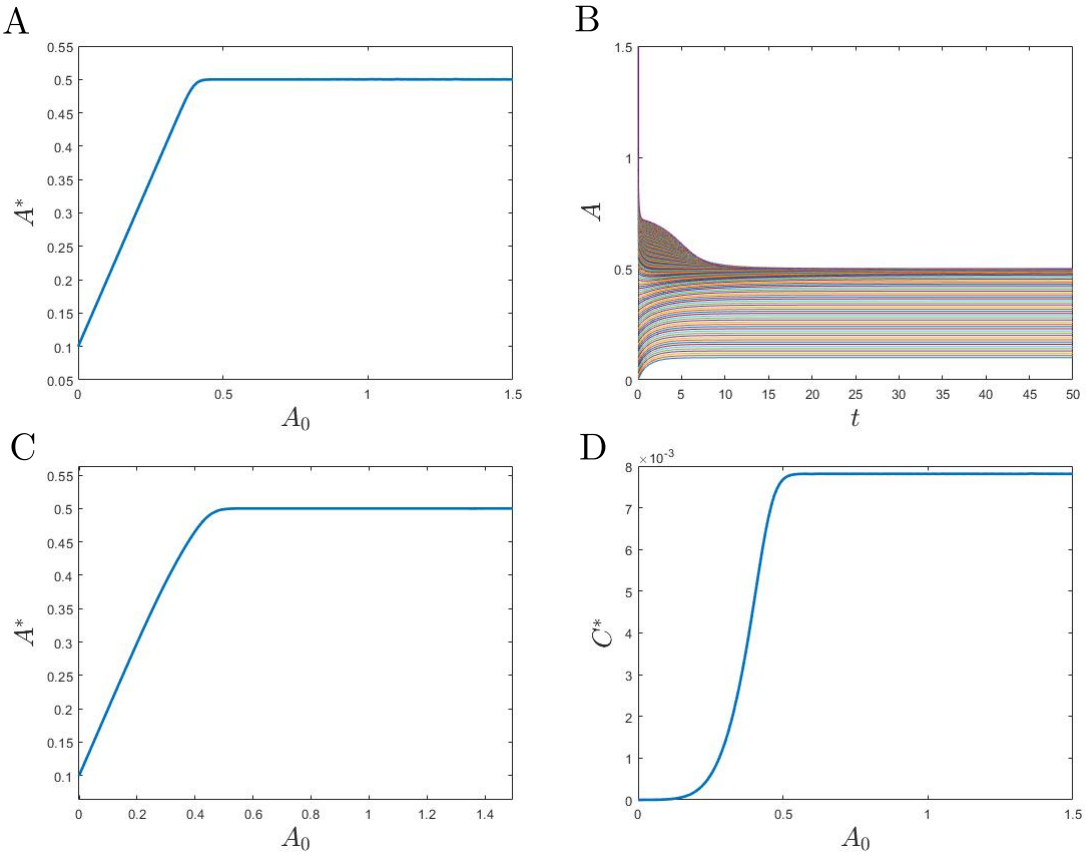

Figure 5.1: (A) Dose response of A against initial concentrations of A_0 in the absolute robustness toy model with $B_0 = 0, \alpha = 2$, and $\beta = 1$. (B) Time trajectories of A for initial conditions ranging from 0 to 1.5. Once $\Omega = A_0 > \beta/\alpha$, then $A^* = \beta/\alpha$ for all initial conditions. (C) Dose response of A against initial concentrations of A_0 in the absolute robustness toy model that incorporates the polymerization reaction with $n = 7$ described in equation 5.2. (D) Dose response of C against initial concentrations of A_0 in the same model as (C). By combining an absolutely robust module with a polymerization module we can force the concentration of the final polymer to saturate a predetermined level.

of monomers will saturate regardless of their initial concentration (Figure 5.1C). Moreover, given that $C^* = A^{*n}$, it follows that C^* is described by a power process that saturates at $(\beta/\alpha)^n$ as is evidenced by Figure 5.1D. Hence, we have shown that it is possible to saturate the concentrations of this polymer and perhaps more general biochemical systems by incorporating modules that induce absolute robustness in the monomers or subunits of similar processes that link repeated elements.

5.1.2 Upper bound of Hill coefficient for the composition of two Hill functions

Take the two Hill functions given by

$$g(x) = \frac{ax^n}{x^n + k_1}$$

and

$$f(x) = \frac{bx^m}{x^m + k_2}$$

where a, b, n, m, k_1 and k_2 are positive constants. Here, the Hill coefficients for f and g are $H_f = m$ and $H_g = n$ respectively. Denote the Hill coefficient of the composition $h(x) = f(g(x))$ to be H_h. We wish to show that $H_h \leq H_f H_g$. The value for H_h is given by

$$H_h = \frac{\ln 81}{\ln \frac{h^{-1}(0.9h_\infty)}{h^{-1}(0.1h_\infty)}}. \tag{5.3}$$

Knowing that

$$h(x) = \frac{b\left(\frac{ax^n}{k_1+x^n}\right)^m}{\left(\frac{ax^n}{k_1+x^n}\right)^m + k_2}$$

we can derive that

$$h_\infty = \lim_{x\to\infty} h(x) = \frac{a^m b}{a^m + k_2}.$$

Moreover, the inverse function of $h(x)$ can be calculated to be

$$h^{-1}(y) = \left(\frac{k_1 \left(\frac{k_2 y}{b-y}\right)^{\frac{1}{m}}}{a - \left(\frac{k_2 y}{b-y}\right)^{\frac{1}{m}}} \right)^{\frac{1}{n}}.$$

Thus, equation 5.3 can be expanded using Wolfram Mathematica to show that

$$H_h = \frac{\ln(81)}{\ln\left(\left(\frac{k_1 0.9^{\frac{1}{m}} \left(\frac{bk_2a^m}{(a^m+k_2)\left(b-\frac{0.9ba^m}{a^m+k_2}\right)} \right)^{\frac{1}{m}}}{a - 0.9^{\frac{1}{m}} \left(\frac{bk_2a^m}{(a^m+k_2)\left(b-\frac{0.9ba^m}{a^m+k_2}\right)} \right)^{\frac{1}{m}}} \right)^{\frac{1}{n}} \left(\frac{k_1 0.1^{\frac{1}{m}} \left(\frac{bk_2a^m}{(a^m+k_2)\left(b-\frac{0.1ba^m}{a^m+k_2}\right)} \right)^{\frac{1}{m}}}{a - 0.1^{\frac{1}{m}} \left(\frac{bk_2a^m}{(a^m+k_2)\left(b-\frac{0.1ba^m}{a^m+k_2}\right)} \right)^{\frac{1}{m}}} \right)^{-\frac{1}{n}} \right)}. \quad (5.4)$$

Now denote

$$\alpha = 0.9 \left(\frac{bk_2a^m}{(a^m+k_2)\left(b-\frac{0.9ba^m}{a^m+k_2}\right)} \right), \quad (5.5)$$

and

$$\beta = 0.1 \left(\frac{bk_2a^m}{(a^m+k_2)\left(b-\frac{0.1ba^m}{a^m+k_2}\right)} \right). \quad (5.6)$$

Substituting the expressions for α and β into equation 5.4 gives that

$$\begin{aligned}
H_h &= \frac{\ln(81)}{\ln\left(\left(\frac{k_1\alpha^{\frac{1}{m}}}{a-\alpha^{\frac{1}{m}}}\right)^{\frac{1}{n}}\left(\frac{k_1\beta^{\frac{1}{m}}}{a-\beta^{\frac{1}{m}}}\right)^{-\frac{1}{n}}\right)}, \\
&= n\frac{\ln(81)}{\ln\left(\frac{k_1\alpha^{\frac{1}{m}}(a-\beta^{\frac{1}{m}})}{k_1\beta^{\frac{1}{m}}(a-\alpha^{\frac{1}{m}})}\right)}, \\
&= n\frac{\ln(81)}{\ln\left(\frac{\alpha^{\frac{1}{m}}}{\beta^{\frac{1}{m}}}\right)+\ln\left(\frac{a-\beta^{\frac{1}{m}}}{a-\alpha^{\frac{1}{m}}}\right)}, \\
&= nm\frac{\ln(81)}{\ln\alpha-\ln\beta+m\ln\frac{a-\beta^{\frac{1}{m}}}{a-\alpha^{\frac{1}{m}}}} \\
&= H_fH_g\frac{\ln(81)}{\ln\alpha-\ln\beta+m\ln\frac{a-\beta^{\frac{1}{m}}}{a-\alpha^{\frac{1}{m}}}}.
\end{aligned}$$

Thus, to prove that $H_h \leq H_fH_g$, it suffices to show that

$$\frac{\ln(81)}{\ln\alpha-\ln\beta+m\ln\frac{a-\beta^{\frac{1}{m}}}{a-\alpha^{\frac{1}{m}}}} \leq 1,$$

or

$$\ln(81) \leq \ln\left(\frac{\alpha}{\beta}\left(\frac{a-\beta^{\frac{1}{m}}}{a-\alpha^{\frac{1}{m}}}\right)^m\right).$$

Taking the exponential of both sides gives

$$81 \leq \frac{\alpha}{\beta}\left(\frac{a-\beta^{\frac{1}{m}}}{a-\alpha^{\frac{1}{m}}}\right)^m. \tag{5.7}$$

The expressions for α and β can be further simplified to

$$\alpha = \frac{9}{\frac{10}{a^m}+\frac{1}{k_2}},$$

and

$$\beta = \frac{1}{\frac{10}{a^m} + \frac{9}{k_2}}.$$

In turn, the ratio of α and β can be derived to be

$$\begin{aligned}
\frac{\alpha}{\beta} &= \frac{81a^m + 90k_2}{a^m + 10k_2}, \\
&= \frac{81a^m + 810k_2 - 720k_2}{a^m + 10k_2}, \\
&= \frac{81(a^m + 10k_2) - 720k_2}{a^m + 10k_2}, \\
&= 81 - \frac{720k_2}{a^m + 10k_2}.
\end{aligned}$$

Substituting for this ratio and replacing α and β with their values in equations 5.5 and 5.6 into inequality 5.7 yields

$$81 \leq \left(81 - \frac{720k_2}{a^m + 10k_2}\right) \left(\frac{a - \left(\frac{1}{\frac{10}{a^m} + \frac{9}{k_2}}\right)^{\frac{1}{m}}}{a - \left(\frac{9}{\frac{10}{a^m} + \frac{1}{k_2}}\right)^{\frac{1}{m}}} \right)^m .$$

Denote the right hand side (RHS) of this inequality to be the function $\Gamma(a, m, k_2)$. Taking the following limit of $\Gamma(a, m, k_2)$ shows that

$$\begin{aligned}
\lim_{a\to\infty} \Gamma(a, m, k_2) &= \lim_{a\to\infty} \left(81 - \frac{720k_2}{a^m + 10k_2}\right) \left(\frac{a - \left(\frac{1}{\frac{10}{a^m} + \frac{9}{k_2}}\right)^{\frac{1}{m}}}{a - \left(\frac{9}{\frac{10}{a^m} + \frac{1}{k_2}}\right)^{\frac{1}{m}}} \right)^m \\
&= (81 - 0) \left(\frac{\lim_{a\to\infty} a - 0}{\lim_{a\to\infty} a - 0} \right)^m \\
&= 81.
\end{aligned}$$

Hence, to prove inequality 5.7, it suffices to show that the partial derivative with respect to a of $\Gamma(a, m, k_2)$ is monotonically decreasing. This is equivalent to showing that the expression on the right hand side of

$$\frac{\partial \Gamma(a,m,k_2)}{\partial a} = \frac{9ma^m \left(\frac{a-\left(\frac{k_2 a^m}{9a^m+10k_2}\right)^{\frac{1}{m}}}{a-9^{\frac{1}{m}}\left(\frac{k_2 a^m}{a^m+10k_2}\right)^{\frac{1}{m}}} \right)^m \left(\frac{9a^m+10k_2}{9^{\frac{1}{m}}\left(\frac{k_2 a^m}{a^m+10k_2}\right)^{\frac{1}{m}}-a} + \frac{9a^m+90k_2}{a-\left(\frac{k_2 a^m}{9a^m+10k_2}\right)^{\frac{1}{m}}} \right)}{\left(a^m+10k_2\right)^2} \tag{5.8}$$

as calculated using Wolfram Mathematica, is always negative. First, note that the denominator and the coefficient $9ma^m$ of the RHS of equation 5.8 are always positive and irrelevant in determining whether this expression is positive or negative. Then, substituting

$$\psi = 9^{\frac{1}{m}} \left(\frac{k_2 a^m}{a^m+10k_2} \right)^{\frac{1}{m}}$$

and

$$\omega = \left(\frac{k_2 a^m}{9a^m+10k_2} \right)^{\frac{1}{m}}$$

into the RHS of equation 5.8 yields an expression that can be simplified to

$$\frac{\partial \Gamma(a,m,k_2)}{\partial a} = \frac{(\omega-\psi)\left(\frac{a-\omega}{a-\psi}\right)^{m-1}}{(a-\psi)^2}.$$

One again, we can discard the denominator of this expression which boils the task of proving inequality 5.7 down to showing that

$$(\omega-\psi)\left(\frac{a-\omega}{a-\psi}\right)^{m-1} < 0. \tag{5.9}$$

One can see that $\omega < \psi$ follows directly from

$$\begin{aligned}
\omega &= \left(\frac{k_2 a^m}{9a^m + 10k_2}\right)^{\frac{1}{m}} \\
&< \left(\frac{k_2 a^m}{a^m + 10k_2}\right)^{\frac{1}{m}} \\
&< \left(\frac{9k_2 a^m}{a^m + 10k_2}\right)^{\frac{1}{m}} \\
&= \psi.
\end{aligned}$$

We can show that $a - \psi > 0$ as follows. First, take the inequality

$$a^m + k_2 > 0$$

which holds true as a, m, and k_2 are all positive constants. Adding $9k_2$ to both sides and raising them to $1/m$ yields

$$(a^m + 10k_2)^{\frac{1}{m}} > 9^{\frac{1}{m}} k_2^{\frac{1}{m}}$$

Multiplying both sides by a and subtracting by $9^{\frac{1}{m}} k_2^{\frac{1}{m}}$ gives

$$a(a^m + 10k_2)^{\frac{1}{m}} - 9^{\frac{1}{m}} a k_2^{\frac{1}{m}} > 0$$

and dividing by $(a^m + 10k_2)^{\frac{1}{m}}$ results in

$$\begin{aligned}
a - \frac{9^{\frac{1}{m}} a k_2^{\frac{1}{m}}}{(a^m + 10k_2)^{\frac{1}{m}}} &= a - \left(\frac{9a^m k_2}{a^m + 10k_2}\right)^{\frac{1}{m}} \\
&= a - \psi > 0
\end{aligned}$$

From this, it immediately follows that $a - \omega$ is also positive and inequality 5.9 is true. Therefore, inequality 5.7 is also true and implies that $H_h \leq H_f H_g$.

□

5.2 Limits to ultrasensitivity by composition of sigmoid-like functions

In this section we show that results derived in section 5.1.2 do not apply to all sigmoid-like functions which initially increase and eventually reach a well-defined saturation point. In other words, given two sigmoid-like functions of the form $f(x)$ and $g(x)$ and their composition $h(x) = f(g(x))$ it does not necessarily follow that $H_h \leq H_f H_g$. First, let

$$f(x) = \begin{cases} x & x < c \\ \\ c & x \geq c \end{cases}$$

and

$$g(x) = \begin{cases} 0 & x < d \\ \\ \frac{a(x-d)}{(x-d)+1} & x \geq d \end{cases}.$$

It is trivial to show that $H_f = 2$ for all values of c by noting that $f^{-1}(0.9f_\infty) = 0.9c$ and $f^{-1}(0.1f_\infty) = 0.1c$ where $f^{-1}(y) = y$ is the inverse function of $f(x)$ when $x < c$. Then taking the formula for the Hill coefficient of f we see that

$$H_f = \frac{\ln 81}{\ln \frac{0.9c}{0.1c}} = 2.$$

Similarly, one can show that

$$H_g = \frac{\ln 81}{\ln \frac{9(0.1ad+0.9a)}{0.1a+0.9ad}} = \frac{\ln 81}{\ln \frac{9(0.1d+0.9)}{0.1+0.9d}}. \tag{5.10}$$

The composition of $f(x)$ and $g(x)$ can be calculated as

$$h(x) = f(g(x)) = \begin{cases} 0 & d > x \\ \frac{a(x-d)}{(x-d)+1} & d \leq x \quad \& \quad \frac{a(x-d)}{(x-d)+1} < c \\ c & d \leq x \quad \& \quad \frac{a(x-d)}{(x-d)+1} \geq c. \end{cases}$$

From this expression, one can derive the Hill coefficient of $h(x)$ to be

$$H_h = \frac{\ln(81)}{\ln\left(\frac{0.8ac}{(1.a-0.9c)(1.ad-0.1cd+0.1c)} + 1\right)}.$$

In the case of H_g in equation 5.10, assume that d is fixed and so the denominator of that expression is constant. As such, the product of

$$H_f H_g = 2\frac{\ln 81}{\ln \frac{9(0.1d+0.9)}{0.1+0.9d}}$$

stays constant and does not depend on c. On the other hand, we have that

$$\lim_{c\to 0} H_h = \lim_{c\to 0} \frac{\ln(81)}{\ln\left(\frac{0.8ac}{(1.a-0.9c)(1.ad-0.1cd+0.1c)} + 1\right)} = \infty.$$

Hence, while $H_f H_g$ remains constant, the value of H_h can be made arbitrarily large. Therefore it does not hold that $H_h \leq H_f H_g$.

□

5.3 Ultrasensitivity of the composition of two general functions

The result of section 5.2 showed that, indeed, it does not necessarily hold that $H_h \leq H_f H_g$ for two sigmoid-like functions. However, in this section, we present a collection of results concerning the ultrasensitivity derived from composing any two increasing functions $f(x)$ and $g(x)$. In doing so, we hope that these results will eventually lead to a more general statement concerning the upper bound for the Hill coefficient $h(x) = f(g(x))$.

5.3.1 Sensitivity for the composition of two functions

Denote $R_f(x)$ to be the sensitivity of a function $f(x)$ with respect to x which is given by

$$R_f(x) = \frac{x}{f(x)} f'(x).$$

Similarly, the sensitivity of $f(g(x))$ to $g(x)$ is defined by

$$R_f(g(x)) = \frac{g(x)}{f(g(x))} f'(g(x)).$$

Lemma 5.1. *Let the composition of f and g be $h = f(g(x))$. The sensitivity of h with respect to x is given by $R_g(x)R_f(g(x))$.*

Proof. By definition,

$$\begin{aligned} R_h(x) &= \frac{x}{h(x)} h'(x), \\ &= \frac{x}{f(g(x))} f'(g(x)) g'(x), \\ &= \frac{x}{g(x)} g'(x) \frac{g(x)}{f(g(x))} f'(g(x)), \\ &= R_g(x) R_f(g(x)). \end{aligned}$$

□

5.3.2 Hill coefficients and sensitivity

Denote u_f and v_f to be the EC10 and EC90 of $f(x)$ respectively.

Lemma 5.2. *The formula for Hill coefficient of $f(x)$ is given by twice the average of the sensitivity function $R_f(e^t)$. That is,*

$$H_f = 2 \frac{\int_{\ln u_f}^{\ln v_f} R_f(e^t)\, dt}{\ln v_f - \ln u_f}.$$

Proof. By definition,

$$H_f = \frac{\ln 81}{\ln(\frac{v_f}{u_f})} = 2 \frac{\ln(\frac{0.9 f_\infty)}{0.1 f_\infty)})}{\ln v_f - \ln u_f} = 2 \frac{\ln f(v_f) - \ln f(u_f)}{\ln v_f - \ln u_f}.$$

Noting that

$$\int \frac{f'(x)}{f(x)}\, dx = \ln f(x) + c$$

we can rewrite the Hill coefficient as

$$H_f = 2\frac{\int_{u_f}^{v_f} \frac{f'(x)}{f(x)}\,dx}{\ln v_f - \ln u_f}.$$

Doing the substitution $x = e^t$ in the integral above, we obtain that

$$H_f = 2\frac{\int_{\ln u_f}^{\ln v_f} e^t \frac{f'(e^t)}{f(e^t)}\,dt}{\ln v_f - \ln u_f} = 2\frac{\int_{\ln u_f}^{\ln v_f} R_f(e^t)\,dt}{\ln v_f - \ln u_f}.$$

□

5.3.3 Upper bounds to the Hill coefficient of a composition

Lemma 5.3. *Let f_∞ to be the $\lim_{x\to\infty} f(x)$ and h_∞ to be the $\lim_{x\to\infty} h(x)$. If $h = f(g(x))$ under the condition that $f_\infty = h_\infty$ and $R_g(x) \leq H_g\,\forall x$, then $H_h \leq H_f H_g$.*

Proof. If $R_g(x) \leq H_g$, then it follows that the average function value of $R_g(x)$ must satisfy

$$\frac{\int_\alpha^\beta R_g(x)\,dx}{\ln\beta - \ln\alpha} \leq H_g,$$

for all values of α and β. Since the range of e^x is $\mathbb{R}$, we can substitute x with e^x in the above inequality to obtain

$$\frac{\int_\alpha^\beta R_g(e^x)\,dx}{\ln\beta - \ln\alpha} \leq H_g,$$

and specifying values of $\alpha = \ln u_h$ and $\beta = \ln v_h$ we have

$$\begin{aligned}\frac{\int_{\ln u_h}^{\ln v_h} R_g(e^x)\,dx}{\ln v_h - \ln u_h} &= \frac{\ln g(v_h) - \ln g(u_h)}{\ln v_h - \ln u_h} \\ &= \frac{\ln g(g^{-1}(f^{-1}(0.9h_\infty))) - \ln g(g^{-1}(f^{-1}(0.1h_\infty)))}{\ln v_h - \ln u_h} \\ &= \frac{\ln f^{-1}(0.9h_\infty) - \ln f^{-1}(0.1h_\infty)}{\ln v_h - \ln u_h} \\ &\leq H_g.\end{aligned} \tag{5.11}$$

Given that $f_\infty = h_\infty$,

$$\begin{aligned}\frac{\ln f^{-1}(0.9h_\infty) - \ln f^{-1}(0.1h_\infty)}{\ln v_h - \ln u_h} &= \frac{\ln f^{-1}(0.9f_\infty) - \ln f^{-1}(0.1f_\infty)}{\ln v_h - \ln u_h}, \\ &= \frac{\ln v_f - \ln u_f}{\ln v_h - \ln u_h},\end{aligned}$$

which can be substituted into (5.11) to yield

$$\frac{\ln v_f - \ln u_f}{\ln v_h - \ln u_h} \leq H_g.$$

Multiplying both sides by $\int_{\ln u_f}^{\ln v_f} R_f(e^t)\,dt$ and dividing by $\ln v_f - \ln u_f$ gives

$$\frac{\int_{\ln u_f}^{\ln v_f} R_f(e^t)\,dt}{\ln v_h - \ln u_h} \leq \frac{\int_{\ln u_f}^{\ln v_f} R_f(e^t)\,dt}{\ln v_f - \ln u_f} H_g. \tag{5.12}$$

Note that substituting e^t with x in the above left-hand side yields

$$\frac{\int_{\ln u_f}^{\ln v_f} R_f(e^t)}{\ln v_h - \ln u_h}\,dt = \frac{\int_{u_f}^{v_f} \frac{f'(x)}{f(x)}\,dx}{\ln v_h - \ln u_h}.$$

In turn, we can substitute x with $g(e^t)$ such that

$$\begin{aligned}
\frac{\int_{u_f}^{v_f} \frac{f'(x)}{f(x)}\,dx}{\ln v_h - \ln u_h} &= \frac{\int_{\ln u_h}^{\ln v_h} \frac{f'(g(e^t))}{f(g(e^t))} g'(e^t)e^t\,dt}{\ln v_h - \ln u_h}, \\
&= \frac{\int_{\ln u_h}^{\ln v_h} \frac{g(e^t)f'(g(e^t))}{f(g(e^t))} \frac{g'(e^t)e^t}{g(e^t)}\,dt}{\ln v_h - \ln u_h}, \\
&= \frac{\int_{\ln u_h}^{\ln v_h} R_g(e^t)R_f(g(e^t))\,dt}{\ln v_h - \ln u_h}, \\
&= \frac{\int_{\ln u_h}^{\ln v_h} R_h(e^t)\,dt}{\ln v_h - \ln u_h},
\end{aligned}$$

with the last step resulting from the application of lemma 5.1. Substituting this expression into the left-hand side of (5.12) and multiplying both sides by 2 gives

$$2\frac{\int_{\ln u_h}^{\ln v_h} R_h(e^t)\,dt}{\ln v_h - \ln u_h} \leq 2\frac{\int_{\ln u_f}^{\ln v_f} R_f(e^t)\,dt}{\ln v_f - \ln u_f} H_g,$$

which by lemma 5.2 is equivalent to

$$H_h \leq H_f H_g.$$

□

Theorem 5.4. *Let $h = f(g(x))$. If $R_g(x) \leq a$ and $R_f(x) \leq b$ for $a \in \mathbb{R}$, then $H_h \leq 2ab$.*

Proof. We have that

$$\begin{aligned}
H_h &= 2\frac{\int_{\ln u_h}^{\ln v_h} R_h(e^t)\,dt}{\ln v_h - \ln u_h},\\
&= 2\frac{\int_{\ln g^{-1}(f^{-1}(0.1h_\infty))}^{\ln g^{-1}(f^{-1}(0.9h_\infty))} \frac{f'(g(e^t))g'(e^t)e^t}{f(g(e^t))}\,dt}{\ln v_h - \ln u_h},\\
&= 2\frac{\int_{f^{-1}(0.1h_\infty)}^{f^{-1}(0.9h_\infty)} \frac{f'(s)}{f(s)}\,dt}{\ln v_h - \ln u_h},\\
&= 2\frac{\int_{f^{-1}(0.1h_\infty)}^{f^{-1}(0.9h_\infty)} R_f(e^t)\,dt}{\ln v_h - \ln u_h},
\end{aligned}$$

where we performed the substitution $s = g(t)$ in the last step. Denote $\bar{v} = f^{-1}(0.9h_\infty)$ and $\bar{u} = f^{-1}(0.1h_\infty)$. Then, the above expression can be written as

$$\begin{aligned}
H_h &= 2\frac{\int_{\bar{u}}^{\bar{v}} R_f(e^t)\,dt}{\ln v_h - \ln u_h},\\
&= 2\frac{\ln \bar{v} - \ln \bar{u}}{\ln v_h - \ln u_h}\frac{\int_{\bar{u}}^{\bar{v}} R_f(e^t)\,dt}{\ln \bar{v} - \ln \bar{u}},\\
&= 2\frac{\ln g(v_h) - \ln g(u_h)}{\ln v_h - \ln u_h}\frac{\int_{\bar{u}}^{\bar{v}} R_f(e^t)\,dt}{\ln \bar{v} - \ln \bar{u}},\\
&= 2\frac{\int_{\ln u_h}^{\ln v_h} R_g(e^t)\,dt}{\ln v_h - \ln u_h}\frac{\int_{\bar{u}}^{\bar{v}} R_f(e^t)\,dt}{\ln \bar{v} - \ln \bar{u}}.
\end{aligned}$$

Since $R_g(e^t) \le a$ and $R_f(e^t) \le b$, it follows that

$$H_h \le 2ab.$$

□

Corollary 5.4.1. *If $R_g(x) \le a$ and $R_f(x) \le b$ and $ab = H_f H_g/2$, then $H_h \le H_g H_f$.*

Lemma 5.5. *Suppose f is an increasing function. If $R_g \le H_g$ and $\frac{v_f}{u_f} \le \frac{\bar{v}}{\bar{u}}$ where $\bar{v} = f^{-1}(0.9h_\infty)$ and $\bar{u} = f^{-1}(0.1h_\infty)$, then $H_h \le H_f H_g$.*

Proof. Applying the natural logarithm to both sides of

$$\frac{v_f}{u_f} \leq \frac{\bar{v}}{\bar{u}}.$$

gives

$$\ln v_f - \ln u_f \leq \ln \bar{v} - \ln \bar{u}.$$

Since $v_h = g^{-1}(f^{-1}(0.9h_\infty))$ and $u_h = g^{-1}(f^{-1}(0.1h_\infty))$, we can write

$$\ln v_f - \ln u_f \leq \ln g(v_h) - \ln g(u_h).$$

The right-hand side can be written in terms of the sensitivity of g as

$$\frac{\ln v_f - \ln u_f}{\ln v_h - \ln u_h} \leq \frac{\int_{\ln u_h}^{\ln v_h} R_g(e^t)\, dt}{\ln v_h - \ln u_h},$$

where we have also divided each side by $\ln v_h - \ln u_h$. Since $R_g(e^t) \leq H_g$, we have that

$$\frac{\ln v_f - \ln u_f}{\ln v_h - \ln u_h} \leq H_g.$$

Multiplying by $\ln 81$ and dividing by $\ln v_f - \ln u_f$

$$\frac{\ln 81}{\ln v_h - \ln u_h} \leq \frac{\ln 81}{\ln v_f - \ln u_f} H_g$$

or

$$H_h \leq H_f H_g.$$

□

5.3.4 Example application of a sensitivity theorem

Define a piecewise saturated function $f(x)$ at a as

$$\begin{cases} f(x) & x < a \\ f(a) & x \geq a. \end{cases} \tag{5.13}$$

We employ the notation $f||a$ to denote a function that saturates at a as described in equation (5.13). Now, consider the functions $f(x) = x^n||a$ and $g(x) = x^n||b$. We wish to show that given $h(x) = f(g(x))$ it follows that $H_h \leq H_g H_f$.

Proof. The Hill coefficient of $f(x) = x^n||a$ is $H_f = 2n$ for all values of a. Similarly, $H_g = 2m$ for all values of b. Meanwhile, the sensitivities of f and g are given by $R_f = n$ and $R_g = m$ in the intervals $[0, a]$ and $[0, b]$. Therefore, by theorem 5.5, we have that $H_h \leq 2nm \leq 4nm = H_g H_f$. □

5.4 Experiments in composing saturated functions

In this section we present calculations of the Hill coefficients for compositions of saturated and non-saturated functions. This work can be related to the mechanism described in section 5.1.1 by suggesting what might be the upper limits to the ultrasensitivity of the composite function resulting from a hypothetical cascade of biochemical signals that incorporate an absolutely robust module.

5.4.1 Saturating a standard Hill function

Consider first the composition of $f(y) = 2y^3/(y^3+1)$ with itself yielding

$$f(f(x)) = \frac{16x^9}{(1+x^3)^3(1+\frac{8x^9}{(1+x^3)^3})}.$$

The Hill coefficient of $f(f(x))$ can be determined to be approximately 6. Now, consider the function g that saturates as follows

$$g(y) = \begin{cases} \frac{2y^3}{1+y^3} & y < \omega \\ \frac{2\omega^3}{1+\omega^3} & y \geq \omega \end{cases}$$

The composition of g and f takes the form

$$g(f(x)) = \begin{cases} \frac{16x^9}{(x^3+1)^3\left(\frac{8x^9}{(x^3+1)^3}+1\right)} & \frac{2x^3}{x^3+1} < \omega \\ \frac{2\omega^3}{1+\omega^3} & \frac{2x^3}{x^3+1} \geq \omega \end{cases}$$

This time, the Hill coefficient of the composition approaches 18 as ω approaches 0. This initially suggests that forcing an early saturation of a response $2y^3/(y^3+1)$ leads to a higher Hill coefficient of the overall composite response in which it finds itself than otherwise.

The observation above likely follows from noting that forced saturations, as those described by our mechanism in section 5.1.1, tend to increase Hill coefficients for standard Hill functions (see Table 5.1). Then, when these forcibly saturated Hill functions denoted by g are composed with another function such as a non-saturated power function f, the Hill coefficient of the resulting composition $f \circ g$ achieves a higher value that appears to be given by $H_{f\circ g} = \frac{1}{2}nm$ where $H_f = n$ and $H_g = m$. The same does not hold true when the power function is saturated but not the Hill function (Table 5.2).

f	H_f	$\lim_{a\to 0} H_{f\|\|a}$
$x/(x+c)$	1	2
$x^2/(x^2+c)$	2	4
$x^3/(x^3+c)$	3	6
$x^4/(x^4+c)$	4	8
x	2	2
x^2	4	4

Table 5.1: The Hill coefficients of the composition of Hill functions as a approaches 0.

g	f	H_g	H_f	$H_{f\circ g}$
$\sqrt{x}$	$x/(x+c)$	1	1	0.72
$x/(x+c)$	x^2	1	4	1.19
$\lim_{a\to 0} x/(x+c)\|\|a$	x^2	2	4	4
$x^2/(x^2+c)$	x^2	2	4	2.38
$\lim_{a\to 0} x^2/(x^2+c)\|\|a$	x^2	4	4	8
$x^3/(x^3+c)$	x^2	3	4	3.57
$\lim_{a\to 0} x^3/(x^3+c)\|\|a$	x^2	6	4	12
$x^4/(x^4+c)$	x^2	4	4	4.76
$\lim_{a\to 0} x^4/(x^4+c)\|\|a$	x^2	8	4	16
$x^2/(x^2+c)$	x^3	2	6	2.52
$\lim_{a\to 0} x^2/(x^2+c)\|\|a$	x^3	4	6	12
$x^3/(x^3+c)$	x^3	3	6	3.79
$\lim_{a\to 0} x^3/(x^3+c)\|\|a$	x^3	6	6	18
$bx/(c+x)$	$x^2\|\|a, b < a$	1	4	1.19
$bx/(c+x)$	$\lim_{a\to 0} x^2\|\|a, b > a$	1	4	4

Table 5.2: The Hill coefficients of the composition of saturated and non-saturated functions.

Chapter 6

Notes on absolute concentration robustness

Material in this chapter was adapted from work by Alvaro Fletcher and German Enciso.

6.1 Introduction

Absolute concentration robustness (ACR) is a property attributed to a chemical species that converges to a steady state which is independent of initial conditions. The following toy model for ACR was proposed by Shinar and Feinberg [41] and is given by the reactions

$$A + B \xrightarrow{\alpha} 2B$$

$$B \xrightarrow{\beta} A$$

Mass action kinetics dictates that the concentrations of B over time can be described by the equation

$$B' = \alpha AB - \beta B$$

and solving for A^* at steady state yields

$$A^* = \frac{\beta}{\alpha}$$

whenever B admits a positive steady state. Since A^* depends solely on rate constants, it is said that A is absolutely robust.

The ability to maintain robustness between inputs and outputs has been shown to increase fitness in biological systems at various scales from the ability of bacteria to find food to proper gene regulation that ensures the development of viable organisms [179, 180, 181, 182, 183, 184]. In this context, absolute concentration robustness can be thought of as the strongest controller available for implementing a constant output in biology. Models of the *E. coli* IDHKP-IDH glyoxylate bypass regulation system and the EnvZ-OmpR osmoregulatory system have actually shown to contain absolutely robust species [41]. The robustness in these models has also been observed experimentally in these systems [182, 185]. Moreover, the ideal housekeeping gene has been described as one which can produce transcripts at a constant rate though this has not been observed with current experimental techniques [42]. It is plausible, however, that a subset of housekeeping genes could be implementing a form of absolute robustness in their regulatory networks to approach this outcome. Hence, it is clear that absolute robustness might be implemented within large biological regulatory networks to achieve nearly perfect control over a target, and it is a network property that could prove useful in the design of synthetic biological circuits when a fixed output is required from a complex biochemical substrate.

In this chapter, we present a collection of results that make use of absolute concentration as a controller for a given property of some biochemical system. In section 6.2, we present preliminary theoretical results on the extension of absolute robustness from a network submodule to the larger parent network. This section aims to provide a formal framework by which absolute robustness could be identified in biochemical components making up a subsystem and thereby shown to be maintained for the encompassing system. Section 6.3 contains an example of a potential mechanism that uses an absolutely robust species for creating a unidirectional dependence over time of one species to another. Lastly, in section 6.4 we extend the EnvZ-OmpR model presented by Shinar-Feinberg [41] to include an osmoregulatory component and show how it can be derived to have absolute robustness from one of the regulatory species.

6.2 Extension of absolute robustness from submodules to parent networks

6.2.1 Formal introduction to chemical reaction networks

Definition 6.1. *A chemical reaction network is a set $\{\mathcal{R}, \mathcal{C}, \mathcal{S}\}$ where $\mathcal{R}$ is a set of reactions, $\mathcal{C}$ is the set of complexes appearing in $\mathcal{R}$, and $\mathcal{S}$ is a set of species that make the complexes in $\mathcal{C}$.*

Given a network $\mathcal{N} = \{\mathcal{R}, \mathcal{C}, \mathcal{S}\}$ with species $\mathcal{S} = \{A_1, A_2, \ldots, A_r, \ldots A_n\}$, any element of $\mathcal{R}$ has the form

$$s_{j1}A_1 + \ldots + s_{jn}A_n \xrightarrow{k_j} t_{j1}A_1 + \ldots + t_{jn}A_n, \tag{6.1}$$

where the left hand side corresponds to the reactants and the right hand side to the products. The term $s_{ji} \in \mathbb{Z}_{\geq 0}$ corresponds to the stoichiometry of the i^{th} species as a reactant of the j^{th} reaction. Similarly, $t_{ji} \in \mathbb{Z}_{\geq 0}$ is the stoichiometry of the i^{th} species as a product of the j^{th} reaction. The set of complexes $\mathcal{C}$ is composed of the elements $s_{j1}A_1 + \ldots + s_{jn}A_n$ and $t_{j1}A_1 + \ldots + t_{jn}A_n$ for all values of j. Lastly, k_j is the rate constant for the j^{th} reaction.

For the remainder of this article, we will operate under the assumption of mass-action kinetics. Let $c_{A_r} \in \mathbb{R}_{\geq 0}$ denote the concentration of a species $A_r \in \mathcal{S}$ and assume there to be m reactions in $\mathcal{R}$, the dynamics of c_{A_r} are then described by

$$f_{A_r}(\vec{c}) = \frac{dc_{A_r}}{dt} = \sum_{j=1}^{m} k_j \vec{c}^{\vec{s}_j}(t_{jr} - s_{jr}), \tag{6.2}$$

where $\vec{s}_j = \begin{bmatrix} s_{j1} & s_{j2} & \ldots & s_{jr} & \ldots & s_{jn} \end{bmatrix}^T$, $\vec{c} = \begin{bmatrix} c_{A_1} & c_{A_2} & \ldots c_{A_r} & \ldots & c_{A_n} \end{bmatrix}^T$, and

$$\vec{c}^{\vec{s}_j} = \prod_{i=1}^{n} c_{A_i}^{s_{ji}}.$$

Denote $\vec{t}_j = \begin{bmatrix} t_{j1} & t_{j2} & \ldots & t_{jr} & \ldots & t_{jn} \end{bmatrix}^T$. A full description of the network dynamics is given by

$$f(\vec{c}) = \frac{d\vec{c}}{dt} = \sum_{j=1}^{m} k_j \vec{c}^{\vec{s}_j}(\vec{t}_j - \vec{s}_j). \tag{6.3}$$

Unless otherwise specified, given a chemical reaction network $\mathcal{N} = \{\mathcal{R}, \mathcal{C}, \mathcal{S}\}$, we will use m to denote the number of reactions in $\mathcal{R}$ for the remainder of this text. Likewise, the set of species $\mathcal{S}$ will be assumed to have the n species $A_1, A_2, \ldots, A_n$.

Definition 6.2. *A steady state of a chemical reaction network $\mathcal{N}$ is defined by a concentration vector $\vec{c}^* = \begin{bmatrix} c^*_{A_1} & c^*_{A_2} & \ldots & c^*_{A_n} \end{bmatrix}$ that satisfies $f(\vec{c}^*) = 0$.*

Definition 6.3. *A species A_r is said to be absolutely robust if there exists $\alpha > 0$ such that for every positive steady state of the network we obtain that $c^*_{A_r} = \alpha$.*

Example 6.1. Consider the following network

$$A + B \xrightarrow{k_1} 2B$$

$$B \xrightarrow{k_2} A$$

with $T = A + B$. By equation 6.2 we can write that $c'_A = k_2 c_B - k_1 c_A c_B$ and $c'_B = k_1 c_A c_B - k_2 c_B$. Note that A has a steady state equal to k_2/k_1 while the steady state of B corresponds to $T - k_2/k_1$. The steady state value of A is dependent solely on rate constants and is said to be absolutely robust.

6.2.2 Submodules within chemical reaction networks

Definition 6.4. *Consider a chemical reaction network $\mathcal{N} = \{\mathcal{R}, \mathcal{C}, \mathcal{S}\}$. Let $\hat{\mathcal{R}} \subseteq \mathcal{R}$. Define $\hat{\mathcal{C}}$ to be the set of all complexes in the reactions $\hat{\mathcal{R}}$. Similarly, define $\hat{\mathcal{S}}$ to be the set of all species that make up the complexes in $\hat{\mathcal{C}}$. A submodule of $\mathcal{N}$ is the chemical reaction network with the set of species $\hat{\mathcal{S}}$, the set of complexes $\hat{\mathcal{C}}$, and the set of reactions $\hat{\mathcal{R}}$.*

For a given submodule $\hat{\mathcal{N}} = \{\hat{\mathcal{S}}, \hat{\mathcal{C}}, \hat{\mathcal{R}}\}$ of $\mathcal{N}$, denote the concentration of $A_r \in \hat{\mathcal{S}}$ by $\hat{c}_{A_r}$. Specifically, $\hat{c}_{A_r}$ is the concentration of A_r when $\hat{\mathcal{N}}$ is analyzed in isolation. Moreover, assume $\hat{\mathcal{R}}$ to be composed of the first q reactions in $\mathcal{R}$. The dynamics of $\hat{c}_{A_r}$ will then be described by

$$\hat{f}_{A_r}(\vec{c}) = \frac{d\hat{c}_{A_r}}{dt} = \sum_{j=1}^{q} k_j \vec{c}^{\vec{s}_j} (t_{jr} - s_{jr}). \tag{6.4}$$

The dynamics of the entire submodule are given by

$$\hat{f}(\vec{c}) = \frac{d\vec{c}}{dt} = \sum_{j=1}^{q} k_j \vec{c}^{\vec{s}_j}(\vec{t}_j - \vec{s}_j). \tag{6.5}$$

A steady state of the submodule will be denoted by $\hat{\vec{c}}^*$ and satisfies $\hat{f}(\hat{\vec{c}}^*) = 0$.

Note 6.2.1. The vector $\vec{c}$ and $\vec{s}_j$ in equations (6.4) and (6.5) are the same as described before. We could go through the motions of restricting these vectors to the species in $\hat{\mathcal{S}}$ but it will be convenient to keep them unchanged. From the definition of submodule, we know that all the species in $\hat{\mathcal{S}}$ are those that appear in $\hat{\mathcal{R}}$. Therefore, it suffices to set q as the upper bound of the sums since $c_{A_i}^{s_{ji}} = 1$ for all $A_i \notin \hat{S}$ when $j = 1, 2, \ldots, q$.

Remark 1. The entries of $\hat{\vec{c}}^*$ corresponding to species $A_i \notin \hat{S}$ can be chosen to be any value by the argument presented in Note 6.2.1.

Example 6.2. Consider the following network

$$A \xrightarrow{k_1} X$$

$$B \xrightarrow{k_2} 2C$$

$$C \xrightarrow{k_3} D$$

$$2D \xrightarrow{k_4} 2A$$

We can form one submodule from this network with the reactions displaying red arrows and another submodule with the reactions displaying green arrows.

6.2.3 Steady state inheritance

Definition 6.5. *Consider a chemical reaction network $\mathcal{N}$ with a positive steady state $\vec{c}^*$. A submodule $\hat{\mathcal{N}}$ of $\mathcal{N}$ is said to have steady state inheritance in $\mathcal{N}$ if $\hat{f}(\vec{c}^*) = 0$.*

Lemma 6.1. *Let A have absolute robustness in a submodule $\hat{\mathcal{N}}$ of $\mathcal{N}$. If $\hat{\mathcal{N}}$ has steady state inheritance in $\mathcal{N}$, then A is absolutely robust in $\mathcal{N}$.*

Proof. Given that a species A is absolutely robust in $\hat{\mathcal{N}}$, it follows that there exists $\alpha > 0$ such that for every positive steady state of the submodule we obtain that $\hat{c}_A^* = \alpha$. Steady state inheritance dictates that $c_A^* = \hat{c}_A^*$. Therefore, $c_A^* = \alpha$ and A has absolute robustness in $\mathcal{N}$. □

Definition 6.6. *A species A is said to be I-absolutely-robust if there exists $\alpha > 0$ such that $f_B(\vec{c}) = 0$ for all $B \in I$ implies $c_A^* = \alpha$.*

Lemma 6.2. *Consider a chemical reaction network $\mathcal{N}$ with submodules $\mathcal{N}_1$ and $\mathcal{N}_2$. Let $\mathcal{S}_1 = \{A_1, \ldots, A_p\}$ be the set of species in $\mathcal{N}_1$, $\mathcal{S}_2$ be the set of species in $\mathcal{N}_2$, and assume $\mathcal{S}_1 \cap \mathcal{S}_2 = \{A_1, \ldots, A_l\}$. If some species $A_r \in \mathcal{S}_1 \cap \mathcal{S}_2$ is $\{l+1, \ldots, p\}$-absolutely-robust in $\mathcal{N}_1$, then A_r is also absolutely robust in $\mathcal{N}$.*

Example 6.3. Consider a network containing the submodules

$$A + B \xrightarrow{k_1} 2B$$

$$B \xrightarrow{k_2} A$$

and

$$A \underset{k_4}{\overset{k_3}{\rightleftharpoons}} X$$

$$2D \xrightarrow{k_5} 2A$$
$$\vdots$$

where the three dots indicate that this submodule can be of an arbitrary size. Now, suppose that B does not appear in the green arrow submodule. Note that A is $\{B\}$-absolutely robust since $c'_B = 0 = k_1 c_A c_B - k_2 c_B$ implies that $c^*_A = k_2/k_1$. Therefore, by lemma 6.2, A is absolutely robust in the entirety of the network.

Definition 6.7. *The stoichiometry matrix denoted as* $\mathbf{\Gamma}$ *is defined by* $[\mathbf{\Gamma}]_{ij} = t_{ji} - s_{ji}$.

Definition 6.8. *The* i^{th} *species in a chemical reaction network is said to have zero stoichiometry in the* j^{th} *reaction if* $[\mathbf{\Gamma}]_{ij} = 0$.

Lemma 6.3. *Suppose that all species in the submodule* $\hat{\mathcal{N}}$ *have zero stoichiometry for all reactions in* $\mathcal{N} - \hat{\mathcal{N}}$. *Then* $\hat{\mathcal{N}}$ *has steady state inheritance in* $\mathcal{N}$.

Proof. Assume without loss of generality that $\hat{\mathcal{S}}$ is composed of the first p species in $\mathcal{S}$. If $t_{ji} - s_{ji} = 0$ for $i = 1, \dots p$ and $j = q+1, \dots m$, then

$$\frac{dc_{A_i}}{dt} = \sum_{j=1}^{q} k_j \vec{c}^{\vec{s}_j}(t_{ji} - s_{ji}),$$

for species $A_1, A_2 \dots, A_p$. In other words, $\hat{f}_{A_i}(\vec{c}) = f_{A_i}(\vec{c})$ for $i = 1, \dots, p$. It follows that $\hat{f}(\vec{c}^*) = 0$. □

Example 6.4. Consider the following network $\mathcal{N}$ with the submodules

$$A + B \xrightarrow{k_1} 3B$$
$$B \xrightarrow{k_2} A$$
$$A + B \underset{k_4}{\overset{k_3}{\rightleftharpoons}} C$$

and

$$X \xrightarrow{k_5} Z$$

$$2X \xrightarrow{k_6} 2Y$$

$$\vdots$$

and proceed on the assumption that A, B, and C have zero stoichiometry in the green arrow submodule. One can calculate that $c_A^* c_B^* = k_2/k_1$ and $c_C^* = k_3 c_A^* c_B^*/k_4 = \frac{k_3 k_2}{k_4 k_1}$. Therefore C has absolute robustness in the red arrow submodule. By lemma 6.3, the submodule satisfies steady state inheritance, and by lemma 6.1, C is absolutely robust in $\mathcal{N}$.

6.2.4 Biological Relevance

Consider the network composed of the submodules

$$A + B \xrightarrow{k_1} 2B$$

$$B \xrightarrow{k_2} A$$

and

$$\emptyset \underset{k_4}{\overset{k_3 A}{\rightleftharpoons}} X$$

$$2X \underset{k_6}{\overset{k_5}{\rightleftharpoons}} C$$

$$D \underset{k_8}{\overset{k_7 C}{\rightleftharpoons}} D_p$$

We can understand X to be a biomolecule that responds to a chemical stimulus in the environment. Moreover, X dimerizes to form a complex C. In turn, C catalyzes the conversion of D to D_p. Specifically, C could be thought as a kinase that phosphorylates D. The system above is described by the following mass action equations:

$$\begin{aligned}
X' &= k_3 A - k_4 X - 2k_5 X^2 + 2k_6 C, \\
C' &= 2k_5 X^2 - 2k_6 C, \\
D' &= -k_7 CD + k_8 D_p, \\
D_p' &= k_7 CD - -k_8 D_p.
\end{aligned}$$

By lemma 6.2, A is absolutely robust in the green arrow submodule. Consequently, solving the equations for X and C at steady state gives that

$$c_X^* = \frac{k_3 A}{k_4} = \frac{k_2 k_3}{k_1 k_4}$$

and

$$c_C^* = \frac{k_5 X}{k_6} = \frac{k_5 k_2^2 k_3^2}{k_6 k_1^2 k_4^2}.$$

Lastly, solving that

$$D_p^* = \frac{k_8 k_6 k_1^2 k_4^2}{k_7 k_5 k_2^2 k_3^2} D^*$$

provides us with means of studying a dose-response of D_p dependent solely on its unphosphorylated precursor D.

This model may be applied to study receptor tyrosine kinases (RTKs). The species X could be considered an activated RTK while A corresponds to the respective ligand. Meanwhile,

C corresponds to RTK dimerization and D to the inactive form of some relay protein. The above theory presents a way to build a linear dependence between the active and inactive form of the relay protein by introduction of particular submodules to the extra-cellular environment.

6.3 Dose-response mirroring through absolute robustness

6.3.1 Absolutely robust dose-responses

Definition 6.9. *A network composed of species* $\{A_1, A_2, \ldots, A_i, \ldots, A_j, \ldots, A_n\}$ *is said to have an absolutely robust dose-response of* A_i *if the concentration of* A_i *at steady state depends exclusively and linearly on the concentration of one other species* A_j*.*

In this section, we wish to exemplify a way to modify a given reaction network so that it obtains an absolutely robust dose-response. In other words, we seek to make the steady state concentration of a species A denoted by A^* be linearly dependent solely upon that of the steady state of another species B denoted by B^*. This process yields a dose-response of A^* that will be a scaled mirror version of the dose-response for B^*. Hence, any property that B^* has will also be present in A^*. For example, suppose B^* responds ultrasensitively to some input I, that is, small amounts of I will elicit no response in B^* until I reaches a critical point after which B^* increases sharply and quickly saturates. Then, since $A^* = cB^*$ for some constant c, it follows that A^* will also respond ultrasensitively to I though with a different saturation point scaled by c. The mechanism exemplified in this section can be extended to include multiple species that mirror the dose response of a particular species potentially reducing the complexity of multiple implementations of certain behaviors such

as ultrasensitivity in biochemical networks.

6.3.2 Mirroring multisite ultrasensitivity to a gene expression network

In a large biochemical network that contains interacting species A and B, it is most likely that the steady state A will be non-linearly dependent on B as well as other species in the network. On the other hand, given this large network, it is unlikely that A will have an absolutely robust dose response with respect to B since A needs to depend solely and linearly on B. However, absolute concentration robustness provides a tentative mechanism by which absolutely robust dose-responses can be implemented within a fixed network of arbitrary complexity. If a species A is absolutely robust and we are able to identify the network topology that enables this robustness, then we can do specific modifications to this topology and obtain the absolutely robust dose-response of A with respect to any species regardless of the other interactions that A might have in the network. Here, we show an example of how a topology that gives rise to an absolutely robust species can be modified to obtain an absolutely robust dose response of a protein with respect to another fully bound multisite protein. The latter protein responds ultrasensitively to an enzyme and we prove that the former protein mirrors this ultrasensitivity at a scale.

Consider first the following gene expression network

$$
\begin{aligned}
&\mathrm{X}_1 \xrightarrow{k_2} \mathrm{X}_1 + \mathrm{X}_2 \\
&\mathrm{X}_2 \xrightarrow{\gamma_2} \emptyset \\
&\mathrm{X}_1 \xrightarrow{\gamma_1} \emptyset \\
&\quad\vdots
\end{aligned}
$$

where X_1 might be thought of as mRNA that gets transcribed into a protein X_2 at a rate k_2. The concentrations of both mRNA and the protein degrade linearly at rates γ_1 and γ_2 respectively. The three dots are meant to imply that additional reactions involving X_1 and X_2 are taking place in the network. Suppose that this system requires that the protein X_2 has an ultrasensitive dose-response that is exclusive to another component in the network. As it stands, X_2 depends linearly on X_1 concentrations which, considering X_1 corresponds to mRNA, likely do not give rise to an ultrasensitive X_2.

To achieve ultrasensitivity in X_2, we turn to the following set of controller reactions proposed in Briat et al. [186]

$$\begin{aligned}
\emptyset &\xrightarrow{\mu} \mathrm{Z}_1 \\
\mathrm{X}_l &\xrightarrow{\theta} \mathrm{X}_l + \mathrm{Z}_2 \\
\mathrm{Z}_1 + \mathrm{Z}_2 &\xrightarrow{\eta} \emptyset \\
\mathrm{Z}_1 &\xrightarrow{k_1} \mathrm{Z}_1 + \mathrm{X}_1
\end{aligned}$$

Assuming mass-action kinetics, we can write

$$\begin{cases}
X_1' = k_1 Z_1 - \gamma_1 X_1, \\
X_l' = k_2 X_1 - \gamma_2 X_l, \\
Z_1' = \mu - \eta Z_1 Z_2, \\
Z_2' = \theta X_l - \eta Z_1 Z_2.
\end{cases}$$

One can verify that $X_l = \mu/\theta$ at steady state by subtracting the equations for Z_1' and Z_2' at steady state which implies that X_l is an absolutely robust species in the above network. In this network, replacing the reaction $\emptyset \xrightarrow{\mu} \mathrm{Z}_1$ with $\mathrm{Y} \xrightarrow{\mu} \mathrm{Y} + \mathrm{Z}_1$ yields that $X_l = \frac{\mu}{\theta} Y$ which does not depend on initial conditions for any other species in the network besides Y. Thus, the modified network now has an absolutely robust dose-response of X_l with respect

to Y. We can repeat this exact analysis with a network that has X_l replaced with the protein X_2. The final result will be once again that $X_2 = \frac{\mu}{\theta} Y$. Hence, to achieve an ultrasensitive X_2 it suffices to find an ultrasensitive Y.

As a potential candidate for species Y, we look at the multisite modification network described by the reactions

$$\mathrm{S}_0 \underset{b_1}{\overset{a_1 E}{\rightleftharpoons}} \mathrm{S}_1 \underset{b_2}{\overset{a_2 E}{\rightleftharpoons}} \mathrm{S}_2 \underset{b_3}{\overset{a_3 E}{\rightleftharpoons}} \mathrm{S}_3$$

where S_i corresponds to the multisite protein S having i modified sites. The transition rate from S_i to S_{i+1} is proportional to the amount of kinase enzyme E. It can be shown that S_3 at steady state has the form

$$S_3 = S_{tot} \frac{A_3 E^3}{1 + A_1 E + A_2 E^2 + A_3 E^3}, \tag{6.6}$$

where $S_{\mathrm{tot}} = \sum_{i=0}^{3} S_i$ and $A_i = \frac{a_1 \ldots a_i}{b_1 \ldots b_i}$. If the rate constants in the multisite system are chosen to be such that A_1 and A_2 become negligibly small, then equation (6.6) resembles the ultrasensitive Hill function with a Hill coefficient of 3. In particular, the steady state of S_3 will respond ultrasensitively to the concentrations of enzymes E.

Now, having Y in our original analysis be replaced by S_3 under conditions of small A_1 and A_2, and combining the controller reactions, multisite protein reactions and our gene expression network yields the system

$$
\begin{aligned}
\mathrm{S}_3 &\xrightarrow{\mu} \mathrm{S}_3 + \mathrm{Z}_1 \\
\mathrm{X}_2 &\xrightarrow{\theta} \mathrm{X}_2 + \mathrm{Z}_2 \\
\mathrm{Z}_1 + \mathrm{Z}_2 &\xrightarrow{\eta} \emptyset \\
\mathrm{Z}_1 &\xrightarrow{k_1} \mathrm{Z}_1 + \mathrm{X}_1 \\
\mathrm{X}_1 &\xrightarrow{\gamma_1} \emptyset \\
\mathrm{X}_1 &\xrightarrow{k_2} \mathrm{X}_1 + \mathrm{X}_2 \\
\mathrm{X}_2 &\xrightarrow{\gamma_2} \emptyset \\
\mathrm{S}_0 \underset{b_1}{\overset{a_1 E}{\rightleftharpoons}} \mathrm{S}_1 &\underset{b_2}{\overset{a_2 E}{\rightleftharpoons}} \mathrm{S}_2 \underset{b_3}{\overset{a_3 E}{\rightleftharpoons}} \mathrm{S}_3 \\
&\vdots
\end{aligned}
$$

As has been shown, the steady state of X_2 is given by $\frac{\mu}{\theta} S_3$. By definition, the system possesses an absolutely robust dose response of X_2 with respect to S_3. The fully bound multisite protein S_3 responds ultrasensitively to enzyme E which immediately implies that X_2 will respond ultrasensitively to E as well. Thus, by incorporating an absolutely robust controller and a multisite modification process into a gene expression network, we were able to take an arbitrary protein within this network and mirror the ultrasensitivity from one species to the specified protein. The generalizability of this approach suggests potential implementations in nature and its simplicity makes a good candidate for the construction of synthetic biological circuits whenever multiple outputs are required to have a predetermined behavior..

6.4 Implementation of absolutely robust osmoregulation in the EnvZ-OmpR system

6.4.1 Introduction to the EnvZ-OmpR system

The EnvZ-OmpR system consists of the sensor kinase EnvZ and the response regulator OmpR which we denote by E and R respectively. E phosphorylates itself into E_p by binding and breaking ATP, denoted by T. E_p catalyzes the transfer of its phosphoryl group to R, giving rise to R_p. Moreover, when E is bound to ATP forming ET, it dephosphorylates R_p. The EnvZ-OmpR can be succinctly described by the following reactions

$$\begin{aligned} \mathrm{E} &\underset{k_2}{\overset{k_1}{\rightleftharpoons}} \mathrm{ET} \xrightarrow{k_{11}N_0} \mathrm{E_p} \\ \mathrm{E_p} + \mathrm{R} &\underset{k_4}{\overset{k_3}{\rightleftharpoons}} \mathrm{E_pR} \xrightarrow{k_5} \mathrm{E} + \mathrm{R_p} \\ \mathrm{ET} + \mathrm{R_p} &\underset{k_7}{\overset{k_6}{\rightleftharpoons}} \mathrm{ETR_p} \xrightarrow{k_8} \mathrm{ET} + \mathrm{R} \end{aligned}$$

presented in work by Shinar et al.[183]. The components of the EnvZ-OmpR system aim to regulate cell osmolarity with respect to its environment. If medium osmolarity is low and cell osmolarity is high, then the solvent such as water rushes through the semi-permeable membrane of the cell. In this case, E exhibits high phosphatase activity which leads to low concentrations of R_p. This leads to R_p binding to high affinity activator sites of the *ompF* gene and upregulates its transcription. In turn, osmolarity inside the cell is lowered. On the other hand, if medium osmolarity is high and cell osmolarity is low, then the solvent within the cell escapes into the medium. In this case, E autophosphorylates at a higher rate thereby increasing the amount of R_p. In turn, R_p binds to low affinity activator sites of the *ompC* gene as well as low affinity suppressor sites of *ompF*. The suppression of *ompF* causes cell osmolarity to rise faster. Ultimately, the underlying mechanisms for osmoregulation rely on increasing or decreasing the amounts of the porin proteins OmpF and OmpC in a manner

that responds adequately to osmotic pressure in the environment [187]. The details by which OmpF and OmpC regulate osmotic pressure are not yet fully understood but their functions have been attributed to their differing pore sizes [188]. In any case, the reaction network model shown above does not account for the osmoregulatory function of the EnvZ-OmpR system. As such, it is unclear whether this network can maintain isotonicity inside the cell in response to environmental perturbations.

In this section, we present a model that incorporates osmolarity and displays absolutely robust isotonicity in the face of osmotic perturbations. We take osmolarity inside the cell to increase at a constant rate possibly due to ions and such particles crossing the semi-permeable cell membrane. Moreover, we assume that the larger size of OmpF pores allows for more efficient release of excess solute into the medium and leads to reductions in cell osmolarity. On the other hand, we assume that the smaller pores of OmpC exist solely for cell maintenance; i.e. for the cell to be able to exchange essential to life particles while in a high osmolarity medium. Ultimately, when the cell is in a high osmolarity medium, it achieves isotonicity by limiting the amount of exiting solute through OmpF while passively letting solute in the medium across its membrane through OmpC.

6.4.2 An osmoregulatory EnvZ-OmpR reaction network model

In the EnvZ-OmpR reaction network shown above, the phosphorylated version of OmpR R_p displays absolute concentration robustness. This property of R_p was previously speculated to play a role in maintaining cell isotonicity but this has not been formally incorporated into a model. Here, we sought to extend the presented EnvZ-OmpR network to carry out osmotic pressure regulation while partially conserving the robustness R_p in the original model as a means to obtain absolutely robust isotonicity. This way, barring extreme depletions of certain biochemical species, the cell will always return to a fixed set point in osmotic pressure

after being temporarily perturbed.

First, we introduce the porin protein OmpF, denoted as F, and incorporate it into the model. We simplify the antagonistic relationship between F and R_p by setting the transcriptional rate of F to be inversely proportional to the concentration of R_p. We also denote the osmolarity inside and outside of the cell by N and N_0 respectively. As mentioned before, N passively increases at a constant rate while F prevents it from becoming exceedingly large by accelerating the rate of internal osmolarity reduction. Furthermore, we set increases in the external osmolarity N_0 to accelerate phosphorylation of EnvZ which subsequently suppresses F and causes osmolarity inside the cell to rise at a faster rate. The extended version of the EnvZ-OmpR model that includes osmoregulation is thus given by the following reactions

$$\begin{aligned}
\mathrm{E} &\underset{k_2}{\overset{k_1}{\rightleftharpoons}} \mathrm{ET} \xrightarrow{k_{11}N_0} \mathrm{E_p} \\
\mathrm{E_p} + \mathrm{R} &\underset{k_4}{\overset{k_3}{\rightleftharpoons}} \mathrm{E_pR} \xrightarrow{k_5} \mathrm{E} + \mathrm{R_p} \\
\mathrm{ET} + \mathrm{R_p} &\underset{k_7}{\overset{k_6}{\rightleftharpoons}} \mathrm{ETR_p} \xrightarrow{k_8} \mathrm{ET} + \mathrm{R} \\
\emptyset &\underset{k_9}{\overset{k_{10}/R_p}{\rightleftharpoons}} \mathrm{F} \\
\emptyset &\underset{\beta F}{\overset{\alpha}{\rightleftharpoons}} \mathrm{N}
\end{aligned}$$

Under mass action kinetics, the new model is described by the following system of differential

equations,

$$\begin{cases} ET' = k_1E - k_2ET - k_{11}N_0ET - k_6ET \cdot R_p + k_7ETR_p + k_8ETR_p, \\ E' = k_2ET + k_5E_pR - k_1E, \\ E_p' = k_{11}N_0ET - k_3E_pR + k_4E_pR, \\ R' = k_4E_pR - k_3E_p \cdot R + k_8ETR_p, \\ E_pR' = k_3E_p \cdot R - k_4E_pR - k_5E_pR, \\ ETR_p' = k_6ET \cdot R_p - k_7ETR_p - k_8ETR_p, \\ R_p' = k_5E_pR - k_6ET \cdot R_p + k_7ETR_p, \\ F' = k_{10}/R_p - k_9F, \\ N' = \alpha - \beta FN. \end{cases}$$

The total number of species that have an attached phosphoryl group is given by

$$P = E_p + R_p + ETR_p + E_pR.$$

Taking the derivative of both sides, substituting the equations for $E_p', R_p', ETR_p', E_pR'$ above, and setting P' at steady state such that $P' = 0$ yields the equation

$$k_{11}N_0ET - k_8ETR_p = 0. \tag{6.7}$$

Moreover, the equation for ETR_p' above at steady state is the following

$$k_6ET \cdot R_p - k_7ETR_p - k_8ETR_p = 0,$$

and solving for ETR_p gives

$$ETR_p = \frac{k_6ET \cdot R_p}{k_7 + k_8}. \tag{6.8}$$

Assuming ETR_p admits a positive steady state, we can substitute equation 6.8 into equation (6.7) to obtain

$$R_p = \frac{k_7 + k_8}{k_6}\left(\frac{k_{11}N_0}{k_8}\right). \tag{6.9}$$

Hence, in this new system, R_p remains robust to all species except to the external osmolarity N_0. However, this is necessary for the system to properly respond to changes in osmolarity.

In contrast to osmolarity, osmotic pressure is a direct result of differences between osmolarity inside and outside the cell. As such, we take N/N_0 to be a general indicator of osmotic pressure within the cell. If the cell is isotonic to its environment, then we would expect that N/N_0 is a constant value. In our system, we have that internal osmolarity changes according to the equation

$$N' = \alpha - \beta F N = 0,$$

and so at steady state the osmolarity becomes

$$N = \frac{\alpha}{\beta F}. \tag{6.10}$$

Moreover, when $F' = 0$ at steady state, we can derive the equation

$$\frac{k_{10}}{R_p} - k_9 F = 0,$$

which gives that

$$F = \frac{k_{10}}{k_9 R_p}. \tag{6.11}$$

Substituting equation 6.11 into equation 6.10 gives the internal osmolarity as a function of

R_p, specifically

$$N = \frac{\alpha k_9 R_p}{\beta k_{10}}.$$

Finally, substituting R_p as given in equation 6.9 yields that

$$\frac{N}{N_0} = \frac{k_{11} k_9 (k_7 + k_8)\alpha}{k_8 k_6 k_{10} \beta}, \tag{6.12}$$

proving that osmotic pressure in this system is absolutely robust, that is, it will converge to the same value regardless of perturbations to the osmotic concentrations.

To observe the effect of absolutely robust osmoregulation in action, we performed a deterministic simulation of the model and plotted osmotic pressure over time with a perturbation at the halfway point (Figure 6.1). At first, the system deviates from its initial high osmotic pressure by rapidly reducing pressure and subsequently approaching an isotonic steady state of 1. Then, at $time = 30$ the system is suddenly perturbed by a sharp reduction in osmotic pressure. However, the system is able to once again return to the original set point in osmotic pressure due to its absolutely robust topology with respect to N/N_0.

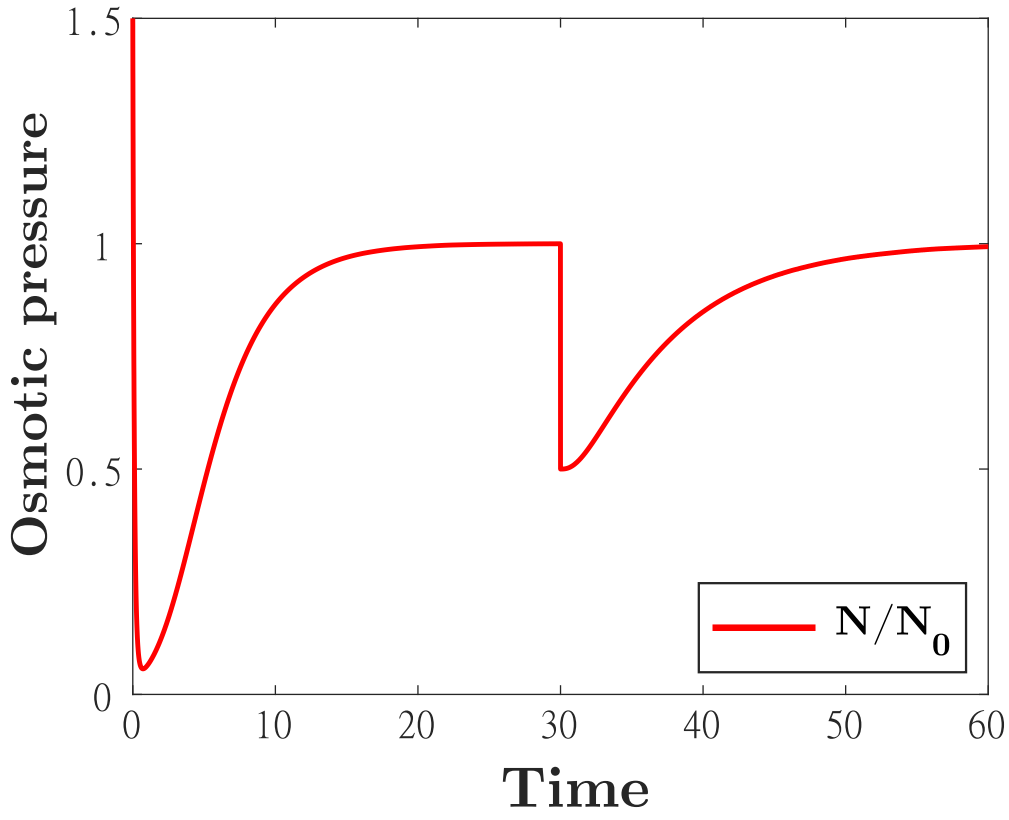

Figure 6.1: Osmotic pressure in our extended EnvZ-OmpR model is absolutely robust and returns to its original set point after environmental perturbations. A deterministic simulation showing osmotic pressure over time in our extended EnvZ-OmpR model. At first, osmotic pressure adjusts to approach isotonicity corresponding to a steady state of 1. After a perturbation is introduced at the halfway point, isotonicity is lost but the system once again returns to isotonicity due its absolutely robust topology with respect to N/N_0.

Chapter 7

Discussion

Gene expression can be controlled through distinct regulations of the chromatin topology that range from the organization of shadow enhancers to the remodeling of chromatin density regions. Each of these strategies can be framed in the context of optimizing for certain properties of gene expression. For example, when taken in this context, shadow enhancers with distinct binding sites might be conserved across many organisms due to their ability of minimizing expression noise compared to enhancers that are built differently [1]. Similarly, chromatin remodeling can be taken to be a mechanism for optimizing ultrasensitive dose-responses to gene-activating TFs which, in turn, leads to lesser noise in gene expression by preventing small fluctuations in upstream signals from turning on genes [3]. In particular, when we take any gene regulatory mechanism as potentially optimizing a feature of gene transcription, these mechanisms are good candidates to be modeled using computational and mathematical approaches. In doing so, we can attempt to distill which features of the system are sufficient or necessary for optimizing properties of interest. The ramifications of this modeling approach ultimately lead to a more comprehensive interpretation of experimental results, insights that transcend the limitations of our experimental tools, and the generation of a new set of hypotheses that are able to guide future experimentation.

In this work, we have focused on modeling gene regulation using CRNs under stochastic dynamics. CRNs are a well-studied modeling approach that has been increasingly used to understand biological systems in recent decades. The wide use of these networks has led to the development of multiple mathematical and computational methods to calculate or approximate the behavior of each species in the network over time [4]. Moreover, the ability to model each network under stochastic dynamics makes them suitable as a framework for understanding gene regulation which typically involves low counts of gene-regulatory elements, switch-like behavior, and second-order moment experimental data [189, 190].

We primarily worked on two gene regulatory systems that precede transcription and arise from regulation of chromatin topology, namely, shadow enhancers as mediators of promoter activation and chromatin remodeling as a modulator of chromatin accessibility under histone acetylation. These two systems reside at the scale of the genome which lies beyond what our current imaging techniques can identify with enough detail in order to derive the dynamics of each regulatory element. Furthermore, each system operates under low numbers of such regulatory elements. In particular, many Gap genes in *Drosophila* genes such as *hunchback*, *Kruppel*, and *knirps* are regulated by only 2 shadow enhancers while the average *Saccharomyces cerevisiae* gene has around 1.4kb which should span approximately 10 nucleosomes [191, 192, 193]. Hence, shadow enhancers and the chromatin are ideal candidates for computational and mathematical modeling and their dynamics are highly suitable for a stochastic approach. Using CRNs to describe these systems allowed for simulated outputs of the gene expression properties that they aim to modulate within a context of being regulatory systems. Under this framework, we were able to derive a set of conditions in each model that are sufficient for recapitulating experimental data and for modulation that can lead to further optimization of such properties. We expect that these results will eventually lead to the development of new experiments that can further uncover the functions of enhancers under stress and elucidate mechanisms for chromatin remodeling and architecture.

7.1 Shadow enhancers can suppress input TF noise through distinct regulatory logic

In Chapter 2 we described a particular system of two enhancers that are known to regulate the transcription of the *Kruppel* gene in *Drosophila*. This system was used as a basis to argue that shadow enhancers lead to lower noise in gene expression than duplicated or single enhancers by having distinct TF binding sites from one another. To prove or disprove this hypothesis, real-time transcriptional data was collected from embryos containing the wildtype shadow enhancers as well as duplicated enhancers and single enhancers. Using this data, the noise in transcription can be calculated for each of these enhancer constructs. Since duplicated enhancers share all their TFs, it follows that equivalent measures of noise between the constructs would disprove the original hypothesis. However, the experimental data showed that the wildtype shadow enhancers displayed the lowest expression noise thus suggesting that TF separation between enhancers could be a plausible explanation for the observed noise buffering effects.

Nevertheless, enhancers operate inside a cell nucleus that is crowded with a platitude of different regulatory proteins and genomic regions that interact in a three-dimensional space [194]. Moreover, current imaging techniques do not allow for concurrent tracking of real-time dynamics of mRNA and several regulating TFs. Hence, it is difficult to conclude that TF separation is a sufficient condition for lowering expression noise. However, to provide further evidence for this hypothesis, we designed a CRN to model the *Kruppel* shadow enhancers. This model was designed to have the minimal amounts of components required to recapitulate the enhancer dynamics described by the real-time mRNA experimental data. As a result, by abstracting away all unnecessary complexity, the only drivers of transcription were the TFs themselves. In other words, no other regulatory element besides the fluctuating TFs could activate gene expression. Hence, by also designing models for the duplicated shadow

enhancers that are based upon the same network topology and assumptions, we were able to compare the measurements of noise between these models and determine whether TF separation alone is indeed sufficient for buffering noise from upstream inputs. In the end, the models also suggested that wildtype shadow enhancers appear to buffer transcriptional noise better than duplicated enhancers through the separation of their TFs.

7.2 Shadow enhancers mediate trade-offs between transcriptional noise and fidelity

After having developed a *Kruppel* enhancer model that can partially recapitulate the dynamics of transcription inside a *Drosophila* embryo, we wished to use such a model to answer another question: can the transcriptional properties of shadow enhancers be recapitulated by a lesser number of enhancers that are bound by an equivalent set of TFs? Chapter 3 presented an attempt to answer these questions by modifying the *Kruppel* model in Chapter 2 to include various numbers of enhancers and binding sites. This time, due to the sheer number of models and simulations, stochastic dynamics for each model were approximated and subsequently summarized as transcriptional noise and fidelity. These two properties are of relevance when considering that making a viable organism likely requires that expression noise during development not be above a certain threshold while fidelity remains above another one. By examining this array of network models that were derived from our previously validated *Kruppel* model, we were able to conclude that shadow enhancers, when they behave additively, might be the result of mere genetic drift as opposed to active selection pressures. On the other hand, sub or superadditive enhancers were noted to cause certain trade-offs in transcriptional modulation of noise and fidelity suggesting that they might widen the fitness landscape in ways that are not possible for a single enhancer.

7.3 Non-cooperative mechanism for bounded and ultrasensitive chromatin remodeling

The work in Chapter 4 focused on chromatin remodeling under histone acetylation. The purpose of this process is to permit or restrict access of transcriptional enzymes to certain regions of DNA by relaxing or constricting certain regions of the chromatin. This is carried out by modifications to the histone tails such as acetylation, which typically opens the chromatin, and methylation which has the opposite effect [147, 148, 149, 150, 151]. Chromatin remodeling has been noted to create sharp boundaries between high and low density chromatin that ultimately allow precise expression or activation of genetic regions without ambiguity and with high tolerance to noise from upstream signals [121, 122, 123, 124]. To achieve this type of regulation, chromatin accessibility needs to respond ultrasensitively to TFs in charge of recruiting HATs [11]. Ultimately, however, it is still not fully understood how chromatin remodeling can achieve this level of ultrasensitivity and yield sharp boundaries between chromatin regions

In order to understand how ultrasensitive chromatin remodeling might operate, we presented a graph-based model of the chromatin in Chapter 4. Previous modeling has showed potential avenues for achieving ultrasensitive chromatin remodeling but usually relying on cooperative assumptions which can lead to defects such as uncontrolled chromatin expansion [11, 127, 129, 130]. In our model, we relied solely on emergent properties of the chromatin and stochastic multisite modifications which proved sufficient for recapitulating ultrasensitive chromatin remodeling without the need for cooperativity. A CRN of histone tail acetylation was used to show that the model responds ultrasensitively to TF concentrations in charge of HAT recruitment. Overall, the model suggested that sharp boundaries between chromatin accessibility regions and ultrasensitive TF dose-responses may be emergent from topological features of the chromatin architecture and nonessential modification sites which

could potentially complement previous approaches that have focused solely on biochemical modifications.

7.4 Function saturation as a mechanism for ultrasensitivity

Finally, chapter 5 did not focus on any particular gene regulatory mechanism but on a property which many of these mechanisms aim to optimize: ultrasensitivity. The ability to respond ultrasensitively to a variety of chemical and environmental signals is desired in gene regulation due to a reduction in ambiguity or noise in the state of system [166, 167]. By constructing ultrasensitive responses, we can prevent insignificant fluctuations in the input to affect the corresponding output. Many examples of ultrasensitive mRNA regulation have been noted by which the surpassing of a given threshold causes sharp transitions into a different but usually active state [168, 169, 170]. There exist several mechanisms for achieving biochemical ultrasensitivity [34, 195, 171, 174, 175, 176], and in this chapter we proposed an additional one. In particular, we showed that by introducing absolutely robust species into polymerization networks we can give rise to saturated processes. This was significant as polymerization is typically not considered in the context of ultrasensitivity as it cannot achieve a saturation point. However, polymerization plays many roles in biochemical processes and has been linked to gene regulatory processes [35, 36]. We expect that these results can be used to explain the ultrasensitivity achieved by composite processes that form biochemical cascades as well as guide the design of synthetic biological circuits that aim to optimize ultrasensitive behavior.

7.5 Model limitations and future work

As is the case with all modeling, however, CRNs and our stochastic approach suffer from certain drawbacks. The fundamental assumption of mass action kinetics underlying our modeling approaches typically relies on the assumption of well-mixed chemical species inside a some form of vat [196, 5]. The fundamental constraint that this assumption imposes is that nuances in spatial dimensions are not taken into account. However, biochemical species inside cell nuclei interact in a three-dimensional space where the concentrations of such species can highly vary across the space of interest [194]. Hence, to counter this lack of spatial dimensionality, we limited both our enhancer and chromatin CRN models to reasonably small neighborhoods of interactions. In the case of enhancers, our models were assumed to operate in the vicinity of the promoter which allowed us to approximate TF fluctuations by introduction of nonconservative reactions rather than having to track individual TFs across space. Meanwhile, our chromatin model limited regions of interest to 16 nucleosomes which, in conjunction with saturation of HATs and TFs, was tentatively sufficient to neglect the spatial dimensions of the chromatin structure when calculating dose-responses with respect to TFs. Nevertheless, there are biochemical processes that cannot be modeled without spatial dimensions. For this reason, we expect that our modeling approaches can be made complementary with models that perhaps sacrifice detail at the level of histone modifications in exchange for more detail at the level of nucleosome remodeling, which is an inherently spatial process. Integration of both of these approaches would likely be the next logical step in modeling gene regulatory systems at the scale of the nucleus.

In addition to the results obtained so far, the models developed in this work have generated a wide range of questions that still remain to be answered. The *Kruppel* model in Chapter 2 was made to recapitulate data from different enhancers constructs to determine differences in noise expression between them. However, the observation that shadow enhancers may act as expression noise buffers was first done in the context of environmental stress, in partic-

ular, temperature. Therefore, given the simplicity of our model, it would be of interest to understand how the model needs to be adapted in order to recapitulate the already available data of *Kruppel* gene expression under stressful temperatures [1]. These adaptations could happen at the level of the network topology or the parameters themselves and potentially generate complementary hypotheses for the observed reductions in expression noise to the one developed in this chapter.

Another feature that could be incorporated in our enhancer model is that of repressors and their respective interactions with activators. In our model we implicitly assumed that enhancers are only bound by activating TFs but in reality many of these proteins also repress gene activity [197]. Naturally, it would be of interest to include these repressors into our network and determine the corresponding effects on noise when compared to additional enhancers. In addition, several modifications could be made to the model to further incorporate known biochemical elements that are involved in enhancer-mediation of transcription albeit at the expense of losing the simplicity of the network which greatly facilitated the original analysis. This and similar modifications could be significant for explaining the quantitative discrepancy between the simulated and experimental noise and allele correlation measurements. As before, this understanding could pinpoint the specific workings that favor shadow enhancers as gene regulatory systems.

The models generated in Chapter 3 proved useful in determining the selection pressures or lack thereof that act on shadow enhancers. Nevertheless, there is still is a need to explore whether the predictions of such models can hold to experimental observations. As was shown in Chapter 2 it is possible to engineer flies that possess duplicated enhancers. By generating a series of these flies with up to 4 *Kruppel* enhancers one could begin by determining whether predictions of decreasing noise with enhancer numbers under our duplication scheme are true. Measuring fidelity in wildtype organisms is challenging, however, recent developments in synthetic biology might permit the incorporation of these circuits into *Drosophila*

embryos [119, 120]. Then, the activating inputs can be varied in these enhancers systems thereby allowing for an estimation of transcriptional fidelity as was done for our models. Ultimately, this would at least provide a fair test to the predictions made by our models which, if true, would set them in a stronger foundation to be applied to different enhancer systems.

We modeled the chromatin in Chapter 4 and showed that independent nucleosome interactions with multisite interactions and a topology prone to percolation effects were sufficient for achieving ultrasensitivity in chromatin remodeling. However, our comparison to experimental data was limited to using a pharmaceutical inhibitor of HATs as a proxy for acetylation in our chromatin accessibility dose-response. To further validate our chromatin model, the ideal scenario would involve measuring chromatin accessibility and histone acetylation levels within a given cell. This is typically achieved through techniques as ChIP-Seq and ATAQ-Seq but it is not possible to perform these assays concurrently on the same individual cell as far as we are aware. Hence, while validation of this model might not be possible at the moment, we expect that further progress of these techniques in this direction would eventually allow the level of data collection described. Once validated, our model could be used to understand chromatin remodeling sensitivity across organisms and uncover the still unclear architecture of the chromatin by comparison of dose-responses between distinct 3D configurations of the model.

Our new mechanism for ultrasensitivity that allowed for saturation of multiple functions was presented in Chapter 5. However, while promising, this mechanism still needs to be applied to concrete biochemical regulators and cascades. Given that polymerization and similar processes play a large role in cellular chemistry, we suggest that finding such cases would be doable given that there are measurements of dose-responses from which Hill coefficients can be derived. Nevertheless, as was the case in Chapter 4, we might find ourselves limited in finding such data outside the context of using pharmaceuticals as proxies for biologically

derived regulators. Hence, once again, we would suggest that incorporation of synthetic biological circuits into well-studied bacterial models such as *E. Coli* could suggest whether our saturation mechanism is compatible with other regulators inside the cell [198].

7.6 Conclusions

We have discussed different processes that lead to gene regulation and developed models to explain the underlying mechanisms behind them. For example, we showed that TF separation between enhancers and nonessential acetylation sites in the chromatin may modulate different aspects of transcription such as noise and ultrasensitivity. However, it is plausible that such mechanisms might be generalizable to other gene regulatory processes. In the following paragraphs we discuss how regulation by enhancers and chromatin enzymes could affect each other and suggest ways by which the mechanisms underlying one system might be implemented in the other.

In Chapter 2 we provided evidence that TF separation between enhancers has a buffering effect on upstream TF noise. It is plausible that this mechanism can be generalized and implemented within other gene regulatory mechanisms such as chromatin remodeling. For example, the existence of different kinds of acetylation enzymes could play a role in reducing unintended expansion of chromatin regions. By potentially having different kinds of modification enzymes, the chromatin could limit the effect of upstream perturbations on histone acetylation enzymes in order to yield the expected transcriptional output. Meanwhile, Chapter 3 showed that increases in TF binding sites led to lower noise in gene expression. As we explained in Chapter 4, HAT enzymes are first recruited by TFs to subsequently acetylate a chromatin neighborhood. An increase in TF binding sites could tentatively lower noise in upstream HAT expression and, consequently, require lower levels of ultrasensitivity for proper chromatin remodeling.

Conversely, the mechanisms discussed that underlie chromatin remodeling may be applied in further inquiry of the workings of shadow enhancers. In Chapter 4 we made mention of nonessential modification sites as key features for higher ultrasensitivity. The concept of nonessential sites as boosters for ultrasensitivity has been proven for general theoretical constructs [30], and, as such, it could be an additional mechanism that enhancers with multiple binding sites could use for increasing the ultrasensitivity of the gene they regulate. Specifically, if nonessential TF binding sites are present within enhancers, then, a critical concentration of TFs would be needed to activate the enhancers while small fluctuations in TFs due to noise would not have this effect.

As we discussed in Chapter 4, longer stretches of the chromatin correspond to higher levels of ultrasensitivity in chromatin remodeling while in chapter 3 we showed that larger numbers of enhancers can decrease transcription noise under certain assumptions. Supposedly, a larger number of enhancers that regulate a gene would require unpacking larger swaths of the chromatin. Therefore, by having more enhancers, the ultrasensitivity of expression for a given gene could increase as the chromatin that contains it is itself more ultrasensitive with respect to acetylation. These assumptions are plausible as shown by the work of Zhang et al. in Figure 7.1 where the three dimensional distance between DNA regions and the Mir9-2 promoter is shown to be minimized at the locations of the enhancers [199]. It can be reasonably speculated that a considerable region of the chromatin needs to be unpacked in order for the DNA to freely fold in the optimal pattern that allows these enhancers to maximally approach the promoter. Thus, in conjunction with our results from Chapter 4, unpacking a large swath of chromatin with more enhancers would yield higher ultrasensitivity than smaller regions with lesser enhancers.

Shadow enhancers and chromatin remodeling are both gene regulatory mechanisms where the latter might be upstream from the former and vice-versa thereby creating a network of feedback loops. TFs are proteins that are also the result of gene expression. A kind of

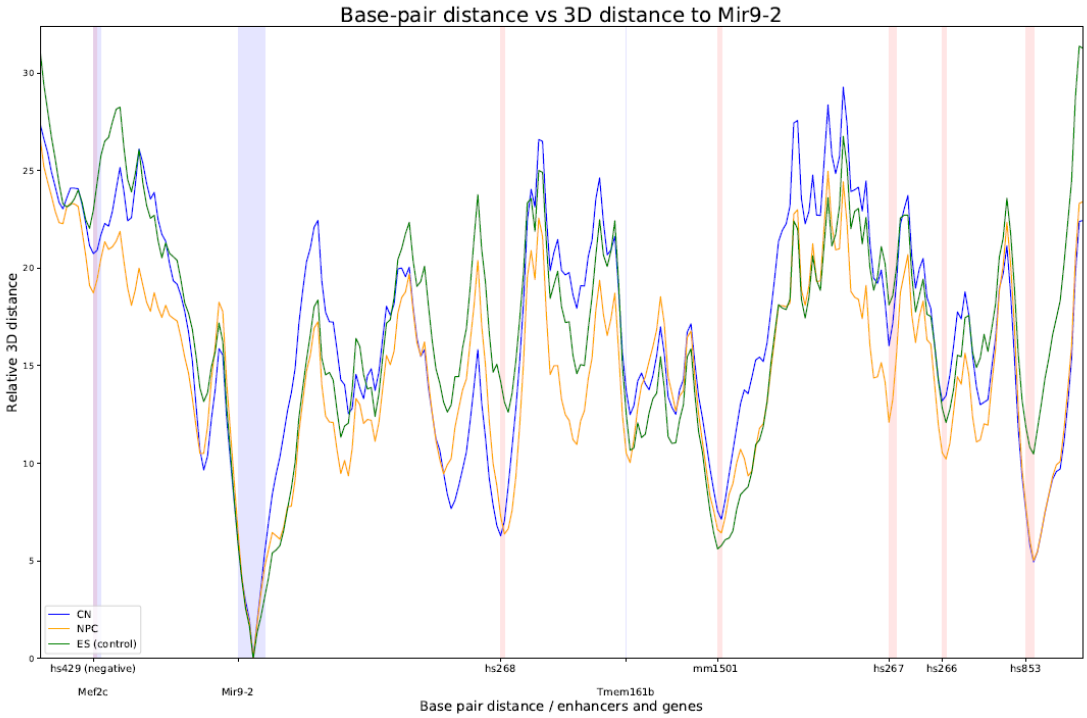

Figure 7.1: A plot showing the predicted distance in three-dimensional space between DNA regions and the non-coding mRNA gene Mir9-2 [199]. The horizontal axis shows base pair locations and the vertical axis the three dimensional distance to Mir9-2. This computational analysis by Zhang et al. accurately predicted the location of enhancers that regulate Mir9-2 (highlighted in yellow and labeled in the x axis) by finding the minima within three-dimensional chromatin interaction data [199]. The data suggests that a swath of the chromatin is folding in particular manner in order to bring all these enhancers in the proximity of the Mir9-2 promoter.

TF was mentioned in Chapter 4 to recruit HAT enzymes in order to acetylate and loosen a chromatin region. It is plausible to say, then, that whenever the TFs in charge of chromatin modifications are less noisy, then the ultrasensitivity required for chromatin expansion does not have to be as high. Regulation of the TF genes by multiple shadow enhancers could be a tentative mechanism for lowering chromatin remodeling noise. Conversely, enhancers are regions of DNA wrapped around chromatin that need to be expanded for them to be active and organized in the proper higher order structures that minimize promoter distance. While shadow enhancers might buffer noise from their TFs, it is clear that a robust chromatin remodeling process is also needed for enhancers to optimally regulate gene expression. In summary, these ideas suggest that a unified CRN model of enhancers and the chromatin could be used for understanding the feedback loops between these two systems. The work done here is a tentative foundation for the development of such models of a similar style to that by Nousiainen et al [108].

Chapter 5 proposed that ultrasensitivity can be modulated by altering dose-response saturation levels through absolutely robust species. This could be implemented in shadow enhancers through forced saturation of their TFs. By doing so, we would raise the ultrasensitivity of the expression of TF that are required for enhancer activation which, in turn, could give rise to ultrasensitive enhancer activation. It might follow that the ultrasensitivity of the regulated gene would also increase as either all shadow enhancers are active or they are not. In the case of chromatin remodeling, the effect of forced saturation on the proportion of acetylated histones was actually displayed in Figure 4.8 of Chapter 4 where modulation of a single parameter led to earlier saturation of the DNA accessibility dose-response. In particular, the Hill coefficient increased to a value of nearly 5 for the lowest saturation measured. While the mechanism at play here does not appear to be the one described in Chapter 5, there is no apparent reason why the same behavior in Figure 4.8 could not be implemented using absolute robustness as described in this mechanism. It would likely suffice to complement the absolutely robust toy model with the acetylated histones A shown in the network

in Figure 4.6. As we have suggested, the mechanism in Chapter 5 may be implemented in multiple gene regulatory systems due its generality and straightforward incorporation with the original network.

This dissertation has shown that stochastic and deterministic CRNs are well-suited to the study of chromatin regulation. Moreover, the large suite of mathematical and computational tools provided by the study of CRNs has proved to be useful for efficiently simulating systems at the genetic level and distilling the properties that allow for such systems to optimize given metrics of gene expression. By identifying the most relevant components in the network and abstracting away the less relevant, we can efficiently and sometimes analytically determine how the system will react to changes in the environment which may manifest as topological changes to the network or updated parameter values. Ultimately, having this family of models applied to the regulation of cellular biochemical processes may accelerate our understanding of genes and their interaction with a constantly changing environmental substrate.

Bibliography

[1] Rachel Waymack et al. "Shadow enhancers can suppress input transcription factor noise through distinct regulatory logic". In: *eLife* 9 (Aug. 17, 2020), e59351. ISSN: 2050-084X. DOI: 10.7554/eLife.59351. URL: https://elifesciences.org/articles/59351 (visited on 04/06/2021).

[2] Yaqi Wang et al. "Characterization of the chromatin accessibility in an Alzheimer's disease (AD) mouse model". In: *Alzheimer's Research & Therapy* 12.1 (Dec. 2020), p. 29. ISSN: 1758-9193. DOI: 10.1186/s13195-020-00598-2. URL: https://alzres.biomedcentral.com/articles/10.1186/s13195-020-00598-2 (visited on 10/14/2021).

[3] Alvaro Fletcher, Ruonan Zhao, and German Enciso. "Non-cooperative mechanism for bounded and ultrasensitive chromatin remodeling". In: *Journal of Theoretical Biology* 534 (Feb. 7, 2022), p. 110946. ISSN: 1095-8541. DOI: 10.1016/j.jtbi.2021.110946.

[4] Pavel Loskot, Komlan Atitey, and Lyudmila Mihaylova. "Comprehensive Review of Models and Methods for Inferences in Bio-Chemical Reaction Networks". In: *Frontiers in Genetics* 10 (2019). ISSN: 1664-8021. URL: https://www.frontiersin.org/articles/10.3389/fgene.2019.00549 (visited on 07/24/2022).

[5] Martin Feinberg. *Foundations of Chemical Reaction Network Theory*. Vol. 202. Applied Mathematical Sciences. Cham: Springer International Publishing, 2019. ISBN: 978-3-030-03857-1 978-3-030-03858-8. DOI: 10.1007/978-3-030-03858-8. URL:

https://link.springer.com/10.1007/978-3-030-03858-8 (visited on 08/10/2022).

[6] Atefeh Kazeroonian et al. "CERENA: ChEmical REaction Network Analyzer—A Toolbox for the Simulation and Analysis of Stochastic Chemical Kinetics". In: *PLOS ONE* 11.1 (Jan. 25, 2016). Ed. by Dennis Salahub, e0146732. ISSN: 1932-6203. DOI: 10.1371/journal.pone.0146732. URL: https://dx.plos.org/10.1371/journal.pone.0146732 (visited on 04/07/2021).

[7] Tong Ihn Lee and Richard A. Young. "Transcriptional Regulation and its Misregulation in Disease". In: *Cell* 152.6 (Mar. 14, 2013), pp. 1237–1251. ISSN: 0092-8674. DOI: 10.1016/j.cell.2013.02.014. URL: https://www.ncbi.nlm.nih.gov/pmc/articles/PMC3640494/ (visited on 07/07/2022).

[8] N. Frankel et al. "Phenotypic robustness conferred by apparently redundant transcriptional enhancers". In: *Nature* 466 (2010). PMID: 20512118, pp. 490–493. DOI: 10.1038/nature09158. URL: https://doi.org/10.1038/nature09158,.

[9] M.W. Perry et al. "Shadow enhancers foster robustness of Drosophila gastrulation". In: *Current Biology* 20 (2010). PMID: 20797865, pp. 1562–1567. DOI: 10.1016/j.cub.2010.07.043. URL: https://doi.org/10.1016/j.cub.2010.07.043,.

[10] M. Osterwalder et al. "Enhancer redundancy provides phenotypic robustness in mammalian development". In: *Nature* 554 (2018). PMID: 29420474, pp. 239–243. DOI: 10.1038/nature25461. URL: https://doi.org/10.1038/nature25461,.

[11] Kim Sneppen, Mille A. Micheelsen, and Ian B. Dodd. "Ultrasensitive gene regulation by positive feedback loops in nucleosome modification". In: *Molecular Systems Biology* 4.182 (2008), pp. 1–5. DOI: 10.1038/msb.2008.21.

[12] Nikolaos Stefanakis, Ines Carrera, and Oliver Hobert. "Regulatory Logic of Pan-Neuronal Gene Expression in C. elegans". In: *Neuron* 87.4 (Aug. 19, 2015), pp. 733–750. ISSN: 1097-4199. DOI: 10.1016/j.neuron.2015.07.031.

[13] Patrick Torbey et al. “Cooperation, cis-interactions, versatility and evolutionary plasticity of multiple cis-acting elements underlie krox20 hindbrain regulation”. In: *PLOS Genetics* 14.8 (Aug. 6, 2018). Publisher: Public Library of Science, e1007581. ISSN: 1553-7404. DOI: 10.1371/journal.pgen.1007581. URL: https://journals.plos.org/plosgenetics/article?id=10.1371/journal.pgen.1007581 (visited on 03/28/2022).

[14] Yongsu Jeong et al. “A functional screen for sonic hedgehog regulatory elements across a 1 Mb interval identifies long-range ventral forebrain enhancers”. In: *Development (Cambridge, England)* 133.4 (Feb. 2006), pp. 761–772. ISSN: 0950-1991. DOI: 10.1242/dev.02239.

[15] Karl R. Degenhardt et al. “Distinct enhancers at the Pax3 locus can function redundantly to regulate neural tube and neural crest expressions”. In: *Developmental Biology* 339.2 (Mar. 15, 2010), pp. 519–527. ISSN: 1095-564X. DOI: 10.1016/j.ydbio.2009.12.030.

[16] C. M. Allan, D. Walker, and J. M. Taylor. “Evolutionary duplication of a hepatic control region in the human apolipoprotein E gene locus. Identification of a second region that confers high level and liver-specific expression of the human apolipoprotein E gene in transgenic mice”. In: *The Journal of Biological Chemistry* 270.44 (Nov. 3, 1995), pp. 26278–26281. ISSN: 0021-9258. DOI: 10.1074/jbc.270.44.26278.

[17] Qiliang Li et al. “Locus control regions”. In: *Blood* 100.9 (Nov. 1, 2002), pp. 3077–3086. ISSN: 0006-4971. DOI: 10.1182/blood-2002-04-1104.

[18] E. Cannavo et al. “Shadow enhancers are pervasive features of developmental regulatory networks”. In: *Current Biology* 26 (2016). PMID: 26687625, pp. 38–51. DOI: 10.1016/j.cub.2015.11.034. URL: https://doi.org/10.1016/j.cub.2015.11.034,.

[19] David U. Gorkin et al. “An atlas of dynamic chromatin landscapes in mouse fetal development”. In: *Nature* 583.7818 (July 2020). Number: 7818 Publisher: Nature

Publishing Group, pp. 744–751. ISSN: 1476-4687. DOI: 10.1038/s41586-020-2093-3. URL: https://www.nature.com/articles/s41586-020-2093-3 (visited on 03/29/2022).

[20] Robin Andersson et al. "An atlas of active enhancers across human cell types and tissues". In: *Nature* 507.7493 (Mar. 2014). Number: 7493 Publisher: Nature Publishing Group, pp. 455–461. ISSN: 1476-4687. DOI: 10.1038/nature12787. URL: https://www.nature.com/articles/nature12787 (visited on 03/29/2022).

[21] Evgeny Z Kvon et al. "Enhancer redundancy in development and disease". In: *Nature Reviews Genetics* (2021), pp. 1–13.

[22] J.W. Hong, D.A. Hendrix, and M.S. Levine. "Shadow enhancers as a source of evolutionary novelty". In: *Science* 321 (2008). PMID: 18772429, p. 1314. DOI: 10.1126/science.1160631. URL: https://doi.org/10.1126/science.1160631,.

[23] C. Scholes et al. "Signal integration by shadow enhancers and enhancer duplications varies across the Drosophila Embryo". In: *Cell Reports* 26 (2019). celrep.2019.01.115, PMID: 30811990, pp. 2407–2418. DOI: 10.1016/j.. URL: https://doi.org/10.1016/j..

[24] J.P. Bothma et al. "Enhancer additivity and non-additivity are determined by enhancer strength in the Drosophila embryo". In: *eLife* 4:e07956 (2015). URL: https://doi.org/10.7554/.

[25] Joao Hespanha. "Moment closure for biochemical networks". In: *2008 3rd International Symposium on Communications, Control and Signal Processing*. 2008 3rd International Symposium on Communications, Control and Signal Processing (ISCCSP). St. Julian's, Malta: IEEE, Mar. 2008, pp. 142–147. ISBN: 978-1-4244-1687-5. DOI: 10.1109/ISCCSP.2008.4537208. URL: http://ieeexplore.ieee.org/document/4537208/ (visited on 06/27/2022).

[26] Shinji Honda et al. “The DMM complex prevents spreading of DNA methylation from transposons to nearby genes in Neurospora crassa”. In: *Genes and Development* 24.5 (2010), pp. 443–454. DOI: 10.1101/gad.1893210.

[27] Gong Hong Wei, De Pei Liu, and Chih Chuan Liang. “Chromatin domain boundaries: Insulators and beyond”. In: *Cell Research* 15.4 (2005), pp. 292–300. DOI: 10.1038/sj.cr.7290298.

[28] Leonid A. Mirny. “Nucleosome-mediated cooperativity between transcription factors”. In: *Proceedings of the National Academy of Sciences of the United States of America* 107.52 (2010), pp. 22534–22539. DOI: 10.1073/pnas.0913805107.

[29] Abbas Ali Saberi. “Recent advances in percolation theory and its applications”. In: *Physics Reports* 578 (2015), pp. 1–32. ISSN: 0370-1573. DOI: https://doi.org/10.1016/j.physrep.2015.03.003.

[30] Liming Wang, Qing Nie, and German Enciso. “Nonessential sites improve phosphorylation switch”. In: *Biophysical Journal* 99.6 (2010), pp. L41–L43. DOI: 10.1016/j.bpj.2010.07.030.

[31] J. T. Finch and A. Klug. “Solenoidal model for superstructure in chromatin”. In: *Proceedings of the National Academy of Sciences of the United States of America* 73.6 (1976), pp. 1897–1901. DOI: 10.1073/pnas.73.6.1897.

[32] Anushree Chatterjee, Yiannis Kaznessis, and Wei-Shou Hu. “Tweaking biological switches through a better understanding of bistability behavior”. In: *Current opinion in biotechnology* 19.5 (Oct. 2008), pp. 475–481. ISSN: 0958-1669. DOI: 10.1016/j.copbio.2008.08.010. URL: https://www.ncbi.nlm.nih.gov/pmc/articles/PMC2766094/ (visited on 07/24/2022).

[33] Qiang Zhang, Sudin Bhattacharya, and Melvin E. Andersen. “Ultrasensitive response motifs: basic amplifiers in molecular signalling networks”. In: *Open Biology* 3.4 (Apr.

2013), p. 130031. ISSN: 2046-2441. DOI: 10.1098/rsob.130031. URL: https://royalsocietypublishing.org/doi/10.1098/rsob.130031 (visited on 05/08/2021).

[34] Germán A. Enciso. "Multisite Mechanisms for Ultrasensitivity in Signal Transduction". In: *Nonautonomous Dynamical Systems in the Life Sciences*. Ed. by Peter E. Kloeden and Christian Pötzsche. Cham: Springer International Publishing, 2013, pp. 199–224. ISBN: 978-3-319-03080-7. DOI: 10.1007/978-3-319-03080-7_6. URL: https://doi.org/10.1007/978-3-319-03080-7_6.

[35] Jeyantt Sankaran et al. "Gene regulation through dynamic actin control of nuclear structure". In: *Experimental Biology and Medicine* 244.15 (Nov. 2019), pp. 1345–1353. ISSN: 1535-3702. DOI: 10.1177/1535370219850079. URL: https://www.ncbi.nlm.nih.gov/pmc/articles/PMC6880144/ (visited on 07/24/2022).

[36] C Matthew Hope et al. "Tuned polymerization of the transcription factor Yan limits off-DNA sequestration to confer context-specific repression". In: *eLife* 7 (Nov. 9, 2018). Ed. by Philip A Cole and Steve Gisselbrecht. Publisher: eLife Sciences Publications, Ltd, e37545. ISSN: 2050-084X. DOI: 10.7554/eLife.37545. URL: https://doi.org/10.7554/eLife.37545 (visited on 07/24/2022).

[37] Leonard Campanello et al. "Signaling through polymerization and degradation: Analysis and simulations of T cell activation mediated by Bcl10". In: *PLOS Computational Biology* 17.5 (May 20, 2021). Publisher: Public Library of Science, e1007986. ISSN: 1553-7358. DOI: 10.1371/journal.pcbi.1007986. URL: https://journals.plos.org/ploscompbiol/article?id=10.1371/journal.pcbi.1007986 (visited on 07/24/2022).

[38] M. Santillán. "On the Use of the Hill Functions in Mathematical Models of Gene Regulatory Networks". In: *Mathematical Modelling of Natural Phenomena* 3.2 (2008). Publisher: EDP Sciences, pp. 85–97. ISSN: 0973-5348, 1760-6101. DOI: 10.1051/mmnp:2008056. URL: https://www.cambridge.org/core/journals/mathematical-

modelling-of-natural-phenomena/article/abs/on-the-use-of-the-hill-functions-in-mathematical-models-of-gene-regulatory-networks/985926A8D13CB5E075C49 (visited on 07/24/2022).

[39] A. V. Hill. "The Combinations of Haemoglobin with Oxygen and with Carbon Monoxide. I". In: *The Biochemical Journal* 7.5 (Oct. 1913), pp. 471–480. ISSN: 0264-6021. DOI: 10.1042/bj0070471.

[40] James E Ferrell. "How responses get more switch-like as you move down a protein kinase cascade". In: *Trends in Biochemical Sciences* 22.8 (1997), pp. 288–289. ISSN: 0968-0004. DOI: https://doi.org/10.1016/S0968-0004(97)82217-7.

[41] Guy Shinar and Martin Feinberg. "Structural Sources of Robustness in Biochemical Reaction Networks". In: *Science* 327.5971 (Mar. 12, 2010). Publisher: American Association for the Advancement of Science, pp. 1389–1391. DOI: 10.1126/science.1183372. URL: https://www.science.org/doi/10.1126/science.1183372 (visited on 07/24/2022).

[42] Nicholas Silver et al. "Selection of housekeeping genes for gene expression studies in human reticulocytes using real-time PCR". In: *BMC Molecular Biology* 7 (Oct. 6, 2006), p. 33. ISSN: 1471-2199. DOI: 10.1186/1471-2199-7-33. URL: https://www.ncbi.nlm.nih.gov/pmc/articles/PMC1609175/ (visited on 07/24/2022).

[43] Mukund Thattai and Alexander van Oudenaarden. "Attenuation of Noise in Ultrasensitive Signaling Cascades". In: *Biophysical Journal* 82.6 (June 1, 2002). Publisher: Elsevier, pp. 2943–2950. ISSN: 0006-3495. DOI: 10.1016/S0006-3495(02)75635-X. URL: https://www.cell.com/biophysj/abstract/S0006-3495(02)75635-X (visited on 07/24/2022).

[44] Sheng Jian Cai and Masayori Inouye. "EnvZ-OmpR Interaction and Osmoregulation in Escherichia coli *". In: *Journal of Biological Chemistry* 277.27 (July 5, 2002). Publisher: Elsevier, pp. 24155–24161. ISSN: 0021-9258, 1083-351X. DOI: 10.1074/

jbc.M110715200. URL: https://www.jbc.org/article/S0021-9258(19)66582-8/abstract (visited on 07/24/2022).

[45] Daniel T. Gillespie. "Exact stochastic simulation of coupled chemical reactions". In: *The Journal of Physical Chemistry* 81.25 (Dec. 1977), pp. 2340–2361. ISSN: 0022-3654, 1541-5740. DOI: 10.1021/j100540a008. URL: https://pubs.acs.org/doi/10.1021/j100540a008 (visited on 06/28/2022).

[46] Daniel T. Gillespie. "Stochastic Simulation of Chemical Kinetics". In: *Annual Review of Physical Chemistry* 58.1 (May 1, 2007), pp. 35–55. ISSN: 0066-426X, 1545-1593. DOI: 10.1146/annurev.physchem.58.032806.104637. URL: https://www.annualreviews.org/doi/10.1146/annurev.physchem.58.032806.104637 (visited on 03/28/2022).

[47] S. Barolo. "Shadow enhancers: frequently asked questions about distributed cis-regulatory information and enhancer redundancy". In: *BioEssays* 34 (2012). PMID: 22083793, pp. 135–141. DOI: 10.1002/bies.201100121. URL: https://doi.org/10.1002/bies.201100121,.

[48] A.T. Garnett, T.A. Square, and D.M. Medeiros. "BMP, wnt and FGF signals are integrated through evolutionarily conserved enhancers to achieve robust expression of Pax3 and zic genes at the zebrafish neural plate border". In: *Development* 139 (2012). PMID: 23034628, pp. 4220–4231. DOI: 10.1242/dev.081497. URL: https://doi.org/10.1242/dev.081497,.

[49] K. Bomblies, N. Dagenais, and D. Weigel. "Redundant Enhancers Mediate Transcriptional Repression of AGAMOUS by APETALA2". In: *Developmental Biology* 216.260–264 (1999). . DOI: p. 9504. DOI: 10.1006/dbio.1999.. URL: https://doi.org/10.1006/dbio.1999..

[50] D. Cheung and J. Ma. "Probing the impact of temperature on molecular events in a developmental system". pt. In: *Scientific Reports* 5.13124 (2015). PMID: 26286011. DOI: 10.1038/srep13124. URL: https://doi.org/10.1038/srep13124,.

[51] J. Chen, V. Nolte, and C. Schlotterer. "Temperature stress mediates decanalization and dominance of gene expression in Drosophila melanogaster". In: *PLOS Genetics* 11:e1004883 (2015). pgen.1004883, PMID: 25719753. DOI: 10.1371/journal.. URL: https://doi.org/10.1371/journal..

[52] D.D. Lam et al. "Partially redundant enhancers cooperatively maintain mammalian pomc expression above a critical functional threshold". In: *PLOS Genetics* 11:e1004935 (2015). PMID: 25671638. DOI: 10.1371/journal.pgen.1004935. URL: https://doi.org/10.1371/journal.pgen.1004935,.

[53] M.W. Perry, A.N. Boettiger, and M. Levine. "Multiple enhancers ensure precision of gap gene-expression patterns in the Drosophila embryo". In: *PNAS* 108.13570–13575 (2011), p. 21 825127. DOI: 10.1073/pnas.1109873108. URL: https://doi.org/10.1073/pnas.1109873108,.

[54] Z. Wunderlich et al. "Kruppel expression levels are maintained through compensatory evolution of shadow enhancers". In: *Cell Reports* 12 (2015). PMID: 26344774, pp. 1740–1747. DOI: 10.1016/j.celrep.2015.08.021. URL: https://.

[55] N.M. Ghiasvand et al. "Deletion of a remote enhancer near ATOH7 disrupts retinal neurogenesis, causing NCRNA disease". In: *Nature Neuroscience* 14.578 (2011). PMID: 21441919, p. 586. DOI: 10.1038/nn.2798. URL: https://doi.org/10.1038/nn.2798,.

[56] S.L. McKnight and O.L. Miller. "Post-replicative nonribosomal transcription units in D. melanogaster embryos". In: *Cell* 17 (1979). PMID: 113103, pp. 551–563. DOI: 10.1016/0092-8674(79)90263-0. URL: https://doi.org/10.1016/0092-8674(79)90263-0,.

[57] Trcek Chubb JR et al. “Transcriptional pulsing of a developmental gene”. In: *Current Biology* 16 (2006). PMID: 16713960, pp. 1018–1025. DOI: 10.1016/j.cub.2006.03.092. URL: https://doi.org/10.1016/j.cub.2006.03.092,.

[58] R.D. Dar et al. “Transcriptional burst frequency and burst size are equally modulated across the human genome”. In: *PNAS* 109 (2012). DOI: pp. 17454–17459. DOI: 10.1073/pnas.1213530109. URL: https://doi.org/10.1073/pnas.1213530109,.

[59] A. Sanchez and I. Golding. “Genetic determinants and cellular constraints in noisy gene expression”. fr. In: *Science* 342 (2013). PMID: 24311680, pp. 1188–1193. DOI: 10.1126/science.1242975. URL: https://doi.org/10.1126/science.1242975,.

[60] D. Zenklusen, D.R. Larson, and R.H. Singer. “Single-RNA counting reveals alternative modes of gene expression in yeast”. In: *Nature Structural & Molecular Biology* 15 (2008). PMID: 1 9011635, pp. 1263–1271. DOI: 10.1038/nsmb.1514. URL: https://doi.org/10.1038/nsmb.1514,.

[61] J.P. Bothma et al. “Dynamic regulation of eve stripe 2 expression reveals transcriptional bursts in living Drosophila embryos”. In: *PNAS* 111 (2014). PMID: 24994903, pp. 10598–10603. DOI: 10.1073/pnas.1410022111. URL: https://.

[62] G. Csardi et al. “Accounting for experimental noise reveals that mRNA levels, amplified by post-transcriptional processes, largely determine steady-state protein levels in yeast”. In: *PLOS Genetics* 11:e1005206 (2015). PMID: 25950722. DOI: 10.1371/journal.pgen.1005206. URL: https://doi.org/10.1371/journal.pgen.1005206,.

[63] M.M.K. Hansen et al. “Cytoplasmic amplification of transcriptional noise generates substantial Cell-to-Cell variability”. In: *Cell Systems* 7 (2018). 08.002, PMID: 30243562, pp. 384–397. DOI: 10.1016/j.cels.2018.. URL: https://doi.org/10.1016/j.cels.2018..

[64] W.J. Blake et al. “Noise in eukaryotic gene expression”. In: *Nature* 422 (2003). PMID: 12687005, pp. 633–637. DOI: 10.1038/nature01546. URL: https://doi.org/10.1038/nature01546,.

[65] M. Lagha, J.P. Bothma, and M. Levine. “Mechanisms of transcriptional precision in animal development”. In: *Trends in Genetics* 28 (2012). PMID: 22513408, pp. 409–416. DOI: 10.1016/j.tig.2012.03.006. URL: https://doi.org/10.1016/j.tig.2012.03.006,.

[66] L.C. Stapel, C. Zechner, and N.L. Vastenhouw. “Uniform gene expression in embryos is achieved by temporal averaging of transcription noise”. In: *Genes & Development* 31 (2017). 302935.117, PMID: 28903980, pp. 1635–1640. DOI: 10.1101/gad.. URL: https://doi.org/10.1101/gad..

[67] A. Raj et al. “Variability in gene expression underlies incomplete penetrance”. In: *Nature* 463 (2010). PMID: 20164922, pp. 913–918. DOI: 10.1038/nature08781. URL: https://doi.org/10.1038/nature08781,.

[68] T. Erdmann, M. Howard, and P.R. Wolde. “Role of spatial averaging in the precision of gene expression patterns”. In: *Physical Review Letters* 103.258101 (2009). PMID: 20366291. DOI: 10.1103/PhysRevLett.103.258101. URL: https://doi.org/10.1103/PhysRevLett.103.258101,.

[69] J.O. Dubuis, R. Samanta, and T. Gregor. “Accurate measurements of dynamics and reproducibility in small genetic networks”. In: *Molecular Systems Biology* 9.639 (2013). PMID: 23340845. DOI: 10.1038/msb.2012.72. URL: https://doi.org/10.1038/msb.2012.72,.

[70] T. Gregor et al. “Probing the limits to positional information”. In: *Cell* 130.153 (2007). PMID: 17632062, p. 164. DOI: 10.1016/j.cell.2007.05.025. URL: https://doi.org/10.1016/j.cell.2007.05.025,.

[71] A. Preiss et al. “Molecular genetics of Kruppel, a gene required for segmentation of the Drosophila embryo”. In: *Nature* 313 (1985). PMID: 3 917552, pp. 27–32. DOI: 10.1038/313027a0. URL: https://doi.org/10.1038/313027a0,.

[72] H.G. Garcia et al. “Quantitative imaging of transcription in living Drosophila embryos links polymerase activity to patterning”. In: *Current Biology* 23 (2013). cub.2013.08.054, PMID: 24139738, pp. 2140–2145. DOI: 10.1016/j.. URL: https://doi.org/10.1016/j..

[73] E. Bertrand et al. “Localization of ASH1 mRNA particles in living yeast”. In: *Molecular Cell* 2 (1998), pp. 437–445. DOI: 10.1016/S1097-2765(00)80143-4. URL: https://doi.org/10.1016/S1097-2765(00)80143-4.

[74] T. Lucas et al. “Live imaging of bicoid-dependent transcription in Drosophila embryos”. In: *Current Biology* 23 (2013). PMID: 24139736, pp. 2135–2139. DOI: 10.1016/j.cub.2013.08.053. URL: https://doi.org/.

[75] B. Lim et al. “Visualization of transvection in living Drosophila Embryos”. In: *Molecular Cell* 70 (2018). PMID: 29606591, pp. 287–296. DOI: 10.1016/j.molcel.2018.02.029. URL: https://doi.org/10.1016/j.molcel.2018.02.029,.

[76] T. Fukaya and M. Levine. “Transvection”. In: *Current Biology* 27:R1047–R1049 (2017). 2017.08.001, PMID: 29017034. DOI: 10.1016/j.cub.. URL: https://doi.org/10.1016/j.cub..

[77] N.C. Lammers et al. *Binary transcriptional control of pattern formation in development*. en. bioRxiv. DOI: 2018. DOI: 10.1101/335919. URL: https://doi.org/10.1101/335919.

[78] R.D. Dar et al. “Transcriptional bursting explains the Noise-Versus-Mean relationship in mRNA and protein levels”. In: *PLOS ONE* 11:e0158298 (2016). PMID: 27467384. DOI: 10.1371/journal.pone.0158298. URL: https://doi.org/10.1371/journal.pone.0158298,.

[79] M.B. Elowitz et al. "Stochastic gene expression in a single cell". In: *Science* 297.1183 (2002). PMID: 12183631. DOI: 10.1126/science.1070919. URL: https://doi.org/10.1126/science.1070919,.

[80] J.M. Raser and E.K. O'Shea. "Noise in gene expression: origins, consequences, and control". fr. In: *Science* 309.2010 (2005). PMID: 16179466. DOI: 10.1126/science.1105891. URL: https://doi.org/10.1126/science.1105891,.

[81] A.M. Arias and P. Hayward. "Filtering transcriptional noise during development: concepts and mechanisms". In: *Nature Reviews Genetics* 7 (2006). PMID: 16369570, pp. 34–44. DOI: 10.1038/nrg1750. URL: https://doi.org/10.1038/nrg1750,.

[82] S.C. Little, M. Tikhonov, and T. Gregor. "Precise developmental gene expression arises from globally stochastic transcriptional activity". In: *Cell* 154 (2013). PMID: 23953111, pp. 789–800. DOI: 10.1016/j.cell.2013.07.025. URL: https://doi.org/10.1016/j.cell.2013.07.025,.

[83] F. He et al. "Probing intrinsic properties of a robust morphogen gradient in Drosophila". In: *Developmental Cell* 15 (2008). PMID: 18854140, pp. 558–567. DOI: 10.1016/j.devcel.2008.09.004. URL: https://doi.org/10.1016/j.devcel.2008.09.004,.

[84] J.P. Bothma et al. "LlamaTags: a versatile tool to image transcription factor dynamics in live embryos". In: *Cell* 173.1810–1822 (2018), p. 29754 814. DOI: 10.1016/j.cell.2018.03.069. URL: https://doi.org/10.1016/j.cell.2018.03.069,.

[85] M. Mir et al. "Dynamic multifactor hubs interact transiently with sites of active transcription in Drosophila embryos". In: *eLife 7:e40497*. PMID: 30589412. 2018. URL: https://doi..

[86] X. Liu et al. "Functional sequestration of transcription factor activity by repetitive DNA". In: *Journal of Biological Chemistry* 282 (2007). M702547200, PMID: 17526489, pp. 20868–20876. DOI: 10.1074/jbc.. URL: https://doi.org/10.1074/jbc..

[87] S. Janssen et al. "Specific gain- and loss-of-function phenotypes induced by satellite-specific DNA-binding drugs fed to Drosophila melanogaster". In: *Molecular Cell* 6 (2000). PMID: 11106741, pp. 1013–1024. DOI: 10.1016/S1097-2765(00)00100-3. URL: https://doi.org/10.1016/S1097-2765(00)00100-3,.

[88] M.A. Laboulaye et al. "Mapping transgene insertion sites reveals complex interactions between mouse transgenes and neighboring endogenous genes". In: *Frontiers in Molecular Neuroscience* 11.385 (2018). PMID: 30405348. DOI: 10.3389/fnmol.2018.00385. URL: https://doi.org/10.3389/fnmol.2018.00385,.

[89] A. Thompson and M.J. Gasson. "Location effects of a reporter gene on expression levels and on native protein synthesis in Lactococcus lactis and Saccharomyces cerevisiae". In: *Applied and Environmental Microbiology* 67 (2001). DOI: pp. 3434–3439. DOI: 10.1128/AEM.67.8.3434-3439.2001. URL: https://doi.org/10.1128/AEM.67.8.3434-3439.2001,.

[90] L. Wei et al. "Regulation by competition: a hidden layer of gene regulatory network". In: *Quantitative Biology* 7.110–121 (2019), pp. 0162–5. DOI: 10.1007/s40484-018-. URL: https://doi.org/10.1007/s40484-018-.

[91] E Preger-Ben Noon et al. "Comprehensive analysis of a cis-Regulatory region reveals pleiotropy in enhancer function". In: *Cell Reports* 22 (2018). PMID: 29539428, pp. 3021–3031. DOI: 10.1016/j.celrep.2018.02.073. URL: https://doi.org/10.1016/j.celrep.2018.02.073,.

[92] L. Dunipace, Z. Akos, and A. Stathopoulos. "Coacting enhancers can have complementary functions within gene regulatory networks and promote canalization". In: *PLOS Genetics* 15:e1008525 (2019). journal.pgen.1008525, PMID: 31830033. URL: https://doi.org/10.1371/.

[93] Ezzat El-Sherif and Michael Levine. "Shadow Enhancers Mediate Dynamic Shifts of Gap Gene Expression in the Drosophila Embryo". In: *Current biology: CB* 26.9 (May 9, 2016), pp. 1164–1169. ISSN: 1879-0445. DOI: 10.1016/j.cub.2016.02.054.

[94] M.W. Perry et al. "Precision of hunchback expression in the Drosophila embryo". In: *Current Biology* 22 (2012). PMID: 23122844, pp. 2247–2252. DOI: 10.1016/j.cub.2012.09.051. URL: https://doi.org/10.1016/j.cub.2012.09.051,.

[95] L. Dunipace, A. Ozdemir, and A. Stathopoulos. "Complex interactions between cis-regulatory modules in native conformation are critical for Drosophila snail expression". In: *Development* 138.4566 (2011). URL: https://doi.org/10.1242/.

[96] J. Yan et al. "Regulatory logic driving stable levels of defective proventriculus expression during terminal photoreceptor specification in flies". In: *Development* 144 (2017). PMID: 28126841, pp. 844–855. DOI: 10.1242/dev.144030. URL: https://doi.org/10.1242/dev.144030,.

[97] M. Hoch et al. "cis-acting control elements for kruppel expression in the Drosophila embryo". In: *The EMBO Journal* 9 (1990). x, PMID: 2114978, pp. 2587–2595. DOI: 10.1002/j.1460-2075.1990.tb07440.. URL: https://doi.org/10.1002/j.1460-2075.1990.tb07440..

[98] J. Jaeger et al. "Dynamical analysis of regulatory interactions in the gap gene system of Drosophila melanogaster". In: *Genetics* 167 (2004). PMID: 15342511, pp. 1721–1737. DOI: 10.1534/genetics.104.027334. URL: https://doi.org/10.1534/genetics.104.027334,.

[99] A. Sanchez and J. Kondev. "Transcriptional control of noise in gene expression". fr. In: *PNAS* 105 (2008). PMID: 18353986, pp. 5081–5086. DOI: 10.1073/pnas.0707904105. URL: https://doi.org/10.1073/pnas.0707904105,.

[100] A. Sanchez et al. "Effect of promoter architecture on the cell-to-cell variability in gene expression". In: *PLOS Computational Biology* 7:e1001100 (2011). pcbi.1001100,

PMID: 21390269. DOI: 10.1371/journal.. URL: https://doi.org/10.1371/journal..

[101] T. Fukaya, B. Lim, and M. Levine. "Enhancer control of transcriptional bursting". In: *Cell* 166 (2016). PMID: 27293191, pp. 358–368. DOI: 10.1016/j.cell.2016.05.025. URL: https://.

[102] Alvaro Fletcher, Zeba Wunderlich, and German Enciso. "Shadow enhancers mediate trade-offs between transcriptional noise and fidelity". In: *Manuscript submitted for publication* (Aug. 7, 2022).

[103] Michael W. Perry et al. "Shadow Enhancers Foster Robustness of Drosophila Gastrulation". In: *Current Biology* 20.17 (Sept. 14, 2010), pp. 1562–1567. ISSN: 0960-9822. DOI: 10.1016/j.cub.2010.07.043. URL: https://www.sciencedirect.com/science/article/pii/S0960982210009450 (visited on 07/19/2022).

[104] Barbora Antosova et al. "The Gene Regulatory Network of Lens Induction Is Wired through Meis-Dependent Shadow Enhancers of Pax6". In: *PLoS genetics* 12.12 (Dec. 2016), e1006441. ISSN: 1553-7404. DOI: 10.1371/journal.pgen.1006441.

[105] Max V. Staller et al. "Shadow enhancers enable Hunchback bifunctionality in the Drosophila embryo". In: *Proceedings of the National Academy of Sciences* 112.3 (Jan. 20, 2015). Publisher: Proceedings of the National Academy of Sciences, pp. 785–790. DOI: 10.1073/pnas.1413877112. URL: https://www.pnas.org/doi/10.1073/pnas.1413877112 (visited on 07/04/2022).

[106] Rok Grah, Benjamin Zoller, and Gašper Tkačik. "Nonequilibrium models of optimal enhancer function". In: *Proceedings of the National Academy of Sciences* 117.50 (Dec. 15, 2020). Publisher: Proceedings of the National Academy of Sciences, pp. 31614–31622. DOI: 10.1073/pnas.2006731117. URL: https://www.pnas.org/doi/10.1073/pnas.2006731117 (visited on 06/29/2022).

[107] Jean-Pierre Changeux. "Allostery and the Monod-Wyman-Changeux model after 50 years". In: *Annual Review of Biophysics* 41 (2012), pp. 103–133. ISSN: 1936-1238. DOI: 10.1146/annurev-biophys-050511-102222.

[108] Kari Nousiainen, Jukka Intosalmi, and Harri Lähdesmäki. "A Mathematical Model for Enhancer Activation Kinetics During Cell Differentiation". In: *Algorithms for Computational Biology*. Ed. by Ian Holmes, Carlos Martín-Vide, and Miguel A. Vega-Rodríguez. Lecture Notes in Computer Science. Cham: Springer International Publishing, 2019, pp. 191–202. ISBN: 978-3-030-18174-1. DOI: 10.1007/978-3-030-18174-1_14.

[109] Guillermo Rodrigo and Juan F. Poyatos. "Genetic Redundancies Enhance Information Transfer in Noisy Regulatory Circuits". In: *PLOS Computational Biology* 12.10 (Oct. 14, 2016). Publisher: Public Library of Science, e1005156. ISSN: 1553-7358. DOI: 10.1371/journal.pcbi.1005156. URL: https://journals.plos.org/ploscompbiol/article?id=10.1371/journal.pcbi.1005156 (visited on 06/22/2022).

[110] Abhyudai Singh and João P. Hespanha. "Approximate Moment Dynamics for Chemically Reacting Systems". In: *IEEE Transactions on Automatic Control* 56.2 (Feb. 2011). Conference Name: IEEE Transactions on Automatic Control, pp. 414–418. ISSN: 1558-2523. DOI: 10.1109/TAC.2010.2088631.

[111] Cédric Feschotte. "Transposable elements and the evolution of regulatory networks". In: *Nature Reviews Genetics* 9.5 (May 2008). Number: 5 Publisher: Nature Publishing Group, pp. 397–405. ISSN: 1471-0064. DOI: 10.1038/nrg2337. URL: https://www.nature.com/articles/nrg2337 (visited on 07/03/2022).

[112] J. Jurka. "Conserved eukaryotic transposable elements and the evolution of gene regulation". In: *Cellular and Molecular Life Sciences* 65.2 (Jan. 1, 2008), pp. 201–

204. ISSN: 1420-9071. DOI: 10.1007/s00018-007-7369-3. URL: https://doi.org/10.1007/s00018-007-7369-3 (visited on 07/03/2022).

[113] Enrique Viguera, Danielle Canceill, and S.Dusko Ehrlich. "Replication slippage involves DNA polymerase pausing and dissociation". In: *The EMBO Journal* 20.10 (May 15, 2001). Publisher: John Wiley & Sons, Ltd, pp. 2587–2595. ISSN: 0261-4189. DOI: 10.1093/emboj/20.10.2587. URL: https://www.embopress.org/doi/full/10.1093/emboj/20.10.2587 (visited on 07/03/2022).

[114] Danielle Canceill, Enrique Viguera, and S. Dusko Ehrlich. "Replication Slippage of Different DNA Polymerases Is Inversely Related to Their Strand Displacement Efficiency *". In: *Journal of Biological Chemistry* 274.39 (Sept. 24, 1999). Publisher: Elsevier, pp. 27481–27490. ISSN: 0021-9258, 1083-351X. DOI: 10.1074/jbc.274.39.27481. URL: https://www.jbc.org/article/S0021-9258(19)52145-7/abstract (visited on 07/03/2022).

[115] Michael Lynch and Georgi K. Marinov. "The bioenergetic costs of a gene". In: *Proceedings of the National Academy of Sciences of the United States of America* 112.51 (Dec. 22, 2015), pp. 15690–15695. ISSN: 0027-8424. DOI: 10.1073/pnas.1514974112. URL: https://www.ncbi.nlm.nih.gov/pmc/articles/PMC4697398/ (visited on 07/03/2022).

[116] François Spitz and Eileen E. M. Furlong. "Transcription factors: from enhancer binding to developmental control". In: *Nature Reviews Genetics* 13.9 (Sept. 2012). Number: 9 Publisher: Nature Publishing Group, pp. 613–626. ISSN: 1471-0064. DOI: 10.1038/nrg3207. URL: https://www.nature.com/articles/nrg3207 (visited on 07/20/2022).

[117] Mark Rebeiz and Miltos Tsiantis. "Enhancer evolution and the origins of morphological novelty". In: *Current Opinion in Genetics & Development*. Developmental mechanisms, patterning and evolution 45 (Aug. 1, 2017), pp. 115–123. ISSN: 0959-

437X. DOI: 10.1016/j.gde.2017.04.006. URL: https://www.sciencedirect.com/science/article/pii/S0959437X16301320 (visited on 07/20/2022).

[118] Farzad Farnoud, Moshe Schwartz, and Jehoshua Bruck. "Estimation of duplication history under a stochastic model for tandem repeats". In: *BMC Bioinformatics* 20.1 (Feb. 6, 2019), p. 64. ISSN: 1471-2105. DOI: 10.1186/s12859-019-2603-1. URL: https://doi.org/10.1186/s12859-019-2603-1 (visited on 07/03/2022).

[119] Justin Crocker and Garth R Ilsley. "Using synthetic biology to study gene regulatory evolution". In: *Current Opinion in Genetics & Development*. Evolutionary genetics 47 (Dec. 1, 2017), pp. 91–101. ISSN: 0959-437X. DOI: 10.1016/j.gde.2017.09.001. URL: https://www.sciencedirect.com/science/article/pii/S0959437X1730014X (visited on 07/20/2022).

[120] Harold M. McNamara, Beatrice Ramm, and Jared E. Toettcher. "Synthetic developmental biology: New tools to deconstruct and rebuild developmental systems". In: *Seminars in Cell & Developmental Biology* (Apr. 26, 2022). ISSN: 1084-9521. DOI: 10.1016/j.semcdb.2022.04.013. URL: https://www.sciencedirect.com/science/article/pii/S1084952122001380 (visited on 07/20/2022).

[121] Guangyao Li and Lei Zhou. "Genome-Wide Identification of Chromatin Transitional Regions Reveals Diverse Mechanisms Defining the Boundary of Facultative Heterochromatin". In: *PLoS One* 8.6 (2013). DOI: 10.1371/journal.pone.0067156.

[122] Hisashi Tamaru. "Confining euchromatin/heterochromatin territory: Jumonji crosses the line". In: *Genes and Development* 24.14 (2010), pp. 1465–1478. DOI: 10.1101/gad.1941010.

[123] Jianrong Wang, Victoria V. Lunyak, and I. King Jordan. "Genome-wide prediction and analysis of human chromatin boundary elements". In: *Nuclei Acids Res.* 40.2 (2012), pp. 511–529. DOI: 10.1093/nar/gkr750.

[124] Jiyong Wang et al. "Chromosome boundary elements and regulation of heterochromatin spreading". In: *Cellular and Molecular Life Sciences* 71.24 (2014), pp. 4841–4852. DOI: 10.1007/s00018-014-1725-x.

[125] D. Michieletto, E. Orlandini, and D. Marenduzzo. "Polymer model with epigenetic recoloring reveals a pathway for the de novo establishment and 3D organization of chromatin domains". In: *Physical Review X* 6.4 (2016), pp. 1–15. DOI: 10.1103/PhysRevX.6.041047. eprint: 1606.04653.

[126] Veit Schwämmle and Ole Nørregaard Jensen. "A Computational Model for Histone Mark Propagation Reproduces the Distribution of Heterochromatin in Different Human Cell Types". In: *PLoS ONE* 8.9 (2013). DOI: 10.1371/journal.pone.0073818. eprint: 1309.7157.

[127] Fabian Erdel and Eric C. Greene. "Generalized nucleation and looping model for epigenetic memory of histone modifications". In: *Proceedings of the National Academy of Sciences* 113.29 (July 19, 2016), E4180–E4189. ISSN: 0027-8424, 1091-6490. DOI: 10.1073/pnas.1605862113. URL: http://www.pnas.org/lookup/doi/10.1073/pnas.1605862113 (visited on 08/25/2021).

[128] Ian B. Dodd and Kim Sneppen. "Barriers and silencers: A theoretical toolkit for control and containment of nucleosome-based epigenetic states". In: *Journal of Molecular Biology* 414.4 (2011), pp. 624–637. DOI: 10.1016/j.jmb.2011.10.027.

[129] C. Hodges and G. R. Crabtree. "Dynamics of inherently bounded histone modification domains". In: *Proceedings of the National Academy of Sciences* 109.33 (Aug. 14, 2012), pp. 13296–13301. ISSN: 0027-8424, 1091-6490. DOI: 10.1073/pnas.1211172109. URL: http://www.pnas.org/cgi/doi/10.1073/pnas.1211172109 (visited on 08/25/2021).

[130] Swagatam Mukhopadhyay and Anirvan M. Sengupta. "The Role of Multiple Marks in Epigenetic Silencing and the Emergence of a Stable Bivalent Chromatin State".

In: *PLoS Computational Biology* 9.7 (July 18, 2013). Ed. by Narendra Maheshri, e1003121. ISSN: 1553-7358. DOI: 10.1371/journal.pcbi.1003121. URL: https://dx.plos.org/10.1371/journal.pcbi.1003121 (visited on 08/25/2021).

[131] Daniel Jost and Cédric Vaillant. "Epigenomics in 3D: importance of long-range spreading and specific interactions in epigenomic maintenance". In: *Nucleic Acids Research* 46.5 (Mar. 16, 2018), pp. 2252–2264. ISSN: 0305-1048, 1362-4962. DOI: 10.1093/nar/gky009. URL: https://academic.oup.com/nar/article/46/5/2252/4818920 (visited on 08/25/2021).

[132] Marissa Vignali et al. "Distribution of acetylated histones resulting from Gal4-VP16 recruitment of SAGA and NuA4 complexes". In: *The EMBO Journal* 19.11 (2000), pp. 2629–2640. DOI: 10.1093/emboj/19.11.2629.

[133] Gary Felsenfeld and James D. McGhee. "Structure of the 30 nm chromatin fiber". In: *Cell* 44.3 (1986), pp. 375–377. DOI: 10.1016/0092-8674(86)90456-3.

[134] Christian Marion and Bernard Roux. "Influence of histone H1 on chromatin structure". In: *Biochemical and Biophysical Research Communications* 94.2 (1980), pp. 535–541. DOI: 10.1016/0006-291X(80)91264-4.

[135] Bing Rui Zhou et al. "Revisit of Reconstituted 30-nm Nucleosome Arrays Reveals an Ensemble of Dynamic Structures". In: *Journal of Molecular Biology* 430.18 (2018), pp. 3093–3110. DOI: 10.1016/j.jmb.2018.06.020.

[136] Eden Fussner et al. "Open and closed domains in the mouse genome are configured as 10-nm chromatin fibres". In: *EMBO Reports* 13.11 (2012), pp. 992–996. DOI: 10.1038/embor.2012.139.

[137] Kazuhiro Maeshima, Satoru Ide, and Michael Babokhov. "Dynamic chromatin organization without the 30-nm fiber". In: *Current Opinion in Cell Biology* 58.30 (2019), pp. 95–104. DOI: 10.1016/j.ceb.2019.02.003.

[138] Kazuhiro Maeshima et al. “Chromatin as dynamic 10-nm fibers”. In: *Chromosoma* 123.3 (2014), pp. 225–237. DOI: 10.1007/s00412-014-0460-2.

[139] Maria Aurelia Ricci et al. “Chromatin Fibers Are Formed by Heterogeneous Groups of Nucleosomes In Vivo”. In: *Cell* 160.6 (Mar. 2015), pp. 1145–1158. ISSN: 00928674. DOI: 10.1016/j.cell.2015.01.054. URL: https://linkinghub.elsevier.com/retrieve/pii/S0092867415001324 (visited on 07/25/2021).

[140] Kazuhiro Maeshima, Saera Hihara, and Mikhail Eltsov. “Chromatin structure: does the 30-nm fibre exist in vivo?” In: *Current Opinion in Cell Biology* 22.3 (June 2010), pp. 291–297. ISSN: 09550674. DOI: 10.1016/j.ceb.2010.03.001. URL: https://linkinghub.elsevier.com/retrieve/pii/S0955067410000256 (visited on 07/25/2021).

[141] Horng D. Ou et al. “ChromEMT: Visualizing 3D chromatin structure and compaction in interphase and mitotic cells”. In: *Science* 357.6349 (July 28, 2017), eaag0025. ISSN: 0036-8075, 1095-9203. DOI: 10.1126/science.aag0025. URL: https://www.sciencemag.org/lookup/doi/10.1126/science.aag0025 (visited on 07/25/2021).

[142] Delphine Quénet, James G. McNally, and Yamini Dalal. “Through thick and thin: The conundrum of chromatin fibre folding in vivo”. In: *EMBO Reports* 13.11 (2012), pp. 943–944. DOI: 10.1038/embor.2012.143.

[143] Chenyi Wu, Andrew Bassett, and Andrew Travers. “A variable topology for the 30 nm chromatin fibre”. In: *EMBO reports* 8.12 (Dec. 2007), pp. 1129–1134. ISSN: 1469-221X, 1469-3178. DOI: 10.1038/sj.embor.7401115. URL: https://onlinelibrary.wiley.com/doi/10.1038/sj.embor.7401115 (visited on 07/23/2021).

[144] Sharon Pepenella, Kevin J. Murphy, and Jeffrey J. Hayes. “Intra- and inter-nucleosome interactions of the core histone tail domains in higher-order chromatin structure”. In: *Chromosoma* 123.1-2 (2014), pp. 3–13. DOI: 10.1007/s00412-013-0435-8.

[145] Wladyslaw A. Krajewski. "On the role of inter-nucleosomal interactions and intrinsic nucleosome dynamics in chromatin function". In: *Biochemistry and Biophysics Reports* 5 (2016), pp. 492–501. DOI: 10.1016/j.bbrep.2016.02.009.

[146] Olga I. Kulaeva et al. "Internucleosomal interactions mediated by histone tails allow distant communication in chromatin". In: *Journal of Biological Chemistry* 287.24 (2012), pp. 20248–20257. DOI: 10.1074/jbc.M111.333104.

[147] Andrew J. Bannister and Tony Kouzarides. "Regulation of chromatin by histone modifications". In: *Cell Research* 21 (2011), pp. 381–395. DOI: 10.1038/cr.2011.22.

[148] P.Y. Kan, T. L. Caterino, and J. J. Hayes. "The H4 Tail Domain Participates in Intra- and Internucleosome Interactions with Protein and DNA during Folding and Oligomerization of Nucleosome Arrays". In: *Molecular and Cellular Biology* 29.2 (2009), pp. 538–546. DOI: 10.1128/mcb.01343-08.

[149] Ju Yeon Lee, Sijie Wei, and Tae Hee Lee. "Effects of histone acetylation by Piccolo NuA4 on the structure of a nucleosome and the interactions between two nucleosomes". In: *Journal of Biological Chemistry* 286.13 (2011), pp. 11099–11109. DOI: 10.1074/jbc.M110.192047.

[150] Zhenhai Li and Hidetoshi Kono. "Distinct Roles of Histone H3 and H2A Tails in Nucleosome Stability". In: *Scientific Reports* 6.31437 (2016), pp. 1–12. DOI: 10.1038/srep31437.

[151] Heather J. Szerlong et al. "Activator-dependent p300 acetylation of chromatin in vitro: Enhancement of transcription by disruption of repressive nucleosome-nucleosome interactions". In: *Journal of Biological Chemistry* 285.42 (2010), pp. 31954–31964. ISSN: 00219258. DOI: 10.1074/jbc.M110.148718.

[152] Sabine M. Görisch et al. "Histone acetylation increases chromatin accessibility". In: *Journal of Cell Science* 118.24 (2005), pp. 5825–5834. DOI: 10.1242/jcs.02689.

[153] Christopher J Fry and Craig L Peterson. "Chromatin remodeling enzymes: who's on first?" In: *Curr Biol.* 11.5 (2001), R185–197. DOI: 10.1016/s0960-9822(01)00090-2.

[154] Gaëlle Legube and Didier Trouche. "Regulating histone acetyltransferases and deacetylases". In: *EMBO Reports* 4.10 (2003), pp. 944–947. DOI: 10.1038/sj.embor.embor941.

[155] Ronen Marmorstein and Sharon Y. Roth. "Histone acetyltransferases: Function, structure, and catalysis". In: *Current Opinion in Genetics and Development* 11.2 (2001), pp. 155–161. DOI: 10.1016/S0959-437X(00)00173-8.

[156] Thomas H. Cormen et al. *Introduction to Algorithms, 3rd Ed*, pp. 658–662. ISBN: 9780262033848.

[157] Claire E. Barnes, David M. English, and Shaun M. Cowley. "Acetylation & Co: an expanding repertoire of histone acylations regulates chromatin and transcription". In: *Essays in Biochemistry* 63.1 (Apr. 23, 2019). Ed. by Nick Gilbert and James Allan, pp. 97–107. ISSN: 0071-1365, 1744-1358. DOI: 10.1042/EBC20180061. URL: https://portlandpress.com/essaysbiochem/article/63/1/97/166/Acetylation-amp-Co-an-expanding-repertoire-of (visited on 07/24/2021).

[158] Siavash K Kurdistani, Saeed Tavazoie, and Michael Grunstein. "Mapping Global Histone Acetylation Patterns to Gene Expression". In: *Cell* 117.6 (June 2004), pp. 721–733. ISSN: 00928674. DOI: 10.1016/j.cell.2004.05.023. URL: https://linkinghub.elsevier.com/retrieve/pii/S0092867404005367 (visited on 07/23/2021).

[159] Linda K. Durrin et al. "Yeast histone H4 N-terminal sequence is required for promoter activation in vivo". In: *Cell* 65.6 (June 1991), pp. 1023–1031. ISSN: 00928674. DOI: 10.1016/0092-8674(91)90554-C. URL: https://linkinghub.elsevier.com/retrieve/pii/009286749190554C (visited on 07/24/2021).

[160] Stuart L. Schreiber and Bradley E. Bernstein. "Signaling Network Model of Chromatin". In: *Cell* 111.6 (Dec. 2002), pp. 771–778. ISSN: 00928674. DOI: 10.1016/

S0092-8674(02)01196-0. URL: https://linkinghub.elsevier.com/retrieve/pii/S0092867402011960 (visited on 07/24/2021).

[161] Vijaysekhar Chellaboina et al. "Modeling and analysis of mass-action kinetics". In: *IEEE Control Systems Magazine* 29.4 (2009), pp. 60–78.

[162] Albert Goldbeter and Daniel E. Koshland Jr. "An amplified sensitivity arising from covalent modification in biological systems". In: *Proc. Natl. Acad. Sci. USA* 78.No 11 (1981), pp. 6840–6844.

[163] Daniel E Koshland, Albert Goldbeter, and Jeffry B Stock. "Amplification and Adaptation in Regulatory and Sensory Systems". In: *Science* 217.4556 (1982), pp. 220–225. DOI: 10.1126/science.7089556.

[164] Zahra Hajihassan and Azra Rabbani-Chadegani. "Studies on the binding affinity of anticancer drug mitoxantrone to chromatin, DNA and histone proteins". In: *Journal of Biomedical Science* 16.1 (2009), pp. 1–7. DOI: 10.1186/1423-0127-16-31.

[165] Shahper N. Khan et al. "Mitoxantrone Induced Impediment of Histone Acetylation and Structural Flexibility of the Protein". In: *Cell Biochemistry and Biophysics* 60.3 (2011), pp. 209–218. DOI: 10.1007/s12013-010-9141-9.

[166] James E. Ferrell. "Tripping the switch fantastic: how a protein kinase cascade can convert graded inputs into switch-like outputs". In: *Trends in Biochemical Sciences* 21.12 (Dec. 1, 1996), pp. 460–466. ISSN: 0968-0004. DOI: 10.1016/S0968-0004(96)20026-X. URL: https://www.sciencedirect.com/science/article/pii/S096800049620026X (visited on 07/25/2022).

[167] J R McCarrey and A D Riggs. "Determinator-inhibitor pairs as a mechanism for threshold setting in development: a possible function for pseudogenes." In: *Proceedings of the National Academy of Sciences of the United States of America* 83.3 (Feb. 1986), pp. 679–683. ISSN: 0027-8424. URL: https://www.ncbi.nlm.nih.gov/pmc/articles/PMC322927/ (visited on 07/25/2022).

[168] Erel Levine et al. "Quantitative Characteristics of Gene Regulation by Small RNA". In: *PLOS Biology* 5.9 (Aug. 21, 2007). Publisher: Public Library of Science, e229. ISSN: 1545-7885. DOI: 10.1371/journal.pbio.0050229. URL: https://journals.plos.org/plosbiology/article?id=10.1371/journal.pbio.0050229 (visited on 07/26/2022).

[169] Derrick H Lenz et al. "The Small RNA Chaperone Hfq and Multiple Small RNAs Control Quorum Sensing in Vibrio harveyi and Vibrio cholerae". In: *Cell* 118.1 (July 9, 2004), pp. 69–82. ISSN: 0092-8674. DOI: 10.1016/j.cell.2004.06.009. URL: https://www.sciencedirect.com/science/article/pii/S0092867404005732 (visited on 07/26/2022).

[170] Pankaj Mehta, Sidhartha Goyal, and Ned S Wingreen. "A quantitative comparison of sRNA-based and protein-based gene regulation". In: *Molecular Systems Biology* 4 (Oct. 14, 2008), p. 221. ISSN: 1744-4292. DOI: 10.1038/msb.2008.58. URL: https://www.ncbi.nlm.nih.gov/pmc/articles/PMC2583084/ (visited on 07/26/2022).

[171] Sun Young Kim and James E. Ferrell. "Substrate Competition as a Source of Ultrasensitivity in the Inactivation of Wee1". In: *Cell* 128.6 (Mar. 23, 2007). Publisher: Elsevier, pp. 1133–1145. ISSN: 0092-8674, 1097-4172. DOI: 10.1016/j.cell.2007.01.039. URL: https://www.cell.com/cell/abstract/S0092-8674(07)00202-4 (visited on 07/25/2022).

[172] Seth Haney, Lee Bardwell, and Qing Nie. "Ultrasensitive Responses and Specificity in Cell Signaling". In: *BMC Systems Biology* 4 (Aug. 25, 2010), p. 119. ISSN: 1752-0509. DOI: 10.1186/1752-0509-4-119. URL: https://www.ncbi.nlm.nih.gov/pmc/articles/PMC2940771/ (visited on 02/13/2021).

[173] Richard I. Joh and Joshua S. Weitz. "To Lyse or Not to Lyse: Transient-Mediated Stochastic Fate Determination in Cells Infected by Bacteriophages". In: *PLoS Computational Biology* 7.3 (Mar. 10, 2011). ISSN: 1553-734X. DOI: 10.1371/journal.pcbi.

1002006. URL: https://www.ncbi.nlm.nih.gov/pmc/articles/PMC3053317/ (visited on 02/13/2021).

[174] C. Y. Huang and J. E. Ferrell. "Ultrasensitivity in the mitogen-activated protein kinase cascade." In: *Proceedings of the National Academy of Sciences* 93.19 (Sept. 17, 1996), pp. 10078–10083. ISSN: 0027-8424, 1091-6490. DOI: 10.1073/pnas.93.19.10078. URL: http://www.pnas.org/cgi/doi/10.1073/pnas.93.19.10078 (visited on 02/13/2021).

[175] Nick I. Markevich, Jan B. Hoek, and Boris N. Kholodenko. "Signaling switches and bistability arising from multisite phosphorylation in protein kinase cascades". In: *The Journal of Cell Biology* 164.3 (Feb. 2, 2004), pp. 353–359. ISSN: 0021-9525. DOI: 10.1083/jcb.200308060. URL: https://www.ncbi.nlm.nih.gov/pmc/articles/PMC2172246/ (visited on 02/14/2021).

[176] Jacque Monod, Jeffries Wyman, and Jean-Pierre Changeux. "On the nature of allosteric transitions: A plausible model". In: *Journal of Molecular Biology* 12.1 (May 1, 1965), pp. 88–118. ISSN: 0022-2836. DOI: 10.1016/S0022-2836(65)80285-6. URL: https://www.sciencedirect.com/science/article/pii/S0022283665802856 (visited on 02/14/2021).

[177] John Condeelis. "How is actin polymerization nucleated in vivo?" In: *Trends in Cell Biology* 11.7 (July 1, 2001), pp. 288–293. ISSN: 0962-8924. DOI: 10.1016/S0962-8924(01)02008-6. URL: https://www.sciencedirect.com/science/article/pii/S0962892401020086 (visited on 07/27/2022).

[178] David Sept. "Microtubule Polymerization: One Step at a Time". In: *Current Biology* 17.17 (Sept. 4, 2007), R764–R766. ISSN: 0960-9822. DOI: 10.1016/j.cub.2007.07.002. URL: https://www.sciencedirect.com/science/article/pii/S0960982207016399 (visited on 07/27/2022).

[179] U. Alon et al. "Robustness in bacterial chemotaxis". In: *Nature* 397.6715 (Jan. 14, 1999), pp. 168–171. ISSN: 0028-0836. DOI: 10.1038/16483.

[180] N. Barkai and S. Leibler. "Robustness in simple biochemical networks". In: *Nature* 387.6636 (June 1997). Number: 6636 Publisher: Nature Publishing Group, pp. 913–917. ISSN: 1476-4687. DOI: 10.1038/43199. URL: https://www.nature.com/articles/43199 (visited on 07/29/2022).

[181] Tau-Mu Yi et al. "Robust perfect adaptation in bacterial chemotaxis through integral feedback control". In: *Proceedings of the National Academy of Sciences* 97.9 (Apr. 25, 2000). Publisher: Proceedings of the National Academy of Sciences, pp. 4649–4653. DOI: 10.1073/pnas.97.9.4649. URL: https://www.pnas.org/doi/10.1073/pnas.97.9.4649 (visited on 07/29/2022).

[182] Eric Batchelor and Mark Goulian. "Robustness and the cycle of phosphorylation and dephosphorylation in a two-component regulatory system". In: *Proceedings of the National Academy of Sciences* 100.2 (Jan. 21, 2003). Publisher: Proceedings of the National Academy of Sciences, pp. 691–696. DOI: 10.1073/pnas.0234782100. URL: https://www.pnas.org/doi/10.1073/pnas.0234782100 (visited on 07/29/2022).

[183] Guy Shinar et al. "Input output robustness in simple bacterial signaling systems". In: *Proceedings of the National Academy of Sciences of the United States of America* 104.50 (Dec. 11, 2007), pp. 19931–19935. ISSN: 1091-6490. DOI: 10.1073/pnas.0706792104.

[184] J. Arjan G. M. de Visser et al. "Perspective: Evolution and detection of genetic robustness". In: *Evolution; International Journal of Organic Evolution* 57.9 (Sept. 2003), pp. 1959–1972. ISSN: 0014-3820. DOI: 10.1111/j.0014-3820.2003.tb00377.x.

[185] D. C. LaPorte, P. E. Thorsness, and D. E. Koshland. "Compensatory phosphorylation of isocitrate dehydrogenase. A mechanism for adaptation to the intracellular environ-

ment". In: *The Journal of Biological Chemistry* 260.19 (Sept. 5, 1985), pp. 10563–10568. ISSN: 0021-9258.

[186] Corentin Briat, Ankit Gupta, and Mustafa Khammash. "Antithetic Integral Feedback Ensures Robust Perfect Adaptation in Noisy Biomolecular Networks". In: *Cell Systems* 2.1 (Jan. 27, 2016). Publisher: Elsevier, pp. 15–26. ISSN: 2405-4712. DOI: 10.1016/j.cels.2016.01.004. URL: https://www.cell.com/cell-systems/abstract/S2405-4712(16)00005-3 (visited on 07/30/2022).

[187] Hirofumi Aiba and Takeshi Mizuno. "Phosphorylation of a bacterial activator protein, OmpR, by a protein kinase, EnvZ, stimulates the transcription of the ompF and ompC genes in Escherichia coli". In: *FEBS Letters* 261.1 (1990), pp. 19–22. ISSN: 1873-3468. DOI: 10.1016/0014-5793(90)80626-T. URL: https://onlinelibrary.wiley.com/doi/abs/10.1016/0014-5793%2890%2980626-T (visited on 07/30/2022).

[188] Linda A. Egger, Heiyoung Park, and Masayori Inouye. "Signal transduction via the histidyl-aspartyl phosphorelay". In: *Genes to Cells* 2.3 (1997), pp. 167–184. ISSN: 1365-2443. DOI: 10.1046/j.1365-2443.1997.d01-311.x. URL: https://onlinelibrary.wiley.com/doi/abs/10.1046/j.1365-2443.1997.d01-311.x (visited on 07/30/2022).

[189] Bruce Alberts et al. "How Genetic Switches Work". In: *Molecular Biology of the Cell. 4th edition* (2002). Publisher: Garland Science. URL: https://www.ncbi.nlm.nih.gov/books/NBK26872/ (visited on 07/24/2022).

[190] Federico Garza de Leon et al. "Tracking Low-Copy Transcription Factors in Living Bacteria: The Case of the lac Repressor". In: *Biophysical Journal* 112.7 (Apr. 11, 2017), pp. 1316–1327. ISSN: 0006-3495. DOI: 10.1016/j.bpj.2017.02.028. URL: https://www.ncbi.nlm.nih.gov/pmc/articles/PMC5390046/ (visited on 07/24/2022).

[191] Michael W. Perry, Alistair N. Boettiger, and Michael Levine. "Multiple enhancers ensure precision of gap gene-expression patterns in the Drosophila embryo". In: *Proceedings of the National Academy of Sciences* 108.33 (Aug. 16, 2011). Publisher: Proceedings of the National Academy of Sciences, pp. 13570–13575. DOI: 10.1073/pnas.1109873108. URL: https://www.pnas.org/doi/10.1073/pnas.1109873108 (visited on 07/25/2022).

[192] Cindy L. White, Robert K. Suto, and Karolin Luger. "Structure of the yeast nucleosome core particle reveals fundamental changes in internucleosome interactions". In: *The EMBO Journal* 20.18 (Sept. 17, 2001), pp. 5207–5218. ISSN: 0261-4189. DOI: 10.1093/emboj/20.18.5207. URL: https://www.ncbi.nlm.nih.gov/pmc/articles/PMC125637/ (visited on 07/25/2022).

[193] Jocelyn Krebs, Elliott Goldstein, and Stephen Kilpatrick. *Lewin's Genes XI*. Burlington, Mass.: Jones & Bartlett Learning., 2014.

[194] Sean R. McGuffee and Adrian H. Elcock. "Diffusion, Crowding & Protein Stability in a Dynamic Molecular Model of the Bacterial Cytoplasm". In: *PLOS Computational Biology* 6.3 (Mar. 5, 2010). Publisher: Public Library of Science, e1000694. ISSN: 1553-7358. DOI: 10.1371/journal.pcbi.1000694. URL: https://journals.plos.org/ploscompbiol/article?id=10.1371/journal.pcbi.1000694 (visited on 07/25/2022).

[195] Nicolas E Buchler and Frederick R Cross. "Protein sequestration generates a flexible ultrasensitive response in a genetic network". In: *Molecular Systems Biology* 5 (May 19, 2009), p. 272. ISSN: 1744-4292. DOI: 10.1038/msb.2009.30. URL: https://www.ncbi.nlm.nih.gov/pmc/articles/PMC2694680/ (visited on 07/25/2022).

[196] F. Horn and R. Jackson. "General mass action kinetics". In: *Archive for Rational Mechanics and Analysis* 47.2 (Jan. 1, 1972), pp. 81–116. ISSN: 1432-0673. DOI: 10.1007/BF00251225. URL: https://doi.org/10.1007/BF00251225 (visited on 07/26/2022).

[197] Susan Gary and Michael Levin. "Transcriptional repression in development". In: *Current Opinion in Cell Biology* 8.3 (June 1, 1996), pp. 358–364. ISSN: 0955-0674. DOI: 10.1016/S0955-0674(96)80010-X. URL: https://www.sciencedirect.com/science/article/pii/S095506749680010X (visited on 07/26/2022).

[198] Steven A. Benner and A. Michael Sismour. "Synthetic biology". In: *Nature Reviews Genetics* 6.7 (July 2005). Number: 7 Publisher: Nature Publishing Group, pp. 533–543. ISSN: 1471-0064. DOI: 10.1038/nrg1637. URL: https://www.nature.com/articles/nrg1637 (visited on 07/26/2022).

[199] Eric Zhang et al. "Modeling of 3D Enhancer-Promoter Interactions Using Experimental Contact Frequency Data". In: *MathBioU & MathExpLR Program* (Aug. 3, 2021).